7-Degree-of-Freedom Hybrid-Manipulator Exoskeleton for Lower-Limb Motion Capture

by

Shaun Bourgeois

B.A.Sc., Simon Fraser University, 2015

Thesis Submitted in Partial Fulfillment of the
Requirements for the Degree of
Master of Applied Science

in the
School of Mechatronic Systems Engineering
Faculty of Applied Sciences

SIMON FRASER UNIVERSITY
Spring 2018

Approval

Name:	**Shaun Bourgeois**
Degree:	**Master of Applied Science**
Title:	**7-Degree-of-Freedom Hybrid-Manipulator Exoskeleton for Lower-Limb Motion Capture**
Examining Committee:	**Chair: Behraad Bahreyni** Associate Professor **Siamak Arzanpour** Senior Supervisor Associate Professor **Edward Park** Co-Supervisor Professor **Flavio Firmani** Supervisor Lecturer **Kevin Oldknow** Internal Examiner Senior Lecturer
Date Defended/Approved:	April 6, 2018

Ethics Statement

The author, whose name appears on the title page of this work, has obtained, for the research described in this work, either:

a. human research ethics approval from the Simon Fraser University Office of Research Ethics

or

b. advance approval of the animal care protocol from the University Animal Care Committee of Simon Fraser University

or has conducted the research

c. as a co-investigator, collaborator, or research assistant in a research project approved in advance.

A copy of the approval letter has been filed with the Theses Office of the University Library at the time of submission of this thesis or project.

The original application for approval and letter of approval are filed with the relevant offices. Inquiries may be directed to those authorities.

Simon Fraser University Library
Burnaby, British Columbia, Canada

Update Spring 2016

Abstract

Lower-limb exoskeletons are wearable robotic systems with a kinematic structure closely matching that of the human leg. In part, this technology can be used to provide clinical assessment and improved independent-walking competency for people living with the effects of stroke, spinal cord injury, Parkinson's disease, multiple sclerosis, and sarcopenia. Individually, these demographics represent approximately: 405 thousand, 100 thousand, 67.5 thousand, 100 thousand, and 5.9 million Canadians, respectively.

Key shortcomings in the current state-of-the-art are: restriction on several of the human leg's primary joint movements, coaxial joint alignments at the exoskeleton-human interface, and exclusion of well-suited parallel manipulator components. A novel exoskeleton design is thus formulated to address these issues while maintaining large ranges of joint motion. Ultimately, a single-leg unactuated prototype is constructed for seven degree-of-freedom joint angle measurements; it achieves an extent of motion-capture accuracy comparable to a commercial inertial-based system during three levels of human mobility testing.

Keywords: lower-limb exoskeleton; motion capture; hybrid manipulator; parallel manipulator; kinematic analysis; electromechanical motion tracking

To my beloved parents and brothers, without whom this work would not have been possible,

and to anyone living with a mobility disability, by whom this work was motivated

Acknowledgements

I would first like to thank my senior supervisor, Dr. Siamak Arzanpour, for his continual support, guidance, and insights throughout my graduate research as well as during my undergraduate capstone project. I would also like to express my gratitude to Dr. Edward Park, my co-supervisor, for his advice, assistance, and encouragement in the duration of my master's program. I will forever value what I have learned from my discussions with them, and I am tremendously grateful to have had the opportunity to work with them and study under their supervision.

Next, I thank Dr. Flavio Firmani and Dr. Kevin Oldknow for their expert advice at pivotal times in this work. Furthermore, I am immensely grateful to them both for sharing their brilliance and mentorship in teaching over the years, which will undoubtedly serve me throughout my career in engineering. I am also indebted to them both for my initial interest and ongoing enthusiasm for robotic manipulators. Their time spent evaluating this thesis is sincerely appreciated.

My gratitude also goes to the Natural Sciences and Engineering Research Council of Canada and Simon Fraser University for the financial support I received.

I am eternally grateful to my father, mother, and brothers. Without their continuous support and encouragement, this work would truly not have been possible. I would also like to express my deepest gratitude to my grandmother, Olga, for contributing in the gift of my laptop, on which most of this work was completed.

A special thank you goes to my dear friend and labmate, Dr. Soheil Sadeqi. His shared software knowledge, research insights, many wisdoms, and friendship were indispensable for this undertaking; I will always cherish the fun and challenging times we had during our years of research. Another thanks to undergraduate co-op students: Puneet Sran, Shiv Patel, Rafiul Islam, and Liam Page for their excellent company and various contributions to the Laboratory for Assistive Robotic Systems. I am also grateful to Dr. Ahmed Arafa, Paul Yoon, and Magnus Musngi for helping me learn to use the Qualisys and Xsens systems.

I also thank my dear friend, Tori, for helping me find the strength within myself to complete this endeavour while reminding me that there's more to life than academia.

Table of Contents

List of Tables

List of Figures

List of Acronyms

Anatomical Motions

Abd.	abduction
Add.	adduction
Dor.	dorsiflexion
Ext.	extension
Ext. Rot.	external rotation
Flex.	flexion
Int. Rot.	internal rotation
Pla.	plantarflexion
Pro.	pronation
Rot.	rotation
Sup.	supination

Existing Exoskeletons and Parallel Manipulators

AE	Agile Eye
ALEX	Active Leg Exoskeleton
BLEEX	Berkeley Lower Extremity Exoskeleton
DGO	Driven Gait Orthosis
eLEGS	Exoskeleton Lower Extremity Gait System
HULC	Human Universal Load Carrier
LEAD	Lower Extremity Assistive Device
LOPES	Lower Extremity Powered Exo-Skeleton
NTU-LEE	Nanyang Technological University's Lower Extremity Exoskeleton
PAM	Pelvic Assist Manipulator
POGO	Pneumatically Operated Gait Orthosis
SAE	Simplified Agile Eye

General

3D	three-dimensional
AC	alternating current
ADC	analog-to-digital conversion
CAD*	computer-aided design

COR	center-of-rotation
CSV	comma-separated values
DARPA	Defense Advanced Research Projects Agency
DC	direct current
DH	Denavit and Hartenberg
DOF	degree-of-freedom
GPI	global performance index
GPIO	general-purpose input/output
IMU	inertial measurement unit
ISR	interrupt service routine
MCU	microcontroller unit
MISO	Master In Slave Out
MoCap	motion capture
MOSI	Master Out Slave In
MS	multiple sclerosis
NaN	not a number
PC	personal computer
PD	Parkinson's disease
Pot.	potentiometer
PPAM	Pleated Pneumatic Artificial Muscle
QTM	Qualisys Track Manager
RSME	root mean square error
SCI	spinal cord injury
SCK	System Clock
SS	Slave Select
STD	standard deviation
USB	Universal Serial Bus

*Note: CAD signifies 'Canadian dollar' if preceded by a monetary value.

Symbols

$\{i\}^{\text{ABC}}$	cartesian frame number i within the generalized ABC manipulator's scope (i.e., ABC is RUS, SAE, RRP, PU, LEG, or SRS)*
$\lvert\mathbf{A}\rvert$	determinant of the generalized matrix $\mathbf{A}$
$\lVert\mathbf{A}\rVert$	2-norm of the generalized matrix $\mathbf{A}$
$\lVert\vec{\mathrm{a}}\rVert$	Euclidean norm of the generalized vector $\vec{\mathrm{a}}$
$\vec{0}_{1\times3}$	one-by-three row vector with all zero-value elements
$\vec{0}_{3\times1}$	three-by-one column vector with all zero-value elements
$\mathbf{0}_{3\times3}$	three-by-three square matrix with all zero-value elements
$\hat{a}$	unit vector specifying the 'approach' direction of a serial manipulator's end-effector, equivalent to the end-effector frame's z-axis
$a\left({}^{j}_{i}\mathbf{T}^{\text{ABC}}\right)$	function that extracts the 'approach' vector (i.e., top three elements of column three) from the input homogeneous transform
$abs(a)$	absolute value of the generalized scalar value a
a_i	center point of the active revolute joint on the RUS manipulator's i^{th} branch
${}^{j}\vec{\mathrm{a}}_i^{\text{RUS}}$	position of a_i represented in terms of the RUS manipulator's j^{th} frame
a_{i-1}	link length Denavit and Hartenberg parameter for the ith link-frame attachment on a serial manipulator
$\operatorname{atan2}(a,b)$	four-quadrant arctangent of the two generalized input numbers a and b
b_i	center point of the passive universal joint on the RUS manipulator's i^{th} branch
${}^{j}\vec{\mathrm{b}}_i^{\text{RUS}}$	position of b_i represented in terms of the RUS manipulator's j^{th} frame
$c(\lambda)$	cosine of the generalized input angle λ
c_i	center point of the passive spherical joint on the RUS manipulator's i^{th} branch
${}^{j}\vec{\mathrm{c}}_i^{\text{RUS}}$	position of c_i represented in terms of the RUS manipulator's j^{th} frame
d_i	link offset Denavit and Hartenberg parameter for the ith link-frame attachment on a serial manipulator
h	z-coordinate of ${}^{4}\vec{\mathrm{c}}_i^{\text{RUS}}$ on the RUS manipulator's i^{th} branch
$\mathbf{I}_{3\times3}$	three-by-three identity matrix
$\mathbf{J}^{\text{ABC}}$	Jacobian matrix of the generalized ABC manipulator
$\mathrm{J}_i^{\text{ABC}}$	i^{th} active joint of the generalized ABC manipulator

$\mathbf{J}_q^{\mathrm{ABC}}$	Jacobian component matrix associated with the active joint variables of the generalized ABC manipulator
$\mathbf{J}_x^{\mathrm{ABC}}$	Jacobian component matrix associated with the end-effector task space coordinates of the generalized ABC manipulator
$\mathrm{J_u}$	passive revolute joint on the SAE's 1st branch
$\mathrm{J_v}$	passive revolute joint adjacent to link $\mathrm{L}_{\mathrm{C1}}^{\mathrm{SAE}}$ on the SAE's 2nd branch
$\mathrm{J_w}$	passive revolute joint adjacent to active joint $\mathrm{J}_2^{\mathrm{SAE}}$ on the SAE's 2nd branch
${}^{3}\mathbf{J}_w^{\mathrm{LEG}}*$	Jacobian matrix based on a pelvis-link point coincident with the hip-joint center and oriented as $\{3\}^{\mathrm{LEG}}$ of the 6R serial-manipulator model of the human leg considered in reverse order (i.e., treating the foot as the base and the pelvis as the end-effector)
k	condition number of a manipulator (i.e., the inverse of local dexterity)
l_1	Euclidean distance between m_1 and the prismatic joint axis of the RRP manipulator
l_2	Euclidean distance between m_1 and m_2 of the RRP manipulator
l_3	Euclidean distance between m_2 and the active spherical joint's projection onto a plane normal to the RRP's passive-revolute-joint axes and containing m_1 and m_2
$\mathrm{L}_i^{\mathrm{ABC}}$	i^{th} link of the generalized ABC manipulator
l_d	distal link length of the RUS manipulator
l_e	Euclidean distance between c_i and c_j passive spherical-joint centers on adjacent i and j branches of the RUS manipulator
l_o	Euclidean distance between the PU manipulator's n_1 and n_2 points
l_p	proximal link length of the RUS manipulator
l_r	Euclidean distance between the PU manipulator's O_1^{PU} and n_1 points
m_1	center point of the revolute joint adjacent to the RRP's prismatic joint
${}^{j}\vec{\mathrm{m}}_1$	position of m_1 represented in terms of the RRP manipulator's j^{th} frame
m_2	center point of the revolute joint adjacent to the RRP manipulator's active spherical joint
${}^{j}\vec{\mathrm{m}}_2$	position of m_2 represented in terms of the RRP manipulator's j^{th} frame
$\hat{n}$	unit vector specifying the 'normal' direction of a serial manipulator's end-effector, equivalent to the end-effector frame's x-axis
n_1	center point of the PU's universal joint
${}^{j}\vec{\mathrm{n}}_1$	position of n_1 represented in terms of the PU manipulator's j^{th} frame
n_2	orthogonal projection of n_1 onto the axis of the PU's prismatic joint

${}^{j}\vec{\mathrm{n}}_2$	position of n_2 represented in terms of the PU manipulator's j^{th} frame
n_3	orthogonal projection of n_1 onto the $\hat{y}_1^{\text{PU}}$ - $\hat{x}_1^{\text{PU}}$ plane
${}^{j}\vec{\mathrm{n}}_3$	position of n_3 represented in terms of the PU manipulator's j^{th} frame
$\hat{o}$	unit vector specifying the 'orientation' direction of a serial manipulator's end-effector, equivalent to the end-effector frame's *y*-axis
O_i^{ABC}	origin of the generalized ABC manipulator's i^{th} frame
${}^{j}\vec{O}_i^{\text{ABC}}$	origin of the generalized ABC manipulator's i^{th} frame represented in terms of its jth frame
P	passive prismatic joint
$\vec{\mathrm{p}}$	vector specifying the position of a serial manipulator's end-effector represented in terms of its local reference frame $\{0\}^{\text{ABC}}$
$p\left({}^{j}_{i}\mathbf{T}^{\text{ABC}}\right)$	function that extracts the 'position' vector (i.e., top three elements of column four) from an input homogeneous transform
${}^{3}\vec{\mathrm{p}}_{i\to w*}$	vector extending from O_i^{LEG} to $w*$, represented in terms of $\{3\}^{\text{LEG}}$
$\vec{q}$	column vector containing the active joint variables of a manipulator
$\vec{q}_{\text{NEUTRAL}}$	vector containing the angular positions of each active joint in the proposed exoskeleton when the wearer's lower limb is posed in its neutral-standing posture
R	passive revolute joint
<u>R</u>	active revolute joint
${}^{j}_{i}\mathbf{R}^{\text{ABC}}$	rotation matrix that converts vector representation from frame $\{i\}^{\text{ABC}}$ to $\{j\}^{\text{ABC}}$ when it is pre-multiplied by this matrix
${}^{j}_{i}\mathbf{R}_{\mathbf{N}}^{\text{ABC}}$	rotation matrix ${}^{j}_{i}\mathbf{R}^{\text{ABC}}$ when its elements are numerically known
${}^{j}_{i}\mathbf{R}_{\mathbf{S}}^{\text{ABC}}$	rotation matrix ${}^{j}_{i}\mathbf{R}^{\text{ABC}}$ when its elements are expressed symbolically (this notation is used to clarify differentiation from ${}^{j}_{i}\mathbf{R}_{\mathbf{N}}^{\text{ABC}}$)
$\mathbf{R}_X(\varepsilon)$	right-hand elemental rotation matrix acting about the *x*-axis and rotating through angle ε; a prime (') or double-prime (") subscript is added to indicate first or second intrinsic rotations, respectively
$\mathbf{R}_Y(\phi)$	right-hand elemental rotation matrix acting about the *y*-axis and rotating through angle ϕ; a prime (') or double-prime (") subscript is added to indicate first or second intrinsic rotations, respectively
$\mathbf{R}_Z(\varphi)$	right-hand elemental rotation matrix acting about the *z*-axis and rotating through angle φ; a prime (') or double-prime (") subscript is added to indicate first or second intrinsic rotations, respectively
$\mathbf{R}_{XY'}(\varepsilon,\phi)$	product of $\mathbf{R}_X(\varepsilon)$ post-multiplied by $\mathbf{R}_{Y'}(\phi)$

$\mathbf{R}_{XY'Z''}(\varepsilon,\phi,\varphi)$	product of $\mathbf{R}_X(\varepsilon)$ successively post-multiplied by $\mathbf{R}_{Y'}(\phi)$ and then $\mathbf{R}_{Z''}(\varphi)$
S	passive spherical joint
<u>S</u>	active spherical joint
$s(\lambda)$	sine of the generalized input angle λ
$\hat{s}_{abi}$	unit vector directed from a_i towards b_i on the RUS manipulator's i^{th} branch
$\hat{s}_{bci}$	unit vector directed from b_i towards c_i on the RUS manipulator's i^{th} branch
$\hat{s}_{Oci}$	unit vector directed from O_i^{RUS} towards c_i on the RUS manipulator's i^{th} branch
${}^j_i\mathbf{T}^{\text{ABC}}$	homogeneous transform containing rotation matrix ${}^j_i\mathbf{R}^{\text{ABC}}$ and the position ${}^j\bar{O}_i^{\text{ABC}}$ to provide both rotational and translational mapping from frame $\{i\}^{\text{ABC}}$ to $\{j\}^{\text{ABC}}$ via pre-multiplication by this matrix
${}^j_i\mathbf{T}_{\mathbf{N}}^{\text{ABC}}$	homogeneous transform ${}^j_i\mathbf{T}^{\text{ABC}}$ when its elements are numerically known
${}^j_i\mathbf{T}_{\mathbf{S}}^{\text{ABC}}$	homogeneous transform ${}^j_i\mathbf{T}^{\text{ABC}}$ when its elements are expressed symbolically (this notation is used to clarify differentiation from ${}^j_i\mathbf{T}_{\mathbf{N}}^{\text{ABC}}$)
$tr(\mathbf{A})$	trace of the generalized matrix $\mathbf{A}$
$\hat{u}$	unit vector identifying the position of the SAE's passive joint $\mathrm{J_u}$ relative to O_0^{SAE}
U	passive universal joint
$\hat{v}$	unit vector identifying the position of the SAE's passive joint $\mathrm{J_v}$ relative to O_0^{SAE}
$\hat{w}$	unit vector identifying the position of the SAE's passive joint $\mathrm{J_w}$ relative to O_0^{SAE}
w^*	center point of the hip joint in the 6R manipulator model of the human lower limb (i.e., the spherical 'wrist' center when the manipulator is regarded in reverse order)
$\bar{x}$	column vector containing a manipulator's end-effector task space coordinates
$x_{1\to2}$	*x*-coordinate of ${}^0\bar{O}_2^{\text{PU}} - {}^0\bar{O}_1^{\text{PU}}$
$x_{2\to1}$	*x*-coordinate of ${}^0\bar{O}_1^{\text{PU}} - {}^0\bar{O}_2^{\text{PU}}$
$\hat{x}_i^{\text{ABC}}$	*x*-axis unit vector of the generalized ABC manipulator's i^{th} frame
${}^j\hat{x}_i^{\text{ABC}}$	$\hat{x}_i^{\text{ABC}}$ represented in terms of the generalized ABC manipulator's j^{th} frame
$y_{1\to2}$	*y*-coordinate of ${}^0\bar{O}_2^{\text{PU}} - {}^0\bar{O}_1^{\text{PU}}$

$y_{2\to1}$	*y*-coordinate of ${}^{0}\vec{O}_{1}^{\mathrm{PU}} - {}^{0}\vec{O}_{2}^{\mathrm{PU}}$
$\hat{y}_i^{\mathrm{ABC}}$	*y*-axis unit vector of the generalized ABC manipulator's i^{th} frame
${}^{j}\hat{y}_i^{\mathrm{ABC}}$	$\hat{y}_i^{\mathrm{ABC}}$ represented in terms of the generalized ABC manipulator's j^{th} frame
$z_{1\to2}$	*z*-coordinate of ${}^{0}\vec{O}_{2}^{\mathrm{PU}} - {}^{0}\vec{O}_{1}^{\mathrm{PU}}$
$z_{2\to1}$	*z*-coordinate of ${}^{0}\vec{O}_{1}^{\mathrm{PU}} - {}^{0}\vec{O}_{2}^{\mathrm{PU}}$
$\hat{z}_i^{\mathrm{ABC}}$	*z*-axis unit vector of the generalized ABC manipulator's i^{th} frame
${}^{j}\hat{z}_i^{\mathrm{ABC}}$	$\hat{z}_i^{\mathrm{ABC}}$ represented in terms of the generalized ABC manipulator's j^{th} frame
α	*x*-axis Euler angle of the SAE manipulator's end-effector orientation derived from its associated rotation matrix using *X*-*Y'*-*Z''* intrinsic ordering of rotations
α_{i-1}	link twist Denavit and Hartenberg parameter for the ith link-frame attachment on a serial manipulator
β	*y*-axis Euler angle of the SAE manipulator's end-effector orientation derived from its associated rotation matrix using *X*-*Y'*-*Z''* intrinsic ordering of rotations
γ	*z*-axis Euler angle of the SAE manipulator's end-effector orientation derived from its associated rotation matrix using *X*-*Y'*-*Z''* intrinsic ordering of rotations
γ_1	initial intrinsic rotation angle about the *x*-axis of $\{1\}^{\mathrm{PU}}$ that produces the $\{1'\}^{\mathrm{PU}}$ frame
γ_2	secondary intrinsic rotation angle about the *y*-axis of $\{1'\}^{\mathrm{PU}}$ that produces the $\{2\}^{\mathrm{PU}}$ frame
γ_3	initial intrinsic rotation angle about the *y*-axis of $\{2\}^{\mathrm{PU}}$ that produces the $\{2'\}^{\mathrm{PU}}$ frame
γ_4	secondary intrinsic rotation angle about the *x*-axis of $\{2'\}^{\mathrm{PU}}$ that produces the $\{1\}^{\mathrm{PU}}$ frame
ζ_1	intrinsic rotation angle about the *z*-axis of $\{1\}^{\mathrm{RRP}}$ that produces the $\{2\}^{\mathrm{RRP}}$ frame
ζ_2	intrinsic rotation angle about the *z*-axis of $\{2\}^{\mathrm{RRP}}$ that produces the $\{1\}^{\mathrm{RRP}}$ frame
θ_i	joint angle Denavit and Hartenberg parameter for the ith link-frame attachment on a serial manipulator
θ_i^{ABC}	angular position of the generalized ABC manipulator's i^{th} active joint
θ_X^{RUS}	*x*-axis Euler angle of the RUS manipulator's end-effector orientation derived from its associated rotation matrix using the Tait-Bryan roll-pitch-yaw convention

θ_Y^{RUS}	*y*-axis Euler angle of the RUS manipulator's end-effector orientation derived from its associated rotation matrix using the Tait-Bryan roll-pitch-yaw convention
θ_Z^{RUS}	*z*-axis Euler angle of the RUS manipulator's end-effector orientation derived from its associated rotation matrix using the Tait-Bryan roll-pitch-yaw convention
μ_{iso}	isotropy index for manipulability performance of a parallel manipulator
υ	local dexterity performance index of a parallel manipulator
ξ_1	constant *z*-axis rotation angle that produces ${}^1\hat{x}_2^{\text{RRP}}$ from the normalized position of ${}^1\vec{\text{m}}_2$ relative to ${}^1\vec{O}_2^{\text{RRP}}$ when projected in the $\hat{y}_1^{\text{RRP}}$ - $\hat{z}_1^{\text{RRP}}$ plane
ξ_2	constant *z*-axis rotation angle that produces ${}^2\hat{x}_1^{\text{RRP}}$ from the normalized position of ${}^2\vec{\text{m}}_1$ relative to ${}^2\vec{O}_1^{\text{RRP}}$ when projected in the $\hat{y}_2^{\text{RRP}}$ - $\hat{z}_2^{\text{RRP}}$ plane
$\sigma_{\max}$	maximum singular value of a Jacobian matrix
$\sigma_{\min}$	minimum singular value of a Jacobian matrix
τ_r	rotational sensitivity performance index of a parallel manipulator
$\vec{\omega}_{pi}$	angular velocity of the proximal link on the RUS manipulator's i^{th} branch

*Note: The ABC abbreviation is a generalized representation of the RUS, SAE, RRP, PU, LEG, or SRS manipulator abbreviations, which are to be defined in the thesis body.

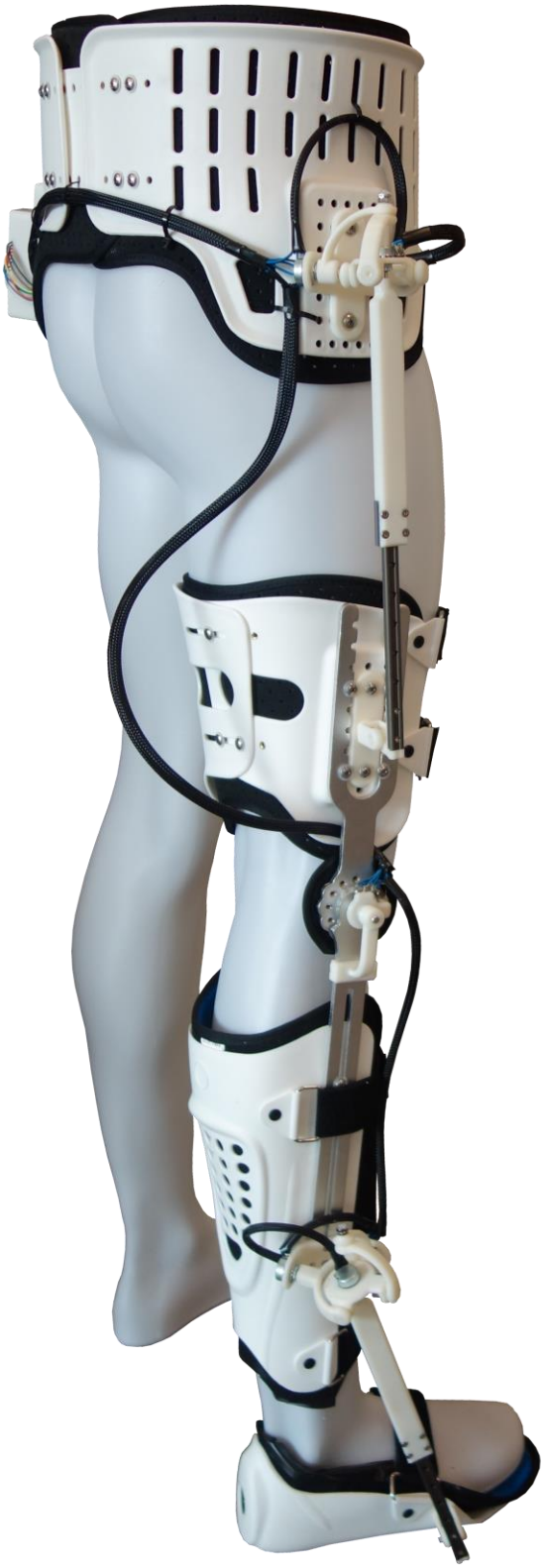

Chapter 1.

Introduction

1.1. Background and Research Scope

Pons et al. define exoskeletons as an instance of wearable robots for which the robotic manipulator's kinematic chain closely corresponds to the anatomical structure of the human body segment with which it interfaces [1]. For the human to retain the same freedom in movement as normally experienced without the exoskeleton, there must be a one-to-one correspondence between the degrees-of-freedom (DOFs) of the anatomical structure and those permitted by the worn manipulator. This complete kinematic compliance is crucial in the design of an ergonomic and non-restrictive exoskeleton. Pons et al. also discuss that the mechanical interface and motion-based functionality of the exoskeleton-human system evokes an inherent aspect of power transfer between the two actors [1]. This presents an opportunity to develop a foundational categorization of exoskeleton devices: those which only accept mechanical power from the interfaced human; those which only supply mechanical power to the interfaced human; and those for which the flux of power transmits in both directions. These categories are intrinsically related to the intended application of the exoskeleton.

Starting with the first-mentioned, an exoskeleton that only receives mechanical power from the human wearer is generally employed for motion capture applications. As mentioned in [1], this may extend to use in motion control for master-slave robotic systems, among other implementations. For these exoskeletons, active joints are sensed but unactuated. One exception is a fully-passive exoskeleton that only serves to support the weight of a heavy payload, thereby augmenting the wearer's ability to carry materials. Next, exoskeletons that provide mechanical power to the joints of the human wearer and not vice versa generally correspond to rehabilitation and personal-use mobility aid applications. The last category, for which power transfer occurs in both directions, encompasses exoskeletons that augment human strength, conserve the wearer's energy, or provide haptic feedback to the human; rehabilitation use can also extend to this group. These latter categories generally incorporate both actuation and sensing capabilities at their active joints. In this thesis, active joints are understood to be

mechanical joints that consume energy to provide sensing or actuation capability, whereas passive joints are both unsensed and unactuated.

The scope of this thesis is exoskeletons that include an interface with the human lower limb; specifically, consideration is limited to those targeting at least one or more of the hip, knee, and ankle joints. Moreover, this thesis focuses on the design and development of a novel unactuated exoskeleton for motion capture applications. The work is done from the perspective that it may lead to the eventual production of an actuated variant for strength augmentation, rehabilitation, or mobility assistance. Nonetheless, the current focus is a justified starting point. An unactuated exoskeleton provides the opportunity for low-cost verification of the designed manipulator's ability to accurately measure and track the wearer's lower-limb posture. In turn, an actuated version's ability to control fine movements and maintain balance depends on this accurate detection of limb posture. More importantly, however, the unactuated forerunner precludes the potential to inflict actuator-related injury on the human wearer if the posture detection becomes erroneous, since this type of power transmission from the device to the user is not possible. The proposed exoskeleton also embodies a contribution to the area of motion capture in its own right. As a result, the research presented in this thesis is motivated by the benefits associated with the exoskeleton applications from all three categories of exoskeleton-human power transfer.

1.2. Research Importance and Motivations

The research associated with this thesis is valuable because it contributes to the state-of-the-art in exoskeleton technology, and in turn aims to improve the effectiveness of exoskeletons in their range of applications. The following subsections outline the significance of the applications that motivate this research: motion capture, rehabilitation, strength augmentation/energy conservation, and personal-mobility assistance. Therein, the exoskeleton usages that may have a positive impact on health and the human condition are the focus and taken as the primary sources of motivation.

1.2.1. Motion Capture

To preface the paragraphs that follow, the assumed scope and definition for motion capture (MoCap) is clarified. Although various techniques exist for surface motion

capture of deformable bodies [2]–[4], this thesis only considers systems intended for rigid-body objects. Therefore, MoCap systems are regarded as any technology that tracks and records the positional state of one or more objects in three-dimensional (3D) space. This state is fully defined by three translational and three rotational degrees-of-freedom. In some contexts, however, only a subset of these task space coordinates is required (e.g., when measuring the angular state of a joint in its socket). An exoskeleton can achieve human-body MoCap by combining position sensors at its active joints with a knowledge of how the active joint measurements map to the angular states of the anatomical joints.

In a clinical context, lower-limb MoCap exoskeletons can be employed as a tool for the assessment of a patient's sensorimotor functions after the onset of a neurological disorder or spinal cord injury. Clinical assessments, including joint mobility tests and gait evaluation, are necessary to gauge and track a patient's health condition over time; this can be decisive in the appropriate selection of rehabilitation therapies and, ultimately, the level of recovery achieved by the patient. Nevertheless, insufficient accuracy, repeatability, and precision in traditional assessment techniques constrain the regularity of its practical implementation [5], potentially to the patient's detriment. In terms of joint angle measurements and tracking, exoskeletons can overcome these limitations by providing a benchmark for objective, reliable, and sensitive angle quantifications [5]; moreover, exoskeleton-based measurements may represent a more time-efficient solution, which helps mitigate the administrative constraints on performing the assessments. However, the kinematic structure of an exoskeleton determines its suitability for this clinical practice. Maggioni et al. note the cruciality that the exoskeleton: (a) include sufficient DOFs to avoid restricting physiological movements, especially those associated with walking, and (b) support a full range-of-motion in those DOFs to prevent artificially saturating diagnostic measurements [5].

As a central example, the assessment of walking gait is used in the early detection of dementia and identification of fall risk in the elderly population. Several studies have found that mild cognitive impairment and cognitive decline syndromes can be predicted from walking speed and its variability during gait [6]–[8]. Early detection of dementia is imperative because the disorder is reversible for up to 11 percent of sufferers, but only if treated in its initial stage; unfortunately, the disorder currently has a high rate of underrecognition, and it is often family members, as opposed to physicians,

that first detect dementia [9]. The disorder also generates a substantial financial burden (e.g., between $157 billion and $215 billion in the United States for 2010) [10], which is primarily linked to long-term care provision. This provides further incentive for advances in preventative technology. Instrumented assessment of gait can also reveal characteristics associated with fall-risk estimation [11]. Avoiding falls is also critical for elderly people, due to the potential severity of the immediate physical consequences and secondary complications associated with them. Terroso et al. reports hip fracture, undifferentiated bone fractures, death or morbidity, and functional decline as the highest-incidence consequences of falls among the elderly in the literature from 1995–2010 [12].

Moreover, the prevalence of dementia and serious falls among the elderly provides motivation for the pursuit of improved MoCap technology. Prince et al. report that an estimated 35.6 million people worldwide were affected by dementia in 2010 [13]. Also in global terms, elderly people require medical attention after a fall approximately 37.3 million times per year [12]. Given the link between these issues and old age, their incidences are also expected to increase with the aging population. This is because growth in the older demographic is outpacing that of the younger population and is expected to continue doing so into the foreseeable future. In Canada, seniors (i.e., people aged 65 years and older) composed 16.9 percent (5.9 million individuals) of the population in 2016 [14], and is projected to reach about 24.2 percent (11.6 million) by 2050 [15]. Correspondingly, the proportion of Canadians aged 64 years and younger is experiencing a downward trend. Globally, the United States Census Bureau approximates that 8.5 percent (i.e., 617.1 million people) of the world population comprised seniors in 2015, and it projects the demographic to become 16.7 percent (i.e., 1.6 billion) by 2050 [16]. This 150 percent expansion is contrasted by an estimated 25.6 percent growth in the working-age sector (i.e., people aged 20 to 64 years) [16].

Walking gait assessment is also a factor in the appropriate selection of rehabilitation therapies for Parkinson’s disease (PD), multiple sclerosis (MS), and chronic obstructive pulmonary disease [17]. Aside from clinical use, other secondary motivations connected to MoCap include its potential to improve athletic performance via exercise analysis, which facilitates customized training on movement technique [18]. MoCap technologies are also indispensable for computer animation and video game development [19]. Finally, MoCap exoskeletons have the propensity to be a useful tool for researchers in fields such as biomedical physiology and kinesiology.

1.2.2. Rehabilitation

Whereas MoCap exoskeletons can be used to objectively assess a patient's health status as discussed in Subsection 1.2.1, actuated lower-limb exoskeletons can be used directly in some rehabilitation therapies by guiding the patient's legs through various movements, especially walking gait. In this context, victims of stroke, spinal cord injury (SCI), Parkinson's disease (PD), and multiple sclerosis (MS) represent the demographics that could likely benefit the most from advances in the exoskeleton technology. Although the present work focuses on an unactuated exoskeleton, which precludes its direct application as a rehabilitation tool, the work may be extended to provide actuated limb guidance in the future.

Stroke occurs when blood flow to the brain is interrupted by a blood clot (ischemic stroke) or ruptured blood vessel (hemorrhagic stroke) [20]. Though mortality rates associated with the disease are high [21], Poli et al. report that hemiparesis and hemiplegia (i.e., weakness or slight paralysis and complete paralysis on one side of the body, respectively) are the most typical consequences for survivors of stroke [22]. In part, these conditions manifest as: weakness in the affected muscles, atypical postural adjustments, loss of mobility, atypical movement behaviours, lack of joint coordination, and loss of sensation. As its name implies, an SCI is any lesion in the spinal cord's neural elements, resulting in partial loss of motor or sensory functions to complete paraplegia or tetraplegia, depending on the severity of the injury [23], [24]. Next, PD and MS are both classified as neurodegenerative diseases. The former is caused by a loss in brain cells responsible for dopamine production, which is involved in controlling body movements; consequently, PD results in tremors, slow and rigid muscle movements, and diminished reflexes, which can lead to loss of balance [25]. MS is considered a primary autoimmune disease that causes inflammation and damage to the myelin of the central nervous system; in terms of mobility, MS can cause difficulty in walking, loss of coordination, weakness, and diminished sensation [26]. As chronic, progressive diseases, the symptoms of PD and MS continually exacerbate with time.

In 2016, there were about 405,000 Canadians living with stroke-related disabilities, with an incidence of 62,000 strokes each year [20]. Meanwhile, the prevalence and incidence of SCI in Canada for 2010 are respectively estimated at 85,556 people living with their effects and 3,675 new injuries per year [27]. In the United

States, these statistics for 2017 are as follows. First, approximately 7.2 million people are survivors of stroke, where roughly 795,000 new or recurrent attacks take place each year [21]. Next, an estimated 285,000 people are living with SCI and about 17,500 new cases occur annually [28]. PD is estimated to affect roughly 67,500 Canadians and 630,000 Americans [25], [29]. Meanwhile, an estimated 100,000 Canadians and about 400,000 Americans suffer from MS [26], [30]. Given the physically debilitating nature of all these conditions, there is a significant socio-economic cost associated with the rehabilitation and ongoing care associated with their treatments. For example, stroke is the leading cause of long-term disability in Canada and the United States, and it directly and indirectly costs $33.9 billion per annum in the United States [20], [21]; PD had an estimated national cost of over $14.4 billion in 2010 [29]. It is also worth mentioning that the prevalence of stroke and PD is positively-correlated with age, so their pervasiveness and socio-economic burden are expected to rise sharply with the aging population and relative growth in the senior demographic [21], [29]. By improving on existing therapies and promoting independent mobility in patients, new exoskeleton technologies aim to relieve some of that burden [31].

Intensive and repetitive gait training is an common rehabilitation therapy for stroke, SCI, PD, and MS patients experiencing lower-limb dysfunction [24], [32]–[34]. What is more, recent studies have found that stroke survivors are more likely to recover a sufficient level of walking ability to support independent mobility if exoskeleton-assisted gait training is used in conjunction with manual physiotherapy than if the latter is used alone [35], [36]. Moreover, several studies have found that exoskeleton-assisted gait training is superior to conventional methods in improving some aspects of walking ability in patients living with PD [37]–[42]. For MS patients, some preliminary studies indicate that exoskeleton-assisted gait training can improve gait competence, but the level of effectiveness relative to conventional methods remains unclear [43]–[48]. For SCI victims, the modern rehabilitative goal is to exploit neural plasticity or neural repair to catalyze functional motor recovery; this has been demonstrated for incomplete SCI using treadmill training with partial bodyweight support [49]. There have been single-subject case reports that suggest treadmill-based exoskeleton-assisted gait training could improve motor function recovery in people with chronic incomplete SCI [50], [51]. Other researchers have found no significant improvement in neuromuscular or cortical activity in three subjects with chronic complete SCI during gait training with an over-ground

exoskeleton [52]. Ultimately, insofar as the author has researched, the current consensus is that insufficient evidence exists to decisively conclude on the efficacy of exoskeleton-based rehabilitation in the restoration of motor function following SCI [24], [33], [34], [53]–[55].

At the very least, however, exoskeleton-based gait trainers reduce the workload associated with conventional methods, which involves several therapists manually guiding the patient's legs through their movements. Consequently, by automating the gait guidance process, rehabilitation exoskeletons allow: longer training sessions, more accurate movements, greater repeatability in gait pattern, better patient monitoring, and reduced administrative cost (i.e., by reducing the number of therapists per patient) [22], [32], [33]. The resulting increase in accessibility to intensive and prolonged rehabilitation is important, given the limited timeframe in which recovery is possible and rehabilitation is most beneficial for stroke and SCI survivors. According to Teasell and Hussein [56], an early outset of rehabilitation after stroke is most effective, as neurological recovery peaks within the first three months of the attack and remaining improvements generally cease six months to three years post-stroke. If exoskeleton gait-trainers are conclusively shown to be effective in the functional motor repair and neurological recovery of SCI victims, the added accessibility these systems provide remains a beneficial factor. These recuperations are generally limited to the year following an SCI event, and additional recovery beyond that point is not typically realized, even with ongoing rehabilitation [24].

1.2.3. Strength Augmentation/Energy Conservation

The research presented in this thesis also has potential future application as a strength-augmentation exoskeleton. This is possible if some or all the proposed exoskeleton's active joints are actuated and controlled to supplement lower-limb power beyond the user's natural ability. The primary motivation in this aspect relates to the prevalence and effects of mobility decline in older adults. Sarcopenia is an age-related phenomenon characterized by the degenerative loss of muscle mass and strength. These qualities tend to decline linearly, causing up to 50 percent loss in muscle mass between the fourth and eighth decade of a person's life [57]. Consequently, mobility disability is common amongst the older demographic. Brown and Flood indicate that one in three older adults experience difficulty walking a distance of three city blocks [58]. In turn, there are profound physical, psychological, and social consequences correlated

with mobility limitation: functional decline in physiological systems, increased mortality rate, reduced social participation, loneliness and depressive symptoms, and diminished quality of life [58]. Again, the pervasiveness of these issues is expected to increase in the future, as the senior demographic is the fastest-growing population segment in North America and most industrialized countries around the world [16].

In one aspect, lower-limb exoskeletons aim to assist the elderly population in maintaining their independent mobility. Alternatively, strength-augmentation exoskeletons can be applied to support the weight of various handheld tools used for industrial work. Aside from conserving the worker's energy and improving their productivity, these types of exoskeletons aim to reduce repeated static strain on the wearer's muscles [59]. Because static muscle load and mechanical stress are risk factors associated with repetitive strain injuries, utilization of these exoskeletons in the relevant occupational settings could help prevent the musculoskeletal disorders, peripheral-nerve-entrapment, and vascular syndromes associated with such workplace conditions [60]. Lastly, emergency personnel (e.g., firefighters) and foot soldiers must often carry heavy equipment in backpacks. So, advancements in strength-augmentation exoskeletons are also motivated by their potential to increase load capacity, reduce likelihood of injury, and improve metabolic performance in these domains [61].

1.2.4. Personal-Mobility Assistance

Finally, the motivation for exoskeleton advancement in the context of personal-mobility assistance is centered on the benefits of upright, exoskeleton-guided walking over continuous wheelchair use. Ranking among the top three types of disability in both populations, the prevalence of mobility disability includes about 1,971,800 Canadians aged 15 years and older along with roughly 7 million adults from the United States [62], [63]. Of the Americans affected by mobility problems, an approximated 2.2 million rely on a wheelchair to conduct daily tasks and achieve mobility [64]. Amongst community-dwellers in Canada, Smith et al. estimate there are 288,800 individuals aged 15 years and older that use either a manual wheelchair, powered wheelchair, or scooter [65]; this does not include Canadians living outside of the community setting. There is also a correlation between the prevalence of wheelchair use and old age [63], which is consistent with the greater prevalence of potentially-immobilizing muscle degeneration, strokes, Parkinson's disease, and falls among the elderly. So, it can be expected that the

rate of wheelchair use will increase in the foreseeable future as the older demographic outpaces other sectors in the growing and aging world population.

Exoskeleton technology is still developmental in the aspect of daily-life assistive devices, and no current systems can yet be considered as a complete substitute for the wheelchair [31], [66]; this is reflected by the United States Food and Drug Administration's classification of powered exoskeletons as Class II devices (i.e., with special controls and moderate to high risk) [67]. Nevertheless, the technology is heading towards daily usage application. Several studies have demonstrated that exoskeleton-guided walking improves secondary conditions arising from the original mobility problem, which are generally aggravated by prolonged sitting in a wheelchair. In people with paraplegia, there is evidence that exoskeleton-assisted walking can ameliorate: functional mobility, joint contractures, neuropathic pain, spasticity, cardiopulmonary and cardiovascular health, bowel and bladder function, risk of urinary tract infections and osteoporosis, pressure ulcers, and edema [52], [55], [67]–[69]. Other possible long-term health benefits are currently under investigation, including diminishment of obesity, hyperglycemia, and general skin integrity complications in these patients [67]. Moreover, studies generally report no serious detrimental events occurring due to exoskeleton use, and the technology is generally considered safe for ambulation in real-world environments [24], [52], [69]–[71].

Aside from the physiological benefits, the act of standing and walking can have social and psychological advantages as well. Loss of mobility and inability to walk is linked to social stigma, diminished social participation, higher rates of depression, and shorter life expectancy [33], [58]. Correspondingly, desire to walk ranks as a top mobility concern of people who have lost the ability due to an SCI and must now rely on a wheelchair [33], [52]. Ultimately, advancements in exoskeleton technology stand to improve the standard of mobility, independence in living, and overall quality of life for individuals affected by paralysis or other mobility problems.

1.3. Thesis Organization

This thesis is composed of seven chapters structured as follows. The present chapter provides background information, an indication of scope, and the motivations for the present work. Chapter 2 opens the thesis body. It provides a brief literature review of

the current methods for accomplishing rigid-body MoCap along with an overview of existing lower-limb exoskeletons. The chapter closes with a listing of research objectives based on the kinematic shortcomings identified in the current state-of-the-art and a high-level proposal of a novel exoskeleton design to meet those objectives. The subsequent three chapters provide the lower-level details and kinematic analyses of the exoskeleton subsystems, where each one builds upon the previous towards a complete kinematic description of the exoskeleton-human system. Specifically, Chapter 3 considers three alternative orientation manipulators for generating 3-DOF rotational motions, and selects the best candidate based on kinematic performance. Chapter 4 presents two options for a mechanism that transfers the orientation manipulator's motions to a targeted human joint; it also justifies the selection of a preferable option. In turn, Chapter 5 provides kinematic analyses of the complete lower-limb exoskeleton-human interface in the contexts of simulation and experimentation. The chapter also includes discussion of some related practical considerations. Chapter 6 closes the thesis body with a description of a physical prototype development and presentation of the results obtained from a MoCap experiment. Finally, Chapter 7 provides conclusions and future works that could stem from the work completed in this thesis. Figure 1.1 provides a visualization of how the thesis body is organized.

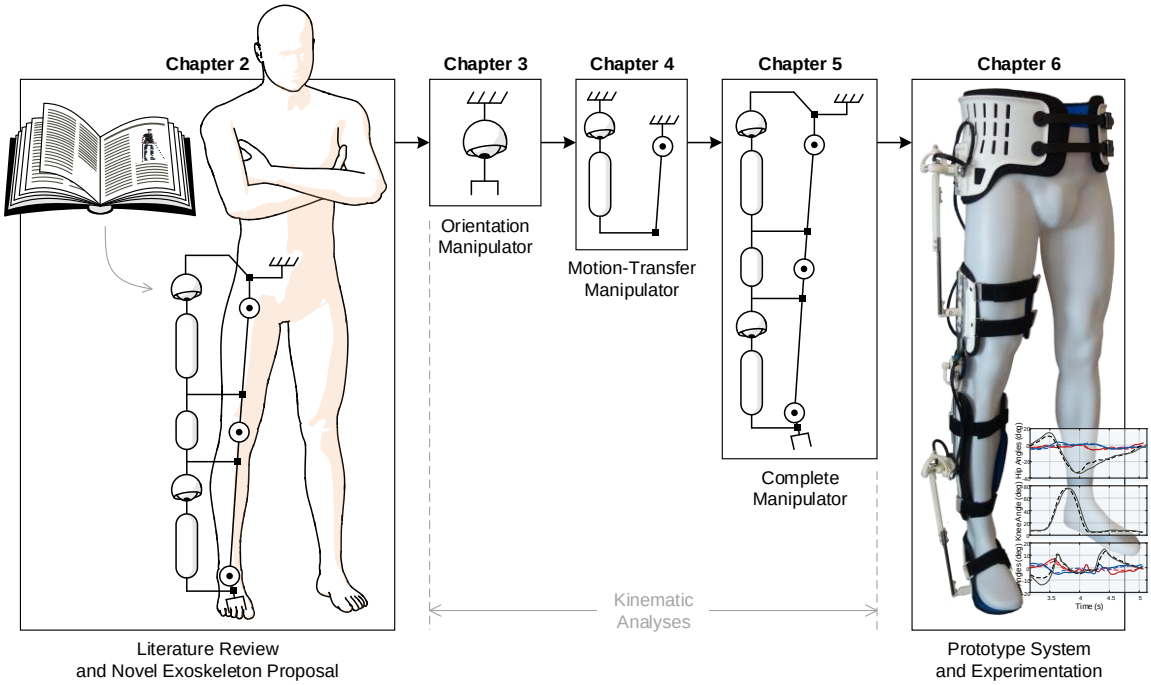

Figure 1.1. Illustration of the topics covered in the thesis body chapters and their logical progression

Chapter 2.

Literature Review and Research Objectives

2.1. Review of Existing Technologies

To provide a sense of the state-of-the-art in motion capture (MoCap) as well as current lower-limb exoskeleton technologies, Subsections 2.1.1 and 2.1.2 reviews the literature on these respective topics. Since MoCap is the immediate intended application, Subsection 2.1.1 includes discussion on the prevalent techniques that compete with the exoskeleton approach, along with already-existing MoCap exoskeleton systems. Next, Subsection 2.1.2 considers any relevant exoskeleton regardless of its intended application. Because there are few exoskeletons developed specifically for MoCap, this subsection provides a more comprehensive picture of the current state-of-the-art in exoskeleton technologies with at least a lower-limb interface. Also, recall that this thesis considers the development of an actuated version of its proposed exoskeleton to be eventual future work, so a review of systems involving actuation is pertinent.

2.1.1. Motion Capture Systems

This subsection presents a brief outline of the operating principles associated with the various rigid-body MoCap techniques described in the literature, along with their individual advantages and disadvantages. Each of the following lower-level subsections focuses on one of the identified categories of relevant MoCap systems: optical, inertial, electromechanical, magnetic, and acoustic. There is a consensus in the literature that these system types encompass the current state-of-the-art in this field [19], [72]–[78]. All systems require a calibration to establish a link between sensor orientations and body segment orientations, so this is not considered an advantage or disadvantage of any system. However, calibration speed in relation to setup time may be considered. Also, all systems' measurements may be degraded by movement artifacts, for which soft-tissue or clothing deformations cause sensor movements that generally cannot be differentiated from the underlying skeletal movements of the targeted body segment. Since this important limitation applies to all system types, it is not listed as a specific disadvantage to each of them.

Optical Motion Capture

Operating Principle

Optical technologies represent the most widely-adopted and commonly-used MoCap technique [72], [73], [78]. These systems can be subcategorized further as passive-marker systems, active-marker systems, and lesser-established markerless systems. Starting with the former two, their operating principle is as follows [75], [77], [79]. Two or more cameras are positioned to be facing towards and outwardly offset from the perimeter of a measurement volume. This volume is defined by the particular arrangement and fields-of-view of the cameras used (i.e., usually in the order of several horizontal square meters by two or three vertical meters). Although other cameras may be used, charged-couple device video cameras are currently the most popular option. Within the measurement volume, the MoCap subject wears markers composed of retroreflective material (passive) or light-emitting diodes (active). With passive markers, infrared stroboscopic lighting and lens filters are generally used to produce high-contrast images in which only the markers are detected. Alternatively, active markers emit infrared light themselves, thus facilitating their high-contrast imaging. Assuming each marker is successfully detected on at least two cameras, computer vision algorithms are then used to derive their geometric coordinates from the synchronized video frames. A triangulation procedure is used to convert the 2D projections captured by the cameras to a 3D position coordinate for each marker. Note that at least two cameras must detect each marker at any given sampling instance to provide enough data for the triangulation computations. Figure 2.1 shows an Optitrack marker-based optical MoCap system with four subjects, 46 cameras, and an atypically large 30ft×60ft×12ft capture volume [80].

Next, as the name implies, markerless optical MoCap systems do not rely on retroreflective nor active markers attached to the subject in order to track their motion. Instead, computer vision algorithms are applied to video of the subject performing movements to extract the subject's human form and posture from the background [74], [75]. Subsequently, a pre-defined model of the body segments and joints is applied to the detected posture to compute joint angle states. Computational approaches that are commonly used involve background scene removal techniques (i.e., silhouette extraction) and various manifold learning algorithms [74], [75]. These markerless methods may use one or more cameras.

Figure 2.1. Photograph of an OptiTrack MoCap system with visible cameras below the truss structure and passive markers on the subjects

Advantages

Modern marker-based optical systems can achieve marker positioning with a sub-millimeter magnitude of error [75], [76]. As a result, this category is the industry standard for accuracy; a caveat is that markerless systems are currently much less accurate. Although marker-based systems only directly provide 3D position data, 6-DOF position and orientation can be obtained if three or more nonaligned markers are placed on a target body segment [73], [76], [77]. Another advantage of these systems is their minimally-intrusive nature [75], [77]; both passive and active markers tend to be small and lightweight, although active markers necessitate the inclusion of a wearable power supply connected to the markers via wires. As straps and wearables have been found to influence subjects' motion behaviors [74], markerless technologies aim to eliminate this probing effect altogether as well as reduce setup time. Optical systems also readily permit multi-subject MoCap studies, and the flexibility associated with wearable markers allows a wide range of task-specific MoCap options. Finally, optical MoCap systems can achieve high-frequency sampling rates (i.e., 500-2000 Hz) and offer the potential for real-time position coordinate synthesis; however, in this real-time context, passive-marker systems must first undergo calibration with a reference image or pre-existing model in order to differentiate between markers [73], [77]. Realtime viewing and quick access to replay is of practical importance, because it allows immediate verification of recording veracity. This helps prevent situations where the entire system setup must be redone to rerecord a motion.

Disadvantages

Despite its status as the most common MoCap method, the marker-based optical approach has several significant issues. The first major functional drawback for marker systems is their tendency for occlusion [19], [75], [77]. This occurs when a segment of the system blocks the view of one or more markers from one or more cameras (e.g., when the arm passes between a camera and pelvic markers). This issue can generally be overcome by using more cameras or placing redundant markers on the subject. However, these fixes respectively come with the expense of increased system cost and increased processing latency, especially for passive-marker systems, which require computational processing to differentiate between markers. Contrarily, active markers are differentiated by sequentially turning on such that only one is detected in each frame recorded by the cameras. But, this multiplexing procedure divides the MoCap sampling frequency by the number of active markers [77]. Also, for active-marker systems, there is a limit on the number of markers that can be tracked (e.g., 512 for Phoenix Technologies' VZ4050 system [81]), and active markers necessitate worn power units and wires that may encumber the subject [75], [77], [82]. Therefore, additional trade-offs are introduced if additional redundant markers are used to combat occlusion. Also note that swapping events (i.e., when markers overlap or cross paths) can complicate the post processing associated with passive-marker systems by potentially causing marker-identification confusion or accidental misidentifications [19], [76], [77].

Depending on the desired application, another major issue with optical marker systems is their limited measuring space and low portability [75], [77]. During a MoCap session, cameras must remain stationary and the subject must remain within the field-of-view area of the cameras. Moreover, the spatial position and orientation of each camera must be known for accurate data processing (i.e., as determined via calibration procedures), so optical systems are usually kept stationary in an indoor location. If any camera is moved even slightly during a MoCap session, recalibration is necessary [19], [72]. This logistically complicates or altogether prevents certain motion activities from being analyzed by this technique. Additionally, another environmental concern for passive-marker systems is sufficient reflected light to permit accurate marker position identification [75]. Note that active markers tend to have a greater detection range than passive ones.

Next, the position-only measurements of marker-based optical systems require three nonaligned markers per limb segment in order to permit orientation computation. This, in addition to the general image-processing nature of the technology, causes higher processing latency than MoCap techniques that measure orientation more directly [73], [75]–[77]. Processing time is increased further if occlusion or swapping errors occur. Furthermore, system setup time for this technology is also drastically longer than for other systems; aside from strategic marker placements, the cameras' positions, orientations, and lens adjustments must be appropriately arranged to define the measurement space, and camera calibrations must be performed. Note that most systems' calibration routine involves establishing a reference frame with a set of precisely positioned markers and moving a calibration wand with precisely-spaced markers about the measurement volume. Finally, compensation for lens distortion, the requirement for precise camera synchronization, and other nuances of the optical hardware all add to the system's complexity. Ultimately, this complexity and the general need for attendant components (e.g., data collection and processing software, calibration hardware, tripods or wall mounts, marker kits, power hubs, etc.) are reflected in the typical price of marker-based optical MoCap systems, which are far and away the costliest amongst alternative technologies. Note that prices are highly dependent on the specific nature of the desired MoCap application; especially important are the required measurement volume size and whether tracking must provide 360-degree coverage, as these considerations can drastically affect how many camera units must be employed.

Markerless optical systems eliminate many of the issues associated with marker-based systems, due to the complete absence of markers, and have significantly lower prices. However, they also have a unique set of shortcomings. First, current markerless technologies require very computationally-expensive processing, and their accuracy is affected by: ambient lighting, background objects within the field-of-view of the camera(s), and predetermined contextual information about the subject (i.e., in establishing a proper human model for the data) [74], [75]. Moreover, as mentioned above, the accuracy of current markerless systems is significantly worse than that of all other MoCap systems considered. Fernández-Baena et al. found mean errors (i.e., relative to a marker-based system) between 6.78–8.98 degrees for the knee, 5.53–9.92 degrees for the hip, and 7.19–13.19 degrees for the shoulder during joint range-of-motion tests using the Microsoft Kinect under controlled laboratory conditions [83].

Ultimately, although markerless technology has a promising potential and currently represents an area of extensive ongoing research [74], [75], its limitations generally prevent it from being a viable MoCap solution outside of video-games controller systems and other applications that do not require high accuracy at present.

Inertial Motion Capture

Operating Principle

Inertial MoCap systems rely on inertial measurement units (IMUs), which make acceleration and rotational velocity measurements from integrated triaxial accelerometers and gyroscopes, respectively [75], [77]. To overcome common issues associated with these two sensors alone, most modern IMUs correct their heading data (i.e., yaw) by also including a triaxial magnetometer. This sensor measures magnetic field vectors. Data from all these sources is fused into a spatial orientation measurement using sophisticated algorithms, most commonly Kalman filters and nonlinear observers. As a microelectromechanical system, present-day IMUs can be built very small and cheaply [77]. They comprise an inertial MoCap system when IMUs are attached to the limb segments of interest and orientation data is synchronously recorded. Figure 2.2 shows a photograph of the Xsens MVN Awinda and Link systems as examples of inertial-based MoCap [84]. Behind the marker-based optical systems, inertial systems have evidently experienced the second highest rate of market adoption for MoCap technologies.

Figure 2.2. Photograph of the Xsens MVN Awinda (left) and Link (right) inertial MoCap systems

Advantages

When properly used, inertial MoCap systems offer accurate orientation measurements within two degrees of root mean square error [75]. Also, calibration is relatively straightforward and quick [75], [77]; it generally involves the subject moving to a known reference posture (e.g., neutral standing) and establishing an association between the sensor axes and targeted anatomical axes. Next, whereas other systems require additional processing (i.e., discrete differentiation) to obtain angular velocity and acceleration data, inertial systems obtain acceleration data directly by virtue of their operating principle [75]. Finally, inertial sensors can be wireless and very small in size, which minimizes their attachment influence on the subject's movements, and the systems are often have moderate to low prices on the market relative to the other MoCap technologies.

Disadvantages

Because inertial sensors measure velocities and accelerations, integration is required to obtain angular position measurements. Thus, inertial measurements are prone to a propagation of errors, called drift [72], [75]. To deal with this and other error issues including bias, deviations, and nonlinearity, efficient algorithms for sensor data fusion and error corrections must be employed. Often, these algorithms must be customized on a case-by-case basis for the specific MoCap application desired, and measurement accuracy is highly dependent on use of a task-appropriate processing algorithm [77]. For example, if the subject's movements are known to be cyclic in advance of the data collection, this constraint should be incorporated into the processing algorithm to achieve the most accurate results possible. Next, if the sensors use magnetometer data to derive spatial orientation, the system is susceptible to error from magnetic interference caused by nearby ferromagnetic objects or other disturbances in the magnetic field. Another shortcoming is that inertial sensors measure 3-DOF rotational orientation measurements but do not provide 3-DOF translational position data when used in the absence of other types of sensors [75], [77]. Finally, although inertial sensors can be wireless, MoCap measurements must be conducted within a certain range of the receiver unit (e.g., 20m for Xsens MVN Awinda and 50m for Link when indoors [84]).

Exoskeleton (Electromechanical) Motion Capture

Operating Principle

Objectively the simplest method of MoCap, traditional exoskeleton systems directly measure anatomical joint angles by aligning a revolute electromechanical sensor (e.g., a potentiometer or encoder) with the targeted joint axis. Mechanical linkages on either side of the rotary sensor attach to the adjacent limb segments surrounding the joint [72], [73], [75]–[77]. Thus, when the joint moves, its angle is measured directly by an electromechanical sensor, which is usually a potentiometer or encoder. Note that potentiometers provide a voltage reading proportional to mechanical angle using a voltage divider. By attaching a conductive wiper to a rotating shaft, the wiper moves with contact across a resistor, which in turn has a known voltage applied to it. Alternatively, encoders typically detect angles via sequential disruptions of light between a source and detector due to a pattern of transparent and opaque materials attached to a rotating shaft. Note that for anatomical joints with multiple DOFs, serially-connected sets of rotary sensors that all intersect the joint have been proposed in the literature. As pictured in Figure 2.3, Metamotion's Gypsy 7 includes 14 sensed DOFs for the entire body with a measurement resolution of 0.125 degrees [85]. The rotations of multi-DOF joints are constrained to a single rotation, and a serial manipulator structure is adopted for each limb. Other advertised features include: data-capture frequency options of 30Hz, 60Hz, and 120Hz, no dropped frames, no data noise, and freedom from a limited measurement volume. Also, note that MoCap exoskeletons are typically referred to as electromechanical systems in the literature.

Figure 2.3. Photograph of Metamotion's Gypsy 7 exoskeleton MoCap system

Aside from the tradition method, more sophisticated sensors may be used to eliminate the need for sensor-joint axis alignment. These include strain gauges attached to steel wire that measures angular bend about two axes [86] and fiber-optic goniometers that measure 1-DOF of bend angle [87]. These sensors can be attached to the limb segments surrounding a joint via straps or tape to measure the angle of the associated joint. As an example, Biometrics offers strain-gauge-based biaxial and monoaxial flexible wire that can be attached with medical tape across a joint to measure up to two angles of rotation [86]. These sensors feature an accuracy ±2 degrees over a range of ±90 degrees, a repeatability of one degree over a 90-degree range, and can be sampled at 50Hz, 100Hz, 200Hz, 500Hz, or 1000Hz. Figure 2.4 shows a picture of the Biometrics' Ultimate Data Acquisition System [86].

Figure 2.4. Photograph of Biometric's Ultimate Data Acquisition System based on wireless biaxial and monoaxial strain gauge sensors

Advantages

There are several features of exoskeleton MoCap systems that can make them advantageous compared to alternatives for a given MoCap task. First, this system type is highly portable and generally unaffected by external or environmental conditions (e.g., measurements are not influenced magnetic interferences, occlusions, etc.) [19], [75]. The simplicity of electromechanical sensors also makes their use relatively straightforward: measurements are obtained quickly, calibration with the human joint is simple, and units are generally inexpensive [19], [72], [73], [75]. Moreover, despite their simplicity, exoskeleton systems are often considered robust, reliable, repeatable, sensitive, and relatively accurate [72], [75], [76]. Allard et al. [72] as well as Everett and Kell [76] report accuracy within one degree for small joint ranges (e.g., hip and knee

flexion/extension during walking gait), and the latter researchers report accuracy within 2.9 degrees for larger angular measurements. In fact, Allard et al. [72] suggest that exoskeleton systems are more accurate than optical MoCap systems for rotational measurements about a single axis joint. Even biaxial flexible wire goniometers are reported to have error less than 2 degrees during wrist range-of-motion tests [88]. While the above provides a general sense of expected accuracy, a specific system's accuracy depends on the quality and type of electromechanical sensor employed in its design, as well as management of some shortcomings that may cause errors as described below. Finally, exoskeleton systems have the unique potential to combine MoCap with haptic feedback in augmented reality, virtual reality, or master-slave robotics applications; this is because it is the only system type that could apply a feedback force onto the human user if actuators are employed at the relevant joints.

Disadvantages

Since exoskeleton MoCap technologies traditionally rely on aligning single-DOF rotational sensors with the targeted biological joint, a main disadvantage is that they restrict the natural range-of-motion of the human joint [19], [72], [75], [77]. For example, system comprising a 1-DOF rotary potentiometer aligned with the hip joint and rigid linkages attached to the pelvis and thigh would prevent the subject from moving with the other two DOFs of the hip perpendicular to the potentiometer axis. This would generally interfere with subject's ability to perform movements in a natural fashion. Moreover, if secondary joint motions are not fully constrained, this exoskeleton-based measurement technique is susceptible to cross-talk, for which measurement of the targeted joint angle is contaminated by rotation in a different angular DOF [72]. Other disadvantages associated with the alignment of sensor and joint axes are: measurement accuracy depends on the precision of this alignment; system design must match the user's morphology (i.e., challenges in accommodation for different limb sizes between subjects); different mechanisms must be designed for each body joint; and alignment or access to some joints is difficult due to their surrounding biological structure (e.g., the large amounts of soft tissue around the hip or the limited attachment sites surrounding the ankle) [72], [76], [77]. Furthermore, few human joints behave like true hinges, and some may undergo axial translations concomitant with rotations (e.g., the knee). Some solutions reported in the literature include adding a self-aligning four-bar mechanism or prismatic joint to the system, or using a flexible wire-type sensors [72], [73], [76].

Another major shortcoming of exoskeleton systems is their inability to provide complete 6-DOF position and orientation measurements for limb segments with respect to a lab room coordinate system [19], [73], [75], [77]. This may be overcome by combining the exoskeleton with one or more different technologies that provide global position and orientation for one limb segment; thereafter, other segments' global positioning can be obtained via their relative position to that first segment, as measured by the exoskeleton. Next, an inherent characteristic of mechanical systems is their tendency for stick-slip and backlash effects, which are a source of nonlinearity in the measurement system [72]. Also, depending on component selection, the electromechanical sensor may be prone to hysteresis [76], or cause jump discontinuities in the measured data due to potentiometer wiper transferring between resistance coils [73]. Aside from choosing sensors insusceptible to these shortcomings, the latter issue can be resolved by interfacing the sensor with the body in such a way that these discontinuity points occur outside of the joint range-of-motion. Finally, exoskeleton systems may have an obtrusive weight or tightly-fastened straps [19], [72], [77]; both of these factors could potentially encumber the subject and inject unnatural influence into their movements. However, Everett and Kell suggest that these systems can generally achieve a lightweight design that does not interfere with the subject's motions [76].

Magnetic Motion Capture

Operating Principle

Magnetic MoCap systems are comprised of a stationary transmitter unit and moving sensor units, both of which contain three mutually-orthogonal wire coils [72], [75], [77]. Current pulses are precisely supplied to each coil of the transmitter to produce identical low-frequency magnetic signals in orthogonal directions, which ultimately represent a spatial orientation frame. The pulses may be either direct current (DC) or alternating current (AC). The transmitter's magnetic fields, along with any environmental field, are measured by each coil of the sensor units. The relative proportions and strength detected along each sensor axis provides 6-DOF position and orientation data for a single sensor unit. Note that the environmental magnetic field is measured in between current pulses and then removed from the sensor orientation measurement. Figure 2.5 shows photographs of Ascension Technology Corporation's Nest of Birds magnetic MoCap system as an example of this technology [89]

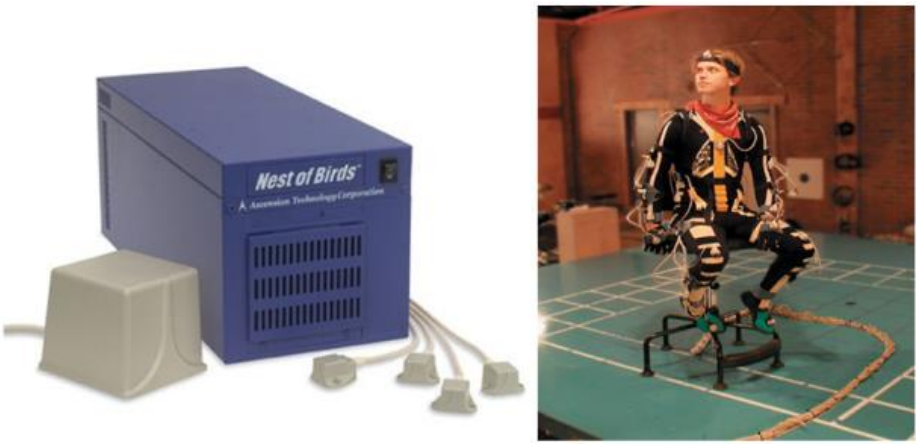

Figure 2.5. Photographs of the Nest of Birds magnetic MoCap system transmitter unit (left) and subject-interfaced sensor units (right)

Advantages

The primary benefit of using a magnetic system over exoskeleton or inertial is that each magnetic sensor provides complete 6-DOF spatial position data [77]. Magnetic systems also eliminate the occlusion problem associated with optical systems and cost significantly less (i.e., comparable in price to current exoskeleton and inertial systems) [19], [75]. Finally, the sensors can be wireless, so they offer less obstruction than electromechanical systems or wired versions of the other MoCap technologies.

Disadvantages

Relative to optical MoCap systems, magnetic systems provide less accurate position data [77]. Moreover, current magnetic systems require the subject to remain within about three meters of a stationary transmitter unit during data capture, which represents a generally smaller measurement volume than other systems [19], [75]. Some magnetic systems offer a portable transmitter hub that can be attached to the subject, although, at the expense of potentially influencing their movements. Present-day systems also rely on multiplexing measurement signals from each sensor, which introduces an inherent compromise between number of sensors used (i.e., body segments tracked) and data sampling frequency. Finally, as expected, magnetic systems are susceptible to electromagnetic interference from ferromagnetic objects near the sensors, which heavily distorts the output signal and ultimately renders the system unusable in certain environments [19], [72], [75], [77]. The amount of distortion is reduced if DC pulses are used to generate the magnetic fields at the transmitter unit instead of AC current [75], but DC systems introduce problems in detecting azimuth [90].

Acoustic Motion Capture

Operating Principle

In acoustic MoCap systems, the main components are an array of acoustic sources (i.e., ultrasonic transmitters) and sets of at least three noncolinear microphones [72]. In operation, acoustic pulses are sent from the sources and are detected at the microphone receivers. Based on the intensity of the signal measured at the microphones and the time between pulse generation and reception, the three-dimensional position of each receiver is determined (i.e., after the signal is sent to a computing device and processed). Thus, using the absolute positions of the receivers as well as their relative positions, acoustic systems measure both the 3-DOF translational position and 3-DOF rotational orientation of each microphone set. By attaching a microphone set to each body segment under evaluation, the position and orientation of those segments can be tracked. From Gabai's and Primo's patent [91], Figure 2.6 shows a schematic of such an acoustic MoCap system prepared for video game application.

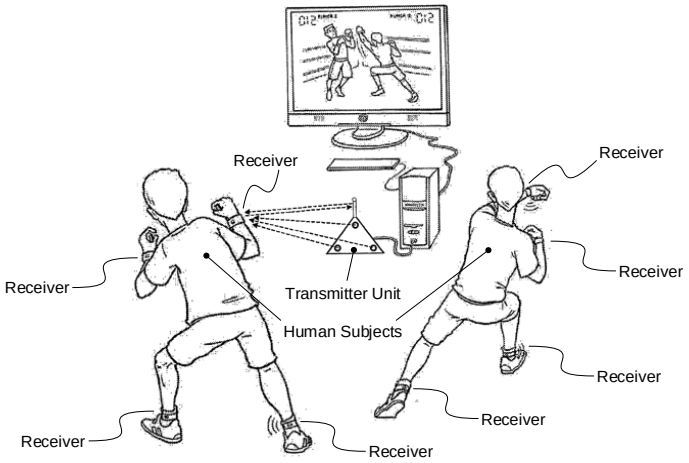

Figure 2.6. Schematic illustration of an acoustic MoCap system for video game applications with human subjects, transmitter, and receivers labeled

Advantages

The strongest characteristics in favor of acoustic MoCap systems is their sensors' ability to provide complete 6-DOF position and orientation data with a high level of accuracy (e.g., reportedly within 0.5mm in translation and 0.5 degrees in rotation) [72]. Also, similar to passive-marker optical, inertial, and magnetic systems, acoustic systems use wireless sensors, which tend to interfere with the subject's movements less than wired or electromechanical solutions [75].

Disadvantages

Despite the highly-accurate 6-DOF sensing capabilities of an individual acoustic MoCap sensor, systems based on this technology have not realized widespread adoption due to some major shortcomings that limit their practical utility. First, if more than one sensor is used, the system is susceptible to acoustic echoes and interferences from the multiple source-sensor pairs [72]; this diminishes the system's ability to track more than one body segment during a MoCap study. Next, acoustic systems are prone to self-occlusion, which occurs when a body segment moves between or altogether blocks the acoustic source or microphone, thereby changing the characteristics of the detected signal. In fact, partial acoustic occlusions are indistinguishable from an increased distance between sensor and receiver [75], which results in erroneous position data. On that note, acoustic systems require preservation of an allowable source-receiver distance range, which limits the workable capture volume for the subject. Finally, acoustic sensors are sensitive to background noises (e.g., wind if used outside) as well as temperature and humidity conditions in the measurement environment [75]. The sum of these shortcomings often makes acoustic systems infeasible in many MoCap contexts.

2.1.2. Lower-Limb Exoskeletons

The number of lower-limb exoskeletons developed specifically for MoCap applications is limited, where the various iterations of Metamotion's Gypsy represent the most prominent commercialized system. Contrarily, there are numerous examples of lower-limb exoskeletons for strength augmentation/energy conservation, rehabilitation, and personal-mobility assistance. The following paragraphs provide a brief review of such systems, focusing on their kinematic structure and examples that interface with at least two of the hip, knee, and ankle joints. The review also aims to include systems that have achieved the most commercial or media prominence at present. However, it is by no means exhaustive, and the reader may refer to the exoskeleton reviews prepared in [92]–[98] for more information on the current state-of-the-art. Also, because the discussion that follows contains reference to body frames and leg joint motions, Figure 2.7 illustrates these frames and the primary motions associated with the hip, knee, and ankle. The schematic also labels the typical upper limits on the anatomical ranges for each joint motion, based on the information provided in [99].

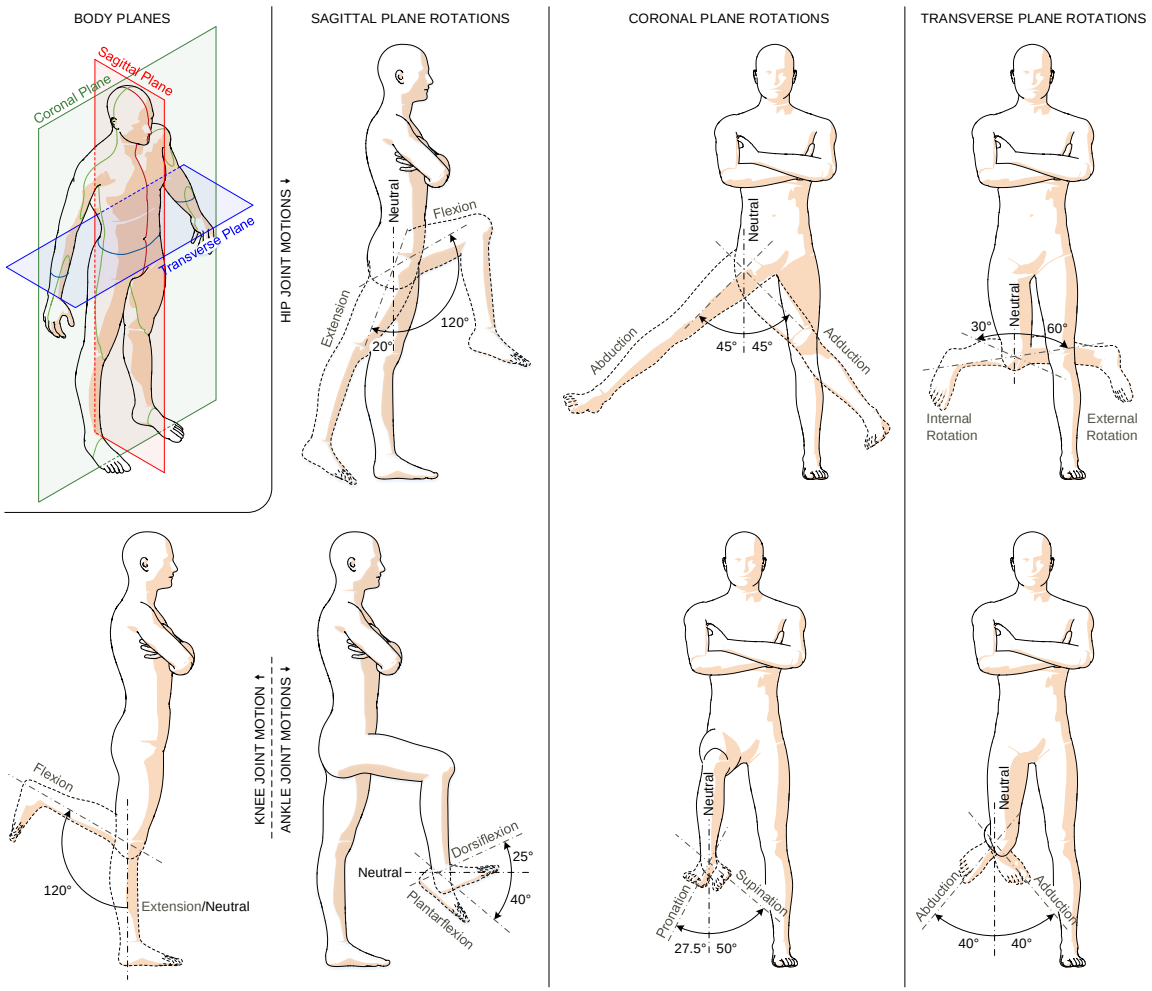

Figure 2.7. Illustrations of the human body frames and the primary rotations and upper-limit ranges-of-motion of the hip, knee, and ankle joints

Note: Because it occurs along the full length of the shank, ankle abduction/adduction is sometimes attributed to the knee joint. This thesis assumes the alternative interpretation and groups it with the ankle, as shown here.

Exoskeletons for Strength Augmentation/Energy Conservation

Exoskeletons designed for strength augmentation are generally intended to support the weight of loads that a user must lift or carry in industrial or military settings. In support of research and development in this field, the United States' Defense Advanced Research Projects Agency (DARPA) began a significant funding initiative for robotic exoskeletons in 2000. First unveiled in 2004, the Berkeley Lower Extremity Exoskeleton (BLEEX) was one these DARPA-funded systems, developed in the University of California, Berkeley's Human Engineering and Robotics Laboratory. The BLEEX design incorporates all major DOFs associated with human leg: three hip DOFs, one knee DOF, and three ankle DOFs [92], [100]. Only those DOFs associated with hip

flexion/extension, knee flexion, and ankle plantarflexion/dorsiflexion are actuated [100]. Subsequent iterations of the BLEEX developed in 2005 are the ExoHiker and ExoClimber, which improve upon the BLEEX's system weight, control, and load-bearing capability [101], [102]; a further improved design, called the Human Universal Load Carrier (HULC) was developed in 2009 with greater load-carrying ability and decreased metabolic cost to the user [103].

Lockheed Martin Corporation since obtained licensing rights of the HULC and developed a fully-unactuated version called FORTIS. Whereas HULC targets military applications, FORTIS functions to support the weight of various industrial tools (i.e., by transmitting gravitational forces to the ground via the exoskeleton structure), allowing human operators to expend less energy while operating the tool [59]. A second human-augmentation system initially funded by DARPA is Sarcos' full-body exoskeleton, which would eventually be named XOS after acquisition by Raytheon [98]. There is limited public information regarding XOS's design and performance [96], [98], so the exoskeleton's kinematic structure cannot be reported here. From 2004 to 2009, the Laboratory of Perceptual Robotics at Scuola Superiore Sant'Anna also developed a full-body exoskeleton called the Body Extender. Devised for general handling of heavy materials, the system has 22 independently-actuated DOFs, including active guidance for all major articulations of the human leg except for ankle adduction/abduction [104]. Both the XOS and Body Extender involve tethered connections to power sources, which limits their portability. Figure 2.8 shows photographs of the BLEEX, HULC, FORTIS, XOS, and Body Extender exoskeletons [59], [100], [103]–[105].

Figure 2.8. Photographs of the BLEEX (far left), HULC (middle-left), FORTIS (middle), XOS (middle-right), and Body Extender (far right)

Another system developed with the intent of supporting heavy payloads is Nanyang Technological University's Lower Extremity Exoskeleton (NTU-LEE) [106]. This system contains actuated joints for hip flexion/extension, knee flexion/extension, and ankle dorsiflexion/plantarflexion; to promote stability, unactuated spring-loaded joints are also included for the hip abduction/adduction and ankle pronation/supination DOFs [92], [106]. However, the system must be tethered to a power source, which limits its practical utility in the field. Next, an exoskeleton developed out of MIT includes a 3-DOF hip, 1-DOF knee, and 2-DOF ankle on each leg (i.e., ankle abduction/adduction is restricted) [61], [92], [107]. This quasi-passive system employs springs at the hip and ankle (i.e., excluding the hip rotation DOF) and a variable damper at the knee. In addition to bearing the weight of loads attached to the user's back, the MIT exoskeleton aims to reduce the user's metabolic expense during walking [61], [107]. To achieve this, the spring components store energy and knee damper dissipates energy at gait stages for which leg muscles perform negative work; the springs subsequently release energy to assist the muscles as they undergo positive mechanical work.

Whereas the previous designs focused on augmentation by extending the user's capacity to hold and sustain external loads beyond normal human capabilities, the next two systems are centered more closely on energy conservation in the absence of a payload. First, Donelan et al. from Simon Fraser University's Locomotion Laboratory have developed a knee exoskeleton for biomechanical energy harvesting. Along the same vein as the MIT exoskeleton, the exoskeleton aims to produce a resistive torque at the appropriate intervals of the user's gait such that device assists leg muscles when they are performing negative mechanical work [108]; this is analogous to regenerative braking in automobiles. Unlike the MIT exoskeleton, Donelan et al.'s exoskeleton uses a generator to store recovered electrical energy with an intended outcome of powering external devices (e.g., for people without immediate access to a power grid). The technology could also be applied to reduce net power requirements for actuated exoskeletons. Finally, Honda's Bodyweight Support Assist guides flexion/extension movements of its user's legs via revolute actuators; it functions to reduce the leg loading and balance maintenance during walking, crouching, and stair-traversal [94]. This exoskeleton's kinematic architecture details are undisclosed in the literature. Figure 2.9 shows photographs of the NTU-LEE, MIT exoskeleton, Donelan et al.'s exoskeleton, and Honda's Bodyweight Support Assist [61], [94], [106], [108].

Figure 2.9. Photographs of the NTU-LEE (far left), MIT exoskeleton (middle-left), Donelan et al.'s exoskeleton (middle-right), and Bodyweight Support Assist (far right)

Exoskeletons for Rehabilitation: Treadmill-Based Gait Trainers

Given their stationary nature, treadmill-based exoskeletons cater exclusively to rehabilitation applications. One of the earliest systems developed was the Driven Gait Orthosis (DGO) by Colombo et al., unveiled in 2000. This exoskeleton system was intended to automate the motion-guidance work done by physiotherapists on incomplete SCI patients during treadmill ambulation exercises [92], [109], [110]. Kinematically composed of two actuated 1-DOF revolute joints corresponding to the hip and knee, the system guides the flexion/extension motions of both these anatomical joints. This allows for longer training sessions and more repeatability in gait motions than manual leg movements. The DGO project became a commercial product, the Lokomat, through the Swiss medical technology company, Hocoma. A similar system called the AutoAmbulator by United States company HealthSouth, and marketed as the ReoAmbulator by Motorika in Israel, is detailed in a United States patent filed in 2001 [93], [111]. As with the Lokomat, the primary manipulator associated with a single leg of these systems is a serial 2-DOF chain, with actuated revolute joints corresponding to flexion/extension motions of the user's hip and knee joints. Figure 2.10 shows images of the DGO, Lokomat, and ReoAmbulator exoskeletons [93], [110]. Note that all of these systems also use a harness to support the user's body weight and position the pelvis, along with straps to passively constrain the ankle joint.

Figure 2.10. Photographs of the DGO (left), Lokomat (middle), and ReoAmbulator (right)

Following those described above, several new treadmill-based exoskeletons aimed to improve on the initial systems by adding supplementary actuated DOFs in hopes of supporting more natural gait movements. In turn, researchers hypothesized the outcome would be higher quality and faster patient recovery in the rehabilitation setting. To start, the Lower Extremity Powered Exo-Skeleton (LOPES) was introduced in 2006. Each leg of the LOPES is a serial manipulator composed of a 2-DOF hip joint, actively supporting flexion/extension and abduction/adduction motions, as well as a 1-DOF knee joint to guide flexion/extension motions [92], [112]. Each of these DOFs are realized as revolute actuators. However, the LOPES system also includes two series-connected prismatic actuators that horizontally position the user's pelvis (i.e., anterior/posterior and medial/lateral motions with respect to the treadmill are actively guided) [112]. Furthermore, the LOPES constrains internal/external rotations of its user's hip joint and leaves the ankle joint completely free; it additionally permits vertical motion of the pelvis but restricts all pelvic rotations.

Also introduced in 2006, the University of California's Biomechatronics Lab developed a pneumatic-based exoskeleton for gait rehabilitation. In one part, this system consists of a Pneumatically Operated Gait Orthosis (POGO), which provides 2-DOF actuation on each leg [93], [113]. These degrees-of-freedom guide flexion/extension motions of the user's hip and knee joints. The second part of the system is the Pelvic Assist Manipulator (PAM), which has 5 DOFs: three translational and two rotational DOFs [113]. The missing rotational DOF from complete pelvic position and orientation control is associated with sagittal plane pelvic tilt, although POGO/PAM passively accommodates this motion [113]. Subsequently, the University of Delaware unveiled

their development of an Active Leg EXoskeleton (ALEX) in 2007 [114]. Similar to the LOPES, each leg of the ALEX contains a 2-DOF hip joint supporting flexion/extension and abduction/adduction motions, along with an actuated 1-DOF knee joint [92], [114]. The most recent third iteration of ALEX also actuates ankle plantarflexion/dorsiflexion motions [115]; the remaining hip and ankle DOFs are restricted. Unlike POGO/PAM, ALEX III uses permanent magnet brushless motors. Furthermore, the ALEX III trunk orthosis permits 4 DOFs that actively guide transverse plane rotations and all three translations of the user's pelvis [115].

Next, Beyl et al. presented a novel exoskeleton targeting the knee in 2008 [116]. Unlike the previous three systems, this design was developed per the hypothesis that different actuators would improve treadmill gait trainer technology, so it did not aim to increase the number of kinematic DOFs from previous systems. Instead, the work focused on the use of Pleated Pneumatic Artificial Muscle (PPAM) to actuate a single revolute DOF at the knee joint [116]. Later named KNEXO, this knee exoskeleton's novelty is centered on the use of the PPAM actuators, and its kinematic structure only includes a passive 1-DOF hip joint allowing flexion/extension motions and the active 1-DOF knee joint [92], [117]. Note that the KNEXO also includes a support arm attached to the user's torso; the arm ensures vertical alignment of the exoskeleton links, bears the weight of the exoskeleton, and can pivot about a vertical axis, but does not support the user's body weight [116]. Figure 2.11 shows the LOPES, POGO/PAM, ALEX III, and KNEXO manipulators [113], [118]–[120].

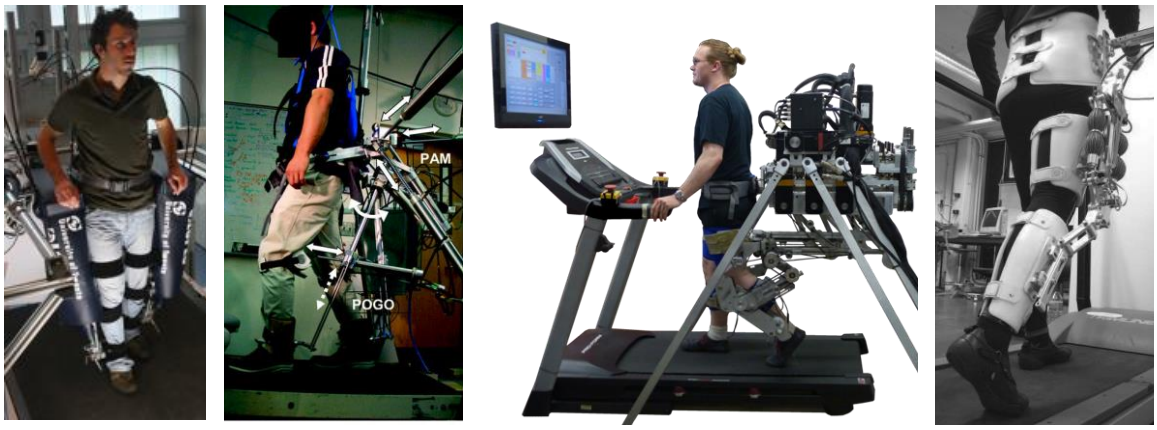

Figure 2.11. Photographs of the LOPES (far left), POGO/PAM (middle-left), ALEX III (middle-right), and KNEXO (far right)

Exoskeletons for Personal-Mobility Aid and Rehabilitation: Over-Ground Systems

Whereas treadmill gait trainers are limited to rehabilitation applications, the inherent mobility of over-ground exoskeletons suits them for alternative use as a personal-mobility aid (e.g., a wheelchair replacement). However, this characteristic concomitantly prevents over-ground systems from including a wall- or ground-fixture to guide pelvic motions or suspend the system's weight. Consequently, over-ground exoskeletons generally require attendant use of crutches to help support the user's bodyweight and maintain their balance. Moreover, most of the current over-ground exoskeleton systems have equivalent kinematic structures for the hip and knee joints: actuated guidance for the flexion/extension of both joints and restriction on the other major DOFs of the hip. Therefore, the main differentiating factor is ankle joint treatment.

Several prominent designs accommodate ankle plantarflexion/dorsiflexion using an unactuated revolute joint, while restricting the other ankle DOFs. The ReWalk is one such system [121]. Developed out of the University of Tsukuba in Japan, Hybrid Assistive Leg 3 (HAL) is another example with this design scheme [122]. Next, the same laboratory that produced the BLEEX went on to develop the Exoskeleton Lower Extremity Gait System (eLEGS) and Austin exoskeletons in 2010–2011 [123], [124]. Separately, both systems became commercialized in the United States as the Ekso GT by Ekso Bionics and Phoenix by SuitX, respectively. Note that the Phoenix design aims to minimize mass, so its knee joints are unactuated. Neither of these exoskeletons contain actuated ankle joints [97], [125], but it is unclear if or how they are passively articulated given the lack of literature regarding their designs. Figure 2.12 shows photographs of the ReWalk, HAL, Ekso GT, and Phoenix systems [125]–[128].

Figure 2.12. Photographs of the ReWalk (far left), HAL (middle-left), Ekso GT (middle-right), and Phoenix (far right)

Several other exoskeletons have been developed with actuated joints corresponding to the hip and knee flexion/extension, but altogether excluding an ankle joint (i.e., leaving the user's foot to rotate freely with respect to the shank). These include the Vanderbilt University exoskeleton [129], Mina from the Institute for Human and Machine Cognition in Florida [130], and Lower Extremity Assistive Device (LEAD) from the National University of Singapore [131]. The former was eventually commercialized as Indego by Parker-Hannifen and subsequently modified to include a foot plate constraining all ankle rotations. The referenced version of the Mina is tethered to a power source, which limits its mobility, but a new version is currently under development that features: new actuators, powered ankles, and foot-plate sensors to facilitate balance control [131]. A Russian-developed system, called ExoAtlet, has seemingly adopted the same restricted-ankle design as the Indego. However, this is not confirmed due to limited public information about the exoskeleton. Finally, GOGOA's HANK exoskeleton includes actuators at the ankle to guide plantarflexion/dorsiflexion motions while restricting other ankle DOFs [132]. Figure 2.13 shows pictures of the Indego, new-version Mina, ExoAtlet, and HANK systems [131]–[134].

Figure 2.13. Photographs of the Indego (far left), Mina (middle-left), ExoAtlet (middle-right), and HANK (far right)

Dissimilar to the other over-ground exoskeletons mentioned, the REX P by REX Bionics actuates more than one DOF at the hip and ankle. Each leg of this system contains five actuated DOFs, which correspond to: hip flexion/extension, hip abduction/adduction, knee flexion/extension, ankle dorsiflexion/plantarflexion, and ankle pronation/supination [135]. REX is also distinguished as a completely self-supporting exoskeleton in the sense that its paraplegic users do not need additional support from crutches during its operation [135]. Figure 2.14 highlights this distinction by showing a

user-interfaced REX P alongside a Pheonix exoskeleton [125], [136]. Note that the former is the only of the above-ground exoskeletons discussed here that does not require its user to hold crutches during operation. Table 2.1 summarizes the kinematic characteristics of one leg (i.e., hip, knee, and ankle if applicable) for each of the exoskeleton systems mentioned above. Note that for treadmill-based systems, the kinematic characteristics associated with the pelvis or torso attachment are not included. Also, different iterations of the same exoskeleton are excluded, along with any design for which the kinematic architecture could not be verified (i.e., XOS, Bodyweight Support Assist, Ekso GT, Phoenix, and ExoAtlet).

Table 2.1. Summary of exoskeleton kinematic characteristics in terms of corresponding anatomical joint motions of the human lower limb

	Hip			*Knee*	*Ankle*		
Exoskeleton	Int./Ext. Rot.	Abd./Add.	Ext./Flex.	Flex./Ext.	Add./Abd.	Pro./Sup.	Pla./Dor.
Strength Augmentation/Energy Conservation Systems							
BLEEX	✓U	✓U	✓U	✓A	✓U	✓U	✓A
Body Extender	✓A	✓A	✓A	✓A	×R	✓A	✓A
NTU-LEE	×R	✓U	✓A	✓A	×R	✓U	✓A
MIT System	✓U	✓U	✓U	✓U	×R	✓U	✓U
SFU System	×F	×F	×F	✓U	×F	×F	×F
Treadmill-Based Gait Trainers							
Lokomat	×R	×R	✓A	✓A	×R	×R	×R
ReoAmbulator	×R	×R	✓A	✓A	×R	×R	×R
LOPES	×R	✓A	✓A	✓A	×F	×F	×F
POGO/PAM	×R	×R	✓A	✓A	×F	×F	×F
ALEX III	×R	✓A	✓A	✓A	×R	×R	✓A
KNEXO	×R	×R	✓U	✓A	×F	×F	×F
Over-Ground Systems							
ReWalk	×R	×R	✓A	✓A	×R	×R	✓U
HAL	×R	×R	✓A	✓A	×R	×R	✓U
Indego	×R	×R	✓A	✓A	×R	×R	×R
Mina (original)	×R	×R	✓A	✓A	×F	×F	×F
LEAD	×R	×R	✓A	✓A	×F	×F	×F
HANK	×R	×R	✓A	✓A	×R	×R	✓A
REX P	×R	✓A	✓A	✓A	×R	✓A	✓A

Note: ✓A, ✓U, ×R, and ×F respectively indicate that the associated DOF is actuated, unactuated, restricted, or free to rotate. Additionally, the SFU System refers to Donelan et al.'s energy-harvesting knee exoskeleton. Lastly, the anatomical motion abbreviations are clarified in the List of Acronyms.

Figure 2.14. Photographs of the REX P's crutchless operation (left) and the crutch-based operation of the Phoenix (right)

Note: Attendant use of crutches is the norm for current over-ground exoskeleton systems.

2.2. Research Objectives

2.2.1. Shortcomings Identified in Existing Lower-Limb Exoskeletons

Although the literature review of lower-limb exoskeletons presented in the previous subsection was not exhaustive, it reveals a definite trend in the current state-of-the-art. As illustrated in Table 2.1, the vast majority of existing lower-limb exoskeletons are restrictive in the sense that they do not provide a one-to-one kinematic compliance with the seven primary DOFs of the human leg. Especially in the existing systems for rehabilitation and mobility assistance applications, this lack of freedom in leg movements generally limits the wearer to only perform sitting-to-standing and walking gait movements, albeit in an often-unnatural manner. It also obstructs many actions associated with daily activity (e.g., restricted hip rotation makes turning while walking difficult).

Moreover, the reviewed lower-limb exoskeleton designs mostly rely on a serial manipulator structure, for which the system links and joints are successively connected in an open kinematic chain. However, a better-suited alternative exists; parallel manipulators use a closed-kinematic-chain architecture to transmit motion through two or more branches from a stationary base link to a moving end-effector link. As such, parallel manipulators generally achieve superior payload-to-weight ratio, speed response, stiffness, and positioning accuracy than their serial-manipulator counterparts

[137], [138]. Each of these characteristics is critical in the design of an exoskeleton. Furthermore, the widely-adopted serial-manipulator architecture in the current state-of-the-art requires that exoskeleton joint axes coincide with anatomical joint axes to avoid undesired interaction forces with the human subject. However, as Zanotto et al. discuss in [139], the exoskeleton-human interface is prone to joint axis misalignments because of variability in anatomic characteristics between and within subjects along with the general complexity of the human musculoskeletal system. Consequently, design schemes that assume joint axis alignments in the exoskeleton-limb interface are susceptible to undesired interaction forces that may jeopardize the safety of the human subject.

2.2.2. Thesis Objectives

In light of these shortcomings associated with existing systems and in keeping with the kinematic characteristics that make a lower-limb exoskeleton suitable for MoCap and other applications, the objectives of this work are:

- **To design a novel lower-limb exoskeleton that: (a)** has kinematic compliance with all seven of the primary human leg DOFs, **(b)** permits a full range-of-motion in all these DOFs for an average subject, and **(c)** does not require coaxial alignments at the exoskeleton-human interface for multi-DOF joints (i.e., the hip and ankle)

- **To incorporate a parallel manipulator in the exoskeleton design that includes at least two active joints** (i.e., at each exoskeleton substructure that corresponds with the 3-DOF human joints: hip and ankle)

- **To construct an unactuated prototype of the designed exoskeleton that interfaces with one human lower limb and can achieve a degree of MoCap accuracy comparable to current inertial systems** (i.e., in terms of tracking the joint angles associated with the seven main DOFs identified in the human leg)

Note that the second objective above considers the perspective that the present work may be extended to an actuated exoskeleton in the future. In that case, the

inclusion of a parallel manipulator exploits the various advantages of parallel manipulators relative to serial manipulators, particularly the increased payload-to-weight, speed response, and stiffness. However, the improved positioning accuracy characteristic also directly benefits the proposed unactuated exoskeleton in its function as a MoCap device.

2.2.3. Design Approach for Fulfilling the Thesis Objectives

Although several designs involving mechanical components that partially encircle the hip and ankle joints were initially considered for this work (i.e., similar to those presented in [140], [141]), these manipulators are prone to interferences with adjacent human-limb segments and insufficient workspace. That is, they are unable to support the complete range-of-motion of the interfaced joint. Consequently, the high-level modular design structure illustrated in Figure 2.15 is adopted for the development of the proposed exoskeleton. Note that the proposed exoskeleton constitutes a hybrid manipulator because it incorporates both open- and closed-loop kinematic chains [142], as will become more clear as the thesis progresses.

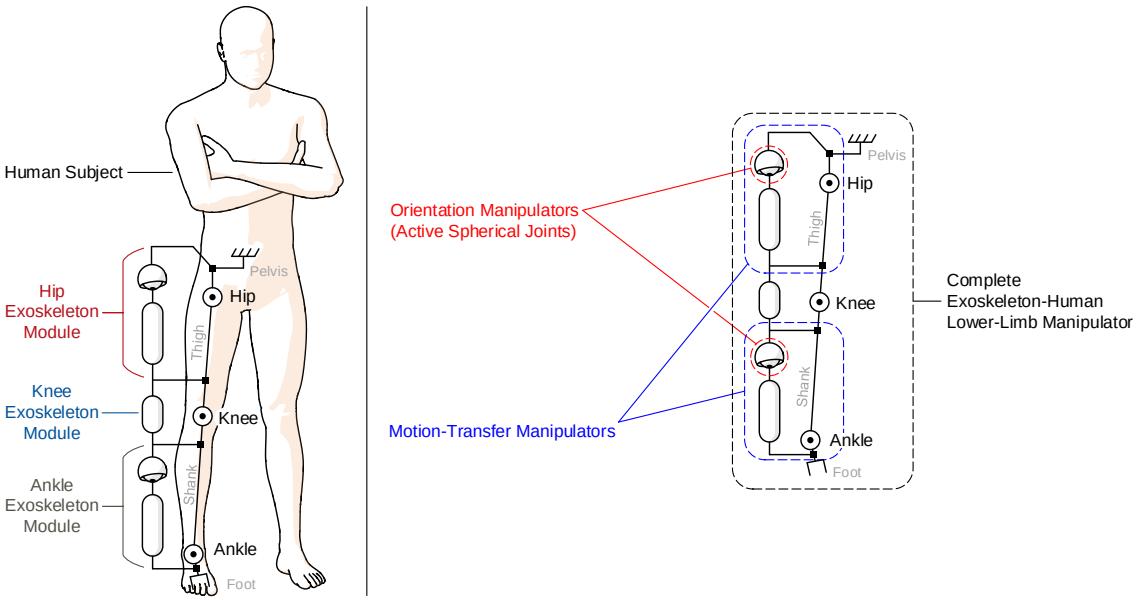

Figure 2.15. The high-level design of the proposed exoskeleton illustrating its modular characteristic (left) and hybrid manipulator structure (right)

As shown on the right side of the figure, the design approach includes an orientation manipulator and motion-transfer manipulator at the hip and ankle joints. The former is fully or in part a parallel manipulator that generates 3 DOFs of rotational motion

at its end-effector. As noted in the figure, this subsystem behaves like an active spherical joint from a black-box perspective; as such, the manipulator it represents includes three active joints. Moreover, the spatial position of the orientation manipulator's center-of-rotation (COR) relative to that of the corresponding anatomical joint is arbitrary, per part (c) of the first objective in Subsection 2.2.2. Next, the motion-transfer manipulator comprises the orientation manipulator, target human joint, and a passive mechanism that transfers spherical rotations between the former two. Depicted by the pill-shaped object below the orientation manipulator in Figure 2.15, the passive mechanism aims to transmit these rotations while limiting interaction forces in the exoskeleton-human system to those associated with torques about the anatomical joint COR. Thus, the motion-transfer manipulator should not induce undesired forces or torques that act to dislocate the human joint.

The novelties associated with the motion-transfer manipulator and some of its components represent the primary contributions of this work. Since the anatomical knee is interpreted here as a single-DOF joint, such a motion-transfer manipulator is not needed at its exoskeleton interface. Therefore, the knee exoskeleton module does not expand upon the current state-of-the-art. Now, as indicated in Figure 1.1, Chapter 3 and Chapter 4 elaborate on the designs and kinematic analyses of the orientation manipulator and motion-transfer manipulator subsystems, respectively. Chapter 5 proceeds to detail the kinematic considerations of the complete exoskeleton-human interface; this includes the approach for kinematically modeling the anatomical joints, hence their intentionally vague representations in Figure 2.15.

Chapter 3.

Kinematic Analyses of Candidate Orientation Manipulators

This chapter focuses on the orientation manipulator component of the proposed exoskeleton, as illustrated in Figure 3.1. To start, Section 3.1 provides background information and a review of existing orientation manipulators. Next, Sections 3.2–3.4 present three orientation manipulators to be considered as candidates for application in the exoskeleton design. Therein, the kinematic architecture, inverse kinematic analysis, forward kinematic analysis, Jacobian analysis, and performance indices associated with each candidate are formulated; a brief explanation of each of these concepts is included in the subsections of Section 3.2. Also note that the base links and local reference frames described for each kinematic architecture are fixed in local scope of manipulator but would eventually move with body segment to which they attach in the exoskeleton system. Whereas the kinematic analyses are fundamental for understanding the manipulators' motions, the Jacobian-derived performance indices provide a means to quantitatively compare their kinematic functionalities. Thus, the indices are then used as the primary factor in the selection of a best candidate in Section 3.5. Finally, a singularity analysis is conducted for the selected manipulator Section 3.6; this is key because the identified singular postures affect the ability to control and interpret end-effector motions.

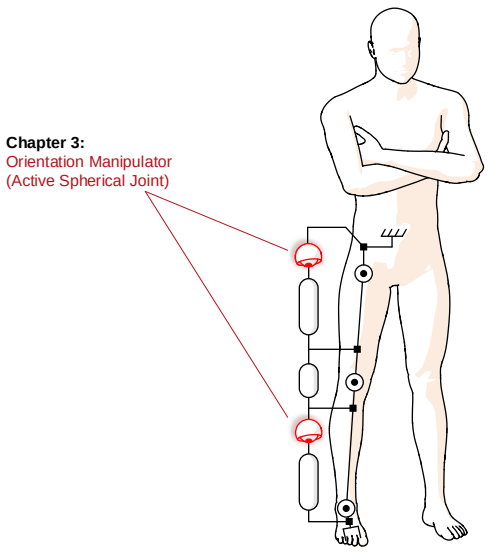

Figure 3.1. Stage of exoskeleton design development covered in Chapter 3

3.1. Background and Review of Orientation Manipulators

An orientation manipulator is one that permits three rotations and no translations about a single point at its end-effector [143]. Thus, orientation manipulators have 3 degrees-of-freedom (DOFs) and are intended to function in a space limited to orientation. In the context of this chapter, task space coordinates, or simply task coordinates, refer to the three rotations necessary to define the manipulator's spatial orientation. Correspondingly, orientation manipulators essentially act as active spherical or ball-and-socket joints. Meanwhile, a spherical manipulator is one for which all its links can only perform spherical motions about a common fixed point; spherical motion occurs when all the particles of the links trace surfaces of concentric spheres when the manipulator moves [142]. A 3-DOF spherical manipulator is a special case of an orientation manipulator; however, mechanisms with fewer than 3 DOFs can be spherical manipulators, so not all spherical manipulators are also orientation manipulators. It is implied in [143] that orientation manipulators are distinct from spherically-wristed serial manipulators, so this thesis considers only parallel and hybrid manipulator types as applicable for classification as orientation manipulators.

Some manipulators with more than 3 DOFs can behave as orientation manipulators if they are controlled or mechanically constrained to only produce three rotations about a stationary point. Appendix A or [144] discuss how this is accomplished using various design manifestations of one 6-DOF manipulator (i.e., the Stewart-Gough platform). For exoskeleton applications, it is possible to use such a 6-DOF manipulator to transfer purely-rotational motions to the targeted human joint without a passive motion-transfer manipulator. However, it is ultimately superfluous to use a manipulator with more than 3 DOFs in an exoskeleton designed to interface with a 3-DOF bodily joint. Therefore, only orientation manipulators will be explored as options for the proposed exoskeleton design; some designs that attain 3-DOF rotational motions with redundant active joints are mentioned in the review to follow but are not considered for employment.

Before reviewing some of the applicable orientation manipulators documented in the literature, note that it is common notation in the fields of robotics and manipulator design to specify mechanism structures by the type and sequence of joints that they employ. 'R', 'U', and 'S' denote revolute, universal, and spherical joints, respectively. An

underline designates a joint as active, while non-underlined joints are passive. For parallel manipulators, a dash is used to distinguish joint sequences belonging to different branches, and if branches have equivalent sequences, a digit preceding a dash identifies the number of same-sequence branches. Also note that a final '/S' distinguishes central mast mechanisms, for which a passive spherical joint connects the end-effector directly to the base link (i.e., in parallel with the branches) to enforce an orientation task space.

In [138], Gosselin and Lavoie review architectures, inverse kinematic analyses, and some performance characteristics of three prominent forms for spherical 3-RRR manipulators. They explore: a generalized form, a form with coplanar active joints, and a form with coaxial active joints. First, for the general form, the base and end-effector can be conceptualized as a pyramid-shaped component and inverted pyramidal component, respectively, which move relative to each other about a shared vertex point. The manipulator's active joints are located at the remaining lower-three vertices of the base pyramid, and their axes are directed along the pyramid edges to all intersect the COR vertex. Now, the latter two forms are special cases of the first. If the base pyramid collapses horizontally, the COR vertex becomes planar with the active joint vertices, yielding coplanar active joints. Alternatively, if the base pyramid collapses vertically, the pyramid edges adjacent to the COR vertex become colinear, yielding coaxial active joints. Gosselin and Lavoie also discuss a 3-UPS/S, noting its unique inverse kinematics solution but generally-reduced workspace relative to the 3-RRR architectures [138]. Ultimately, Gosselin et al. went on to develop a mechanical design and dynamic performance analysis for one case of the generalized 3-RRR form. Named the Agile Eye, this design is characterized by a 90-degree angle between adjacent active joint axes along with a 90-degree angle between each adjacent joint along the manipulator branches [145]–[147]. Since then, further kinematic studies, including forward kinematic analyses, have been conducted regarding the Agile Eye and general spherical 3-RRR form [148]–[150].

In the past decade, several lesser-established orientation manipulators have also been explored. In [151], Gallardo-Alvarado et al. present kinematic, velocity, acceleration, and performance analyses of a 3-RRRS/S mast mechanism that features revolute joints with non-intersecting axes. For ankle rehabilitation applications, Wang et al. have proposed a (3-RUS)-RRR redundantly-actuated orientation manipulator and

devised forward and inverse kinematic, workspace, performance, and singularity analyses for the device [152]. Cui et al. also developed a redundantly-actuated orientation manipulator with a 4-UPS/S architecture and intention for solar panel positioning applications [153]. Finally, Enferadi and Shahi detail the forward and inverse kinematics, optimization of workspace, and singularity analysis for an original 3-RSS/S spherical parallel manipulator in [154]. Note that incorporating redundant actuation in a manipulator's design can eliminate singularities and improve accuracy, stiffness, workspace, payload, acceleration, force distribution among active joints, and force transmission uniformity at the end-effector [155]; however, its disadvantages include challenges in control, increased complexity in the kinematic and dynamic analyses, and increased materials and cost. Redundant actuation is avoided in the initial development of the exoskeleton for this thesis, but may be worth considering in a later design iteration depending on the level of system performance achieved in its absence.

3.2. Candidate #1: 3-RUS/S Parallel Manipulator

The first candidate orientation manipulator to be explored is a novel 3-RUS/S central mast mechanism. The developments made in the following subsections embody a contribution of this master's thesis; they are also described in the Ph.D. thesis of Sadeqi [156], with whom the author devised and analyzed the proposed manipulator.

3.2.1. Kinematic Architecture

As its structural name implies, the proposed 3-RUS/S parallel manipulator includes three branches with equivalent joint sequences. Per the depictions in Figure 3.2, each branch connects an outer base structure to a central end-effector by way of revolute, universal, and spherical joints in succession, where the revolute joint is active, and the others are passive. Furthermore, the end-effector connects to the base link through a spherical joint, which constrains it to 3-DOF rotational motions. This constraint is denoted by the ending '/S' in the device's architecture designation. Aside from the manipulator's articular layout, there are several important design aspects to note. First, the rotational axes for each of the active revolute joints exist within a single plane, and the COR of the end-effector (i.e., the constraining spherical joint's center) also lies in that plane. Next, the active joints are equidistant from the end-effector COR and from each

other. The final spherical joints in each branch are also equidistant from each other. Finally, the proximal links from the three branches (i.e., those nearer to the end-effector's COR) all have equal length, as do the distal links (i.e., those further from the COR), but the proximal and distal link lengths are not necessarily equal. Hereafter, this manipulator will be referred to by the name: RUS.

The origin of the manipulator's local reference frame, $\{0\}^{\text{RUS}}$, is coincident with the end-effector's COR. Moreover, the $\hat{z}_0^{\text{RUS}}$ axis is normal to the plane containing the COR and active joint axes, and $\hat{x}_0^{\text{RUS}}$ intersects the axis of one active joint at a right angle. The branch associated with this intersected joint is denoted by the number 1, while the adjacent branch positioned counter-clockwise with respect to $\hat{z}_0^{\text{RUS}}$ is designated with 2, and the final branch with 3. The positions of the active, universal, and spherical joints on each branch are given by a_i, b_i, and c_i, respectively, where the subscript i differentiates the three branches (i.e., i = 1, 2, 3). Correspondingly, the active joints' angles are given by θ_i^{RUS}, where the subscript again identifies the branch number.

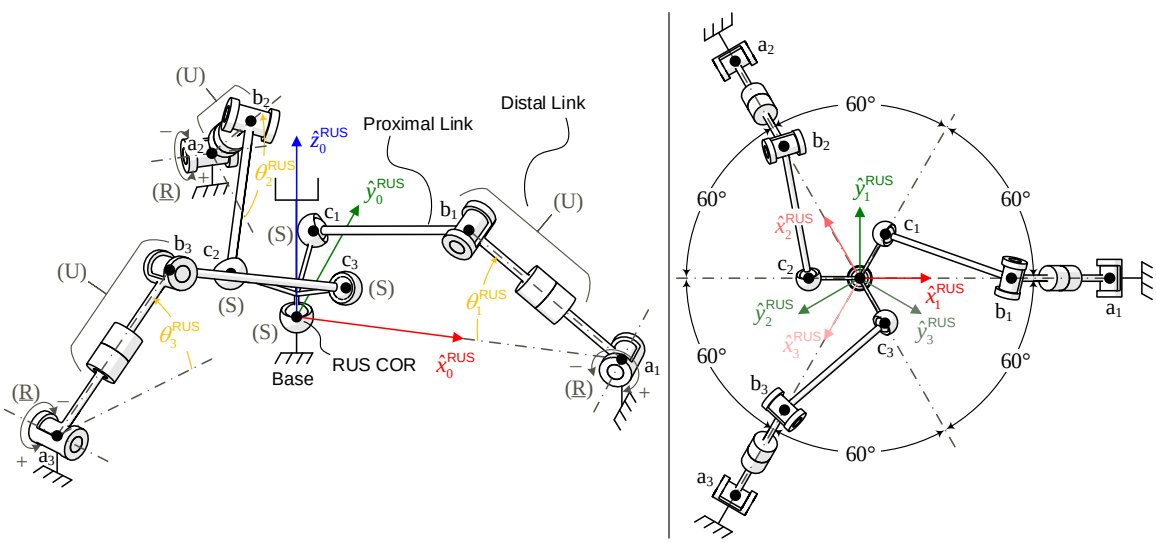

Figure 3.2. Schematic of the RUS with joint center, joint variable, and local reference frame labels (left); top view of the RUS in its home configuration with frame $\{1\}^{\text{RUS}}$, $\{2\}^{\text{RUS}}$, and $\{3\}^{\text{RUS}}$ labels (right)

Note: Since the link between the two revolute joints constituting a universal joint can be considered as having zero length, the line $\overline{\mathrm{a}_i\mathrm{b}_i}$ represents the distal-link length of branch i ($\overline{\mathrm{b}_i\mathrm{c}_i}$ represents the proximal link span).

In addition to the local reference frame, four other frames are used to evaluate the manipulator's motions in the kinematic analyses to follow. The first three of these frames, $\{1\}^{\text{RUS}}$, $\{2\}^{\text{RUS}}$, and $\{3\}^{\text{RUS}}$, specify the directions in which the active joints are

located. As illustrated in the right-side image of Figure 3.2, a_i is intersected by the $\hat{x}_i^{\mathrm{RUS}}$ axis, for i = 1, 2, and 3, while each $\hat{z}_i^{\mathrm{RUS}}$ axis is coaxial with $\hat{z}_0^{\mathrm{RUS}}$. Therefore, the $\{1\}^{\mathrm{RUS}}$, $\{2\}^{\mathrm{RUS}}$, and $\{3\}^{\mathrm{RUS}}$ frames are respectively defined relative to $\{0\}^{\mathrm{RUS}}$ by fixed rotations of 0 degrees, 120 degrees, and 240 degrees about the positive $\hat{z}_0^{\mathrm{RUS}}$ axis. In turn, pre-multiplication by one of the matrices, ${}^{0}_{i}\mathbf{R}^{\mathrm{RUS}}$, transforms a vector's $\{i\}^{\mathrm{RUS}}$-frame representation to $\{0\}^{\mathrm{RUS}}$ representation. Alternatively, pre-multiplication by the transpose rotation matrix, ${}^{i}_{0}\mathbf{R}^{\mathrm{RUS}}$, allows positions defined in the local reference frame to be expressed in the corresponding branch-specific frame. Equations (3.1) specify these rotation matrices:

$$
\begin{gathered}
{}^{0}_{1}\mathbf{R}^{\mathrm{RUS}} = \mathbf{I}_{3\times3}\,,\ {}^{0}_{2}\mathbf{R}^{\mathrm{RUS}} = \mathbf{R}_Z\left(120°\right) = \begin{bmatrix} c\left(120°\right) & -s\left(120°\right) & 0 \\ s\left(120°\right) & c\left(120°\right) & 0 \\ 0 & 0 & 1 \end{bmatrix}, \text{ and} \\
{}^{0}_{3}\mathbf{R}^{\mathrm{RUS}} = \mathbf{R}_Z\left(240°\right) = \begin{bmatrix} c\left(240°\right) & -s\left(240°\right) & 0 \\ s\left(240°\right) & c\left(240°\right) & 0 \\ 0 & 0 & 1 \end{bmatrix}
\end{gathered}
\tag{3.1}
$$

where $c(\ )$ and $s(\ )$ represent the cosine and sine functions, respectively; this notation will be used throughout the remainder of the thesis.

The last frame, $\{4\}^{\mathrm{RUS}}$, which is not shown in Figure 3.2, moves with the RUS's end-effector to specify its rotations with respect to the local reference frame. The $\{4\}^{\mathrm{RUS}}$ frame is fixed to the end-effector such that ${}^{0}_{4}\mathbf{R}^{\mathrm{RUS}}$ equals $\mathbf{I}_{3\times3}$ when the manipulator is arranged in its home configuration. Note that the RUS's home configuration is achieved when the manipulator displays the rotational symmetry shown of the right side of Figure 3.2. In this state, a 60 degree offset about $\hat{z}_0^{\mathrm{RUS}}$ separates the $\hat{x}_0^{\mathrm{RUS}}$ - $\hat{y}_0^{\mathrm{RUS}}$ plane projections of ${}^{0}\vec{\mathrm{c}}_i^{\mathrm{RUS}}$ and ${}^{0}\vec{\mathrm{b}}_i^{\mathrm{RUS}}$ as well as ${}^{0}\vec{\mathrm{c}}_i^{\mathrm{RUS}}$ and ${}^{0}\vec{\mathrm{b}}_j^{\mathrm{RUS}}$, where j designates the branch immediately counter-clockwise to branch i. Here and hereafter, the left-side superscripts indicate the frame in which vectors are being interpreted, as explained in the prefatory Symbols section. The home configuration also causes all universal joint positions ${}^{0}\vec{\mathrm{b}}_i^{\mathrm{RUS}}$ to share a common positive z-coordinate value; similarly, the three vectors ${}^{0}\vec{\mathrm{c}}_i^{\mathrm{RUS}}$ have equal z-coordinate values in this configuration.

3.2.2. Inverse Kinematic Analysis

The generalized inverse kinematics problem associated with a manipulator is to determine the set of joint variable values in terms of a known position and orientation of the end-effector [157]. As an orientation manipulator, the RUS's end-effector position remains constant with respect to local reference frame, so its inverse kinematic analysis only involves a known orientation, given by ${}^{0}_{4}\mathbf{R}^{\text{RUS}}_{\mathbf{N}}$; the '$\mathbf{N}$' subscript indicates that numerical values are established for each element in the rotation matrix. The analytical approach used here is to first find expressions for the positions of each joint that correspond to the known end-effector orientation, and then use the joint position information to deduce the required active-joint states. This process is outlined below in three stages: determination of ${}^{0}\vec{c}^{\text{RUS}}_{i}$, ${}^{0}\vec{a}^{\text{RUS}}_{i}$, and then ${}^{0}\vec{b}^{\text{RUS}}_{i}$ positions.

Determination of the Branches' Spherical Joint Positions

The branches' spherical joints are attached directly to the RUS manipulator's end-effector link, so the c_i points have fixed positions with respect to the end-effector frame $\{4\}^{\text{RUS}}$. That is, the elements of ${}^{4}\vec{c}^{\text{RUS}}_{i}$ are constant and known from the mechanical design of the end-effector. In order to represent the positions of the c_i points with respect to the local reference frame after any arbitrary rotations of the end-effector, each ${}^{4}\vec{c}^{\text{RUS}}_{i}$ vector is pre-multiplied by the known ${}^{0}_{4}\mathbf{R}^{\text{RUS}}_{\mathbf{N}}$ rotation matrix as follows:

$$ {}^{0}\vec{c}^{\text{RUS}}_{i} = {}^{0}_{4}\mathbf{R}^{\text{RUS}}_{\mathbf{N}}\,{}^{4}\vec{c}^{\text{RUS}}_{i}\,,\ i = 1, 2, 3 \tag{3.2} $$

Determination of the Branches' Rotary Joint Positions

The positions of the a_i points are constant and known with respect to the local reference frame because they are fixed to the base link. However, for the sake of generality in the analysis of each manipulator branch, the remainder of the inverse kinematics derivations occur with respect to the three branch-specific frames: $\{1\}^{\text{RUS}}$, $\{2\}^{\text{RUS}}$, and $\{3\}^{\text{RUS}}$. Therefore, positions ${}^{0}\vec{a}^{\text{RUS}}_{i}$ and ${}^{0}\vec{c}^{\text{RUS}}_{i}$ are redefined in their corresponding generalized branch frame as follows:

$$ {}^{i}\vec{c}^{\text{RUS}}_{i} = {}^{i}_{0}\mathbf{R}^{\text{RUS}}\,{}^{0}\vec{c}^{\text{RUS}}_{i} \ \text{ and } \ {}^{i}\vec{a}^{\text{RUS}}_{i} = {}^{i}_{0}\mathbf{R}^{\text{RUS}}\,{}^{0}\vec{a}^{\text{RUS}}_{i} \tag{3.3} $$

for i = 1, 2, 3. Recall that each rotation matrix ${}^{0}_{i}\mathbf{R}^{\text{RUS}}$ is fully defined in Equations (3.1).

Determination of the Branches' Universal Joint Positions

Now, the positions of the b_i points can be determined using a geometric-analysis approach. Considering the ith branch's proximal link and its attachment to the end-effector, the known spherical joint c_i position defines a sphere of possible b_i locations; the radius of the sphere is given by the proximal link length. Similarly, the distal link's connection to the ith branch's active revolute joint limits the possible b_i positions to a circle in the $\hat{x}_i^{RUS}$ - $\hat{z}_i^{RUS}$ plane, where the circle radius is equal to the distal link length. Because both geometric conditions must be met, the solutions for the ith branch's b_i position are the intersection points of the proximal link sphere and distal link circle, as illustrated in Figure 3.3. Note that i = 1, 2, 3 is implied for the remainder of Section 3.2.

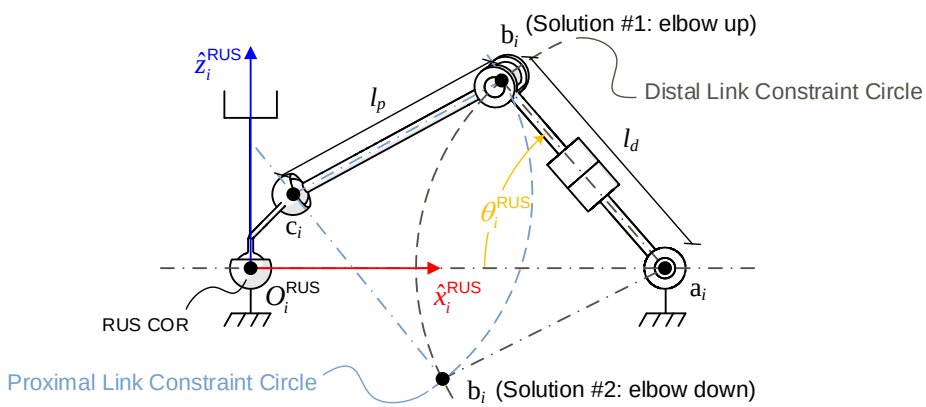

Figure 3.3. Isolated i^{th} RUS branch with possible inverse-kinematic b_i solutions

The branch link lengths relate to branch joint positions via the Euclidean norm of the vectors that span the links:

$$l_d = \left\| {}^{i}\vec{b}_i^{RUS} - {}^{i}\vec{a}_i^{RUS} \right\| = \sqrt{\left(x_{bi} - x_{ai}\right)^2 + \left(y_{bi} - y_{ai}\right)^2 + \left(z_{bi} - z_{ai}\right)^2} \tag{3.4}$$

$$l_p = \left\| {}^{i}\vec{b}_i^{RUS} - {}^{i}\vec{c}_i^{RUS} \right\| = \sqrt{\left(x_{bi} - x_{ci}\right)^2 + \left(y_{bi} - y_{ci}\right)^2 + \left(z_{bi} - z_{ci}\right)^2} \tag{3.5}$$

where l_d and l_p are the distal and proximal link lengths, respectively. Also note that x_{ji} denotes the x-coordinate of joint j's position on branch i when represented in frame $\{i\}^{RUS}$, and likewise for the y- and z-coordinates. Frames $\{1\}^{RUS}$, $\{2\}^{RUS}$, and $\{3\}^{RUS}$ are all defined such that the y-coordinates of ${}^{i}\vec{a}_i^{RUS}$ and ${}^{i}\vec{b}_i^{RUS}$ are both equal to zero (i.e., the a_i and b_i points lie in the $\hat{x}_i^{RUS}$ - $\hat{z}_i^{RUS}$ plane). Therefore, Equations (3.4) and (3.5) can be simplified and rearranged to respectively yield:

$$l_d^2 = x_{bi}^2 - 2x_{bi}x_{ai} + x_{ai}^2 + z_{bi}^2 - 2z_{bi}z_{ai} + z_{ai}^2 \tag{3.6}$$

$$l_p^2 = x_{bi}^2 - 2x_{bi}x_{ci} + x_{ci}^2 + z_{bi}^2 - 2z_{bi}z_{ci} + z_{ci}^2 + y_{ci}^2 \tag{3.7}$$

Since x_{bi} and z_{bi} are the only unknown variables, Equations (3.6) and (3.7) can be interpreted as the distal link circle equation and the circular projection of the proximal link sphere onto the $\hat{x}_i^{\text{RUS}}$ - $\hat{z}_i^{\text{RUS}}$ plane, respectively. If the expression equal to $\left(x_{bi}^2 + z_{bi}^2\right)$ is isolated in Equation (3.6) and then substituted into Equation (3.7), the resulting equation represents the line passing through the two circles' intersection points:

$$l_p^2 = l_d^2 + 2x_{bi}x_{ai} - x_{ai}^2 + 2z_{bi}z_{ai} - z_{ai}^2 - 2x_{bi}x_{ci} + x_{ci}^2 - 2z_{bi}z_{ci} + z_{ci}^2 + y_{ci}^2 \tag{3.8}$$

Next, separating x_{bi} in Equation (3.8), substituting its equivalent expression back into Equation (3.6), and applying the quadratic formula to the resulting equation provides two possible z_{bi} solutions:

$$z_{bi} = \frac{-B_0 \pm \sqrt{B_0^2 - 4A_0C_0}}{2A_0} \tag{3.9}$$

where equivalences for the new variables introduced in Equation (3.9) are as follows:

$$\begin{gathered} A_0 = \frac{F_0^2}{E_0^2} + 1,\ B_0 = \frac{2D_0F_0}{E_0^2} - \frac{2F_0x_{ai}}{E_0} - 2z_{ai},\ C_0 = \frac{D_0^2}{E_0^2} - \frac{2D_0x_{ai}}{E_0} + x_{ai}^2 + z_{ai}^2 - l_d^2, \\ D_0 = y_{ci}^2 + l_d^2 - x_{ai}^2 - z_{ai}^2 + x_{ci}^2 + z_{ci}^2 - l_p^2,\ E_0 = 2\left(x_{ci} - x_{ai}\right), \text{ and } F_0 = 2\left(z_{ai} - z_{ci}\right) \end{gathered} \tag{3.10}$$

As shown in Figure 3.3, the two solutions represent 'elbow up' and 'elbow down' configurations, for which the b_i point is respectively either above or below the c_i point (i.e., relative to $\hat{z}_0^{\text{RUS}}$). For the intended design, the addition result, or 'elbow up' configuration, is the appropriate one.

Final Inverse Kinematics Equation

With z_{bi} calculated, x_{bi} can be determined as the only remaining unknown variable from Equation (3.8). Subsequently, the ith branch's active joint angle is computed as:

$$\theta_i^{\text{RUS}} = \text{atan2}\left(z_{bi}, x_{ai} - x_{bi}\right) \tag{3.11}$$

This completes the inverse kinematics solution for the generalized i^{th} branch. In practice, the algorithm must be carried out three times: once for each branch of the RUS.

3.2.3. Forward Kinematic Analysis

Contrary to the inverse kinematics problem, the generalized forward kinematics problem requires development of the end-effector position and orientation in terms of a known set of joint variable values [157]. However, since the RUS is an orientation manipulator, only the end-effector orientation needs to be determined. Thus, the active

joint variables θ_1^{RUS}, θ_2^{RUS}, and θ_3^{RUS} are assumed to be known inputs, while the end-effector's orientation is unknown and must be resolved. The following subsections outline one geometric approach for the forward kinematic analysis.

Determination of the Branches' Universal Joint Positions

Each universal joint position, b_i, can be expressed directly in terms of the corresponding active joint variable, θ_i^{RUS}, as follows:

$$ {}^{i}\vec{\mathrm{b}}_i^{\text{RUS}} = \begin{bmatrix} \left\| {}^{i}\vec{\mathrm{a}}_i^{\text{RUS}} \right\| - l_d \cos\left(\theta_i^{\text{RUS}}\right) \\ 0 \\ l_d \sin\left(\theta_i^{\text{RUS}}\right) \end{bmatrix} \tag{3.12} $$

The end-effector orientation is affected by each branch configuration, so its orientation is most sensibly represented in terms of the local reference frame $\{0\}^{\text{RUS}}$. To facilitate this goal, the position vectors are then pre-multiplied by the appropriate rotation matrices from Equations (3.1) to represent them in terms of the local reference frame $\{0\}^{\text{RUS}}$:

$$ {}^{0}\vec{\mathrm{b}}_i^{\text{RUS}} = {}^{0}_{i}\mathbf{R}^{\text{RUS}}\, {}^{i}\vec{\mathrm{b}}_i^{\text{RUS}} \tag{3.13} $$

Determination of the Branches' Spherical Joint Positions

The next task is to determine the c_i positions of the spherical joints connecting the end-effector to the proximal link of each branch. Considering the geometric constraint imposed by the proximal links' fixed lengths, the set of feasible c_i positions is given by a spherical surface with radius l_p centered at b_i for each of i = 1, 2, and 3:

$$ \left(x_{ci} - x_{bi}\right)^2 + \left(y_{ci} - y_{bi}\right)^2 + \left(z_{ci} - z_{bi}\right)^2 = l_d^2 \tag{3.14} $$

This is true because the joint at b_i is a universal joint. Additionally, the constraint established by spherical joints' fixed positions on the end-effector limits the possible c_i positions to a spherical surface with radius $\left\| {}^{0}\vec{\mathrm{c}}_i^{\text{RUS}} \right\|$ and centered at the $\{0\}^{\text{RUS}}$ origin:

$$ x_{ci}^2 + y_{ci}^2 + z_{ci}^2 = \left\| {}^{0}\vec{\mathrm{c}}_i^{\text{RUS}} \right\|^2 \tag{3.15} $$

Upon asserting both constraints simultaneously, the feasible c_i positions reduce to the circle of intersection between the two spherical surfaces for each branch i; note that the circle of possible solutions collapses to a point if the ith branch proximal link axis becomes aligned such that it intersects the $\{0\}^{\text{RUS}}$ origin, O_i^{RUS}. Also note that in Equations (3.14) and (3.15), the x-, y-, and z- coordinate values are taken with respect to the local reference frame, $\{0\}^{\text{RUS}}$. Figure 3.4 illustrates an example of the possible

solution space for c_i after imposing the two geometric constraints on one generalized branch of the RUS manipulator.

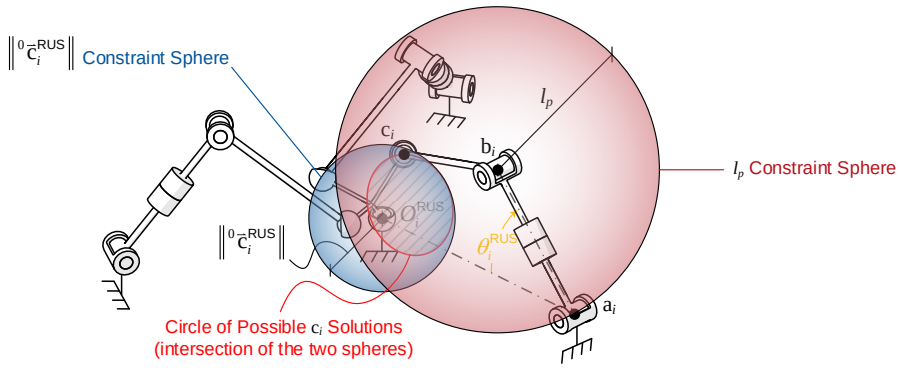

Figure 3.4. Visualization of the circle of possible c_i solutions after asserting the proximal-link length and spherical-joint-to-origin length constraints

Note: The l_p constraint sphere intersects c_i but not necessarily a_i.

As the branches' spherical joints are installed at known positions on the end-effector, each c_i point is located at a fixed distance from each adjacent c_j point:

$$\left\|\vec{c}_i^{RUS} - \vec{c}_j^{RUS}\right\| = l_e \tag{3.16}$$

where i and j = 1, 2, 3, but $i \neq j$. After applying this final constraint per the manipulator's chosen mechanical design parameters, the solution set for the c_i positions reduces to one or more points (i.e., assuming the chosen active joint variables do not cause any geometric constraint to be violated). This is obtained by applying a numerical approach to solving the system of equations given in (3.14)–(3.16). Depending on the joint variable and design parameter selections, some input angles may yield several solutions while others may result in a unique solution as exemplified in Figure 3.5.

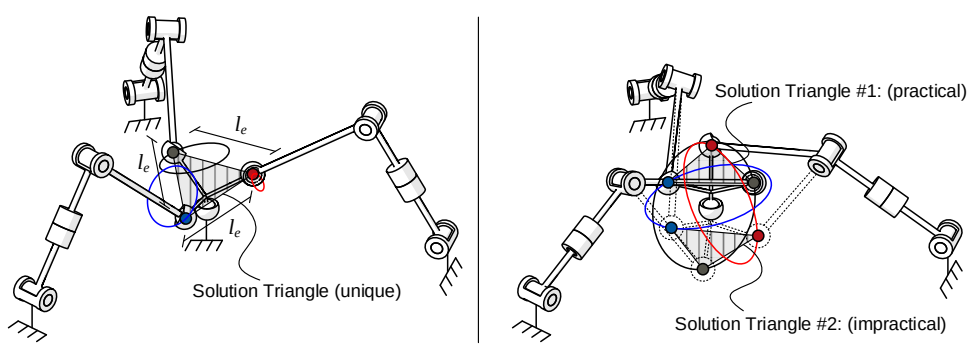

Figure 3.5. Visualization of a unique (left) and multiplicity of solutions (right) for the c_i position set after asserting the proximal link, spherical joint-to-origin, and spherical joint-to-spherical joint length constraints

Note: The circles shown in these images represent the possible c_i solutions after asserting the proximal-link length and spherical-joint-to-origin length constraints like in Figure 3.4.

The left side of Figure 3.5 illustrates an example configuration that only has one forward kinematic solution. Contrarily, the right side of Figure 3.5 shows a configuration for which six mathematically-feasible solutions exist: the two that are shown (i.e., where both results yield coaxial $\hat{z}_0^{\text{RUS}}$ and $\hat{z}_4^{\text{RUS}}$ axes) and four others that cause the $\hat{z}_4^{\text{RUS}}$ axis to lie within the $\hat{x}_0^{\text{RUS}}$ - $\hat{y}_0^{\text{RUS}}$ plane. The latter four are not illustrated in Figure 3.5 to facilitate visual clarity. In the configuration shown on the right side of the figure, the three constraint circles are all relatively large, which allows for the multiplicity of possible solutions. However, there is only one practically reachable solution, as labeled in the right-side image, because all other solutions would result in collisions between mechanical parts or geometric constraint violations during any end-effector path followed to reach said solutions. This observation leads to the following general rule for choosing the appropriate forward kinematic result for the RUS manipulator.

In the case of multiple solutions, the one for which all c_i points' *z*-coordinates are positive should be selected; there is usually only one possible assembly mode that achieves this condition when a multiplicity of solutions exist. If no such solution is available, one method to choose an appropriate assembly mode is to select the one that maximizes the number of c_i points with positive *z*-coordinates. However, upon qualitatively observing the RUS manipulator's movement behavior, if the first case is not true (i.e., all c_i *z*-coordinates being positive), the manipulator's links tend to interfere with each other. Therefore, in practice, the manipulator's workspace should be limited (e.g., via mechanical stops) to solutions that maintain positive *z*-coordinates for all c_i points. Generally, this workspace limitation reduces the possible solution set for the ${}^{0}\vec{\mathrm{c}}_i^{\text{RUS}}$ positions to a single solution, assuming geometric constraints are appropriately observed. However, special treatment is necessary to deal with the one active joint state that causes the two nearest c_i and c_j points to be equidistant from b_i (i.e., select the solution that maintains motion continuity).

Determination of the End-Effector Orientation

The final task in the forward kinematics process is to determine the end-effector's orientation with respect to the local reference frame $\{0\}^{\text{RUS}}$. This orientation, given by the ${}^{0}_{4}\mathbf{R}^{\text{RUS}}$ rotation matrix, can be constructed from the ${}^{0}\vec{\mathrm{c}}_i^{\text{RUS}}$ solutions from the preceding paragraphs. To start, since the $\{4\}^{\text{RUS}}$ frame's $\hat{z}_4^{\text{RUS}}$ axis is normal to the plane containing all three c_i points, it is given by:

$$ {}^{0}\hat{z}_4^{\text{RUS}} = \frac{\left({}^{0}\vec{c}_3^{\text{RUS}} - {}^{0}\vec{c}_2^{\text{RUS}}\right)\times\left({}^{0}\vec{c}_1^{\text{RUS}} - {}^{0}\vec{c}_2^{\text{RUS}}\right)}{\left\|\left({}^{0}\vec{c}_3^{\text{RUS}} - {}^{0}\vec{c}_2^{\text{RUS}}\right)\times\left({}^{0}\vec{c}_1^{\text{RUS}} - {}^{0}\vec{c}_2^{\text{RUS}}\right)\right\|} \tag{3.17} $$

Next, the direction of the $\hat{x}_4^{\text{RUS}}$ axis is provided by a vector originating at c_2 and leading to the halfway point of the vector pointing from c_3 to c_1 (see Figure 3.2), so:

$$ {}^{0}\hat{x}_4^{\text{RUS}} = \frac{{}^{0}\vec{c}_3^{\text{RUS}} - {}^{0}\vec{c}_2^{\text{RUS}} + \frac{1}{2}\left({}^{0}\vec{c}_1^{\text{RUS}} - {}^{0}\vec{c}_3^{\text{RUS}}\right)}{\left\|{}^{0}\vec{c}_3^{\text{RUS}} - {}^{0}\vec{c}_2^{\text{RUS}} + \frac{1}{2}\left({}^{0}\vec{c}_1^{\text{RUS}} - {}^{0}\vec{c}_3^{\text{RUS}}\right)\right\|} \tag{3.18} $$

Finally, the third axis of $\{4\}^{\text{RUS}}$ is yielded from the cross product of the previous two, and the ${}^{0}_{4}\mathbf{R}^{\text{RUS}}$ matrix can then be fully populated:

$$ {}^{0}_{4}\mathbf{R}^{\text{RUS}} = \begin{bmatrix} {}^{0}\hat{x}_4^{\text{RUS}} & {}^{0}\hat{y}_4^{\text{RUS}} & {}^{0}\hat{z}_4^{\text{RUS}} \end{bmatrix}, \text{ where } {}^{0}\hat{y}_4^{\text{RUS}} = {}^{0}\hat{z}_4^{\text{RUS}} \times {}^{0}\hat{x}_4^{\text{RUS}} \tag{3.19} $$

This completes the forward kinematics procedure.

3.2.4. Kinematic Analysis Verification

Since the inverse and forward kinematic analyses were developed as a novel contribution, simulation-based verifications have been conducted to confirm their correctness. The verification procedure involved kinematic algorithm development using MATLAB's SimMechanics software and CAD modeling with SolidWorks, as will be described further in the subsections below. Table 3.1 lists the design parameters for the RUS manipulator selected during the verification study. Note that the chosen parameter set produces an angle of 51.1137 degrees (i.e., with respect to the $\hat{x}_0^{\text{RUS}}$ - $\hat{y}_0^{\text{RUS}}$ plane) for each joint variable θ_i^{RUS} when the manipulator is arranged in its home configuration. Furthermore, to facilitate the presentation of end-effector orientation results, the Tait-Bryan roll-pitch-yaw convention is used to derive Euler angles from rotation matrices:

$$ \theta_Y^{\text{RUS}} = \operatorname{atan2}\left(-p_{31}, \pm\sqrt{p_{11}^2 + p_{21}^2}\right), \ \theta_Z^{\text{RUS}} = \operatorname{atan2}\left(\frac{p_{21}}{c\theta_Y^{\text{RUS}}}, \frac{p_{11}}{c\theta_Y^{\text{RUS}}}\right), \text{ and } \theta_X^{\text{RUS}} = \operatorname{atan2}\left(\frac{p_{32}}{c\theta_Y^{\text{RUS}}}, \frac{p_{33}}{c\theta_Y^{\text{RUS}}}\right) \tag{3.20} $$

This applies when the end-effector orientation is expressed as:

$$ {}^{0}_{4}\mathbf{R}_{\mathbf{N}}^{\text{RUS}} = \begin{bmatrix} p_{11} & p_{12} & p_{13} \\ p_{21} & p_{22} & p_{23} \\ p_{31} & p_{32} & p_{33} \end{bmatrix} \text{ and} $$

$$ {}^{0}_{4}\mathbf{R}_{\mathbf{S}}^{\text{RUS}} = \mathbf{R}_Z\left(\theta_Z^{\text{RUS}}\right)\mathbf{R}_Y\left(\theta_Y^{\text{RUS}}\right)\mathbf{R}_X\left(\theta_X^{\text{RUS}}\right) = \tag{3.21} $$

$$ \begin{bmatrix} c\theta_Z^{\text{RUS}}c\theta_Y^{\text{RUS}} & c\theta_Z^{\text{RUS}}s\theta_Y^{\text{RUS}}s\theta_X^{\text{RUS}} - s\theta_Z^{\text{RUS}}c\theta_X^{\text{RUS}} & c\theta_Z^{\text{RUS}}s\theta_Y^{\text{RUS}}c\theta_X^{\text{RUS}} + s\theta_Z^{\text{RUS}}s\theta_X^{\text{RUS}} \\ s\theta_Z^{\text{RUS}}c\theta_Y^{\text{RUS}} & s\theta_Z^{\text{RUS}}s\theta_Y^{\text{RUS}}s\theta_X^{\text{RUS}} + c\theta_Z^{\text{RUS}}c\theta_X^{\text{RUS}} & s\theta_Z^{\text{RUS}}s\theta_Y^{\text{RUS}}c\theta_X^{\text{RUS}} - c\theta_Z^{\text{RUS}}s\theta_X^{\text{RUS}} \\ -s\theta_Y^{\text{RUS}} & c\theta_Y^{\text{RUS}}s\theta_X^{\text{RUS}} & c\theta_Y^{\text{RUS}}c\theta_X^{\text{RUS}} \end{bmatrix} $$

in which a '$\mathbf{N}$' subscript denotes a numerical representation and an '$\mathbf{S}$' subscript denotes symbolic representation. The positive square root term is chosen for θ_Y^{RUS} to maintain a range of [–90 90] degrees in accordance with the device's workspace limitation. The roll-pitch-yaw convention is revisited in the complete-system analysis of Section 5.2.

Table 3.1. RUS manipulator design parameters employed for kinematic verifications

Parameter (i.e., for i = 1, 2, 3)	**Value** (mm)
Distal Link Length, l_d	120
Proximal Link Length, l_p	120
Base Link Outer Radius, $\left\lVert {}^{0}\vec{a}_i^{\text{RUS}} \right\rVert$	200
Spherical Joint Connection Radius, $\left\lVert {}^{0}\vec{c}_i^{\text{RUS}} \right\rVert$	65.6220
Spherical Joint Separation Distance, l_e	86.6025
Spherical Joint Connection Points (End-Effector Frame):	${}^{4}\vec{c}_1^{\text{RUS}}$ = [25.2500 36.8061 42.5000]^T ${}^{4}\vec{c}_2^{\text{RUS}}$ = [–42.5000 0 42.5000]^T ${}^{4}\vec{c}_3^{\text{RUS}}$ = [21.2500 –36.8061 42.5000]^T

Inverse Kinematic Algorithm Validation

The first step of the inverse kinematics verification process was to prepare a computer-aided design (CAD) model assembly using SolidWorks. The model was then exported and converted for use in MATLAB's SimMechanics simulation environment. Next, the simulation model's end-effector was directly provided with three time-varying signals for the Euler angles that define its spatial orientation per Equation (3.21). Specifically, the following signals were used on the basis that they produce a wide variety of end-effector orientations for validity testing:

$$ \theta_X^{\text{RUS}} = 0.2\sin(5t)\,,\ \theta_Y^{\text{RUS}} = 0.25\sin\left(4t + \frac{\pi}{6}\right),\ \text{and}\ \theta_Z^{\text{RUS}} = 0.3\sin\left(0.3t + \frac{\pi}{3}\right) \tag{3.22} $$

Additionally, the inverse kinematic algorithm was coded alongside the SimMechanics simulation blocks (i.e., within the Simulink graphical programming environment) and provided with the same end-effector orientation inputs. Finally, virtual position sensors were connected to the SimMechanic model's active joints to record the angular state signals corresponding with the end-effector's simulated motions. For each active joint, Figure 3.6 shows an overlay of the joint signal results obtained from the two independent sources: the coded inverse kinematic algorithm and the simulation's virtual sensors. The agreement between the algorithm and simulation results suggests that the inverse kinematics solution developed in Subsection 3.2.2 is valid.

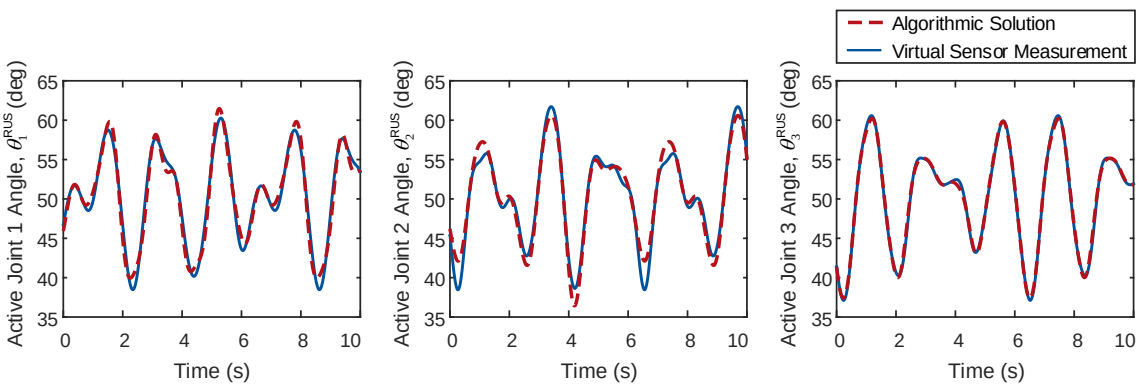

Figure 3.6. Active joint angle vs. time plots produced from an inverse kinematic algorithm and simulation to confirm analysis correctness

Forward Kinematic Algorithm Validation

In practice, the forward kinematic algorithm employs a numerical approximation method to find one or more possible solutions for Equations (3.14)–(3.16), which yield the c_i point positions. As a result, it is more computationally expensive than the inverse kinematic algorithm, so the forward kinematic algorithm considers a set of three single-configuration examples instead of continuous-time signals. The validation is fulfilled by comparing forward kinematic algorithm results with those obtained by arranging the simulation model's active joints in accordance with the considered configurations. A virtual sensor was again used to measure the model's end-effector orientation.

For the first manipulator configuration considered, active joint values are set to:

$$\theta_i^{\text{RUS}} = 30° \text{ for } i = 1, 2, 3 \tag{3.23}$$

Given the rotational symmetry of the RUS manipulator, the expectation is that these active joint values will produce an end-effector rotation exclusively about the $\hat{z}_0^{\text{RUS}}$ axis.

Upon substituting the design parameters and active joint angles into Equation (3.12) of Subsection 3.2.3, the ${}^{i}\vec{b}_i^{\text{RUS}}$ positions are computed as:

$$ {}^{i}\vec{b}_i^{\text{RUS}} = \begin{bmatrix} 96.0770 \\ 0 \\ 60 \end{bmatrix} \text{mm for } i = 1, 2, 3 \tag{3.24} $$

The coordinates above are equal for each branch universal joint because they are represented with respect to their corresponding branch-specific frame $\{i\}^{\text{RUS}}$. When expressed in the local reference frame $\{0\}^{\text{RUS}}$ per Equation (3.13), the positions become:

$$ {}^{0}\vec{b}_1^{\text{RUS}} = \begin{bmatrix} 96.0770 \\ 0 \\ 60 \end{bmatrix} \text{mm}, \ {}^{0}\vec{b}_2^{\text{RUS}} = \begin{bmatrix} -48.0385 \\ 83.2051 \\ 60 \end{bmatrix} \text{mm, and } {}^{0}\vec{b}_3^{\text{RUS}} = \begin{bmatrix} -48.0385 \\ -83.2051 \\ 60 \end{bmatrix} \text{mm} \tag{3.25} $$

As mentioned earlier, a numerical method is then used to determine all possible solutions for the c_i positions given the geometric constraints corresponding to Equations (3.14)–(3.16). Next, per the selection criteria outlined in Subsection 3.2.3, ${}^{0}\vec{c}_i^{\text{RUS}}$ solutions with negative *z*-coordinates are rejected. This yields a single solution set:

$$ {}^{0}\vec{c}_1^{\text{RUS}} = \begin{bmatrix} -12.2973 \\ 48.4642 \\ 42.5000 \end{bmatrix} \text{mm}, \ {}^{0}\vec{c}_2^{\text{RUS}} = \begin{bmatrix} -35.8226 \\ -34.8818 \\ 42.5000 \end{bmatrix} \text{mm, and } {}^{0}\vec{c}_3^{\text{RUS}} = \begin{bmatrix} 48.1199 \\ -13.5823 \\ 42.5000 \end{bmatrix} \text{mm} \tag{3.26} $$

The ${}^{0}\vec{c}_i^{\text{RUS}}$ solutions lead to a fully-defined ${}^{0}_{4}\mathbf{R}_{\mathbf{N}}^{\text{RUS}}$ matrix from Equations (3.17)–(3.19):

$$ {}^{0}_{4}\mathbf{R}_{\mathbf{N}}^{\text{RUS}} = \begin{bmatrix} 0.9264 & 0.2640 & -0.2685 \\ -0.2140 & 0.9558 & 0.2015 \\ 0.3098 & -0.1292 & 0.9420 \end{bmatrix} = \begin{bmatrix} p_{11} & p_{12} & p_{13} \\ p_{21} & p_{22} & p_{23} \\ p_{31} & p_{32} & p_{33} \end{bmatrix} \tag{3.27} $$

Finally, Euler angles can be derived from the ${}^{0}_{4}\mathbf{R}_{\mathbf{N}}^{\text{RUS}}$ matrix using Equation (3.20) to yield:

$$ \theta_X^{\text{RUS}} = 0°, \ \theta_Y^{\text{RUS}} = 0°, \text{ and } \theta_Z^{\text{RUS}} = 44.2377° \tag{3.28} $$

As expected, the equal active joint angles produced a pure rotation about the $\hat{z}_0^{\text{RUS}}$ axis in this example.

Repeating the approach undergone for the above example, two more manipulator configurations were analyzed to produce the results summarized in Table 3.2. Subsequently, the simulation code established for the inverse kinematics verification was used with slight modification to validate the forward kinematics results. That is, the simulation model's active joint angles were set to equal those used in each of the example configurations, and a virtual sensor was attached to the model's end-effector to

measure ${}^{0}_{4}\mathbf{R}_{\mathbf{N}}^{\text{RUS}}$. The corresponding Euler angles were then derived per Equation (3.20). Ultimately, the algorithmic and simulation results matched to at least the number of digits presented for each of the example manipulator configurations considered, which supports the validity of the forward kinematics solution derived in Subsection 3.2.3.

Table 3.2. Numeric example summary for the forward kinematics verification procedure of the RUS manipulator

Example No. 2: $\theta_1^{\text{RUS}} = 60°$, $\theta_2^{\text{RUS}} = 65°$, and $\theta_3^{\text{RUS}} = 58°$	
${}^{1}\vec{b}_1^{\text{RUS}} = [140 \quad 0 \quad 103.9230]^T$ mm	${}^{0}\vec{b}_1^{\text{RUS}} = [140 \quad 0 \quad 103.9230]^T$ mm
${}^{2}\vec{b}_2^{\text{RUS}} = [149.2858 \quad 0 \quad 108.7569]^T$ mm	${}^{0}\vec{b}_2^{\text{RUS}} = [-74.6429 \quad 129.2853 \quad 108.7569]^T$ mm
${}^{3}\vec{b}_3^{\text{RUS}} = [136.4097 \quad 0 \quad 101.7658]^T$ mm	${}^{0}\vec{b}_3^{\text{RUS}} = [-68.2048 \quad -118.1343 \quad 101.7658]^T$ mm
${}^{0}\vec{c}_1^{\text{RUS}} = [55.6038 \quad 26.3629 \quad 22.7918]^T$ mm	$\theta_X^{\text{RUS}} = -19.7198°$
${}^{0}\vec{c}_2^{\text{RUS}} = [-27.1140 \quad 39.5823 \quad 44.7697]^T$ mm	$\theta_Y^{\text{RUS}} = 5.6925°$
${}^{0}\vec{c}_3^{\text{RUS}} = [7.4693 \quad -39.4974 \quad 51.8692]^T$ mm	$\theta_Z^{\text{RUS}} = -38.1977°$
Example No. 3: $\theta_1^{\text{RUS}} = 50°$, $\theta_2^{\text{RUS}} = 55°$, and $\theta_3^{\text{RUS}} = 60°$	
${}^{1}\vec{b}_1^{\text{RUS}} = [122.8655 \quad 0 \quad 91.9253]^T$ mm	${}^{0}\vec{b}_1^{\text{RUS}} = [122.8655 \quad 0 \quad 91.9253]^T$ mm
${}^{2}\vec{b}_2^{\text{RUS}} = [131.1708 \quad 0 \quad 98.2982]^T$ mm	${}^{0}\vec{b}_2^{\text{RUS}} = [-65.5854 \quad 113.5973 \quad 98.2982]^T$ mm
${}^{3}\vec{b}_3^{\text{RUS}} = [140 \quad 0 \quad 103.9230]^T$ mm	${}^{0}\vec{b}_3^{\text{RUS}} = [-70 \quad -121.2436 \quad 103.9230]^T$ mm
${}^{0}\vec{c}_1^{\text{RUS}} = [27.3475 \quad 47.0899 \quad 36.6184]^T$ mm	$\theta_X^{\text{RUS}} = -7.8105°$
${}^{0}\vec{c}_2^{\text{RUS}} = [-53.1098 \quad 38.0944 \quad 5.8662]^T$ mm	$\theta_Y^{\text{RUS}} = -18.0479°$
${}^{0}\vec{c}_3^{\text{RUS}} = [-19.8830 \quad -22.1257 \quad 58.4925]^T$ mm	$\theta_Z^{\text{RUS}} = -13.0091°$

3.2.5. Jacobian Analysis

Background Information on the Jacobian Matrix

The Jacobian matrix, $\mathbf{J}$, transforms active joint velocities in the joint space to end-effector velocities in the end-effector space for both serial and parallel manipulators [142]. Joint space and end-effector space are vector spaces respectively comprised of the manipulator's joints variables (i.e., active joint positions) and all the possible task coordinates of the end-effector. To be exact, two component Jacobian matrices form this relation as:

$$\mathbf{J}_q \dot{\vec{q}} = \mathbf{J}_x \dot{\vec{x}} \tag{3.29}$$

where $\vec{q}$ represents the set of joint variables, $\vec{x}$ denotes the end-effector's task space coordinates, and $\mathbf{J}_q$ and $\mathbf{J}_x$ are the Jacobian component matrices. For parallel manipulators, the overall Jacobian is constructed such that:

$$\dot{\vec{q}} = \mathbf{J}\,\dot{\vec{x}}\text{, where } \mathbf{J} = \mathbf{J}_q^{-1}\mathbf{J}_x \tag{3.30}$$

As a result of this relationship, the Jacobian provides a means to linearly quantify the degree to which active joint errors (i.e., bounded differences $\Delta\,\vec{q}$) translate to inaccuracy in the end-effector (i.e., $\Delta\,\vec{x}$) [143]. This quantification is fulfilled by a set of kinetostatic performance indices: manipulability, dexterity, and sensitivity. Each of these indices has a distinct physical significance on the kinematic performance of a manipulator, so they are often used as a metric for comparing manipulator designs or architectures. The discussion of these indices and their meanings is included in Subsection 3.2.6.

Among other things, the Jacobian is also used to determine the singular conditions of a manipulator. Singular conditions exist at manipulator configurations that cause one or both Jacobian component matrices to have a determinant equal to zero. There are three types: an inverse kinematic singularity occurs when $\mathbf{J}_q$ is singular; a direct kinematic singularity occurs when $\mathbf{J}_x$ is singular; and a combined singularity occurs when both $\mathbf{J}_q$ and $\mathbf{J}_x$ are singular [142]. Arranging an orientation manipulators in an inverse or direct kinematic singularity configuration would respectively cause its end-effector to become immovable in certain directions (i.e., lose one or more DOFs) or move without any change in position of the system's active joints (i.e., gain one or more DOFs), respectively [142]. For combined singularities, both of those conditions can occur simultaneously for some infinitesimal motions. As these would undoubtedly affect the functionality of the proposed exoskeleton device, it is important to determine all active joint angle sets that produce singular conditions in the selected orientation manipulator. This is done in Section 3.6. In practice, the exoskeleton's workspace should exclude any configuration that corresponds to a singularity in its orientation manipulator subsystem (e.g., via mechanical stops and/or limits coded in the system's software, especially for actuated devices).

Jacobian Formulation for the RUS Manipulator

This subsection employs the conventional velocity vector-loop method, as described in [142], to generate the Jacobian matrix for the RUS manipulator. For a given point on a parallel manipulator's structure, the velocity vector is developed by a vector

loop that meets at that point from two different directions. Moreover, one loop must be made for each active joint in the system, and every loop closure must contain vectors passing through the fixed base link, end-effector link, and all links of a branch. Generally, the velocities of the passive joints in each branch can be removed by multiplying the velocity vector-loop equation with a vector perpendicular to all vectors of the passive joint rates. Once the undesired passive joint rates are eliminated, the resulting equations can be combined to yield the Jacobian matrix.

Recall from the start of Subsection 3.2.5 that $\vec{q}$ is a vector containing the active joint variables and $\vec{x}$ is a vector that defines the manipulator's end-effector position and orientation. Since the RUS manipulator possesses three active revolute joints and three rotational DOFs at its end-effector, the $\dot{\vec{q}}^{\text{RUS}}$ and $\dot{\vec{x}}^{\text{RUS}}$ vectors can be written as:

$$\dot{\vec{q}}^{\text{RUS}} = \begin{bmatrix} \dot{\theta}_1^{\text{RUS}} & \dot{\theta}_2^{\text{RUS}} & \dot{\theta}_3^{\text{RUS}} \end{bmatrix}^{\text{T}} \text{ and } \dot{\vec{x}}^{\text{RUS}} = \begin{bmatrix} \dot{\theta}_X^{\text{RUS}} & \dot{\theta}_Y^{\text{RUS}} & \dot{\theta}_Z^{\text{RUS}} \end{bmatrix}^{\text{T}} \tag{3.31}$$

As can be deduced from Figure 3.3, a loop-closure equation for the ith branch is:

$$\overline{\mathrm{a}_i\mathrm{b}_i} + \overline{\mathrm{b}_i\mathrm{c}_i} = \overline{\mathrm{a}_i O_i^{\text{RUS}}} + \overline{O_i^{\text{RUS}}\mathrm{c}_i} \tag{3.32}$$

where $\overline{\mathrm{a}_i\mathrm{b}_i}$ is a vector spanning the distal link from point a_i to b_i and $\overline{\mathrm{b}_i\mathrm{c}_i}$ is a vector from b_i to c_i on the proximal link. Likewise, $\overline{\mathrm{a}_i O_i^{\text{RUS}}}$ is a vector originating at a_i and leading to O_i^{RUS}, and $\overline{O_i^{\text{RUS}}\mathrm{c}_i}$ completes the loop by connecting O_i^{RUS} to c_i. These latter two vectors represent the fixed base link vector and end-effector link vector, respectively. Note that O_i^{RUS} represents the RUS's COR and origin of the branch-specific frames; it is coincident with O_0^{RUS}, the local reference frame origin. Performing the time-derivate of Equation (3.32) formulates a velocity vector-loop equation:

$$l_d \dot{\vec{q}}^{\text{RUS}} \times \hat{s}_{abi} + l_p \vec{\omega}_{pi} \times \hat{s}_{bci} = \left\| {}^0\vec{\mathrm{c}}_i^{\text{RUS}} \right\| \dot{\vec{x}}^{\text{RUS}} \times \hat{s}_{Oci} \tag{3.33}$$

where $\hat{s}_{abi}$, $\hat{s}_{bci}$, and $\hat{s}_{Oci}$ are unit vectors pointing along $\overline{\mathrm{a}_i\mathrm{b}_i}$, $\overline{\mathrm{b}_i\mathrm{c}_i}$, and $\overline{O_i^{\text{RUS}}\mathrm{c}_i}$, respectively; $\vec{\omega}_{pi}$ is the angular velocity of the proximal link on the ith branch. To remove this passive joint rate, the dot product of both sides of Equation (3.33) with $\hat{s}_{bci}$ is performed:

$$l_d \dot{\vec{q}}^{\text{RUS}} \left(\hat{s}_{abi} \times \hat{s}_{bci} \right) = \left\| {}^0\vec{\mathrm{c}}_i^{\text{RUS}} \right\| \dot{\vec{x}}^{\text{RUS}} \left(\hat{s}_{Oci} \times \hat{s}_{bci} \right) \tag{3.34}$$

When written once for each manipulator branch i = 1, 2, and 3, Equation (3.34) can be arranged to form the two component Jacobian matrices:

$$\mathbf{J}_q^{\text{RUS}} \dot{\vec{q}} = \mathbf{J}_x^{\text{RUS}} \dot{\vec{x}} \tag{3.35}$$

where the $\mathbf{J}_q^{\text{RUS}}$ and $\mathbf{J}_x^{\text{RUS}}$ matrices are given by [156]:

$$\mathbf{J}_x^{\text{RUS}} = \begin{bmatrix} l_d\left(\hat{s}_{ab1}\times\hat{s}_{bc1}\right)^{\mathrm{T}} \\ l_d\left(\hat{s}_{ab2}\times\hat{s}_{bc2}\right)^{\mathrm{T}} \\ l_d\left(\hat{s}_{ab3}\times\hat{s}_{bc3}\right)^{\mathrm{T}} \end{bmatrix} \text{ and}$$

$$\mathbf{J}_q^{\text{RUS}} = \begin{bmatrix} \left\|{}^0\bar{\mathrm{c}}_i^{\text{RUS}}\right\|\left(\hat{s}_{Oc1}\times\hat{s}_{bc1}\right) & 0 & 0 \\ 0 & \left\|{}^0\bar{\mathrm{c}}_i^{\text{RUS}}\right\|\left(\hat{s}_{Oc2}\times\hat{s}_{bc2}\right) & 0 \\ 0 & 0 & \left\|{}^0\bar{\mathrm{c}}_i^{\text{RUS}}\right\|\left(\hat{s}_{Oc3}\times\hat{s}_{bc3}\right) \end{bmatrix} \tag{3.36}$$

Therefore, the complete Jacobian matrix for the 3-RUS/S manipulator is:

$$\mathbf{J}^{\text{RUS}} = \left(\mathbf{J}_q^{\text{RUS}}\right)^{-1}\mathbf{J}_x^{\text{RUS}} =$$

$$\begin{bmatrix} \left\|{}^0\bar{\mathrm{c}}_i^{\text{RUS}}\right\|\left(\hat{s}_{Oc1}\times\hat{s}_{bc1}\right) & 0 & 0 \\ 0 & \left\|{}^0\bar{\mathrm{c}}_i^{\text{RUS}}\right\|\left(\hat{s}_{Oc2}\times\hat{s}_{bc2}\right) & 0 \\ 0 & 0 & \left\|{}^0\bar{\mathrm{c}}_i^{\text{RUS}}\right\|\left(\hat{s}_{Oc3}\times\hat{s}_{bc3}\right) \end{bmatrix}^{-1} \begin{bmatrix} l_d\left(\hat{s}_{ab1}\times\hat{s}_{bc1}\right)^{\mathrm{T}} \\ l_d\left(\hat{s}_{ab2}\times\hat{s}_{bc2}\right)^{\mathrm{T}} \\ l_d\left(\hat{s}_{ab3}\times\hat{s}_{bc3}\right)^{\mathrm{T}} \end{bmatrix} \tag{3.37}$$

3.2.6. Performance Indices

With its Jacobian matrix developed, the RUS manipulator's performance indices can now be formulated. These indices are a function of the end-effector's task space coordinates, of which there are three. However, upon calculating and analyzing the performance indices, only two of the end-effector's rotations will be considered as independent variables while the third remains in its neutral home-configuration value. This allows the index values to be visualized as a surface that varies in height with changes in the values of the two selected task coordinates. Moreover, only the pairings of θ_X^{RUS} with θ_Y^{RUS} and θ_X^{RUS} with θ_Z^{RUS} as independent variables will be considered, because the rotational symmetry of the RUS causes the third possible pairing to be a rotated version of the latter. If the RUS manipulator is selected for inclusion in the forthcoming exoskeleton design, the pairing that achieves the best performances will be matched with the human joint rotations that involve the greatest ranges-of-motion. Finally, the design parameters listed in Table 3.1 are used in the performance index formulations below, and a range of [–0.2 0.2] radians is considered for the task coordinate workspace of the manipulator during the studies. Note that within the context of frame rotations in this thesis, a prime symbol (') denotes a current-frame (i.e., intrinsic) rotation; a double-prime ('') signifies a secondary intrinsic rotation (i.e., about the updated frame following a first intrinsic rotation).

Manipulability

For parallel manipulators, articular forces and end-effector positioning errors tend to become very large near singular configurations [143]. Therefore, in terms of analyzing parallel-manipulator design, the ability to quantify proximity to a singular configuration is quite valuable. Manipulability is the performance indices used to make this quantification. It can also be interpreted as a measurement of a manipulator's capacity to transfer a particular velocity to its end-effector from its active joints [158]. For nonredundant manipulators, Yoshikawa defined the manipulability measure as the absolute value of the Jacobian's determinant [159]:

$$\mu = abs\left(\left|\mathbf{J}\right|\right) \tag{3.38}$$

where $abs(\ )$ denotes absolute value and $|\ |$ signifies matrix determinant.

Geometrically, manipulability represents the volume of the ellipsoid that results when a unit sphere is mapped from a manipulator's n-dimensional joint space into Cartesian space via the Jacobian matrix and a constant proportionality factor [160], where n is the number of active joints contained within the manipulator. Now, the level of performance achieved by a manipulator in uniformly transmitting velocity to its end-effector in all directions of motion is positively correlated to the isotropy of its manipulability ellipsoid [161]. The isotropy index for manipulability is defined as [162]:

$$\mu_{\text{iso}} = \frac{\sigma_{\min}}{\sigma_{\max}} \tag{3.39}$$

where $\sigma_{\max}$ and $\sigma_{\min}$ are, respectively, the maximum and minimum singular values of the Jacobian. This isotropy index for manipulability is the first performance indicator that will be used to compare candidate orientation manipulators in Section 3.5. Its value lies in the range of [0 1]. If a manipulator achieves the upper limit of 1 for a given configuration, it can transmit velocity uniformly from its active joints to its end-effector along all applicable directions. Contrarily, a value of 0 occurs at singular configuration, which prevents velocity transmission to the end-effector in one or more directions or permits end-effector motion without the active joints changing their positional states.

Figure 3.7 presents surface plots the isotropy index for manipulability of the RUS manipulator for the two end-effector task coordinate pairings selected above. The figure also shows the variability in the index across the considered manipulator workspace. As per the norm for parallel manipulators, the manipulability value is greatest near its home

configuration (i.e., when the end-effector angles both have a value of 0). The θ_X^{RUS} - θ_Y^{RUS} pairing displays a greater average manipulability than the θ_X^{RUS} - θ_Z^{RUS} pairing, but both schemes achieve approximately the same variability.

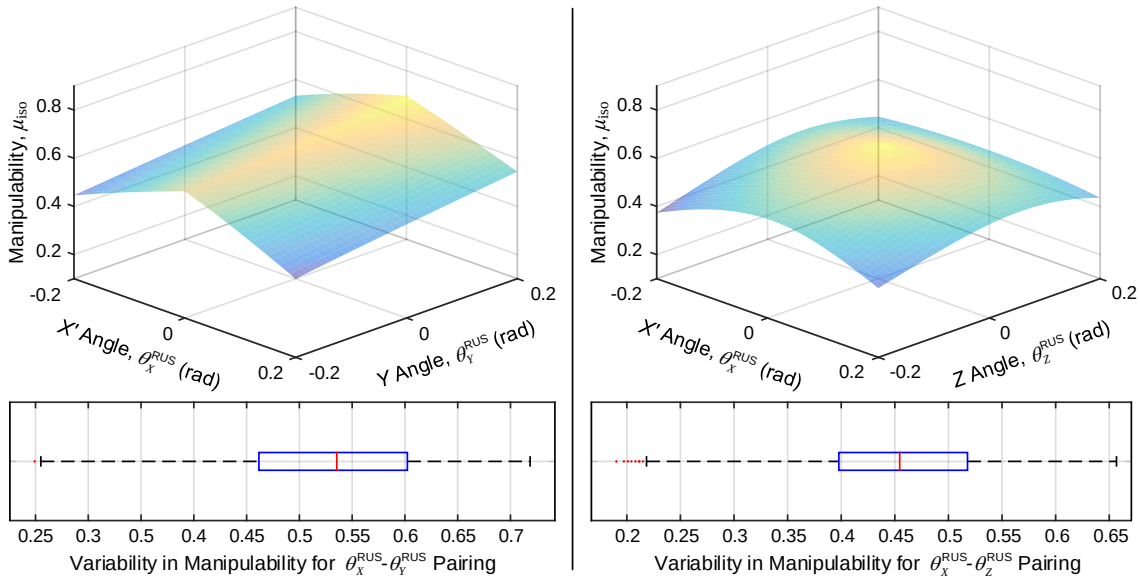

Figure 3.7. Surface plots and box plots of the RUS's manipulability for an end-effector range of [–0.2 0.2] radians and two rotation angle pairings

Dexterity (Condition Number)

For orientation parallel manipulators, such as the candidate devices discussed throughout this chapter, the articular position measurements of the active joints are used to determine the spatial orientation of the end-effector. Therefore, any errors in the articular measurements lead a discrepancy between the expected and actual end-effector orientation [143]. This discrepancy can be quantified as the product of the errors in active joint positions and an amplification factor, which Stoughton and Arai designate as the condition number, k [163]. The kinematic accuracy of a manipulator depends on its condition number, which is formulated from the Jacobian as [163]–[165]:

$$k = \|\mathbf{J}\|\|\mathbf{J}^{-1}\| \tag{3.40}$$

where $\|\mathbf{J}\|$ is the Jacobian's 2-norm:

$$\|\mathbf{J}\| = \sqrt{tr\left(\frac{1}{n}\mathbf{J}\mathbf{J}^{\mathrm{T}}\right)} \tag{3.41}$$

Recall that n represents the number of active joints in the manipulator and, thus, the dimension of the Jacobian matrix; $tr(\ )$ denotes the matrix trace function.

Now, the local dexterity index, ν, has been adopted as the measure of a manipulator's kinematic accuracy [166]. This performance criterion is given by the inverse of the condition number:

$$\nu = \frac{1}{k} = \frac{1}{\|\mathbf{J}\|\|\mathbf{J}^{-1}\|} \tag{3.42}$$

Like the isotropy index for manipulability, local dexterity is limited in value from 0 to 1. Again, 0 corresponds with a singularity condition in the Jacobian. Higher values indicate greater accuracy in end-effector motion generation for a given manipulator configuration, and a value of 1 for the local dexterity index denotes isotropy [162].

Figure 3.8 shows the local dexterity results for the two end-effector rotation combinations considered for the RUS manipulator. Similar to the isotropy index for manipulability, the performance is again greatest when the manipulator is posed in the vicinity of its home configuration and falls as it departs from that configuration. When θ_X^{RUS} and θ_Y^{RUS} are treated as the independent variables in the index's formulation, a greater average dexterity and lesser variability in dexterity is achieved across the considered manipulator workspace than when the θ_X^{RUS}-θ_Z^{RUS} pairing is used. This supports an exoskeleton design that matches the θ_X^{RUS} and θ_Y^{RUS} rotations of the RUS with the two largest range-of-motion DOFs of the targeted human joint.

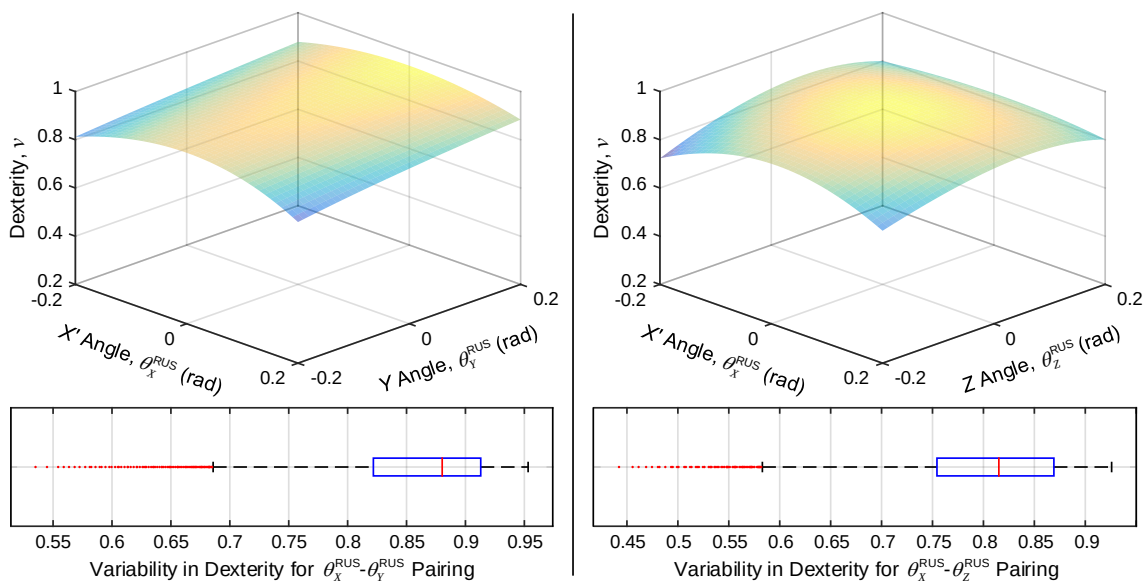

Figure 3.8. Surface plots and box plots of the RUS's dexterity for an end-effector range of [–0.2 0.2] radians and two rotation angle pairings

Rotational Sensitivity

The practical meaning associated the rotational sensitivity index is the degree to which active joint displacements affect a parallel manipulator's end-effector orientation. Specifically, Cardou et al. define it as the maximum-magnitude rotation of the end-effector induced by a unit-norm displacement in an active joint [160]. As such, the index is given by:

$$\tau_r = \|\mathbf{J}\| \tag{3.43}$$

where Cardou et al. recommend that either a 2-norm or ∞-norm is used to obtain the scalar sensitivity value [160]. The former is chosen for the performance analysis of each candidate manipulator in this chapter to provide consistent basis for comparison. Note that the rotational sensitivity index has a lower limit of 0, but unlike the previous indices, its value has an unbounded upper limit. Also in contrast to manipulability and dexterity, performance quality is generally negatively correlated with increased value of the sensitivity index; highly sensitive manipulator configurations may pose control instabilities, while end-effector positioning resolution improves with decreasing sensitivity value.

Figure 3.9 presents the rotational sensitivity surface plots and variabilities for the two different task coordinate pairings and their evaluation workspace of [–0.2 0.2] radians. As can be observed from the surface plots, the RUS manipulator's sensitivity tends to increase as its posture departs from the home configuration. Additionally, the average sensitivity and overall variability associated with the θ_X^{RUS} - θ_Y^{RUS} task coordinate pairing are lesser than those of the alternative pairing. Therefore, the former scheme is more robust regarding sensitivity. Because they are superior for all three of the considered indices, the performance values for the θ_X^{RUS} - θ_Y^{RUS} end-effector rotation pairing will be used during the candidate orientation manipulator comparison in Section 3.5.

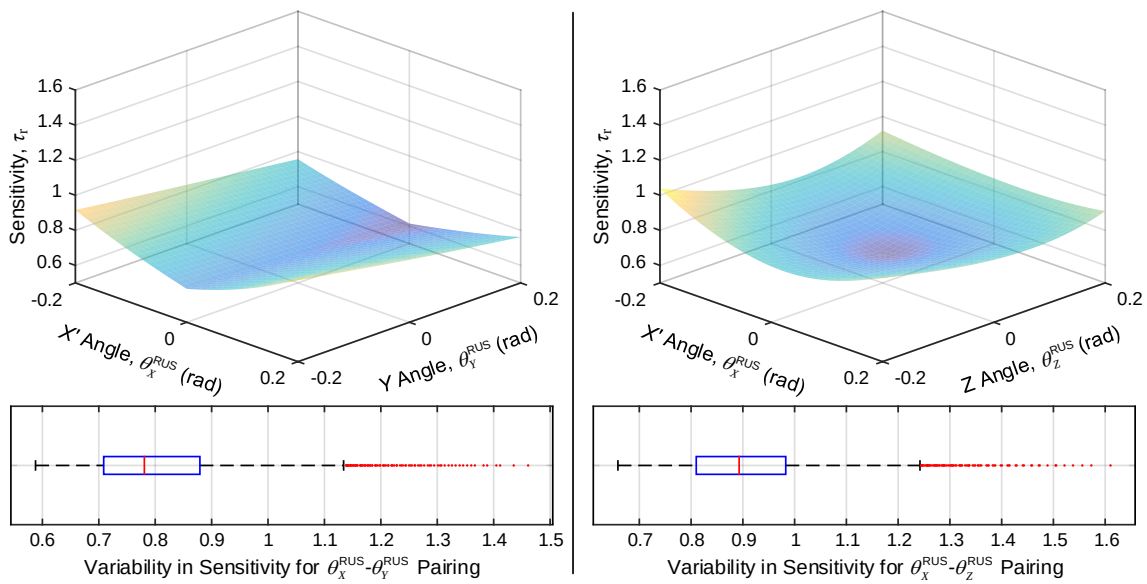

Figure 3.9. Surface plots and box plots of the RUS's sensitivity for an end-effector range of [–0.2 0.2] radians and two rotation angle pairings

Global Manipulability Index for Optimizing the 3-RUS/S Design

The manipulability, dexterity, and rotational sensitivity performance indices discussed above are considered local metrics because they only pertain to the selected design parameters used during their formulations (see Table 3.1). However, Gosselin has proposed the concept of a global performance index (GPI) as a means to evaluate performances associated with a varying selection of design parameters for a given manipulator workspace [167]:

$$GPI = \frac{\int (PI)\, dW}{\int dW} \tag{3.44}$$

where 'PI' indicates the performance index under global analysis and 'W' denotes the considered workspace. As such, the GPI yields the average value for a chosen performance index across all chosen workspace orientations. Iteratively computing the GPI for a set of different design parameters facilitates the performance comparison of various designs for the manipulator. Hence, the GPI concept lends itself to design optimization.

The variables selected for the design optimization of the RUS manipulator are the ratio of a branch's spherical joint connection radius to active joint connection radius (i.e., relative to the local reference frame origin: $\left\| {}^{0}\vec{c}_i^{RUS} \right\| / \left\| {}^{0}\vec{a}_i^{RUS} \right\|$) and the end-effector-frame height of the spherical joints (i.e., the shared *z*-coordinate of the ${}^{4}\vec{c}_i^{RUS}$ positions).

The latter will be represented by h here. Figure 3.10 presents the GPI results for manipulability when different combinations of these design variables are selected. The optimization solution takes the form of a linear function between the two design variables:

$$\begin{bmatrix}0 & 0 & 1\end{bmatrix} \cdot {}^{4}\vec{c}_i^{\,\mathrm{RUS}} = h = 334.6 \frac{\left\| {}^{0}\vec{c}_i^{\,\mathrm{RUS}} \right\|}{\left\| {}^{0}\vec{a}_i^{\,\mathrm{RUS}} \right\|} - 0.5 \tag{3.45}$$

which corresponds to the peak line across the GPI surface plot. Note that the optimized design is very similar if obtained through use of dexterity or sensitivity as the GPI. Also note that the units for h should be millimeters to maintain consistency with the constant values in Equation (3.45).

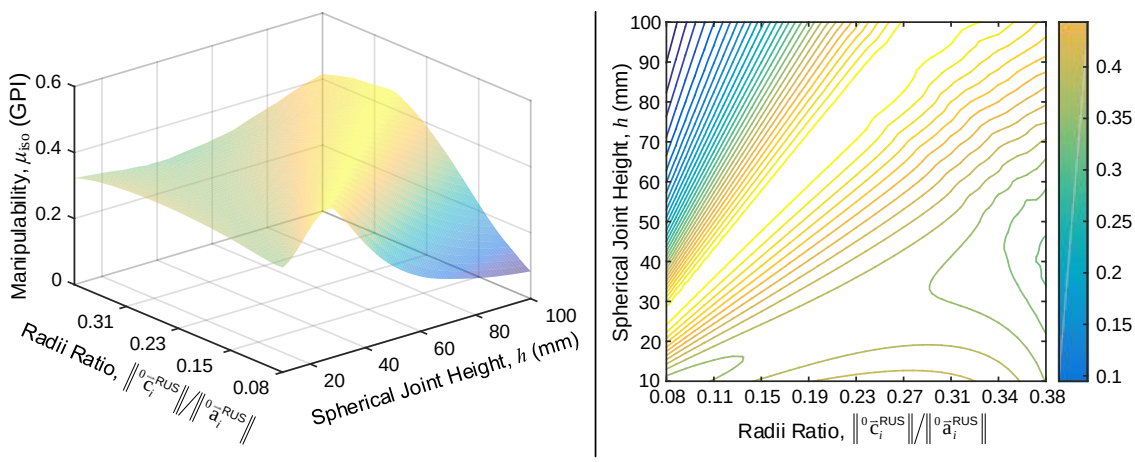

Figure 3.10. Surface and contour plots of the RUS's global manipulability in terms of the $\left\| {}^{0}\vec{c}_i^{\,\mathrm{RUS}} \right\| / \left\| {}^{0}\vec{a}_i^{\,\mathrm{RUS}} \right\|$ and h design variables and considering an end-effector range of [–0.2 0.2] radians for θ_X^{RUS} and θ_Y^{RUS}

3.3. Candidate #2: 3-RRR (Agile Eye) Parallel Manipulator

For the second candidate orientation manipulator, the well-established Agile Eye (AE) manipulator discussed in Section 3.1 is taken into consideration. First developed by Gosselin and Hamel [145], this parallel manipulator's architecture can be expressed as 3-RRR because it comprises three branches that each have three revolute joints, the first of which being active. Figure 3.11 shows several schematic illustrations of the manipulator. The reader is referred to Appendix B or [168] for a review of the AE's kinematic and Jacobian analyses along with details on its manipulability, dexterity, and rotational sensitivity performances for the same manipulator workspace as considered for the RUS. The journal article, which the author co-wrote, also reports experimental

findings from a preliminary evaluation of the AE for potential use in a hip exoskeleton system (i.e., based on its ability to track motions associated with human walking gait). Note that there are eight solutions associated with both the AE's inverse and forward kinematics; interestingly, however, four of the forward kinematic assembly modes will always correspond to singular configurations in the manipulator [169].

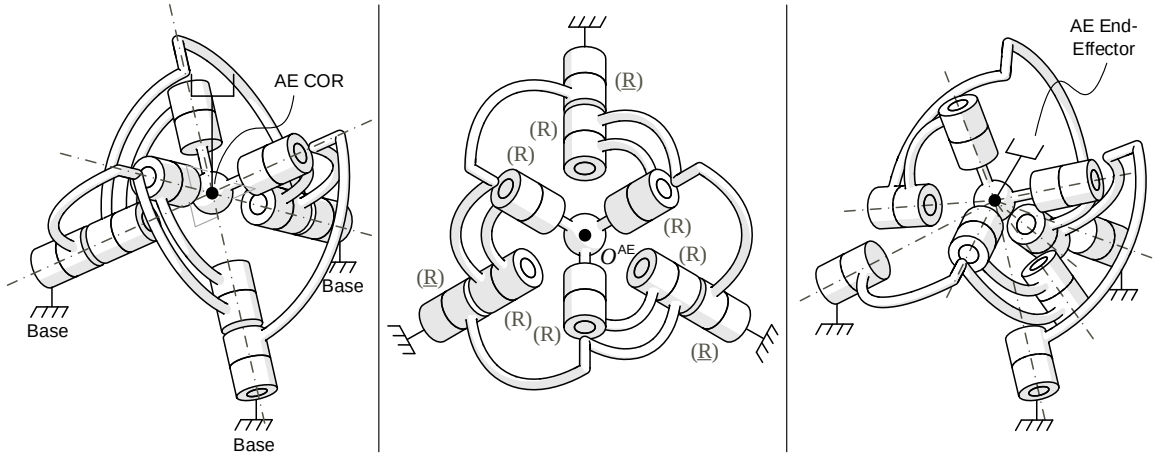

Figure 3.11. Schematic illustrations of the AE in its home configuration from side and top views (left and middle) as well as an arbitrary posture (right)

Note: All frames in the local scope of the Agile Eye have their origin coincident with the COR point. Also, the right-side image demonstrates the spherical motion achieved by the device, as all joint axes intersect the COR for any manipulator orientation.

3.4. Candidate #3: (RR-RRR)R (Simplified Agile Eye) Hybrid Manipulator

The third candidate orientation manipulator is based on the Simplified Agile Eye (SAE) developed by Gosselin and Caron [170]. As its name implies, the SAE is a simplified version of the original Agile Eye mentioned in Section 3.3 above.

3.4.1. Kinematic Architecture

The SAE's architecture can be represented as RR-RRR, because one branch connects its base to its end-effector via an active revolute joint serially connected to a passive revolute joint, and the other branch is comprised of an active revolute joint followed by two passive revolute joints. Each joint is aligned perpendicularly to its adjacent joint(s) from the same branch. Like the original Agile Eye, all the SAE's joint axes intersect at a common point, the end-effector's COR, for all configurations in the parallel manipulator's workspace. It is also a spherical manipulator. Whereas the SAE

alone has two DOFs, if another active revolute joint is attached to the SAE's end-effector such that the new joint's axis intersects the other joint axes at the same common point, the resulting hybrid manipulator can achieve 3-DOF spherical motions about the COR at its new end-effector (i.e., the final active joint's output link). The hybrid manipulator's architecture can thus be denoted as (RR-RRR)R, where the brackets indicate that the final joint is connected to the isolated SAE's end-effector. Such a hybrid version was previously used as part of a 6-DOF haptic device for a Virtual Reality system in [171].

Figure 3.12 shows three schematic models of the SAE that help establish the joint, link, and frame notations used in the kinematic analyses to follow. On the left side of the figure, the hybridized SAE is shown in its home configuration, for which all active joint variables are assigned a zero value. The left-side image also includes labels for the manipulator's links, joints, and COR point. This COR is selected as the origin for all link frames, including the local reference frame. The middle image of Figure 3.12 illustrates the isolated SAE parallel manipulator (i.e., RR-RRR without the third active joint) and the first three link frames used in its kinematic analyses: $\{0\}^{SAE}$, $\{1\}^{SAE}$, and $\{2\}^{SAE}$. Note that frame $\{0\}^{SAE}$ is the local reference frame fixed to the manipulator's base link. The middle image also shows three unit-length direction vectors, $\hat{u}$, $\hat{v}$, and $\hat{w}$, that identify the positions of the SAE's passive joints in their positive directions. Finally, the right-side image of Figure 3.12 shows a schematic of the hybridized SAE, including the frame attached to the link that the final active joint adds to the manipulator (i.e., the hybrid SAE's end-effector).

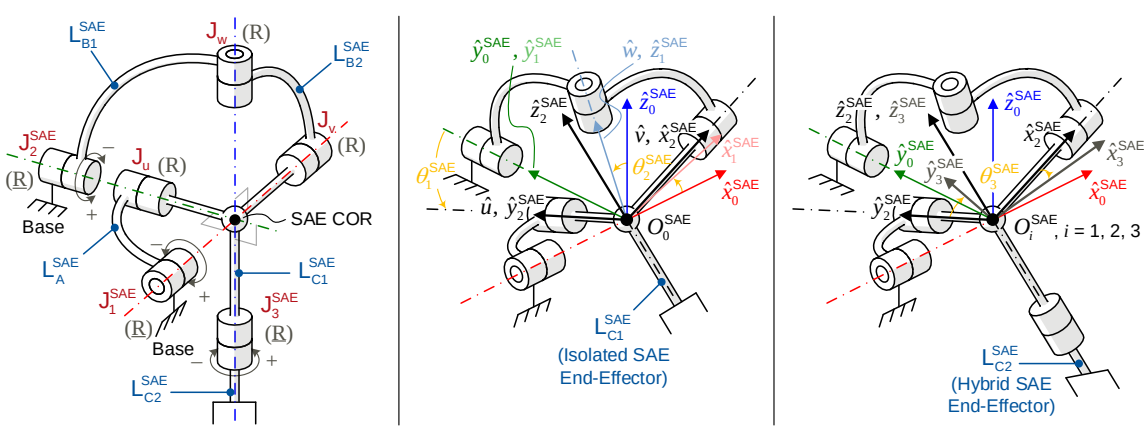

Figure 3.12. Schematic of the SAE with joint and link labels (left), isolated SAE (middle) and hybrid SAE (right) with frame and joint variable labels

Note: Given the directional assumptions for the active joints shown in the left image, the signs of the values associated with θ_1^{SAE}, θ_2^{SAE}, and θ_3^{SAE} in the middle and right images would be negative, positive, and negative, respectively.

The local reference frame $\{0\}^{\text{SAE}}$ is oriented such that its $\hat{x}_0^{\text{SAE}}$ axis is collinear with active joint J_1^{SAE} and its $\hat{y}_0^{\text{SAE}}$ axis is collinear with active joint J_2^{SAE}; this is possible because of the orthogonal arrangement of J_1^{SAE} and J_2^{SAE}. Applying the rotational right-hand rule to Figure 3.12, note that J_1^{SAE} shares direction with $\hat{x}_0^{\text{SAE}}$, whereas the direction of J_2^{SAE} opposes that of $\hat{y}_0^{\text{SAE}}$. Next, frame $\{1\}^{\text{SAE}}$ is defined such that the following equalities are true for all manipulator configurations:

$$\hat{y}_1^{\text{SAE}} = \hat{y}_0^{\text{SAE}} \text{ and } \hat{z}_1^{\text{SAE}} = \hat{w} \tag{3.46}$$

Now, by the design of links $\text{L}_{\text{A}}^{\text{SAE}}$, $\text{L}_{\text{B1}}^{\text{SAE}}$, $\text{L}_{\text{B2}}^{\text{SAE}}$, and $\text{L}_{\text{C1}}^{\text{SAE}}$, $\hat{u}$ and $\hat{v}$ are orthogonal, and $\hat{v}$ and $\hat{w}$ are orthogonal. It follows that frame $\{2\}^{\text{SAE}}$ (i.e., the isolated SAE end-effector frame) is defined such that:

$$\hat{y}_2^{\text{SAE}} = \hat{u} \text{ and } \hat{x}_2^{\text{SAE}} = \hat{v} \tag{3.47}$$

Lastly, frame $\{3\}^{\text{SAE}}$ has its $\hat{z}_3^{\text{SAE}}$ axis equal to $\hat{z}_2^{\text{SAE}}$ for all manipulator configurations, and its $\hat{x}_3^{\text{SAE}}$ and $\hat{y}_3^{\text{SAE}}$ axes are defined to assert that:

$${}^0_1\mathbf{R}^{\text{SAE}} = {}^0_2\mathbf{R}^{\text{SAE}} = {}^0_3\mathbf{R}^{\text{SAE}} = \mathbf{I}_{3\times3} \tag{3.48}$$

when the hybrid SAE is arranged in its home configuration.

3.4.2. Inverse Kinematic Analysis

The 2-DOF SAE's creators indicate that its inverse kinematics is trivial [172], and its kinematic analyses have been previously published in [173] and [174], where the latter treats the manipulator more generally as a spherical four-bar linkage. Additionally, the original 3-DOF Agile Eye's kinematics have been documented extensively in [138], [147]–[150], [169], [175]. For completeness, the inverse kinematics solution for the SAE is reformulated below with an approach similar to that found in [149] for the original Agile Eye. This section considers the inverse kinematics problem for both the isolated SAE as well as the hybrid (<u>R</u>R-<u>R</u>RR)<u>R</u> manipulator, beginning with the former.

Isolated 2-DOF SAE

Per the definition of the inverse kinematics problem for a generalized manipulator, the position and orientation of the isolated SAE's end-effector frame $\{2\}^{\text{SAE}}$ is numerically given at the start of this analysis:

$$ {}^{0}_{2}\mathbf{T}_{\mathbf{N}}^{\text{SAE}} = \begin{bmatrix} q_{11} & q_{12} & q_{13} & 0 \\ q_{21} & q_{22} & q_{23} & 0 \\ q_{31} & q_{32} & q_{33} & 0 \\ 0 & 0 & 0 & 1 \end{bmatrix} = \begin{bmatrix} {}^{0}_{2}\mathbf{R}_{\mathbf{N}}^{\text{SAE}} & \vec{0}_{3\times1} \\ \vec{0}_{1\times3} & 1 \end{bmatrix} \tag{3.49} $$

where each term q_{ij} for i, j = 1, 2, 3 is known. Since the manipulator's COR is selected as the origin for all link frames, including the local reference frame, each homogeneous transform has a zeroed position vector (i.e., $\vec{0}_{3\times1}$) in the top three rows of the matrix's fourth column. Consequently, the remainder of the kinematic analyses will only consider rotation matrices.

As shown in Figure 3.12 and discussed above, the $\hat{y}_2^{\text{SAE}}$ axis of ${}^{0}_{2}\mathbf{R}_{\mathbf{N}}^{\text{SAE}}$ identifies the position of joint J_u, which is connected to active joint J_1^{SAE} via link L_A^{SAE}. In fact, the *y*-component of ${}^{0}\hat{y}_2^{\text{SAE}}$ represents $\cos\left(\theta_1^{\text{SAE}}\right)$ while the *z*-component of ${}^{0}\hat{y}_2^{\text{SAE}}$ represents $\sin\left(\theta_1^{\text{SAE}}\right)$. This is more obvious if the symbolic ${}^{0}_{2}\mathbf{R}_{\mathbf{S}}^{\text{SAE}}$ rotation matrix is composed using ordered *X* then *Y'* Euler angles; the *X* rotation angle is θ_1^{SAE} for this order, given the direct connection from J_1^{SAE} to the end-effector through L_A^{SAE}:

$$ {}^{0}_{2}\mathbf{R}_{\mathbf{N}}^{\text{SAE}} = \begin{bmatrix} q_{11} & q_{12} & q_{13} \\ q_{21} & q_{22} & q_{23} \\ q_{31} & q_{32} & q_{33} \end{bmatrix} = {}^{0}_{2}\mathbf{R}_{\mathbf{S}}^{\text{SAE}} = \mathbf{R}_{XY'}\left(\theta_1^{\text{SAE}}, \beta\right) = \begin{bmatrix} c\beta & 0 & s\beta \\ s\theta_1^{\text{SAE}} s\beta & c\theta_1^{\text{SAE}} & -s\theta_1^{\text{SAE}} c\beta \\ -c\theta_1^{\text{SAE}} s\beta & s\theta_1^{\text{SAE}} & c\theta_1^{\text{SAE}} c\beta \end{bmatrix} \tag{3.50} $$

where β is the unknown *Y'* rotation angle. The active joint angle θ_1^{SAE} is thus given by:

$$ \theta_1^{\text{SAE}} = \operatorname{atan2}\left(q_{32}, q_{22}\right) \tag{3.51} $$

Next, recalling that frame $\{1\}^{\text{SAE}}$ is defined such that the *z*-axis of ${}^{0}_{1}\mathbf{R}^{\text{SAE}}$ identifies J_w and noting the connection of J_w to J_2^{SAE} via link L_{B1}^{SAE}, ${}^{0}_{1}\mathbf{R}^{\text{SAE}}$ can be symbolically defined in terms of θ_2^{SAE} as follows:

$$ {}^{0}_{1}\mathbf{R}_{\mathbf{S}}^{\text{SAE}} = \mathbf{R}_Y\left(-\theta_2^{\text{SAE}}\right) = \begin{bmatrix} c\theta_2^{\text{SAE}} & 0 & -s\theta_2^{\text{SAE}} \\ 0 & 1 & 0 \\ s\theta_2^{\text{SAE}} & 0 & c\theta_2^{\text{SAE}} \end{bmatrix} \text{ where } \hat{w} = \hat{z}_1^{\text{SAE}} = \begin{bmatrix} -s\theta_2^{\text{SAE}} \\ 0 \\ c\theta_2^{\text{SAE}} \end{bmatrix} \tag{3.52} $$

By the design of link L_{B2}^{SAE}, $\hat{v}$ and $\hat{w}$ are orthogonal, and $\hat{v}$ is given by ${}^{0}\hat{x}_2^{\text{SAE}}$. Therefore, the dot product between the two vectors yields an equation in terms of θ_2^{SAE}:

$$ \hat{w} \cdot \hat{v} = \begin{bmatrix} -s\theta_2^{\text{SAE}} \\ 0 \\ c\theta_2^{\text{SAE}} \end{bmatrix} \cdot \begin{bmatrix} q_{11} \\ q_{21} \\ q_{31} \end{bmatrix} = -q_{11}\sin\left(\theta_2^{\text{SAE}}\right) + q_{31}\cos\left(\theta_2^{\text{SAE}}\right) = 0 \tag{3.53} $$

Consequently, there are two solutions for θ_2^{SAE}:

$$ \theta_2^{\text{SAE}} = \operatorname{atan2}\left(\pm q_{31}, \pm q_{11}\right) \tag{3.54} $$

Physically, the two solutions correspond to the $\mathrm{L}_{\mathrm{B1}}^{\mathrm{SAE}}$ - $\mathrm{L}_{\mathrm{B2}}^{\mathrm{SAE}}$ link branch being below or above the isolated SAE end-effector's top surface, respectively. For the design under evaluation, this branch is positioned above the end-effector's top surface for zeroed values of θ_1^{SAE} and θ_2^{SAE}, so the solution involving $+q_{31}$ and $+q_{11}$ from Equation (3.54) is selected as the appropriate one (i.e., θ_2^{SAE} should equal zero if ${}^{0}_{2}\mathbf{R}_{\mathbf{N}}^{\mathrm{SAE}}$ is $\mathbf{I}_{3\times3}$). Note that if the arrangement of branches connecting the base to link $\mathrm{L}_{\mathrm{C1}}^{\mathrm{SAE}}$ were swapped (i.e., if the base-$\mathrm{L}_{\mathrm{B1}}^{\mathrm{SAE}}$ connection position was mirrored in the $\hat{x}_0^{\mathrm{SAE}}$ - $\hat{z}_0^{\mathrm{SAE}}$ plane, all else unchanged), then the $\mathrm{J}_2^{\mathrm{SAE}}$ joint direction would be the same as that of $\hat{y}_0^{\mathrm{SAE}}$; as a result, the solutions for θ_2^{SAE} would become:

$$\theta_2^{\mathrm{SAE}} = \mathrm{atan2}\left(\pm q_{31}, \mp q_{11}\right) \tag{3.55}$$

and the solution involving $+q_{11}$ would be appropriate for that alternative assembly scheme. This completes the inverse kinematic analysis for the isolated SAE, where Equations (3.51) and (3.54) provide the final solutions for the active joint angles.

Hybrid 3-DOF SAE

If a third active revolute joint is mounted on the 2-DOF SAE end-effector such that its axis of action coincides with $\hat{z}_2^{\mathrm{SAE}}$, then the inverse kinematics procedure must be adjusted. First, the problem assumes that the orientation of the hybrid SAE's end-effector frame $\{3\}^{\mathrm{SAE}}$ is given numerically:

$${}^{0}_{3}\mathbf{R}_{\mathbf{N}}^{\mathrm{SAE}} = \begin{bmatrix} r_{11} & r_{12} & r_{13} \\ r_{21} & r_{22} & r_{23} \\ r_{31} & r_{32} & r_{33} \end{bmatrix} \tag{3.56}$$

where each of the nine matrix elements has a known value. In this new case, the hybrid manipulator's end-effector orientation includes an additional rotation about the $\hat{z}_2^{\mathrm{SAE}}$ axis. Therefore, the numerical end-effector orientation can be equated to a symbolic rotation matrix constructed from the intrinsically-ordered *X-Y'-Z"* Euler angle set:

$${}^{0}_{3}\mathbf{R}_{\mathbf{N}}^{\mathrm{SAE}} = {}^{0}_{3}\mathbf{R}_{\mathbf{S}}^{\mathrm{SAE}} = \mathbf{R}_{XY'Z''}\left(\alpha,\beta,\gamma\right) = \begin{bmatrix} c\beta c\gamma & -c\beta s\gamma & s\beta \\ s\alpha s\beta c\gamma + c\alpha s\gamma & -s\alpha s\beta s\gamma + c\alpha c\gamma & -s\alpha c\beta \\ -c\alpha s\beta c\gamma + s\alpha s\gamma & c\alpha s\beta s\gamma + s\alpha c\gamma & c\alpha c\beta \end{bmatrix} \tag{3.57}$$

which in turn has the two inverse kinematic solution sets:

$$\beta = \mathrm{atan2}\left(r_{13}, \pm\sqrt{{r_{11}}^2 + {r_{12}}^2}\right),\ \alpha = \mathrm{atan2}\left(-\frac{r_{23}}{c\beta}, \frac{r_{33}}{c\beta}\right), \text{ and } \gamma = \mathrm{atan2}\left(-\frac{r_{12}}{c\beta}, \frac{r_{11}}{c\beta}\right) \tag{3.58}$$

A direct connection exists from $\mathrm{J}_1^{\mathrm{SAE}}$, acting along the $\hat{x}_0^{\mathrm{SAE}}$ axis, to link $\mathrm{L}_{\mathrm{C1}}^{\mathrm{SAE}}$ via $\mathrm{L}_{\mathrm{A}}^{\mathrm{SAE}}$. Similarly, there is a direct connection from $\mathrm{J}_3^{\mathrm{SAE}}$, acting along the coaxial $\hat{z}_2^{\mathrm{SAE}}$ and $\hat{z}_3^{\mathrm{SAE}}$ axes, to the hybrid manipulator's end-effector. Because these two conditions are true, the following equations are valid:

$$\theta_1^{\mathrm{SAE}} = \alpha \text{ and } \theta_3^{\mathrm{SAE}} = \gamma \tag{3.59}$$

The positive-root solution for β from (3.58) is selected as the appropriate one for the present design, because it yields zeroed values for θ_1^{SAE} and θ_3^{SAE} when ${}^0_3\mathbf{R}_{\mathbf{N}}^{\mathrm{SAE}}$ is the $\mathbf{I}_{3\times3}$ identity matrix. Finally, ${}^0_2\mathbf{R}_{\mathbf{N}}^{\mathrm{SAE}}$ can be reconstructed by substituting the selected solutions for β and θ_1^{SAE} from Equations (3.58) and (3.59) into Equation (3.50), and then θ_2^{SAE} can be solved using the appropriate selection from Equation (3.54), given the intended manipulator assembly. This yields solutions for each active joint angle, thus completing the inverse kinematic analysis for the hybrid SAE.

3.4.3. Forward Kinematic Analysis

An advantage of the SAE over the original Agile Eye architecture is that the former has a simpler forward kinematic analysis, which permits only four assembly modes in contrast to the AE's eight possible assembly modes [172]. Like Subsection 3.4.2, this subsection addresses the forward kinematics problem for the SAE in two parts: the 2-DOF SAE in isolation, and then the hybrid SAE.

Isolated 2-DOF SAE

The values of active joint angles θ_1^{SAE} and θ_2^{SAE} are known for the forward kinematics problem, and the desired output is the orientation of frame $\{2\}^{\mathrm{SAE}}$ (i.e., numerically as ${}^0_2\mathbf{R}_{\mathbf{N}}^{\mathrm{SAE}}$). To start this analysis, the symbolic ${}^0_2\mathbf{R}_{\mathbf{S}}^{\mathrm{SAE}}$ matrix can be constructed the same way as in Equation (3.50) during the inverse kinematics development:

$${}^0_2\mathbf{R}_{\mathbf{S}}^{\mathrm{SAE}} = \mathbf{R}_X\left(\theta_1^{\mathrm{SAE}}\right)\mathbf{R}_{Y'}\left(\beta\right) = \begin{bmatrix} c\beta & 0 & s\beta \\ s\theta_1^{\mathrm{SAE}}s\beta & c\theta_1^{\mathrm{SAE}} & -s\theta_1^{\mathrm{SAE}}c\beta \\ -c\theta_1^{\mathrm{SAE}}s\beta & s\theta_1^{\mathrm{SAE}} & c\theta_1^{\mathrm{SAE}}c\beta \end{bmatrix} \tag{3.60}$$

Thus, the forward kinematics solution requires solving for the unknown angle denoted by β.

From their definitions, $\hat{v}$ and $\hat{w}$ can be expressed as:

$$\hat{v} = \begin{bmatrix} c\beta \\ s\theta_1^{\text{SAE}} s\beta \\ -c\theta_1^{\text{SAE}} s\beta \end{bmatrix} \text{ and } \hat{w} = \begin{bmatrix} -s\theta_2^{\text{SAE}} \\ 0 \\ c\theta_2^{\text{SAE}} \end{bmatrix} \tag{3.61}$$

Next, the orthogonality of $\hat{v}$ and $\hat{w}$ yields:

$$\hat{w} \cdot \hat{v} = -c\beta s\theta_2^{\text{SAE}} - c\theta_1^{\text{SAE}} c\theta_2^{\text{SAE}} s\beta = 0 \tag{3.62}$$

Since θ_1^{SAE} and θ_2^{SAE} are known, β has two solutions:

$$\beta = \operatorname{atan2}\left(\mp s\theta_2^{\text{SAE}}, \pm c\theta_1^{\text{SAE}} c\theta_2^{\text{SAE}}\right) \tag{3.63}$$

which physically represent the SAE's link $\text{L}_{\text{C1}}^{\text{SAE}}$ being upright or upside-down. For the present design, zeroed θ_1^{SAE} and θ_2^{SAE} values should produce $\mathbf{I}_{3\times3}$ upon substitution into Equation (3.63) followed by (3.60), so the solution with negative sine and positive cosine terms in Equation (3.63) is selected. Note that if the SAE is constructed with swapped connections from the base to link $\text{L}_{\text{A}}^{\text{SAE}}$ and base to link chain $\text{L}_{\text{B1}}^{\text{SAE}}$-$\text{L}_{\text{B2}}^{\text{SAE}}$, the only forward kinematics adjustment is that β is computed as:

$$\beta = \operatorname{atan2}\left(\pm s\theta_2^{\text{SAE}}, \pm c\theta_1^{\text{SAE}} c\theta_2^{\text{SAE}}\right) \tag{3.64}$$

where the positive-term solution is appropriate for an upright assembly mode.

Hybrid 3-DOF SAE

When the active revolute joint J_3^{SAE} is attached to link $\text{L}_{\text{C1}}^{\text{SAE}}$ to complete the hybrid orientation manipulator, as illustrated in Figure 3.12, the forward kinematics problem requires a solution for ${}^0_3\mathbf{R}_{\mathbf{N}}^{\text{SAE}}$. Because it acts along the $\hat{z}_2^{\text{SAE}}$ axis, this additional joint simply adds an intrinsic *z*-axis rotation to the matrix developed in Equation (3.60), yielding:

$$\begin{aligned} {}^0_3\mathbf{R}^{\text{SAE}} &= \mathbf{R}_{XY'Z''}\left(\theta_1^{\text{SAE}}, \beta, \theta_3^{\text{SAE}}\right) = \\ &\begin{bmatrix} c\beta c\theta_3^{\text{SAE}} & -c\beta s\theta_3^{\text{SAE}} & s\beta \\ s\theta_1^{\text{SAE}} s\beta c\theta_3^{\text{SAE}} + c\theta_1^{\text{SAE}} s\theta_3^{\text{SAE}} & -s\theta_1^{\text{SAE}} s\beta s\theta_3^{\text{SAE}} + c\theta_1^{\text{SAE}} c\theta_3^{\text{SAE}} & -s\theta_1^{\text{SAE}} c\beta \\ -c\theta_1^{\text{SAE}} s\beta c\theta_3^{\text{SAE}} + s\theta_1^{\text{SAE}} s\theta_3^{\text{SAE}} & c\theta_1^{\text{SAE}} s\beta s\theta_3^{\text{SAE}} + s\theta_1^{\text{SAE}} c\theta_3^{\text{SAE}} & c\theta_1^{\text{SAE}} c\beta \end{bmatrix} \end{aligned} \tag{3.65}$$

where β is known from Equation (3.63) and θ_1^{SAE} and θ_3^{SAE} are known for the forward kinematics problem. Thus, Equations (3.63) and (3.65) represent the forward kinematics solution for the hybridized 3-DOF SAE.

The SAE's inverse and forward kinematic analyses are new contributions insofar as the author has researched. A series of soundness checks were performed on a simulation model to verify that the kinematic algorithms produced reasonable results.

This was done for end-effector motions that can be visually confirmed (e.g., pure rotations about each of the local reference frame axes). However, given the simplicity of these analyses along with the highly analogous approach of their development to the proven AE kinematic analyses, development of a plot demonstrating kinematic analysis verification for the SAE is foregone for the sake of brevity.

3.4.4. Jacobian Analysis

Recall from the beginning of Chapter 3 that $\vec{q}$ and $\vec{x}$ respectively denote the active joint variables and angle set defining the orientation of an orientation manipulator's end-effector. Thus, in the context of the SAE, these vectors are:

$$\vec{q}^{\,\text{SAE}} = \begin{bmatrix} \theta_1^{\text{SAE}} \\ \theta_2^{\text{SAE}} \end{bmatrix} \text{ and } \vec{x}^{\,\text{SAE}} = \begin{bmatrix} \alpha \\ \beta \end{bmatrix} \tag{3.66}$$

where

$$\alpha = \theta_1^{\text{SAE}} \text{ and } \beta = \operatorname{atan2}\left(-s\theta_2^{\text{SAE}}, c\theta_1^{\text{SAE}} c\theta_2^{\text{SAE}}\right) \tag{3.67}$$

Because the final active joint cannot contribute to the development of a singular configuration, the hybridized form of the SAE is not considered here in its Jacobian analysis. Taking the time-derivatives of the two equations in Equation (3.67) yields:

$$\dot{\alpha} = \dot{\theta}_1^{\text{SAE}} \text{ and } \dot{\beta} = \frac{s\theta_2^{\text{SAE}}\left(s\theta_1^{\text{SAE}} c\theta_2^{\text{SAE}} + c\theta_1^{\text{SAE}} s\theta_2^{\text{SAE}}\right)\dot{\theta}_1^{\text{SAE}} - c\theta_1^{\text{SAE}}\left(c\theta_2^{\text{SAE}}\right)^2 \dot{\theta}_2^{\text{SAE}}}{\left(c\theta_1^{\text{SAE}}\right)^2\left(c\theta_2^{\text{SAE}}\right)^2 + \left(s\theta_2^{\text{SAE}}\right)^2} \tag{3.68}$$

Expressing this in matrix form produces:

$$\begin{bmatrix} 1 & 0 \\ s\theta_2^{\text{SAE}}\left(s\theta_1^{\text{SAE}} c\theta_2^{\text{SAE}} + c\theta_1^{\text{SAE}} s\theta_2^{\text{SAE}}\right) & -c\theta_1^{\text{SAE}}\left(c\theta_2^{\text{SAE}}\right)^2 \end{bmatrix} \begin{bmatrix} \dot{\theta}_1^{\text{SAE}} \\ \dot{\theta}_2^{\text{SAE}} \end{bmatrix} = \begin{bmatrix} 1 & 0 \\ 0 & \left(c\theta_1^{\text{SAE}}\right)^2\left(c\theta_2^{\text{SAE}}\right)^2 + \left(s\theta_2^{\text{SAE}}\right)^2 \end{bmatrix} \begin{bmatrix} \dot{\alpha} \\ \dot{\beta} \end{bmatrix} \tag{3.69}$$

Thus, the Jacobians of the isolated SAE are:

$$\mathbf{J}_q^{\text{SAE}} = \begin{bmatrix} 1 & 0 \\ s\theta_2^{\text{SAE}}\left(s\theta_1^{\text{SAE}} c\theta_2^{\text{SAE}} + c\theta_1^{\text{SAE}} s\theta_2^{\text{SAE}}\right) & -c\theta_1^{\text{SAE}}\left(c\theta_2^{\text{SAE}}\right)^2 \end{bmatrix},$$
$$\mathbf{J}_x^{\text{SAE}} = \begin{bmatrix} 1 & 0 \\ 0 & \left(c\theta_1^{\text{SAE}}\right)^2\left(c\theta_2^{\text{SAE}}\right)^2 + \left(s\theta_2^{\text{SAE}}\right)^2 \end{bmatrix}, \text{ and } \mathbf{J}^{\text{SAE}} = \left(\mathbf{J}_q^{\text{SAE}}\right)^{-1} \mathbf{J}_x^{\text{SAE}} \tag{3.70}$$

3.4.5. Performance Indices

In this subsection, the SAE's manipulability, dexterity, and sensitivity performance indices have been computed using the same methods as discussed in Subsection 3.2.6 for the RUS manipulator. Figure 3.13 shows surface plots and box plots of each index for the SAE manipulator. Since the Jacobian matrix was derived for the isolated SAE, there is only one pairing option for the independent variables in the indices' surface plots: the two angles that define the orientation of the isolated SAE end-effector (i.e., α and β). From Subsection 3.2.6, the rotation pairing that achieves the best manipulator performance should be matched with the largest movements of its target joint in the exoskeleton design. Because these movements are normally flexion/extension and abduction/adduction for the hip and ankle joints of the human lower limb, the implied assumption here is that the axes associated with the α and β rotations would both lie in the transverse plane of the subject's body. Moreover, the considered workspace for these variables is [–0.2 0.2] radians, which is consistent with the performance index plots associated with the previous candidate manipulators. Finally, note that a GPI for optimizing the design of the SAE is not derived because the SAE's Jacobian matrix does not depend on the relative dimensions of its branch links. As a result, the relative sizes of the SAE's links can be adjusted without inducing any changes in its performance, provided that essential design conditions are not violated (i.e., the orthogonality of adjacent joints). GPI analysis is also irrelevant for the original 3-DOF Agile Eye for the same reasoning.

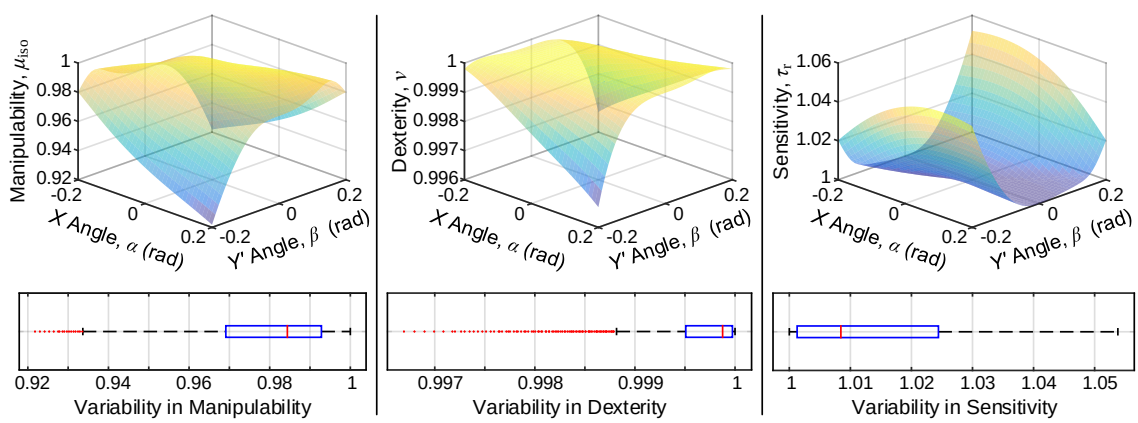

Figure 3.13. Surface plots and box plots of the SAE's manipulability (left), dexterity (middle), and sensitivity (right) for a [–0.2 0.2] radians range in end-effector orientation angles α and β

3.5. Comparison of the Candidate Orientation Manipulators and Selection

To facilitate the selection of the most desirable orientation manipulator amongst the three candidates considered for implementation in the exoskeleton system, a decision matrix has been developed. First, however, Figure 3.14 provides a review of the three manipulator architectures for the reader's reference.

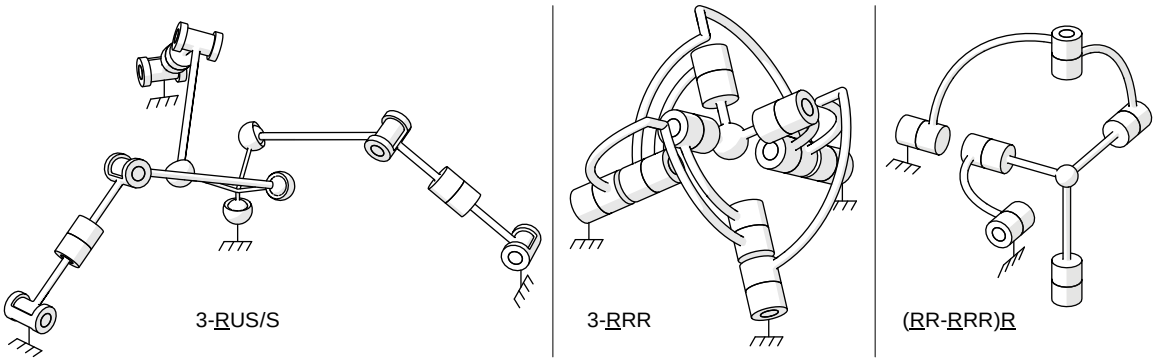

Figure 3.14. Schematic models of the RUS (left), AE (middle), and SAE (right) orientation manipulators

As shown in Table 3.3, the design criteria used to identify the best alternative are: the manipulator's manipulability, dexterity, and rotational sensitivity indices as well as the number joints included in their designs. The scores assigned to each candidate regarding performance are based on the average index value achieved across the considered [–0.2 0.2] workspace. To obtain scores limited to the range of 1 to 10 (i.e., with larger values associating with a more desirable design than smaller values), the average index values have been multiplied by 10 for manipulability and dexterity. As smaller index values are preferable for rotational sensitivity, scores in its category have been developed by subtracting the average index values from 10. Furthermore, to promote distinction between the candidates' scores, they include precision to the nearest tenth decimal place.

The number of joints in the candidate manipulator designs is included in the decision matrix because it reflects three practically-significant factors: propensity for end-effector positioning error, mechanical compactness, and fabrication complexity. From experience with parallel manipulator fabrication, physical joints contain imperfections that tend to add one or more unwanted DOFs (e.g., small radial or axial translations in revolute joints), albeit often with insignificant ranges when considered in isolation.

However, in the context of a complete parallel manipulator, undesirable movements in branch joints can compound into appreciable backlash at the end-effector and cause positioning errors. Next, the physical space occupied by the manipulator tends to increase with the number of joints, and consequently links, in its design. Although it may not a concern in some robotics applications, compactness is an especially important design consideration for exoskeletons; bulky designs tend to use more materials, which consequently increases system weight and cost. Functionally, bulkiness may encumber an exoskeleton's user, while discretion is also a social concern for people who use an exoskeleton for mobility assistance. Lastly, the number of joints is correlated with a manipulator's fabrication complexity. Simple designs generally involve less fabrication time and susceptibility to mechanical malfunctions than more complex ones. For all these reasons, it is preferable for a manipulator to possess a minimal number of joints.

Accordingly, the scores for the joint number category are developed for each candidate as follows. The alternatives with the most and least joints are assigned scores of 1 and 10, respectively, and then the remaining candidate score is mapped between those limits such that the joint count differences relative to the other candidates are proportional to the corresponding score differences. Since universal joints constructed from two revolute joints with perpendicular and intersecting axes tend to be less costly and have a larger range of rotations than traditional universal joints (e.g., that of a drive shaft), each instance of a universal joint is counted as two joints; the revolute and spherical joints are both counted as one joint for each instance. Finally, the weighting between performance and joint count criteria is selected as a 60%-40% split, with each performance index taking on an equal weighting value.

Table 3.3. Decision matrix for the orientation manipulator selection

		Orientation Manipulator Alternatives		
Decision Criteria	**Weight**	RUS	AE	SAE
Manipulability	2	5.4	8.0	9.8
Dexterity	2	8.8	9.8	10.0
Rotational Sensitivity	2	9.2	8.9	9.0
Joint Count	4	1.0	6.1	10.0
Score Total:		50.8	77.8	97.6
Relative Rank:		3	2	1

Note: The Relative Rank values order the candidates from most to least desirable in ascending order (i.e., 1 is most desirable and 3 is least desirable).

Normally it is good practice to evaluate the sensitivity of decision matrix results to changes in the criteria weighting. However, in this case, the SAE manipulator's scores are superior to those of the other options for all decision criteria considered; thus, the SAE will be found the most desirable regardless of the weighting selections. Because the scores for each decision criteria are based on quantifiable properties of the candidate manipulators, there is very little subjectivity in the selection of the SAE as the best option for the given decision criteria. Moreover, although it is not considered in the decision matrix because it is difficult to quantify objectively in this case, the complexity of the inverse and forward kinematic algorithms associated with each manipulator is also important to consider. Greater complexity results in increased computational expense, which in turn limits the rate of output data in the case of real-time applications (e.g., mobility-assistance exoskeletons) and increases processing time for non-real-time applications (e.g., motion-capture exoskeletons that require post-processing of data). The kinematic algorithm may also influence electronic hardware selections due to its affect on code storage requirements and complexity level of the required computations. Ultimately, the SAE is also superior in this regard, because its kinematic algorithms should require the fewest number of computations if coded efficiently.

One negative characteristic of the SAE is that it is a hybrid manipulator and not a true parallel manipulator like the RUS and AE. Therefore, the SAE does not fully attain the advantages of parallel manipulators over serial manipulator counterparts, such as improved payload-to-weight ratio (see Subsection 2.2.1 for further details). However, since the focal objective in this thesis is to develop an unactuated exoskeleton for motion-capture (MoCap) applications, several of these advantages are irrelevant at present. If the immediate goal was to design and develop an actuated exoskeleton, the hybrid form of the SAE would be a more critical aspect to consider in the manipulator selection process.

3.6. Singularity Analysis of the Selected Orientation Manipulator

As mentioned in the Jacobian's background information of Subsection 3.2.5, the functionality of the selected orientation manipulator diminishes at singular configurations. Therefore, the singular conditions of the SAE manipulator are identified and discussed in this section. Recall the third active joint of the hybrid SAE cannot contribute to the

development of a singular configuration, so the following discussion pertains to the isolated SAE unless stated otherwise.

Per Equation (3.70), the $\mathbf{J}_q^{\text{SAE}}$ Jacobian becomes singular when either or both $\cos\left(\theta_1^{\text{SAE}}\right)=0$ and $\cos\left(\theta_2^{\text{SAE}}\right)=0$, which occurs for $\theta_1^{\text{SAE}}=90°+d180°$ or $\theta_2^{\text{SAE}}=90°+d180°$, where d is an integer. If the latter inverse kinematic singularity condition is met, then passive joint J_w becomes coaxial with J_1^{SAE}, which mechanically prevents instantaneous end-effector rotations about the $\hat{z}_0^{\text{SAE}}$ axis. Even if the third active joint is added to form the 3-DOF hybrid version of the manipulator, J_1^{SAE} and J_3^{SAE} are coaxial and motions about that axis are locked (i.e., one DOF is lost). This condition concurrently causes the SAE end-effector to resist torques about $\hat{z}_0^{\text{SAE}}$ without any torques applied from the active joints. The left side of Figure 3.15 illustrates an example of this inverse kinematic singularity. Next, given the orthogonality between $\hat{u}$ and $\hat{v}$ as well as between $\hat{v}$ and $\hat{w}$, the former singular condition corresponds to a physical situation in which all the J_u, J_v, and J_w joint axes lie in the same plane. Thus, the manipulator loses its ability to rotate about its $\hat{z}_2^{\text{SAE}}$ axis. That is, the J_2^{SAE} active joint becomes locked and $\theta_1^{\text{SAE}}=\alpha$ becomes the only available rotation via J_1^{SAE}. The end-effector can also resist torques about $\hat{z}_2^{\text{SAE}}$ without action from the manipulator's active joints for this singular configuration, as indicated in the middle image of Figure 3.15.

Now, the $\mathbf{J}_x^{\text{SAE}}$ Jacobian becomes singular when both $\cos\left(\theta_1^{\text{SAE}}\right)=0$ and $\sin\left(\theta_2^{\text{SAE}}\right)=0$, occurring for $\theta_1^{\text{SAE}}=90°+d180°$ and $\theta_2^{\text{SAE}}=d180°$ where d is an integer. This represents a direct kinematic singularity for which the passive J_u and J_w joints are aligned coaxially. Physically, this allows the SAE end-effector to rotate freely about these joint axes without any attendant rotations in any of the active joints, thus adding a DOF to link $\text{L}_{\text{C1}}^{\text{SAE}}$ rotations. Concomitant to the additional DOF, the SAE end-effector cannot resist torques about that axis. Moreover, this direct kinematic singularity condition includes the first inverse kinematic singular condition, so it always materializes as a combined singularity for which one uncontrollable DOF is added to the end-effector and one DOF is lost. As a consequence, the two inverse kinematic singularities cannot occur simultaneously without the manipulator physically breaking. Furthermore, within the combined singular condition, the possibility arises for both J_1^{SAE} and J_2^{SAE} active joints to become locked if J_v becomes coaxial with J_2^{SAE}. In this special circumstance, an infinitesimal rotation of passive joint J_w unlocks J_1^{SAE}, and a subsequent infinitesimal rotation of J_1^{SAE} unlocks J_2^{SAE}. The middle and right-side images of Figure 3.15

respectively depict the general combined singularity and the special circumstance for which both active joints of the isolated SAE become locked.

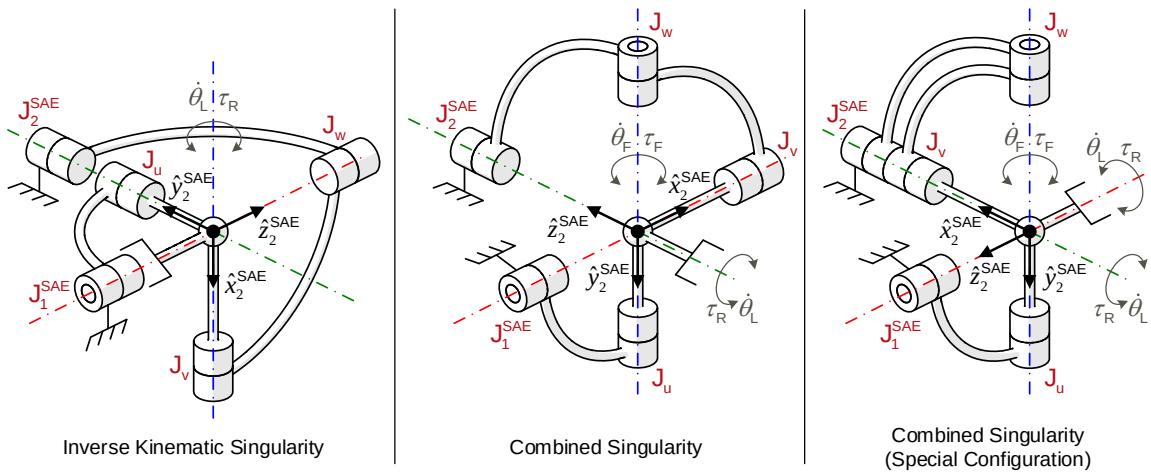

Figure 3.15. Examples of the self-contained inverse kinematic singularity (left), general combined singularity (middle), and combined singularity's special configuration (right)

Note: Infinitesimal motions lost, torques resisted, motions gained, and torques that cannot be resisted by the SAE end-effector are denoted by $\dot{\theta}_L$, τ_R, $\dot{\theta}_F$, and τ_F, respectively (i.e., 'F' stands for 'free').

Per manipulator-analysis theory, when the third active joint is added to create the hybrid SAE, a DOF in end-effector rotation is lost anytime J_3^{SAE} becomes coaxial with either J_1^{SAE} or J_2^{SAE}. However, these alignments are encompassed by the isolated SAE's singular conditions, as can be observed in Figure 3.15. Therefore, the J_3^{SAE} joint cannot contribute to the formation of a new singularity. Note that for the combined singularity configurations, the possible redundant alignments of J_1^{SAE} or J_2^{SAE} with J_3^{SAE} can reintroduce the lost DOF caused by the former joint becoming locked, but the overall manipulator still loses at least one of its intended 3-DOF rotations.

Chapter 4.

Kinematic Analyses of Candidate Motion-Transfer Manipulators

With the selection of an orientation manipulator completed in Chapter 3, this chapter advances to the investigation of two different motion-transfer manipulator possibilities. These manipulators transfer the 3-DOF rotational motions generated by the orientation manipulator about its center-of-rotation (COR) to a corresponding set of 3-DOF rotations about the COR of a targeted human joint. The following sections detail the kinematic architecture along with the inverse and forward kinematic analyses of the two proposed manipulators. These represent novel contributions offered by this thesis, as well as that of Sadeqi [156], who collaborated with the author in their developments. The novelty of the manipulators is supported by their inclusion in a successful international patent application and subsequent publication [176]. Figure 4.1 revisits the high-level schematic of the proposed lower-limb exoskeleton and highlights the current stage in its design development process.

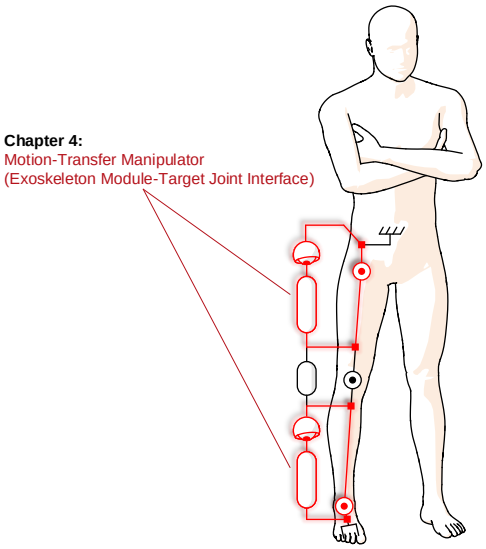

Figure 4.1. Stage of exoskeleton design development covered in Chapter 4
Note: The motion-transfer manipulator applies to both the hip and ankle exoskeleton modules, whereas the knee exoskeleton module does not expand upon the current state-of-the-art (see Subsection 2.2.3).

4.1. Candidate #1: SRRP/S Manipulator

4.1.1. Kinematic Architecture

Figure 4.2 shows the mechanism architecture for the first motion-transfer manipulator. The selected orientation manipulator is considered as an active spherical joint, while the targeted human joint is interpreted as a passive spherical joint. It is passive in the sense that it is not powered by man-made actuators or monitored directly by man-made sensors. The motion-transfer manipulator is then composed of a serial chain that connects these two spherical joints. In this case, the motion-transfer manipulator comprises a sequence of two revolute joints followed by a prismatic joint, all passive, leading from the active spherical joint to the target human joint. Therefore, an appropriate structural name for the parallel manipulator is SRRP/S. Like in Chapter 3, the ending '/S' represents the spherical constraint imposed on the exoskeleton module by the human joint with which it interfaces. For this design, it is important to note that the R, R, and P joint axes are parallel to each other. Also, between the prismatic and human joints, there is an assumedly rigid connection binding the exoskeleton chain end to the human limb segment inferior to the target body joint; likewise, the shared base of the active spherical joint and human joint implies a rigid connection between the orientation manipulator's base link and the body segment superior to the targeted human joint.

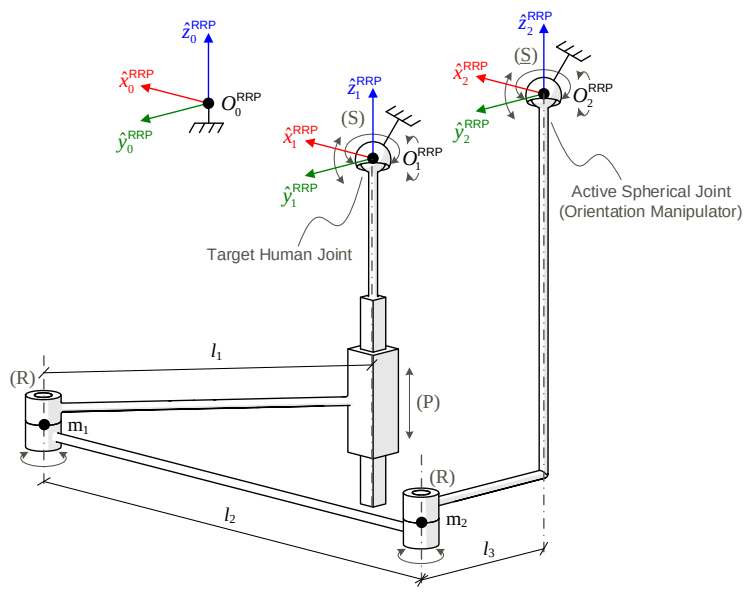

Figure 4.2. Schematic of the RRP motion-transfer manipulator in its home configuration with labels for frames, joint types, significant points, and link lengths

In Figure 4.2 and hereafter, the abbreviation RRP represents this motion-transfer manipulator and is used to distinguish frames and rotations associated with it. The local reference frame, $\{0\}^{\text{RRP}}$, is fixed to manipulator's base link and remains stationary in this local context. Frames $\{1\}^{\text{RRP}}$ and $\{2\}^{\text{RRP}}$ are respectively attached to the target human joint and orientation manipulator outputs. These frames undergo 3-DOF rotations with their associated joints, and their origins are coincident with the COR of those joints. As a result, the $\{1\}^{\text{RRP}}$ and $\{2\}^{\text{RRP}}$ frame origins do not translate with respect to the $\{0\}^{\text{RRP}}$ reference frame. Consequently, the ${}^{0}\vec{O}_{1}^{\text{RRP}}$ and ${}^{0}\vec{O}_{2}^{\text{RRP}}$ origin positions are design parameters and, as such, their coordinates are assumed to be known and constant in the following kinematic analyses. No particular spatial alignments exist between the three frame origins. However, in its home configuration, each frame is oriented equivalently as shown in Figure 4.2 (i.e., ${}^{0}_{1}\mathbf{R}^{\text{RRP}} = \mathbf{I}_{3\times3}$ and ${}^{0}_{2}\mathbf{R}^{\text{RRP}} = \mathbf{I}_{3\times3}$ in the home posture). Furthermore, the *z*-axes of $\{1\}^{\text{RRP}}$ and $\{2\}^{\text{RRP}}$ remain parallel with the passive joint axes. Finally, m_1 and m_2 are points coincident to the centers of the first and second revolute joints, where the former is adjacent to the prismatic joint and the latter is adjacent to the active spherical joint. Within a plane normal to the passive joint axes, l_1 denotes the Euclidean distance between m_1 and the prismatic joint axis, l_2 represents the distance between m_1 and m_2, and l_3 indicates the distance between m_2 and the active spherical joint's planar projection.

4.1.2. Inverse Kinematic Analysis

Here, the inverse kinematic analysis is treated as the problem of deriving the active spherical joint's orientation from a numerically-known orientation of the human target spherical joint, both in terms of the local reference frame, $\{0\}^{\text{RRP}}$. To start, per the design of the proposed motion-transfer manipulator, each of the two revolute and one prismatic joint axes are parallel with each other as well as the *z*-axes of both $\{1\}^{\text{RRP}}$ and $\{2\}^{\text{RRP}}$ frames. Thus, the *z*-axis of the active spherical joint's orientation is mechanically constrained to be equal to that of the known target joint orientation. Consequently, the active spherical joint orientation relates to the target joint orientation via a single intrinsic *z*-axis rotation:

$$ {}^{0}_{1}\mathbf{R}_{\mathbf{N}}^{\text{RRP}}\mathbf{R}_{Z'}\left(\zeta_1\right) = {}^{0}_{2}\mathbf{R}^{\text{RRP}} \tag{4.1} $$

where the inverse kinematics task is to determine the unknown rotation angle, ζ_1. Note that the '$\mathbf{N}$' subscript again designates a numerically-known rotation matrix.

The inverse kinematics problem now reduces to a two-dimensional analysis of the RRP's projection onto the $\hat{x}_1^{\text{RRP}}$ - $\hat{y}_1^{\text{RRP}}$ plane. In this context, the manipulator behaves as a four-bar mechanism of sorts. As shown in Figure 4.3, the $\{1\}^{\text{RRP}}$ and $\{2\}^{\text{RRP}}$ frame origins act as the base-connected endpoints of the four-bar mechanism, with the two passive revolute joints and their adjacent links completing the device. However, the planar mechanism is atypical in that human joint rotations about the $\hat{x}_1^{\text{RRP}}$ or $\hat{y}_1^{\text{RRP}}$ axes cause the ${}^1\vec{O}_2^{\text{RRP}}$ projection point to move relative to the ${}^1\vec{O}_1^{\text{RRP}}$ origin. Since both ${}^0\vec{O}_2^{\text{RRP}}$ and ${}^0_1\mathbf{R}^{\text{RRP}}$ are known for the inverse kinematics problem, the location of that moving endpoint can be determined by the *x*- and *y*-coordinates of the following vector:

$$ {}^1\vec{O}_2^{\text{RRP}} = {}^1_0\mathbf{R}^{\text{RRP}}\,{}^0\vec{O}_2^{\text{RRP}} = \left({}^0_1\mathbf{R}^{\text{RRP}}\right)^{\text{T}}\,{}^0\vec{O}_2^{\text{RRP}} \tag{4.2} $$

Also, note that the position of the first revolute joint relative to frame $\{1\}^{\text{RRP}}$, as given by ${}^1\vec{\mathrm{m}}_1$, is a constant parameter decided by the design of the exoskeleton's chain-end component (i.e., the structure that attaches to the human limb segment). Therefore, the coordinates of ${}^1\vec{\mathrm{m}}_1$ are constant and known in this analysis.

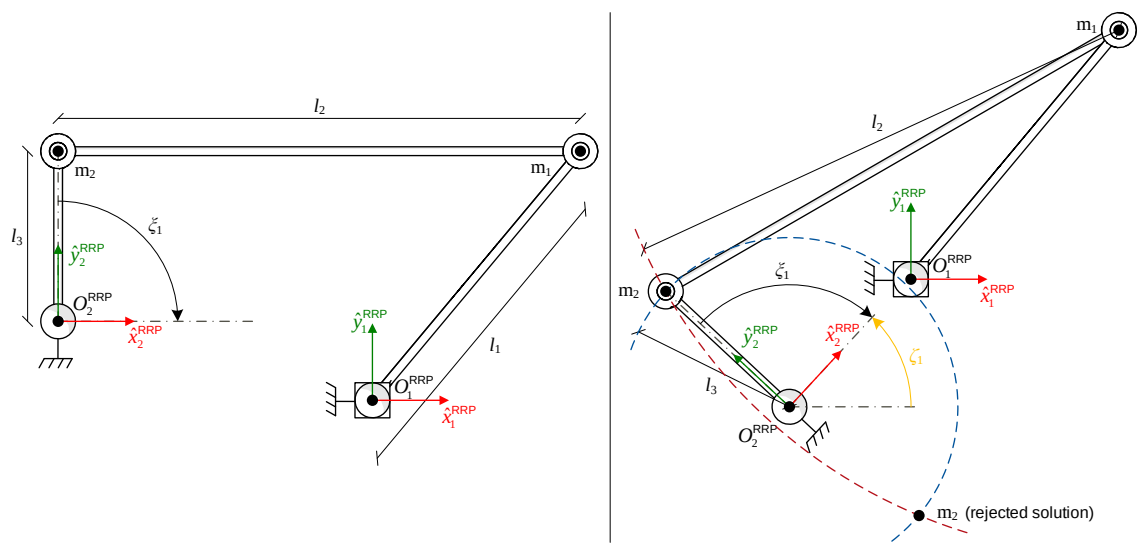

Figure 4.3. Schematic views of the RRP from the *x*-*y* plane of frame $\{1\}^{\text{RRP}}$ in its home configuration (left) and an arbitrary posture (right) with the m_2 and inverse kinematic solutions indicated

The planar position of the second revolute joint, ${}^1\vec{\mathrm{m}}_2$, can be solved by asserting the geometric constraints associated with the adjacent link's lengths. Specifically, the two feasible ${}^1\vec{\mathrm{m}}_2$ positions are found at the intersection points of a circle centered at ${}^1\vec{\mathrm{m}}_1$ and a circle centered at ${}^1\vec{O}_2^{\text{RRP}}$, with respective radii of l_2 and l_3. Note that the following coordinate variables will be used in this analysis:

$$ {}^{1}\vec{\mathrm{m}}_1 = \begin{bmatrix} x_{m1} & y_{m1} & z_{m1} \end{bmatrix}^{\mathrm{T}} \text{ and } {}^{1}\vec{O}_2^{\mathrm{RRP}} = \begin{bmatrix} x_{O2} & y_{O2} & z_{O2} \end{bmatrix}^{\mathrm{T}} \tag{4.3} $$

Also, the l_2 and l_3 link lengths are clarified in Figure 4.2 and Figure 4.3. The circle intersection points then occur at:

$$ \begin{bmatrix} x_{m2} & y_{m2} \end{bmatrix} = \begin{bmatrix} \dfrac{-B_1 \pm \sqrt{B_1^2 - 4A_1C_1}}{2A_1} & D_1 x_{m2} + E_1 \end{bmatrix} \tag{4.4} $$

where x_{m2} and y_{m2} are the *x*- and *y*-coordinates of ${}^{1}\vec{\mathrm{m}}_2$, and Equations (4.5) define the substitution variables introduced in Equation (4.4).

$$ \begin{gathered} A_1 = D_1^2 + 1,\ B_1 = 2\left(D_1E_1 - x_{m1} - D_1 y_{m1}\right),\ C_1 = x_{m1}^2 + E_1^2 - 2E_1 y_{m1}^2 + y_{m1}^2 - l_2^2, \\ D_1 = \frac{x_{m1} - x_{O2}}{y_{O2} - y_{m1}}, \text{ and } E_1 = \frac{l_3^2 + x_{O2}^2 + y_{O2}^2 - l_2^2 - x_{m1}^2 - y_{m1}^2}{2\left(y_{O2} - y_{m1}\right)} \end{gathered} \tag{4.5} $$

From the two solutions described in Equation (4.4), the subtraction result is selected as the appropriate one for the design scheme considered (see the right side of Figure 4.3).

Analogous to the position of m_1 relative to the target joint frame $\{1\}^{\mathrm{RRP}}$, the $\hat{x}_2^{\mathrm{RRP}}$-$\hat{y}_2^{\mathrm{RRP}}$ planar position of m_2 is known and constant relative to the active joint frame $\{2\}^{\mathrm{RRP}}$; that is, its coordinates are decided by the selections of the RRP manipulator's l_3 link design. As a result, there exists a known and constant *z*-axis rotation that produces the ${}^{1}\hat{x}_2^{\mathrm{RRP}}$ axis from the normalized position of ${}^{1}\vec{\mathrm{m}}_2$ relative to ${}^{1}\vec{O}_2^{\mathrm{RRP}}$:

$$ {}^{1}\hat{x}_2^{\mathrm{RRP}} = \mathbf{R}_Z\left(\xi_1\right) \frac{{}^{1}\vec{\mathrm{m}}_2 - {}^{1}\vec{O}_2^{\mathrm{RRP}}}{\left\| {}^{1}\vec{\mathrm{m}}_2 - {}^{1}\vec{O}_2^{\mathrm{RRP}} \right\|} = \begin{bmatrix} c\xi_1 & -s\xi_1 \\ s\xi_1 & c\xi_1 \end{bmatrix} \frac{{}^{1}\vec{\mathrm{m}}_2 - {}^{1}\vec{O}_2^{\mathrm{RRP}}}{\left\| {}^{1}\vec{\mathrm{m}}_2 - {}^{1}\vec{O}_2^{\mathrm{RRP}} \right\|} = \begin{bmatrix} x_{x2} \\ y_{x2} \end{bmatrix} \tag{4.6} $$

where ξ_1 is the known rotation angle and the vectors in the above equation are their two-dimensional versions (i.e., only *x*- and *y*-coordinates are considered). Upon solving Equations (4.2) and (4.4)–(4.6), the intrinsic *z*-axis rotation that relates the human joint orientation to active spherical joint orientation is given by:

$$ \zeta_1 = \operatorname{atan2}\left(y_{x2}, x_{x2}\right) \tag{4.7} $$

This represents the inverse kinematics solution for the RRP when substituted into Equation (4.1).

4.1.3. Forward Kinematic Analysis

The forward kinematic analysis for the RRP motion-transfer manipulator is essentially equivalent to the inverse kinematics procedure carried out step-by-step in reverse order. As the *z*-axis orientation equivalence still exists between frames $\{1\}^{\mathrm{RRP}}$

and $\{2\}^{\text{RRP}}$, the forward kinematics solution entails finding an intrinsic *z*-axis rotation that produces the human joint orientation from a known active spherical joint orientation:

$$ {}^{0}_{2}\mathbf{R}^{\text{RRP}}_{\mathbf{N}}\mathbf{R}_{Z'}\left(\zeta_2\right) = {}^{0}_{1}\mathbf{R}^{\text{RRP}} \tag{4.8} $$

Here, ζ_2 is to be determined and the '$\mathbf{N}$' subscript indicates that the corresponding rotation matrix is numerically known.

To start, recall that the position of the m_2 point's projection onto the $\hat{x}_2^{\text{RRP}}$ - $\hat{y}_2^{\text{RRP}}$ plane is known and constant relative to the active joint frame $\{2\}^{\text{RRP}}$. Next, the position of the target human joint relative to the $\{2\}^{\text{RRP}}$ frame can be determined as:

$$ {}^{2}\vec{O}_1^{\text{RRP}} = {}^{2}_{0}\mathbf{R}^{\text{RRP}}\,{}^{0}\vec{O}_1^{\text{RRP}} = \left({}^{0}_{2}\mathbf{R}^{\text{RRP}}\right)^{\mathrm{T}}\,{}^{0}\vec{O}_1^{\text{RRP}} \tag{4.9} $$

The possible $\hat{x}_2^{\text{RRP}}$ - $\hat{y}_2^{\text{RRP}}$ planar positions of m_1 are subsequently found at the intersection of two circles: one centered at ${}^{2}\vec{\mathrm{m}}_2$ with radius l_2, and the other centered at ${}^{2}\vec{O}_1^{\text{RRP}}$ with a radius of l_1. This is illustrated in Figure 4.4. Equation (4.10) provides the corresponding solutions expressed in terms of frame $\{2\}^{\text{RRP}}$:

$$ \begin{bmatrix} x_{m1} & y_{m1} \end{bmatrix} = \begin{bmatrix} \dfrac{-B_2 \pm \sqrt{B_2^2 - 4A_2C_2}}{2A_2} & D_2x_{m1} + E_2 \end{bmatrix} \tag{4.10} $$

where Equations (4.11) provide the substitutions for the new variables used therein and the addition result is appropriate for the proposed assembly mode.

$$ \begin{gathered} A_2 = D_2^2 + 1,\ B_2 = 2\left(D_2E_2 - x_{m2} - D_2y_{m2}\right),\ C_2 = x_{m2}^2 + E_2^2 - 2E_2y_{m2}^2 + y_{m2}^2 - l_2^2, \\ D_2 = \frac{x_{m2} - x_{O1}}{y_{O1} - y_{m2}},\ \text{and}\ E_2 = \frac{l_1^2 + x_{O1}^2 + y_{O1}^2 - l_2^2 - x_{m2}^2 - y_{m2}^2}{2\left(y_{O1} - y_{m2}\right)} \end{gathered} \tag{4.11} $$

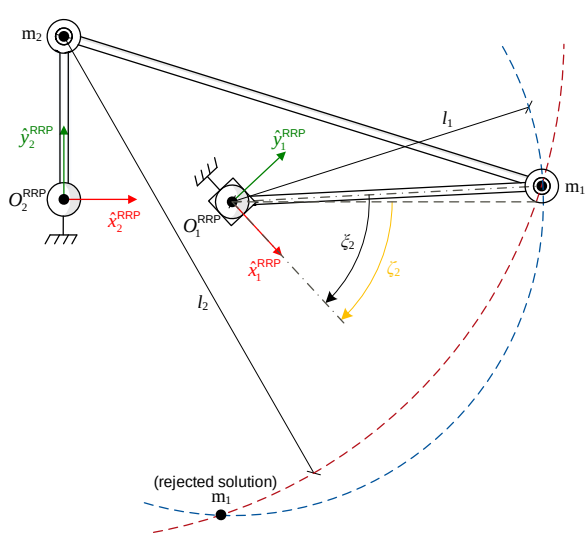

Figure 4.4. Schematic view of the RRP from the *x-y* plane of frame $\{2\}^{\text{RRP}}$ with the m_1 and forward kinematic solutions indicated

Next, the direction of the $\hat{x}_1^{\text{RRP}}$ axis within the $\hat{x}_2^{\text{RRP}}$ - $\hat{y}_2^{\text{RRP}}$ coordinate system is resolved using the known angle, ξ_2, between it and the $\left(\vec{\mathrm{m}}_1 - \vec{O}_1^{\text{RRP}}\right)$ vector, as established by the manipulator's design (see Figure 4.4):

$$ {}^{2}\hat{x}_1^{\text{RRP}} = \mathbf{R}_Z\left(\xi_2\right)\frac{{}^{2}\vec{\mathrm{m}}_1 - {}^{2}\vec{O}_1^{\text{RRP}}}{\left\|{}^{2}\vec{\mathrm{m}}_1 - {}^{2}\vec{O}_1^{\text{RRP}}\right\|} = \begin{bmatrix} c\xi_2 & -s\xi_2 \\ s\xi_2 & c\xi_2 \end{bmatrix}\frac{{}^{2}\vec{\mathrm{m}}_1 - {}^{2}\vec{O}_1^{\text{RRP}}}{\left\|{}^{2}\vec{\mathrm{m}}_1 - {}^{2}\vec{O}_1^{\text{RRP}}\right\|} = \begin{bmatrix} x_{x1} \\ y_{x1} \end{bmatrix} \tag{4.12} $$

The *z*-coordinate of the ${}^{2}\vec{\mathrm{m}}_1$ and ${}^{2}\vec{O}_1^{\text{RRP}}$ vectors are again dropped during the computation of Equation (4.12). Finally, the forward kinematic solution is completed by solving for the ζ_2 angle via the four-quadrant arctangent function:

$$ \zeta_2 = \operatorname{atan2}\left(y_{x1}, x_{x1}\right) \tag{4.13} $$

4.2. Candidate #2: SPU/S Manipulator

4.2.1. Kinematic Architecture

The kinematic architecture of the second motion-transfer manipulator candidate is quite similar to the first, but with two major modifications. First, the passive prismatic joint is placed adjacent to the active spherical joint, instead of the target human joint. Second, the passive revolute joint axes are reoriented such that the first is skew with the prismatic joint axis and the second is perpendicular to both the first revolute and prismatic joint axes, as illustrated in Figure 4.5. If there was no offset between the prismatic and first revolute joint axes, the three passive joint axes would form a mutually orthogonal set. Furthermore, because the two revolute joint axes intersect at a right angle, they can be interpreted as a single universal joint. Therefore, the closed kinematic chain created by the motion-transfer manipulator and interfaced human joint is described as SPU/S in generalized shorthand form. The implied assumption is that the active spherical joint comprises the selected orientation manipulator from Chapter 3, so the longhand structural name for the exoskeleton-target joint system is (RR-RRR)RPU/S, because the Simplified Agile Eye was chosen. Note that the final '/S' represents the targeted human joint. Also, a rigid connection again exists between the exoskeleton and human body segments at two sites: one above and one below the targeted joint.

The abbreviation PU signifies the motion-transfer manipulator design described here and will be used to distinguish frames and frame rotations associated with this design in the kinematic analyses to follow. Analogous to the RRP design, the $\{0\}^{\text{PU}}$ frame

acts as a reference frame in the local context of this system; $\{1\}^{PU}$ is fixed to the target human joint and tracks its motions; and $\{2\}^{PU}$ is fixed to and moves with the active spherical joint. The latter two frames have origins at the human joint COR and active spherical joint COR, respectively, and these origin points do not translate with respect to the local reference frame. The $\hat{z}_2^{PU}$ axis is coincident with the passive prismatic joint axis. Additionally, an arbitrary spatial offset may exist between each of the three frame origins. The PU motion-transfer manipulator achieves its home configuration when each of its frames' axes are oriented in the same directions (i.e., ${}^0_1\mathbf{R}^{PU} = \mathbf{I}_{3\times3}$ and ${}^0_2\mathbf{R}^{PU} = \mathbf{I}_{3\times3}$). Next, the points n_1 and n_2 respectively denote the universal joint center (i.e., the intersection point of the two revolute joint axes) and the orthogonal projection of that point onto the passive prismatic joint axis. An n_3 point specifies the position of the universal joint center's orthogonal projection onto the $\hat{y}_1^{PU}$ - $\hat{z}_1^{PU}$ plane.

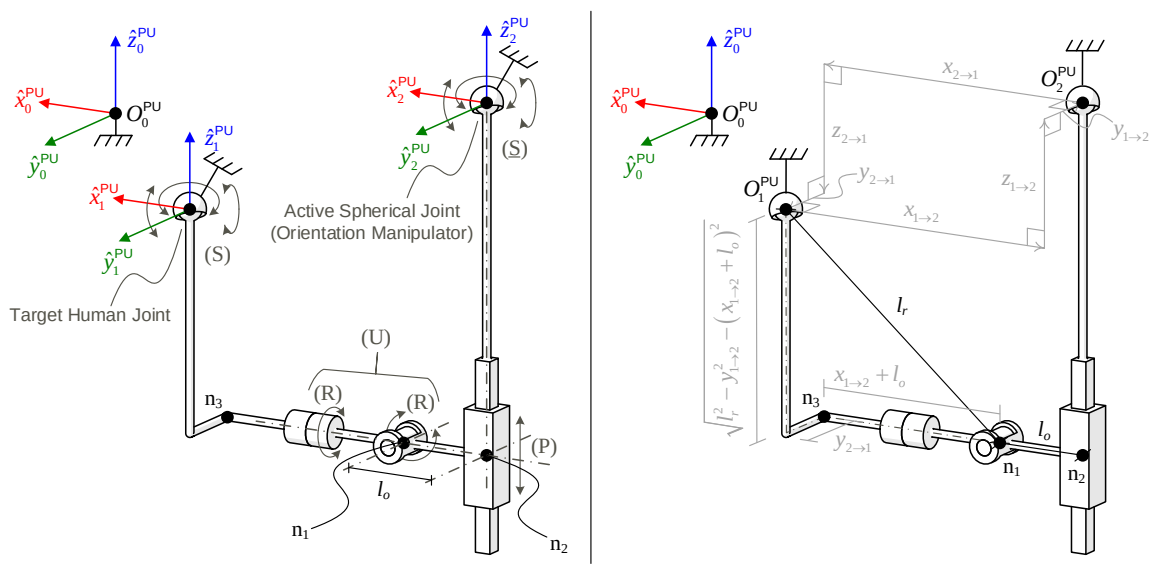

Figure 4.5. Schematic of the PU motion-transfer manipulator in its home configuration with labels for frames, joint types, and significant points (left) and additional length constants (right)

As shown on the right side of Figure 4.5, l_o denotes the Euclidean distance between n_1 and n_2, while l_r indicates that between O_1^{PU} and n_1. Other design dimensions will be expressed in terms of l_o, l_r, and the constant displacement coordinates between ${}^0\vec{O}_1^{PU}$ and ${}^0\vec{O}_2^{PU}$, which are labeled in Figure 4.5 and defined here:

$$ {}^0\vec{O}_2^{PU} - {}^0\vec{O}_1^{PU} = \begin{bmatrix} x_{1\to2} & y_{1\to2} & z_{1\to2} \end{bmatrix} \text{ and } {}^0\vec{O}_1^{PU} - {}^0\vec{O}_2^{PU} = \begin{bmatrix} x_{2\to1} & y_{2\to1} & z_{2\to1} \end{bmatrix} \tag{4.14} $$

Note that these coordinates are signed scalars (e.g., $x_{1\to 2}$ is negative while $x_{2\to 1}$ is positive for the assumed frame orientations and relative origin positions shown in Figure 4.5). The coordinate values are also assumed to be known design parameters.

4.2.2. Inverse Kinematic Analysis

The inverse kinematic analysis for the PU requires the formulation of the active spherical joint orientation in terms of a numerically-known target human-joint orientation. To begin, note that only the universal joint in the PU design permits relative rotation between the $\{1\}^{\text{PU}}$ and $\{2\}^{\text{PU}}$ frames. These two rotational DOFs can be interpreted as intrinsic *X'* and *Y''* rotations as the targeted limb segment encounters the two revolute joints comprising the universal joint. Therefore, a symbolic relationship between the human joint and active spherical joint orientations exists as follows:

$$ {}^{0}_{2}\mathbf{R}^{\text{PU}} = {}^{0}_{1}\mathbf{R}^{\text{PU}}_{\mathbf{N}}\mathbf{R}_{X'}(\gamma_1)\mathbf{R}_{Y''}(\gamma_2) = {}^{0}_{1}\mathbf{R}^{\text{PU}}_{\mathbf{N}}\begin{bmatrix} c\gamma_2 & 0 & s\gamma_2 \\ s\gamma_1 s\gamma_2 & c\gamma_1 & -s\gamma_1 c\gamma_2 \\ -c\gamma_1 s\gamma_2 & s\gamma_1 & c\gamma_1 c\gamma_2 \end{bmatrix} = {}^{0}_{1}\mathbf{R}^{\text{PU}}_{\mathbf{N}}\,{}^{1}_{2}\mathbf{R}^{\text{PU}}_{\mathbf{S}} \tag{4.15} $$

where '$\mathbf{N}$' and '$\mathbf{S}$' subscripts respectively denote numerical and symbolic matrices.

Considering the leading *X'* rotation first, note that the $\{1\}^{\text{PU}}$ frame position of O_2^{PU} can be found, because its local reference frame representation is known and constant:

$$ {}^{1}\vec{O}_2^{\text{PU}} = \left({}^{0}_{1}\mathbf{R}^{\text{PU}}_{\mathbf{N}}\right)^{\text{T}}\,{}^{0}\vec{O}_2^{\text{PU}} = {}^{1}_{0}\mathbf{R}^{\text{PU}}_{\mathbf{N}}\,{}^{0}\vec{O}_2^{\text{PU}} = \begin{bmatrix} x_{O2} & y_{O2} & z_{O2} \end{bmatrix}^{\text{T}} \tag{4.16} $$

Moreover, the position of n_1 is constant in terms of frame $\{1\}^{\text{PU}}$ and is known in terms of several design parameters as:

$$ {}^{1}\vec{\mathrm{n}}_1 = \begin{bmatrix} x_{1\to 2} + l_o & y_{1\to 2} & -\sqrt{l_r^2 - y_{1\to 2}^2 - \left(x_{1\to 2} + l_o\right)^2} \end{bmatrix}^{\text{T}} \tag{4.17} $$

Now, when the manipulator is viewed from the $\hat{y}_1^{\text{PU}}$ - $\hat{z}_1^{\text{PU}}$ plane, as illustrated on the left side of Figure 4.6, the planar projections of ${}^{1}\vec{O}_2^{\text{PU}}$ and ${}^{1}\vec{\mathrm{n}}_1$ both lie on the planar projection of the prismatic joint axis and, thus, the $\hat{z}_2^{\text{PU}}$ axis. Consequently, the γ_1 angle associated with the intrinsic *X'* rotation is given by:

$$ \gamma_1 = \operatorname{atan2}\left(y_{1\to 2} - y_{O2}, z_{O2} + \sqrt{l_r^2 - y_{1\to 2}^2 - \left(x_{1\to 2} + l_o\right)^2}\right) \tag{4.18} $$

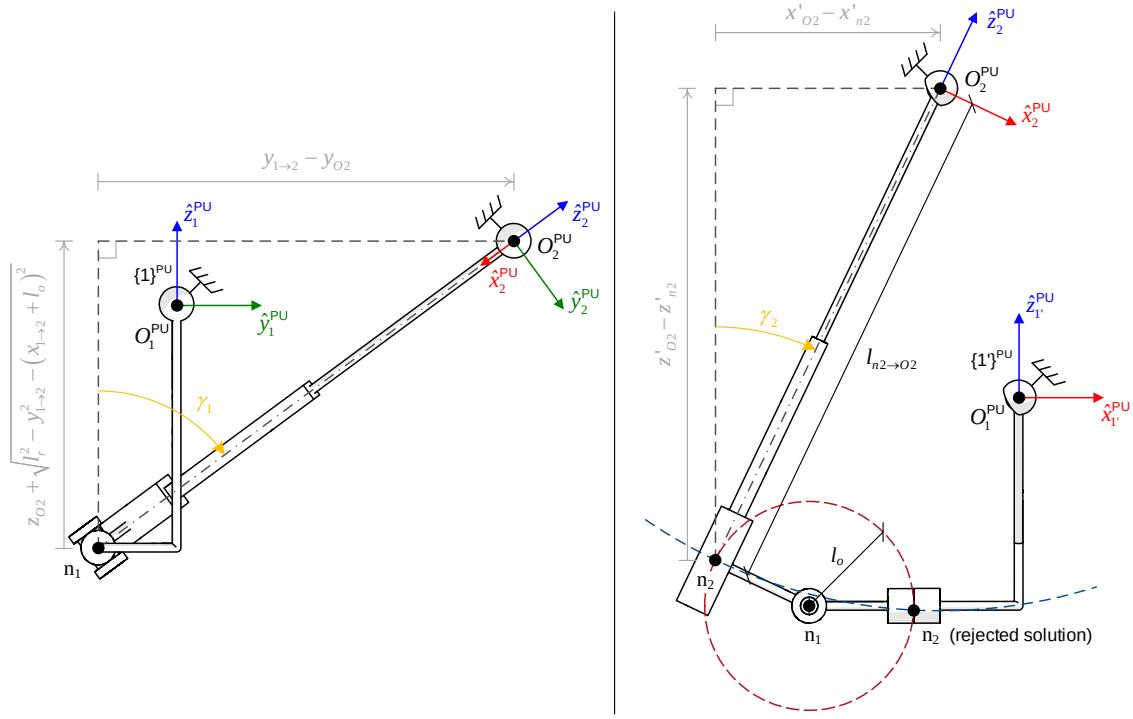

Figure 4.6. Schematic view of the PU from the *y-z* plane of frame $\{1\}^{PU}$ (left) and the *x-z* plane of frame $\{1'\}^{PU}$ (right) with n_2 and inverse kinematic solutions indicated

Note: The ${}^{1}\hat{y}_2^{PU}$ axis has no component in the $\hat{x}_1^{PU}$ direction, as predicted by the ${}^{1}_{2}\mathbf{R}_S^{PU}$ rotation matrix in Equation (4.15).

To find the final intrinsic *Y″* rotation, the PU manipulator is examined from the plane normal to the $\{1\}^{PU}$ frame's updated *y* axis after undergoing the intrinsic *X′* rotation. For clarity, this intermediate frame will be denoted as $\{1'\}^{PU}$, and the current viewing plane is that defined by $\hat{x}_{1'}^{PU}$ - $\hat{z}_{1'}^{PU}$ as shown in the right-side image of Figure 4.6. The positions of O_2^{PU} and n_1 are represented in terms of $\{1'\}^{PU}$ via pre-multiplication by the transpose of the matrix associated with the leading intrinsic *X′* rotation:

$$ {}^{1'}\vec{O}_2^{PU} = \left(\mathbf{R}_{X'}(\gamma_1)\right)^{T}\, {}^{1}\vec{O}_2^{PU} = {}^{1'}_{1}\mathbf{R}^{PU}\, {}^{1}\vec{O}_2^{PU} = \begin{bmatrix} x'_{O2} & y'_{O2} & z'_{O2} \end{bmatrix}^{T} \tag{4.19} $$

$$ {}^{1'}\vec{n}_1 = \left(\mathbf{R}_{X'}(\gamma_1)\right)^{T}\, {}^{1}\vec{n}_1 = {}^{1'}_{1}\mathbf{R}^{PU}\, {}^{1}\vec{n}_1 = \begin{bmatrix} x'_{n1} & y'_{n1} & z'_{n1} \end{bmatrix}^{T} \tag{4.20} $$

The next task is to determine the position of the n_2 point, because the angle of the line connecting n_2 and O_2^{PU} within the $\{1'\}^{PU}$ frame represents the desired γ_2 angle. The Euclidean distance between n_2 and O_2^{PU} is presently unknown, but is yielded by applying the Pythagorean theorem to the right triangle composed of those two points and n_1:

$$ l_{n2\to O2} = \sqrt{\left\| {}^{1'}\vec{O}_2^{PU} - {}^{1'}\vec{n}_1 \right\|^2 - l_o^2} \tag{4.21} $$

where $\| \ \|$ denotes the Euclidean norm. Next, two theoretically feasible locations for the n_2 point occur at the intersection points of two circles in the $\hat{x}_{1'}^{PU}$ - $\hat{z}_{1'}^{PU}$ plane. The first circle is centered at the planar projection of n_1 with a radius of l_o, and the second circle is centered at the projection of O_2^{PU} with a radius of $l_{n2\to O2}$. These two solutions are:

$$x'_{n2} = \frac{-B_3 \pm \sqrt{B_3^2 - 4A_3C_3}}{2A_3}, \ z'_{n2} = \frac{F_3 - D_3 x'_{n2}}{E_3} \tag{4.22}$$

where the equivalencies for the variables introduced above are:

$$A_3 = \left(\frac{D_3}{E_3}\right)^2 + 1, \ B_3 = 2\left(z'_{n1}\frac{D_3}{E_3} - \frac{D_3F_3}{E_3^2} - x'_{n1}\right),$$
$$C_3 = x'^2_{n1} + \left(\frac{F_3}{E_3}\right)^2 + z'^2_{n1} - 2z'_{n1}\frac{F_3}{E_3} - l_o^2, \ D_3 = 2\left(x'_{O2} - x'_{n1}\right), \ E_3 = 2\left(z'_{O2} - z'_{n1}\right)^2, \tag{4.23}$$
$$\text{and } F_3 = l_o^2 - l_{n2\to O2}^2 - x'^2_{n1} + x'^2_{O2} - z'^2_{n1} + z'^2_{O2}$$

In Equation (4.22), the lesser quadratic root for x'_{n2} is appropriate for the proposed design and frame definitions because it corresponds to a scenario in which the prismatic joint acts along an axis that passes outside of the universal joint. Contrarily, the greater quadratic root corresponds to an erroneous configuration for which the prismatic joint axis passes through the universal joint, and so it is rejected here. Finally, the intrinsic *Y″* rotation is given by:

$$\gamma_2 = \operatorname{atan2}\left(x'_{O2} - x'_{n2}, z'_{O2} - z'_{n2}\right) \tag{4.24}$$

Upon computing γ_1 and γ_2 from Equations (4.18) and (4.24), respectively, and then applying the results to Equation (4.15), the orientation of the active spherical joint with respect to the local reference frame is solved. Thus, the inverse kinematic analysis for the PU is complete.

4.2.3. Forward Kinematic Analysis

For the forward kinematics problem, the orientation of the active spherical joint is numerically known with respect to the local reference frame:

$${}^0_2\mathbf{R}_{\mathbf{N}}^{PU} = \begin{bmatrix} q_{11} & q_{12} & q_{13} \\ q_{21} & q_{22} & q_{23} \\ q_{31} & q_{32} & q_{33} \end{bmatrix} \tag{4.25}$$

where the '$\mathbf{N}$' subscript indicates that each element q_{ij} of the matrix is numerically known. The task is then to derive a symbolic rotation matrix that relates the known active joint orientation to the target human joint orientation. To start, notice again that as the active joint frame $\{2\}^{\text{PU}}$ proceeds along the PU manipulator's kinematic chain to the human joint, there are only two possible rotations. These are a *y*-axis rotation arising at the first revolute joint (i.e., the one adjacent to the prismatic joint) followed by an intrinsic *x*-axis rotation due to the second revolute joint. Therefore, post-multiplying the known active joint orientation by rotation matrices corresponding to intrinsic *Y'* then *X''* rotations yields the target human joint orientation:

$$ {}^{0}_{1}\mathbf{R}^{\text{PU}} = {}^{0}_{2}\mathbf{R}^{\text{PU}}_{\mathbf{N}}\mathbf{R}_{Y'}\left(\gamma_3\right)\mathbf{R}_{X''}\left(\gamma_4\right) = {}^{0}_{2}\mathbf{R}^{\text{PU}}_{\mathbf{N}}\begin{bmatrix} c\gamma_3 & s\gamma_3 s\gamma_4 & s\gamma_3 c\gamma_4 \\ 0 & c\gamma_4 & -s\gamma_4 \\ -s\gamma_3 & c\gamma_3 s\gamma_4 & c\gamma_3 c\gamma_4 \end{bmatrix} = {}^{0}_{2}\mathbf{R}^{\text{PU}}_{\mathbf{N}}\,{}^{2}_{1}\mathbf{R}^{\text{PU}}_{\mathbf{S}} \tag{4.26} $$

Again, the '$\mathbf{S}$' subscript denotes the symbolic nature of its associated matrix. The unknown rotation angles γ_3 and γ_4 can be determined geometrically as follows.

Starting with the *y*-axis rotation, γ_3, consider the PU manipulator viewed from the $\hat{x}_2^{\text{PU}}$ - $\hat{z}_2^{\text{PU}}$ plane, as shown in the left and middle images of Figure 4.7. From the geometry illustrated in the figure, the desired angle can be computed using the four-quadrant arctangent function as follows:

$$ \gamma_3 = \operatorname{atan2}\left(z_{n1} - z_{n3}, x_{n3} - x_{n1}\right) \tag{4.27} $$

So, the values for the z_{n1}, z_{n3}, x_{n1}, and x_{n3} variables must be determined. These variables represent a subset of the coordinates of ${}^{2}\vec{n}_1$ and ${}^{2}\vec{n}_3$, which are respectively represented as:

$$ {}^{2}\vec{n}_1 = \begin{bmatrix} x_{n1} & y_{n1} & z_{n1} \end{bmatrix}^{\text{T}} \text{ and } {}^{2}\vec{n}_3 = \begin{bmatrix} x_{n3} & y_{n3} & z_{n3} \end{bmatrix}^{\text{T}} \tag{4.28} $$

Also, the $\{0\}^{\text{PU}}$ frame positions for $\vec{O}_1^{\text{PU}}$ and $\vec{O}_2^{\text{PU}}$ are design parameters assumed to be known, so the former can be expressed in terms of the $\{2\}^{\text{PU}}$ frame as per:

$$ {}^{2}\vec{O}_1^{\text{PU}} = \left({}^{0}_{2}\mathbf{R}^{\text{PU}}_{\mathbf{N}}\right)^{\text{T}}\,{}^{0}\vec{O}_1^{\text{PU}} = {}^{2}_{0}\mathbf{R}^{\text{PU}}_{\mathbf{N}}\,{}^{0}\vec{O}_1^{\text{PU}} = \begin{bmatrix} x_{O1} & y_{O1} & z_{O1} \end{bmatrix}^{\text{T}} \tag{4.29} $$

The position of ${}^{2}\vec{n}_1$ may occur at any intersection between a sphere of radius l_r centered at ${}^{2}\vec{O}_1^{\text{PU}}$ and the line defined by $x = l_o$ and $y = 0$ in the $\{2\}^{\text{PU}}$ coordinate system. Therefore, the two solutions for z_{n1} are:

$$ z_{n1} = z_{O1} \pm \sqrt{l_r^2 - \left(l_o - x_{O1}\right)^2 - y_{O1}^2} \tag{4.30} $$

The addition result in Equation (4.30) is infeasible because it corresponds to a scenario in which the targeted limb segment is inverted and extending upwards instead of

downwards from the associated human joint (e.g., the upper leg extending upwards from the hip joint). This is of course contrary to the intended assembly mode. Next, x_{n1} is given directly by the l_o offset length:

$$x_{n1} = l_o \tag{4.31}$$

As shown in the middle image of Figure 4.7, the possible positions of n_3 are limited to the intersection points between circle of radius $\left(x_{1\to 2} + l_o\right)$ centered at n_1 and a sphere of radius $\sqrt{l_r^2 - \left(x_{1\to 2} + l_o\right)^2}$ centered at O_1^{PU}. These intersection points exist within the $\hat{x}_2^{\mathrm{PU}}$ - $\hat{z}_2^{\mathrm{PU}}$ plane. Therefore, the equations associated with these two geometric constraints are respectively:

$$\left(x_{1\to 2} + l_o\right)^2 = \left(x_{n3} - x_{n1}\right)^2 + \left(z_{n3} - z_{n1}\right)^2 \tag{4.32}$$

$$l_r^2 - \left(x_{1\to 2} + l_o\right)^2 = \left(x_{n3} - x_{O1}\right)^2 + \left(z_{n3} - z_{O1}\right)^2 + y_{O1}^2 \tag{4.33}$$

Upon expanding these equations, isolating for $\left(x_{n3}^2 + z_{n3}^2\right)$ in both, and then combining the results, a linear equation in terms of the unknown x_{n3} and z_{n3} variables is yielded:

$$z_{n3} = \frac{2x_{n3}\left(x_{n1} - x_{O1}\right) + 2\left(x_{1\to 2} + l_o\right)^2 - l_r^2 - x_{n1}^2 - z_{n1}^2 + x_{O1}^2 + y_{O1}^2 + z_{O1}^2}{2\left(z_{O1} - z_{n1}\right)} \tag{4.34}$$

Next, the expression for z_{n3} given in Equation (4.34) is substituted into Equation (4.33) to produce a quadratic equation in terms of x_{n3}. The quadratic roots are given by:

$$x_{n3} = \frac{-B_4 \pm \sqrt{B_4^2 - 4A_4C_4}}{2A_4} \tag{4.35}$$

where the solution containing addition is appropriate for the intended assembly mode (i.e., the universal joint should always remain between the human limb and manipulator's prismatic joint). Moreover, Equations (4.36) provide the equivalent expressions for each of the new variables introduced in Equation (4.35).

$$\begin{gathered} A_4 = \frac{F_4^2}{E_4^2} + 1,\ B_4 = \frac{2D_4F_4}{E_4^2} - \frac{2F_4z_{O1}}{E_4} - 2x_{O1}, \\ C_4 = \frac{D_4^2}{E_4^2} - \frac{2D_4z_{O1}}{E_4} + x_{O1}^2 + y_{O1}^2 + z_{O1}^2 - l_r^2 + \left(x_{1\to 2} + l_o\right)^2, \\ D_4 = 2\left(x_{1\to 2} + l_o\right)^2 - l_r^2 - x_{n1}^2 - z_{n1}^2 + x_{O1}^2 + y_{O1}^2 + z_{O1}^2,\ E_4 = 2\left(z_{O1} - z_{n1}\right), \text{ and} \\ F_4 = 2\left(x_{n1} - x_{O1}\right) \end{gathered} \tag{4.36}$$

The value of z_{n3} is subsequently determined by substituting the solution for x_{n3} into Equation (4.34). Using the results for z_{n1}, z_{n3}, x_{n1}, and x_{n3}, the human joint's Y' rotation can be found via Equation (4.27). Applying this rotation to frame $\{2\}^{\mathrm{PU}}$ yields an intermediate

frame {2'}^{PU}. That is, new $\hat{x}_{2'}^{PU}$ and $\hat{z}_{2'}^{PU}$ axes are obtained from $\hat{x}_{2}^{PU}$ and $\hat{z}_{2}^{PU}$ after the γ_3 *y*-axis rotation.

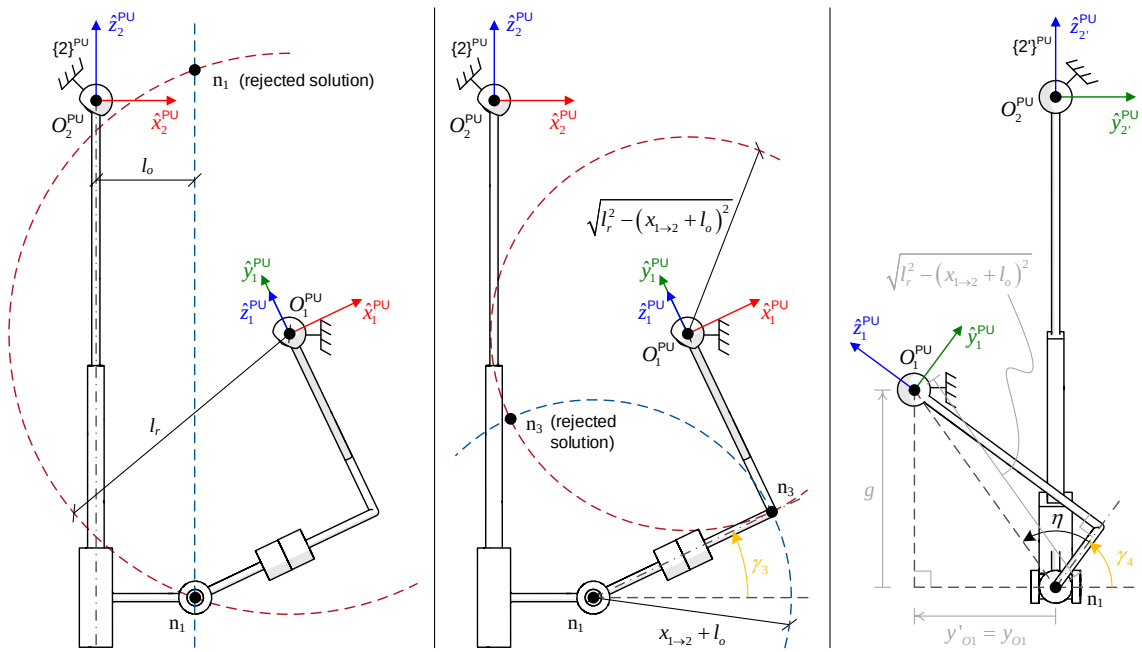

Figure 4.7. Schematic view of the PU from the *x-z* plane of frame {2}^{PU} (left and middle) and the *y-z* plane of frame {2'}^{PU} (right) with n_1, n_3, and forward kinematic solutions indicated

Note: The ${}^{2}\hat{x}_{1}^{PU}$ axis has no component in the $\hat{y}_{2}^{PU}$ direction, as predicted by the ${}^{2}_{1}\mathbf{R}_{S}^{PU}$ rotation matrix in Equation (4.26).

Next, the intrinsic *X''* rotation angle, γ_4, can be realized by observing the manipulator normal to the {2'}^{PU} frame's $\hat{x}_{2'}^{PU}$ axis. As shown in the right-side image of Figure 4.7, the unknown rotation angle can be acquired as:

$$\gamma_4 = \operatorname{atan2}(g, y_{O1}) - \eta \tag{4.37}$$

The η angle is a constant that can be obtained from other design parameters as per:

$$\eta = \operatorname{atan2}\left(\sqrt{l_r^2 - y_{1\to2}^2 - (x_{1\to2} + l_o)^2}, y_{2\to1}\right) \tag{4.38}$$

where the reader may refer to Figure 4.5 for clarification of the length parameters used here. As for the g variable introduced in Equation (4.37), its value can be obtained using the Pythagorean theorem as:

$$g = \pm\sqrt{l_r^2 - y_{O1}^2 - (x_{1\to2} + l_o)^2} \tag{4.39}$$

where the known right-triangle side lengths are illustrated on the right side of Figure 4.7. The positive solution for g is taken as the appropriate assembly mode because the target

human joint is meant to lie in between the active spherical joint and universal joint centers in terms of $\hat{z}_2^{PU}$. The solutions for γ_3 and γ_4 per Equations (4.27) and (4.37) represent the PU's forward kinematic solution when combined with Equation (4.26).

4.3. Comparison of the Candidate Motion-Transfer Manipulators and Selection

Figure 4.8 presents side-by-side schematic illustrations of the RRP and PU motion-transfer manipulators. Although the two designs comprise the same set of joints with differing arrangements, the RRP design has several disadvantages in relation to the PU. First, the RRP design requires special attention regarding the link lengths and shapes associated with the four-bar subsystem, as inappropriate selections may cause collisions and interference with the targeted human limb. Consequently, the RRP also generally requires greater lengths between system joints, thus resulting in a bulkier design. As mentioned in Section 3.5, bulkiness is detrimental to the design of an exoskeleton in terms of weight, cost, user encumberment, and discretion. Lastly, in practice, the parallel nature of the RRP's passive joints cause an amplified degree of backlash when subject to torques or forces in the plane normal to these joint axes. For these reasons, the PU manipulator is selected as the preferable option; therefore, it is incorporated in the complete exoskeleton design to be discussed further in Chapter 5 and Chapter 6.

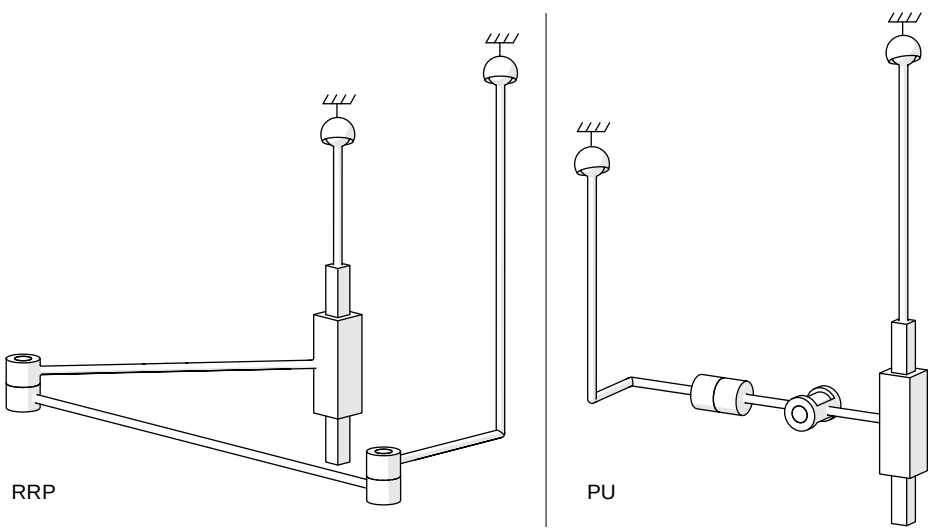

Figure 4.8. Schematic models of the RRP (left) and PU (right) motion-transfer manipulators

Chapter 5.

Kinematic Analysis of the Human Lower Limb and Considerations for the Exoskeleton-Limb Interface

This chapter considers the kinematics of the overall exoskeleton-limb manipulator preceded by the human lower limb as a subsystem of that comprehensive mechanism. The present stages in the overall progression towards a completed exoskeleton design and analysis are highlighted in Figure 5.1. Recall from Chapter 1 that the proposed exoskeleton targets the primary leg joints that contribute to the spatial positioning of the foot relative to the pelvis (i.e., the innominate bone). These are the hip, knee, and ankle. Also note that the primary motions of these joints, along with their normal ranges [99], are illustrated and labelled in Figure 2.7 in Chapter 2. That figure also provides a visualization of the common body planes (i.e., the sagittal, coronal, and transverse), which help specify anatomical directions. The discussions in this and the next chapter refer to these human joint-motion definitions extensively. Moreover, the anatomical ranges of motion for each joint define the intended workspace for the kinematic model of the human leg, which is developed and analyzed in isolation from the exoskeleton in Section 5.1. After that, Section 5.2 explains how the developments from Chapter 3 and Chapter 4 combine with those from Section 5.1 to provide a complete kinematic description of the exoskeleton-limb system from a high-level perspective.

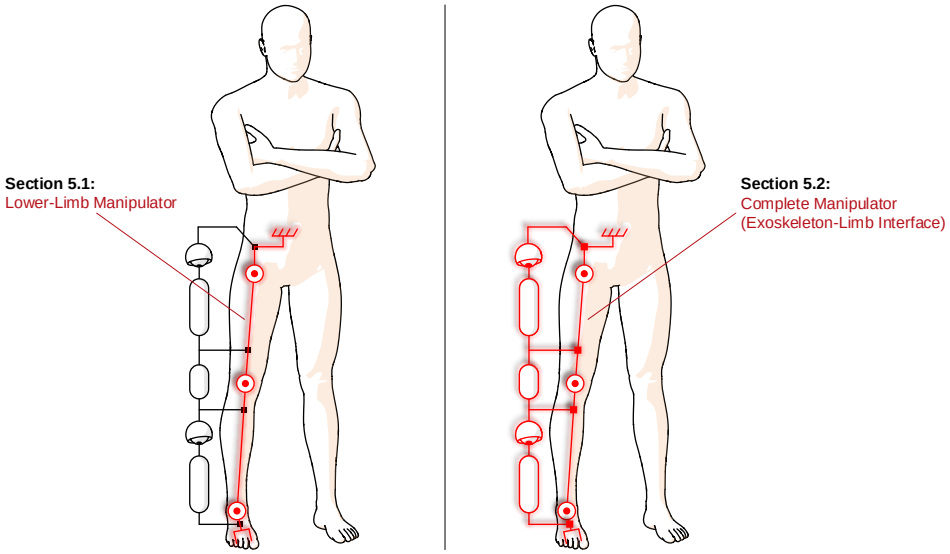

Figure 5.1. Stages of exoskeleton design development covered in Chapter 5

5.1. Kinematic Analyses of the Human Lower Limb

This section begins with the development of a serial manipulator model of the human leg for simulation use, along with the rationale for representing the leg in the selected form. Note that although the kinematic model is based on the movement capabilities of the human lower limb, it largely simplifies the actual leg anatomy. Next, in Subsection 5.1.2, the forward kinematic solution for the lower-limb model is formulated. Subsection 5.1.3 uses Pieper's wrist-partitioned method to develop the inverse kinematics solution for the serial-manipulator limb. Note that the kinematic analyses of the general 6R serial manipulator have already been thoroughly documented in the literature; these analyses are reformulated here for completeness, but do not represent a novel contribution. Subsequently, Subsection 5.1.4 advances on to the development of an unconventional Jacobian matrix. This Jacobian is used in Subsection 5.1.5 to identify the singular configurations of the lower-limb model, which are in turn compared to the anatomical workspace of the human leg as defined by the joint ranges-of-motion shown in Figure 2.7.

5.1.1. Kinematic Architecture for Simulations (6R Serial Manipulator)

Anatomical Justification for the Lower-Limb Kinematic Model

The human hip is a synovial ball-and-socket joint [99] and, as such, its articulations can be described by the 3-DOF spherical rotations shown in Figure 2.7. The magnitude of joint play (i.e., the amount of allowable translational motion at the joint) is small for the hip [177], so all translational DOFs are considered negligible. Thus, the human hip is modeled as a 'spherical wrist': a series of three revolute joints for which adjacent joint axes have perpendicular alignment and all joint axes intersect at a common center-of-rotation (COR) point.

The dominant motions that occur at the human knee joint are sagittal-plane flexions and extensions [99], as shown in Figure 2.7. However, the knee is considered a modified hinge joint, in part because its rotational axis translates during joint motion [99]. Consequently, the joint is often designed as a four-bar linkage mechanism in prosthetic devices; the other predominant approach is a single-axis knee design [178]. The other main reason for classifying the knee as a modified hinge joint is that it plays a part in

axial rotations of the lower leg, or shank. Though, because these rotations occur along the full length of the shank, they are typically either attributed to the knee joint as medial/lateral rotations or to the ankle joint as adduction/abduction rotations. In this thesis, the latter attribution is adopted, so the knee joint is modeled as a single-DOF joint. Moreover, the knee is represented here as a single-axis revolute joint instead of a four-bar linkage mechanism to support the approach of modeling the leg as a serial manipulator and facilitate the kinematic analysis and simulation/verification processes.

The human ankle joint complex comprises two sub-joints: the talocrural joint and the subtalar joint [179]. Collectively, the ankle permits three rotations of the foot with respect to the shank; these are plantarflexion/dorsiflexion in the sagittal plane, pronation/supination in the coronal plane, and adduction/abduction in the transverse plane, as illustrated in Figure 2.7. Note that the adduction/abduction movement also involves rotation of the tibia and fibula along the shank [180], as mentioned earlier. Neither of the sub-joint axes remain fixed during ankle movement [181], but the axis movement has no practical significance, particularly regarding plantarflexion/dorsiflexion rotations [99]. Therefore, the translational aspects of motion between the foot and shank will be neglected. Another concern is the total degrees-of-freedom associated with the leg's kinematic model, and the impact that has on its kinematic analysis. Since the manipulator operates in 3D space, for a given end-effector (i.e., foot) position and orientation within its dextrous workspace, the manipulator would have an infinite number of inverse kinematics solutions if it contains more than 6 DOFs. Although a 'best' solution could be identified via an optimization procedure, it is somewhat unnecessary to include the ankle's transverse plane motion capability due to the limited nature of these rotations. Ankle adduction/abduction can only occur when the knee is flexed; this DOF is also generally unused for movements associated with basic mobility, such as walking [182], and during proprioceptive training and ankle rehabilitation exercises [183]. Therefore, the ankle joint is modeled here as two revolute joints with intersecting axes, similar to the 2-DOF monocentric model employed by Scott and Winter [184].

Proposed 6R Kinematic Model for the Human Lower Limb

With the selections made for the kinematic representations of each of the considered leg joints, Figure 5.2 presents schematic illustrations of the complete human lower-limb model. These illustrations focus on the right leg. At the start of the serial

chain, a point on the pelvis (i.e., the innominate bone) is selected as the inertial reference frame origin. Note that the lower limb's reference frame represents the global reference frame for the entire exoskeleton-human system. A base link then connects the pelvis to the hip joint, which is depicted by joints $J_1^{LEG} - J_3^{LEG}$ in Figure 5.2. The base link length provides the medial/lateral offset between the global frame origin and hip joint, while the intermediate links between joints J_1^{LEG}, J_2^{LEG}, and J_3^{LEG} respectively specify the hip's superior/inferior offset from the global origin and the knee's medial/lateral offset from the hip. A fourth link connects the hip joint to the knee joint, joint J_4^{LEG}, and a fifth link connects the knee to the first of the ankle joints. The fourth link parameterizes the upper-leg length, while the fifth link specifies both the inferior and anterior/posterior offsets between the knee and ankle joints. The sixth link, between the two ankle joints (i.e., J_5^{LEG} and J_6^{LEG}), provides the medial/lateral offset between the knee and ankle. Finally, an end-effector link represents the foot and positions the manipulator's end-effector at some point on the tip of the foot. Since the model manipulator comprises six serially-connected revolute joints, an appropriate structural name is 6R. Note that an underline, which identifies active joints, is excluded from this structural name to highlight the fact that the model represents biological joints as opposed to man-made actuators; this is consistent with the naming convention from Chapter 4 (see Subsection 4.1.1 for an explanation).

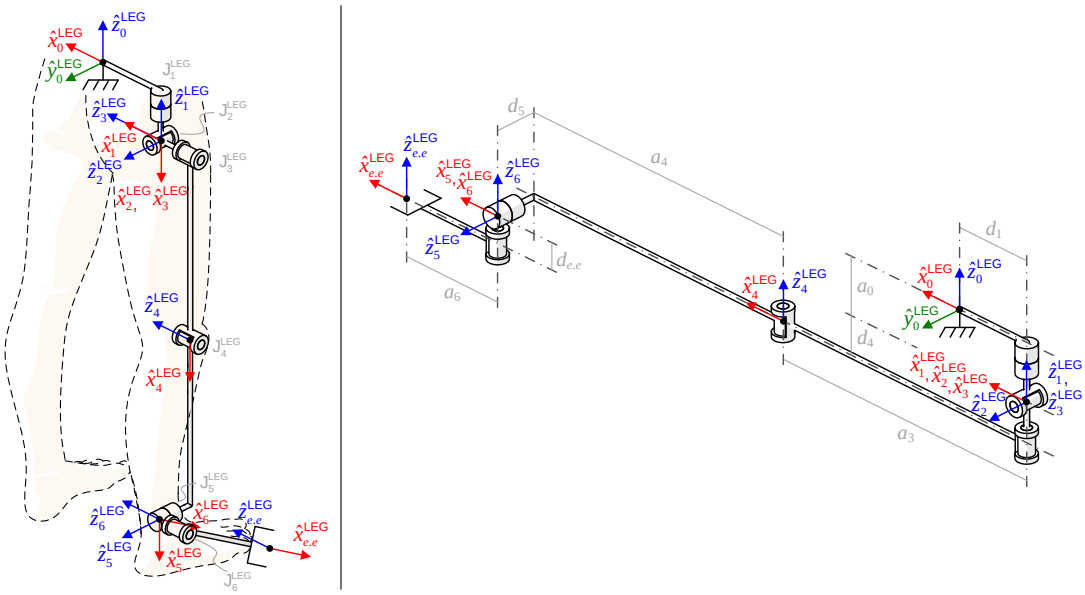

Figure 5.2. Schematic illustration of the 6R human lower-limb model in a neutral posture with frame axis and joint labels (left) and in its zero-displacement configuration with link length and offset labels (right)

Two common conventions exist for the attachment of frames to the links of a serial manipulator: one proposed by Denavit and Hartenberg (DH) and the other by Craig; these conventions establish a mathematical representation for the physical manipulator and facilitate its kinematic analyses. As they are shown in Figure 5.2, the link frame attachments for the leg model are made in accordance with the Craig convention [185]. This convention employs the DH scheme for parameterizing the link dimensions and relative orientations between frames, as given in Table 5.1 for the proposed leg model. The DH parameters specify: the common normal distance between adjacent joint axes (link length); the angle between the adjacent joint-axis projections onto a plane perpendicular to the common normal (link twist); the distance along a joint axis that separates adjacent common-normal lines (link offset); and the angle of rotation between adjacent common-normal lines about a joint axis (joint angle). Thus, the link length and offset parameters provide the constant distances between the hip, knee, and ankle joints, along with the length of the foot and position of the global origin point on the pelvis; these dimensions are labelled on the right side of Figure 5.2. Note that the corresponding anatomical measurements vary from person to person.

Table 5.1. DH parameters of the 6R kinematic model for the human right leg

Link, i–1	Link Twist, α_{i-1}	Link Length, a_{i-1}	Link Offset, d_i	Joint Angle, θ_i	Link, i
0	0°	$-a_0$	$-d_1$	θ_1	1
1	–90°	0	0	θ_2	2
2	90°	0	0	θ_3	3
3	0°	a_3	$-d_4$	θ_4	4
4	–90°	a_4	d_5	θ_5	5
5	90°	0	0	θ_6	6
6	0°	a_6	$-d_{e.e}$	0	$e.e$

Note: Here, each a_{i-1} and d_i is assumedly a positive value. Thus, to create a left-leg model, a_0, d_4, and $d_{e.e}$ values should be negated while maintaining the orientations of each link frame. Also, $e.e$ is an abbreviation for end-effector.

Since all joints in the leg model are revolute, the joint angles θ_i are treated as the variables that define the manipulator's posture. Given the Craig convention's definition for joint angle, there exists a zero-displacement configuration of the serial manipulator for which all joint angles are equal to zero. This posture is shown on the right side of Figure 5.2. Also, note that in the figure and kinematic analysis to follow, a 'LEG' superscript is used to distinguish frames and frame axes associated with the leg model from those of the different manipulators explored in this thesis. However, unlike previous chapters, the superscript notation is dropped from the joint variables in this chapter to declutter the presentation of kinematic formulations.

5.1.2. Forward Kinematic Analysis

Recall that the forward kinematics problem is that in which the joint variable values are known and the end-effector task coordinates must be determined (i.e., the 3D position and orientation of the end-effector). For serial manipulators, the forward kinematics solution is trivial. Homogeneous transforms are systematically developed to relate one link frame to the next, as per the chosen frame-attachment convention, and then the transforms are multiplied in ascending-order succession. Note that homogeneous transforms are constructions that combine the rotation matrix and translation vector that fully define the relative position and orientation between two right-handed coordinate frames in 3D space. The homogeneous transform relating link i–1 to link i per the Craig convention for link-frame attachments is given by [185]:

$$ {}^{i-1}_{\ \ i}\mathbf{T}^{\text{LEG}}\left(\alpha_{i-1}, a_{i-1}, d_i, \theta_i\right) = \begin{bmatrix} c\theta_i & -s\theta_i & 0 & a_{i-1} \\ s\theta_i c\alpha_{i-1} & c\theta_i c\alpha_{i-1} & -s\alpha_{i-1} & -d_i s\alpha_{i-1} \\ s\theta_i s\alpha_{i-1} & c\theta_i s\alpha_{i-1} & c\alpha_{i-1} & d_i c\alpha_{i-1} \\ 0 & 0 & 0 & 1 \end{bmatrix} \tag{5.1} $$

where the frame attachments and DH parameters associated with the kinematic model for the lower limb are detailed in Subsection 5.1.1. Therefore, the set of transforms between each consecutive frame in the right-leg manipulator is:

$$ \begin{gathered} {}^{0}_{1}\mathbf{T}^{\text{LEG}} = \begin{bmatrix} c\theta_1 & -s\theta_1 & 0 & -a_0 \\ s\theta_1 & c\theta_1 & 0 & 0 \\ 0 & 0 & 1 & -d_1 \\ 0 & 0 & 0 & 1 \end{bmatrix}, \ {}^{1}_{2}\mathbf{T}^{\text{LEG}} = \begin{bmatrix} c\theta_2 & -s\theta_2 & 0 & 0 \\ 0 & 0 & 1 & 0 \\ -s\theta_2 & -c\theta_2 & 0 & 0 \\ 0 & 0 & 0 & 1 \end{bmatrix}, \\ {}^{2}_{3}\mathbf{T}^{\text{LEG}} = \begin{bmatrix} c\theta_3 & -s\theta_3 & 0 & 0 \\ 0 & 0 & -1 & 0 \\ s\theta_3 & c\theta_3 & 0 & 0 \\ 0 & 0 & 0 & 1 \end{bmatrix}, \ {}^{3}_{4}\mathbf{T}^{\text{LEG}} = \begin{bmatrix} c\theta_4 & -s\theta_4 & 0 & a_3 \\ s\theta_4 & c\theta_4 & 0 & 0 \\ 0 & 0 & 1 & -d_4 \\ 0 & 0 & 0 & 1 \end{bmatrix}, \\ {}^{4}_{5}\mathbf{T}^{\text{LEG}} = \begin{bmatrix} c\theta_5 & -s\theta_5 & 0 & a_4 \\ 0 & 0 & 1 & d_5 \\ -s\theta_5 & -c\theta_5 & 0 & 0 \\ 0 & 0 & 0 & 1 \end{bmatrix}, \ {}^{5}_{6}\mathbf{T}^{\text{LEG}} = \begin{bmatrix} c\theta_6 & -s\theta_6 & 0 & 0 \\ 0 & 0 & -1 & 0 \\ s\theta_6 & c\theta_6 & 0 & 0 \\ 0 & 0 & 0 & 1 \end{bmatrix}, \\ {}^{6}_{e.e}\mathbf{T}^{\text{LEG}} = \begin{bmatrix} 1 & 0 & 0 & a_6 \\ 0 & 1 & 0 & 0 \\ 0 & 0 & 1 & -d_{e.e} \\ 0 & 0 & 0 & 1 \end{bmatrix} \end{gathered} \tag{5.2} $$

Recall that $c(\ )$ is an abbreviation for the cosine function and $s(\ )$ represents the sine function. Note that each element of the ${}^{6}_{e.e}\mathbf{T}^{\text{LEG}}$ is a constant, because only the joint angles, θ_i, are variables.

Now, as described above, successive multiplication of the transforms in Equations (5.2) yields the forward kinematics solution:

$$ {}^{0}_{e.e}\mathbf{T}^{\text{LEG}} = {}^{0}_{1}\mathbf{T}^{\text{LEG}}\,{}^{1}_{2}\mathbf{T}^{\text{LEG}}\,{}^{2}_{3}\mathbf{T}^{\text{LEG}}\,{}^{3}_{4}\mathbf{T}^{\text{LEG}}\,{}^{4}_{5}\mathbf{T}^{\text{LEG}}\,{}^{5}_{6}\mathbf{T}^{\text{LEG}}\,{}^{6}_{e.e}\mathbf{T}^{\text{LEG}} = \begin{bmatrix} {}^{0}\hat{x}_{e.e} & {}^{0}\hat{y}_{e.e} & {}^{0}\hat{z}_{e.e} & {}^{0}\vec{O}_{e.e} \\ 0 & 0 & 0 & 1 \end{bmatrix} \quad (5.3) $$

This equation represents the forward kinematics solution because it provides the human right leg's end-effector orientation (i.e., $[\ {}^{0}\hat{x}_{e.e} \quad {}^{0}\hat{y}_{e.e} \quad {}^{0}\hat{z}_{e.e}\ ] = {}^{0}_{e.e}\mathbf{R}^{\text{LEG}}$) and position (i.e., ${}^{0}\vec{O}_{e.e}$) with respect to the global reference frame as a function of the joint variables. Note that the forward kinematic solution for the human left lower limb is carried out in same manner with negated terms at each instance of a_0, d_4, and $d_{e.e}$.

In terms of simulating the lower limb's motion trajectories using MATLAB or some other computer program that requires complete task-coordinate specification, it is necessary to know the homogeneous transforms relating the inertial reference frame, $\{0\}^{\text{LEG}}$, to the frames attached to the thigh, shank, and foot links. The thigh corresponds to frame $\{3\}^{\text{LEG}}$, the shank to frame $\{4\}^{\text{LEG}}$, and the foot to frame $\{6\}^{\text{LEG}}$. Therefore, the following transforms can be used to specify their respective positions and orientations during simulations:

$$ {}^{0}_{3}\mathbf{T}^{\text{LEG}} = {}^{0}_{1}\mathbf{T}^{\text{LEG}}\,{}^{1}_{2}\mathbf{T}^{\text{LEG}}\,{}^{2}_{3}\mathbf{T}^{\text{LEG}} = \begin{bmatrix} c\theta_1 c\theta_2 c\theta_3 - s\theta_1 s\theta_3 & -c\theta_1 c\theta_2 s\theta_3 - s\theta_1 c\theta_3 & c\theta_1 s\theta_2 & -a_0 \\ s\theta_1 c\theta_2 c\theta_3 + c\theta_1 s\theta_3 & -s\theta_1 c\theta_2 s\theta_3 + c\theta_1 c\theta_3 & s\theta_1 s\theta_2 & 0 \\ -s\theta_2 c\theta_3 & s\theta_2 s\theta_3 & c\theta_2 & -d_1 \\ 0 & 0 & 0 & 1 \end{bmatrix}, $$

$$ {}^{0}_{4}\mathbf{T}^{\text{LEG}} = {}^{0}_{3}\mathbf{T}^{\text{LEG}}\,{}^{3}_{4}\mathbf{T}^{\text{LEG}} = {}^{0}_{3}\mathbf{T}^{\text{LEG}} \begin{bmatrix} c\theta_4 & -s\theta_4 & 0 & a_3 \\ s\theta_4 & c\theta_4 & 0 & 0 \\ 0 & 0 & 1 & -d_4 \\ 0 & 0 & 0 & 1 \end{bmatrix}, \text{ and} \quad (5.4) $$

$$ {}^{0}_{6}\mathbf{T}^{\text{LEG}} = {}^{0}_{3}\mathbf{T}^{\text{LEG}}\,{}^{3}_{4}\mathbf{T}^{\text{LEG}}\,{}^{4}_{5}\mathbf{T}^{\text{LEG}}\,{}^{5}_{6}\mathbf{T}^{\text{LEG}} = {}^{0}_{3}\mathbf{T}^{\text{LEG}} \begin{bmatrix} c\theta_4 c\theta_5 c\theta_6 - s\theta_4 s\theta_6 & -c\theta_4 c\theta_5 s\theta_6 - s\theta_4 c\theta_6 & c\theta_4 s\theta_5 & a_4 c\theta_4 - d_5 s\theta_4 + a_3 \\ s\theta_4 c\theta_5 c\theta_6 + c\theta_4 s\theta_6 & -s\theta_4 c\theta_5 s\theta_6 + c\theta_4 c\theta_6 & s\theta_4 s\theta_5 & a_4 s\theta_4 - d_5 c\theta_4 \\ -s\theta_5 c\theta_6 & s\theta_5 s\theta_6 & c\theta_5 & -d_4 \\ 0 & 0 & 0 & 1 \end{bmatrix} $$

Note that the latter two transforms of Equations (5.4) are left in the form of a multiplication to reduce complexity for the reader. Also note that in practice, these forward kinematic transform multiplications would be systematically carried out in a computer algorithm.

5.1.3. Inverse Kinematic Analysis

The inverse kinematics problem is that in which the end-effector task coordinates (i.e., its spatial position and orientation) are known and the joint variable values must be determined. As such, a numerical homogeneous transform is assumedly established with end-effector position and orientation information:

$$ {}^{0}_{e.e}\mathbf{T}^{\text{LEG}}_{\mathbf{N}} = \begin{bmatrix} \hat{n} & \hat{o} & \hat{a} & \vec{\mathrm{p}} \\ 0 & 0 & 0 & 1 \end{bmatrix} = \begin{bmatrix} n_x & o_x & a_x & p_x \\ n_y & o_y & a_y & p_y \\ n_z & o_z & a_z & p_z \\ 0 & 0 & 0 & 1 \end{bmatrix} \tag{5.5} $$

where the unit vectors represent the normal ($\hat{n}$), orientation ($\hat{o}$), and approach ($\hat{a}$) directions of the end-effector, and $\vec{\mathrm{p}}$ denotes its position. Equating the numerical matrix of Equation (5.5) with the symbolic solution for the forward kinematics yields:

$$ \begin{bmatrix} \hat{n} & \hat{o} & \hat{a} & \vec{\mathrm{p}} \\ 0 & 0 & 0 & 1 \end{bmatrix} = {}^{0}_{e.e}\mathbf{T}^{\text{LEG}}_{\mathbf{N}} = {}^{0}_{e.e}\mathbf{T}^{\text{LEG}}_{\mathbf{S}} = \\ {}^{0}_{1}\mathbf{T}^{\text{LEG}}(\theta_1)\,{}^{1}_{2}\mathbf{T}^{\text{LEG}}(\theta_2)\,{}^{2}_{3}\mathbf{T}^{\text{LEG}}(\theta_3)\,{}^{3}_{4}\mathbf{T}^{\text{LEG}}(\theta_4)\,{}^{4}_{5}\mathbf{T}^{\text{LEG}}(\theta_5)\,{}^{5}_{6}\mathbf{T}^{\text{LEG}}(\theta_6)\,{}^{6}_{e.e}\mathbf{T}^{\text{LEG}} \tag{5.6} $$

where the final ${}^{6}_{e.e}\mathbf{T}^{\text{LEG}}$ is a matrix of known constants.

When considered in forward order (i.e., from link frame $\{0\}^{\text{LEG}}$ to frame $\{e.e\}^{\text{LEG}}$), the serial manipulator model of the human lower limb is not spherically-wristed because the link between frames $\{4\}^{\text{LEG}}$ and $\{5\}^{\text{LEG}}$ has an associated length and offset. One option to approach this inverse kinematics problem is to use the generalized solution developed by Raghavan and Roth [186], which employs dialytic elimination. Alternatively, if considered in reverse-order, the human leg manipulator can be evaluated using Pieper's wrist-partitioned method, as described in [187] and [188]. In this case, the 3-DOF hip joint is considered as the 'wrist', and the links and joints spanning from the foot to upper-leg comprise the 'main-arm' of the manipulator. Because it is simpler and less computationally-expensive, the latter approach is employed for developing the lower-limb manipulator's inverse kinematics solution.

However, some preliminary operations must be performed before the wrist-partition method can be applied to reverse-order lower-limb manipulator. If the manipulator is considered as originating at link frame $\{e.e\}^{\text{LEG}}$ and proceeding to frame $\{0\}^{\text{LEG}}$, then the analogous form of Equation (5.6) is given by:

$$\left({}^{0}_{e.e}\mathbf{T}^{\text{LEG}}_{\mathbf{N}}\right)^{-1} = {}^{e.e}_{0}\mathbf{T}^{\text{LEG}}_{\mathbf{N}} = {}^{e.e}_{6}\mathbf{T}^{\text{LEG}}\,{}^{6}_{5}\mathbf{T}^{\text{LEG}}\left(\theta_6\right){}^{5}_{4}\mathbf{T}^{\text{LEG}}\left(\theta_5\right){}^{4}_{3}\mathbf{T}^{\text{LEG}}\left(\theta_4\right){}^{3}_{2}\mathbf{T}^{\text{LEG}}\left(\theta_3\right){}^{2}_{1}\mathbf{T}^{\text{LEG}}\left(\theta_2\right){}^{1}_{0}\mathbf{T}^{\text{LEG}}\left(\theta_1\right) \tag{5.7}$$

where the inverse of a homogeneous transform is given by:

$${}^{i}_{j}\mathbf{T}^{-1} = \begin{bmatrix} {}^{i}_{j}\mathbf{R}^{\mathrm{T}} & -{}^{i}_{j}\mathbf{R}^{\mathrm{T}}\,{}^{i}\vec{O}_j \\ \vec{0}_{1\times3} & 1 \end{bmatrix} = {}^{j}_{i}\mathbf{T} \text{ where } {}^{j}_{i}\mathbf{T} = \begin{bmatrix} {}^{j}_{i}\mathbf{R} & {}^{j}\vec{O}_i \\ \vec{0}_{1\times3} & 1 \end{bmatrix} \tag{5.8}$$

Now, for a true spherically-wristed manipulator, the final transform is a matrix of known constants that specifies the end-effector's fixed position and orientation relative to the final wrist joint; it does not contain any joint variable. Correspondingly, the second-to-last transform does not include any translation component (i.e., $\vec{\mathrm{p}} = \vec{0}_{3\times1}$) for a traditional spherically-wristed manipulator. Contrarily, ${}^{1}_{0}\mathbf{T}^{\text{LEG}}\left(\theta_1\right)$ contains both the θ_1 joint variable and the translation between the 'wrist' center, O_1^{LEG}, and global origin, O_0^{LEG}. The latter is analogous to the end-effector position when the manipulator is considered reverse-order. Therefore, to yield the symbolic 'wrist' center position from Equation (5.7), ${}^{1}_{0}\mathbf{T}^{\text{LEG}}\left(\theta_1\right)$ should be moved to the left-hand side as follows:

$${}^{e.e}_{0}\mathbf{T}^{\text{LEG}}_{\mathbf{N}}\left({}^{1}_{0}\mathbf{T}^{\text{LEG}}\left(\theta_1\right)\right)^{-1} = {}^{e.e}_{6}\mathbf{T}^{\text{LEG}}\,{}^{6}_{5}\mathbf{T}^{\text{LEG}}\left(\theta_6\right){}^{5}_{4}\mathbf{T}^{\text{LEG}}\left(\theta_5\right){}^{4}_{3}\mathbf{T}^{\text{LEG}}\left(\theta_4\right){}^{3}_{2}\mathbf{T}^{\text{LEG}}\left(\theta_3\right){}^{2}_{1}\mathbf{T}^{\text{LEG}}\left(\theta_2\right) \tag{5.9}$$

However, in doing so, the θ_1 joint variable becomes grouped with the known numerical values, which precludes the continuation of the wrist partitioned method.

To remove this unwanted grouping, the ${}^{1}_{0}\mathbf{T}^{\text{LEG}}$ transform is instead separated into purely translational and rotational components:

$${}^{0}_{1}\mathbf{T}^{\text{LEG}} = {}^{0}_{0*}\mathbf{T}^{\text{LEG}}\,{}^{0*}_{1}\mathbf{T}^{\text{LEG}} = \begin{bmatrix} 1 & 0 & 0 & -a_0 \\ 0 & 1 & 0 & 0 \\ 0 & 0 & 1 & -d_1 \\ 0 & 0 & 0 & 1 \end{bmatrix}\begin{bmatrix} c\theta_1 & -s\theta_1 & 0 & 0 \\ s\theta_1 & c\theta_1 & 0 & 0 \\ 0 & 0 & 1 & 0 \\ 0 & 0 & 0 & 1 \end{bmatrix} = \begin{bmatrix} c\theta_1 & -s\theta_1 & 0 & -a_0 \\ s\theta_1 & c\theta_1 & 0 & 0 \\ 0 & 0 & 1 & -d_1 \\ 0 & 0 & 0 & 1 \end{bmatrix} \tag{5.10}$$

Substituting Equation (5.10) into (5.6), and then pre-multiplying both sides by $\left({}^{0}_{0*}\mathbf{T}^{\text{LEG}}\right)^{-1}$ and post-multiplying both sides by $\left({}^{6}_{e.e}\mathbf{T}^{\text{LEG}}\right)^{-1}$ yields:

$$\begin{bmatrix} 1 & 0 & 0 & a_0 \\ 0 & 1 & 0 & 0 \\ 0 & 0 & 1 & d_1 \\ 0 & 0 & 0 & 1 \end{bmatrix} \begin{bmatrix} \hat{n} & \hat{o} & \hat{a} & \vec{p} \\ 0 & 0 & 0 & 1 \end{bmatrix} \begin{bmatrix} 1 & 0 & 0 & -a_6 \\ 0 & 1 & 0 & 0 \\ 0 & 0 & 1 & d_{e.e} \\ 0 & 0 & 0 & 1 \end{bmatrix} = {}^{0*}_{1}\mathbf{T}^{\text{LEG}}\,{}^{1}_{2}\mathbf{T}^{\text{LEG}}\,{}^{2}_{3}\mathbf{T}^{\text{LEG}}\,{}^{3}_{4}\mathbf{T}^{\text{LEG}}\,{}^{4}_{5}\mathbf{T}^{\text{LEG}}\,{}^{5}_{6}\mathbf{T}^{\text{LEG}} \tag{5.11}$$

$$\therefore,\ {}^{0*}_{6}\mathbf{T}^{\text{LEG}}\left(\theta_1,\theta_2,\theta_3,\theta_4,\theta_5,\theta_6\right) =$$

$$\begin{bmatrix} n_x & o_x & a_x & p_x + a_0 - n_x a_6 + a_x d_{e.e} \\ n_y & o_y & a_y & p_y - n_y a_6 + a_y d_{e.e} \\ n_z & o_z & a_z & p_z + d_1 - n_z a_6 + a_z d_{e.e} \\ 0 & 0 & 0 & 1 \end{bmatrix} = \begin{bmatrix} n_x & o_x & a_x & p_x' \\ n_y & o_y & a_y & p_y' \\ n_z & o_z & a_z & p_z' \\ 0 & 0 & 0 & 1 \end{bmatrix} \tag{5.12}$$

where all matrix elements on the left-hand side of Equation (5.11) are known constants for the inverse kinematics problem. Equation (5.12) can then be expressed in reverse order by inverting the transforms on both sides of the equation:

$${}^{6L}_{0*}\mathbf{T}^{\text{LEG}}\left(\theta_{1L},\theta_{2L},\theta_{3L},\theta_{4L},\theta_{5L},\theta_{6L}\right) =$$

$$\begin{bmatrix} n_x & o_x & a_x & p_x' \\ n_y & o_y & a_y & p_y' \\ n_z & o_z & a_z & p_z' \\ 0 & 0 & 0 & 1 \end{bmatrix}^{-1} = \begin{bmatrix} n_x & n_y & n_z & -n_x p_x' - n_y p_y' - n_z p_z' \\ o_x & o_y & o_z & -o_x p_x' - o_y p_y' - o_z p_z' \\ a_x & a_y & a_z & -a_x p_x' - a_y p_y' - a_z p_z' \\ 0 & 0 & 0 & 1 \end{bmatrix} = \begin{bmatrix} n_x & n_y & n_z & p_x'' \\ o_x & o_y & o_z & p_y'' \\ a_x & a_y & a_z & p_z'' \\ 0 & 0 & 0 & 1 \end{bmatrix} \tag{5.13}$$

$$\therefore,\ {}^{6}_{5}\mathbf{T}^{\text{LEG}}\left(\theta_6\right){}^{5}_{4}\mathbf{T}^{\text{LEG}}\left(\theta_5\right){}^{4}_{3}\mathbf{T}^{\text{LEG}}\left(\theta_4\right){}^{3}_{2}\mathbf{T}^{\text{LEG}}\left(\theta_3\right){}^{2}_{1}\mathbf{T}^{\text{LEG}}\left(\theta_2\right){}^{1}_{0*}\mathbf{T}^{\text{LEG}}\left(\theta_1\right) =$$

$$\begin{bmatrix} n_x & n_y & n_z & p_x'' \\ o_x & o_y & o_z & p_y'' \\ a_x & a_y & a_z & p_z'' \\ 0 & 0 & 0 & 1 \end{bmatrix} \tag{5.14}$$

This completes the preliminary operations for the inverse kinematics, and the wrist-partitioned method may now proceed.

The position of the 'wrist' with respect to frame $\{6\}^{\text{LEG}}$ (i.e., as given by $\vec{p}'' = \begin{bmatrix} p_x'' & p_y'' & p_z'' \end{bmatrix}^{\text{T}}$) depends only on joint variables θ_6, θ_5, and θ_4. Pre-multiplying both sides of Equation (5.14) by ${}^{5}_{6}\mathbf{T}^{\text{LEG}}$ produces the following position vector in the upper three rows of the result's fourth column:

$$\begin{bmatrix} p_x''c\theta_6 - p_y''s\theta_6 \\ -p_z'' \\ p_x''s\theta_6 + p_y''c\theta_6 \end{bmatrix} = \begin{bmatrix} -a_3c\theta_4c\theta_5 - d_4s\theta_5 - a_4c\theta_5 \\ a_3c\theta_4s\theta_5 - d_4c\theta_5 + a_4s\theta_5 \\ a_3s\theta_4 - d_5 \end{bmatrix} \tag{5.15}$$

By squaring and adding all elements on both sides of Equation (5.15), the following equation is obtained:

$$\left(2a_3a_4\right)c\theta_4+\left(-2a_3d_5\right)s\theta_4=p_x''^2+p_y''^2+p_z''^2-a_3^2-d_4^2-a_4^2-d_5^2 \tag{5.16}$$

Equation (5.16) produces two solutions for θ_4 after applying tangent-of-the-half-angle substitutions:

$$\begin{gathered}\theta_4=\operatorname{atan2}\left(B_5,A_5\right)\pm\operatorname{atan2}\left(\sqrt{A_5^2+B_5^2-C_5^2},C_5\right),\text{ where } A_5=2a_3a_4,\\ B_5=-2a_3d_5,\text{ and } C_5=p_x''^2+p_y''^2+p_z''^2-a_3^2-d_4^2-a_4^2-d_5^2\end{gathered} \tag{5.17}$$

Two solutions for θ_6 can be subsequently determined from the bottom elements from the vectors of Equation (5.15) using the same method of tangent-of-the-half-angle substitutions:

$$\theta_6=\operatorname{atan2}\left(p_x'',p_y''\right)\pm\operatorname{atan2}\left(\sqrt{p_y''^2+p_x''^2-\left(a_3s\theta_4-d_5\right)^2},a_3s\theta_4-d_5\right) \tag{5.18}$$

Next, the top and middle elements of the vectors in Equation (5.15) provide two equations in terms of θ_5 that can be solved as:

$$\begin{gathered}\theta_5=\operatorname{atan2}\left(A_6,B_6\right)\text{ where } A_6=d_4\left(p_y''s\theta_6-p_x''c\theta_6\right)-p_z''\left(a_3c\theta_4+a_4\right)\text{ and}\\ B_6=d_4p_z''+\left(a_3c\theta_4+a_4\right)\left(p_y''s\theta_6-p_x''c\theta_6\right)\end{gathered} \tag{5.19}$$

Thus, there is one solution for θ_5 associated with each combination of θ_4 and θ_6, for a total of four solutions in the 'main-arm' kinematics.

With the solutions for θ_6, θ_5, and θ_4, the solution set for ${}^{3}_{6}\mathbf{R}^{\text{LEG}}_{\mathbf{N}}$ can be determined through joint-variable substitution into its constituent forward kinematic transforms. Moreover, a numerical matrix corresponding to the only remaining unknown joint variables (i.e., θ_3, θ_2, and θ_1), ${}^{3}_{0*}\mathbf{R}^{\text{LEG}}_{\mathbf{N}}$, can be produced by pre-multiplying the numerically-known ${}^{6}_{0*}\mathbf{R}^{\text{LEG}}_{\mathbf{N}}$ matrix from Equations (5.13) and (5.14) by ${}^{3}_{6}\mathbf{R}^{\text{LEG}}_{\mathbf{N}}$:

$$\begin{gathered}{}^{3}_{0*}\mathbf{R}^{\text{LEG}}_{\mathbf{N}}={}^{3}_{6}\mathbf{R}^{\text{LEG}}_{\mathbf{N}}\,{}^{6}_{0*}\mathbf{R}^{\text{LEG}}_{\mathbf{N}}=\\ \begin{bmatrix}c\theta_4c\theta_5c\theta_6-s\theta_4s\theta_6 & -c\theta_4c\theta_5s\theta_6-s\theta_4c\theta_6 & c\theta_4s\theta_5\\ s\theta_4c\theta_5c\theta_6+c\theta_4s\theta_6 & -s\theta_4c\theta_5s\theta_6+c\theta_4c\theta_6 & s\theta_4s\theta_5\\ -s\theta_5c\theta_6 & s\theta_5s\theta_6 & c\theta_5\end{bmatrix}\begin{bmatrix}n_x & n_y & n_z\\ o_x & o_y & o_z\\ a_x & a_y & a_z\end{bmatrix}=\begin{bmatrix}r_{11} & r_{12} & r_{13}\\ r_{21} & r_{22} & r_{23}\\ r_{31} & r_{32} & r_{33}\end{bmatrix}=\\ {}^{3}_{2}\mathbf{R}^{\text{LEG}}\left(\theta_3\right){}^{2}_{1}\mathbf{R}^{\text{LEG}}\left(\theta_2\right){}^{1}_{0*}\mathbf{R}^{\text{LEG}}\left(\theta_1\right)\end{gathered} \tag{5.20}$$

where r_{ij} represent known values for i, j = 1, 2, 3. Post-multiplying both sides of Equation (5.20) by ${}^{0*}_{1}\mathbf{R}^{\text{LEG}}$ yields:

$$\begin{bmatrix}r_{11}c\theta_1+r_{12}s\theta_1 & -r_{11}s\theta_1+r_{12}c\theta_1 & r_{13}\\ r_{21}c\theta_1+r_{22}s\theta_1 & -r_{21}s\theta_1+r_{22}c\theta_1 & r_{23}\\ r_{31}c\theta_1+r_{32}s\theta_1 & -r_{31}s\theta_1+r_{32}c\theta_1 & r_{33}\end{bmatrix}=\begin{bmatrix}c\theta_2c\theta_3 & s\theta_3 & -s\theta_2c\theta_3\\ -c\theta_2s\theta_3 & c\theta_3 & s\theta_2s\theta_3\\ s\theta_2 & 0 & c\theta_2\end{bmatrix} \tag{5.21}$$

Isolating the third-row, second-column elements of the matrices in Equation (5.21) yields the following equation and subsequent solution set for θ_1:

$$\frac{s\theta_1}{c\theta_1} = \frac{r_{32}}{r_{31}} \text{ and } \therefore,\ \theta_1 = \text{atan2}\left(\pm r_{32}, \pm r_{31}\right) \tag{5.22}$$

The first- and third-column elements of the third row in Equation (5.21) then provide one solution for θ_2 in terms of θ_1:

$$\theta_2 = \text{atan2}\left(r_{31}c\theta_1 + r_{32}s\theta_1, r_{33}\right) \tag{5.23}$$

Finally, again referring to Equation (5.21), the first- and second-row elements of the second column produce a single solution for θ_3, also in terms of θ_1:

$$\theta_3 = \text{atan2}\left(-r_{11}s\theta_1 + r_{12}c\theta_1, -r_{21}s\theta_1 + r_{22}c\theta_1\right) \tag{5.24}$$

This completes the inverse kinematic analysis for the lower-limb manipulator.

Ultimately, there are eight solutions (i.e., four 'main-arm' and two 'wrist' solutions) in the inverse kinematics of the human lower limb when it is modeled as a 6-DOF serial manipulator per Figure 5.2. The correct inverse kinematics solution is selected as the joint angle set that matches the normal capabilities of the biological human leg (i.e., the solution set that does not hyperextend any of the leg joints). Here, this solution set is the one comprised by the addition solutions from both Equations (5.17) and (5.18) and the solution with the positive terms from Equation (5.22). Note that the inverse kinematics solution for the human left leg can be formulated in the same way, except with negated terms at each instance of a_0, d_4, and $d_{e.e}$.

5.1.4. Jacobian Analysis of the Reverse-Order Manipulator

In this subsection, a Jacobian matrix associated with the lower-limb manipulator is developed as an intermediate step towards the objective of identifying the mechanism's singularities. Typically, Jacobians are matrices that provide a mapping between the joint rates in actuator space to the velocity state in end-effector space [142]. However, when considered in forward-order, the 6R serial manipulator modeling the human leg does not contain a spherical wrist at its final three joints. Therefore, a Jacobian developed from the forward-order manipulator cannot be simplified to include a 3-by-3 matrix of zeros in its upper right-side quadrant. In turn, such a Jacobian's determinant, which is required for the manipulator's singularity analysis, is more complicated than that of a Jacobian that does have a $\mathbf{0}_{3\times3}$ matrix in the upper-right

quadrant. Therefore, the manipulator will again be considered in reverse, because the reverse-order manipulator is spherically-wristed. This permits development of such a simplified Jacobian as outlined in the remainder of this subsection. Recall that the reverse-order consideration involves treating the end-effector as the base, the base as the end-effector, and joint numbers as proceeding in descending order.

The reverse-order manipulator's Jacobian matrix is based on a point on the base link that is coincident with the 'wrist' center, w*, and oriented with respect to frame $\{3\}^{\text{LEG}}$. In this context, the 'wrist' center is coincident with the origins of frames $\{1\}^{\text{LEG}}$, $\{2\}^{\text{LEG}}$, and $\{3\}^{\text{LEG}}$. The fundamental difference between the proposed reverse-order Jacobian and the standard Jacobian is that the former maps joint rates to the base link's velocity state while the latter maps joint rates to the end-effector's velocity state. Therefore, the reverse-order Jacobian cannot be used in velocity or static force analyses of the manipulator, as these require transformation mapping between joint rates and the end-effector velocity state. To signify this fundamental difference, the reverse-order Jacobian and terms that derive from it will be designated with an asterisk (*) marking.

Using the conventional method for the serial-manipulator Jacobian development, as described in [142], the reverse-order Jacobian, ${}^{3}\mathbf{J}_{w}^{\text{LEG}}*$, is formulated as:

$$ {}^{3}\mathbf{J}_{w}^{\text{LEG}}* = \begin{bmatrix} {}^{3}\hat{z}_{6}^{\text{LEG}} \times {}^{3}\vec{\mathrm{p}}_{6\to w*} & {}^{3}\hat{z}_{5}^{\text{LEG}} \times {}^{3}\vec{\mathrm{p}}_{5\to w*} & {}^{3}\hat{z}_{4}^{\text{LEG}} \times {}^{3}\vec{\mathrm{p}}_{4\to w*} & \vec{0}_{3\times1} & \vec{0}_{3\times1} & \vec{0}_{3\times1} \\ {}^{3}\hat{z}_{6}^{\text{LEG}} & {}^{3}\hat{z}_{5}^{\text{LEG}} & {}^{3}\hat{z}_{4}^{\text{LEG}} & {}^{3}\hat{z}_{3}^{\text{LEG}} & {}^{3}\hat{z}_{2}^{\text{LEG}} & {}^{3}\hat{z}_{1}^{\text{LEG}} \end{bmatrix} \tag{5.25} $$

The upper-right three vectors within the matrix are zero vectors because joints $\mathrm{J}_{1}^{\text{LEG}}$, $\mathrm{J}_{2}^{\text{LEG}}$, and $\mathrm{J}_{3}^{\text{LEG}}$ do not contribute to the linear velocity of the 'wrist' when the manipulator is considered in reverse-order. Moreover, the ${}^{3}\vec{\mathrm{p}}_{i\to w*}$ vectors introduced in Equation (5.25), i = 4, 5, 6, are vectors that extend from O_{i}^{LEG} to w*; also, each of these vectors is represented with respect to frame $\{3\}^{\text{LEG}}$ per their left-side superscripts. Since O_{3}^{LEG} is coincident with the 'wrist', these ${}^{3}\vec{\mathrm{p}}_{i\to w*}$ vectors can be obtained as:

$$ {}^{3}\vec{\mathrm{p}}_{6\to w*} = -p\left({}^{3}_{6}\mathbf{T}^{\text{LEG}}\right),\ {}^{3}\vec{\mathrm{p}}_{5\to w*} = -p\left({}^{3}_{5}\mathbf{T}^{\text{LEG}}\right),\ \text{and}\ {}^{3}\vec{\mathrm{p}}_{4\to w*} = -p\left({}^{3}_{4}\mathbf{T}^{\text{LEG}}\right) \tag{5.26} $$

where $p(\ )$ represents a function that extracts the position vector (i.e., the top three elements of column four) from the input homogeneous transform. Similarly, the z-axis direction vectors can be determined as:

$$ {}^{3}\hat{z}_{i}^{\text{LEG}} = a\left({}^{3}_{i}\mathbf{T}^{\text{LEG}}\right) \text{ for } i = 1, 2, 3, 4, 5, 6 \tag{5.27} $$

where $a(\ )$ extracts the approach or z-axis vector (i.e., the top three elements of column three) from the input transform. Each of the required homogeneous transforms from

Equations (5.26) and (5.27) can be obtained using appropriate multiplications of the basic transforms outlined in Equation (5.2) along with possible inversions per Equation (5.8).

Upon applying Equations (5.26) and (5.27) to each of the required transforms, the set of *z*-axis directions and position vectors for the ${}^{3}\mathbf{J}_{w}^{\text{LEG}}*$ Jacobian are obtained:

$$ {}^{3}\hat{z}_{6}^{\text{LEG}} = \begin{bmatrix} c\theta_4 s\theta_5 \\ s\theta_4 s\theta_5 \\ c\theta_5 \end{bmatrix}; {}^{3}\hat{z}_{5}^{\text{LEG}} = \begin{bmatrix} -s\theta_4 \\ c\theta_4 \\ 0 \end{bmatrix}; {}^{3}\hat{z}_{4}^{\text{LEG}} = {}^{3}\hat{z}_{3}^{\text{LEG}} = \begin{bmatrix} 0 \\ 0 \\ 1 \end{bmatrix}; {}^{3}\hat{z}_{2}^{\text{LEG}} = \begin{bmatrix} s\theta_3 \\ c\theta_3 \\ 0 \end{bmatrix}; {}^{3}\hat{z}_{1}^{\text{LEG}} = \begin{bmatrix} -s\theta_2 c\theta_3 \\ s\theta_2 s\theta_3 \\ c\theta_2 \end{bmatrix} \quad (5.28) $$

$$ {}^{3}\vec{\mathrm{p}}_{6\to w*} = {}^{3}\vec{\mathrm{p}}_{5\to w*} = \begin{bmatrix} -a_4 c\theta_4 + d_5 s\theta_4 - a_3 \\ -a_4 s\theta_4 - d_5 c\theta_4 \\ d_4 \end{bmatrix}; \; {}^{3}\vec{\mathrm{p}}_{4\to w*} = \begin{bmatrix} -a_3 \\ 0 \\ d_4 \end{bmatrix} \quad (5.29) $$

Note that it is intuitively sensible for ${}^{3}\hat{z}_{4}^{\text{LEG}}$ to be equal to ${}^{3}\hat{z}_{3}^{\text{LEG}}$ because the $\mathrm{J}_{3}^{\text{LEG}}$ and $\mathrm{J}_{4}^{\text{LEG}}$ axes are parallel; the first two position vectors in Equation (5.29) are equal because frame origins O_{5}^{LEG} and O_{6}^{LEG} are coincident. Finally, by substituting the vectors of Equations (5.28) and (5.29) into Equation (5.25) and performing the cross products, the ${}^{3}\mathbf{J}_{w}^{\text{LEG}}*$ Jacobian is found:

$$ {}^{3}\mathbf{J}_{w}^{\text{LEG}}* = \left[\begin{array}{ccc:ccc} d_4 s\theta_4 s\theta_5 + c\theta_5\left(a_4 s\theta_4 + d_5 c\theta_4\right) & d_4 c\theta_4 & 0 & 0 & 0 & 0 \\ -d_4 c\theta_4 s\theta_5 + c\theta_5\left(d_5 s\theta_4 - a_4 c\theta_4 - a_3\right) & d_4 s\theta_4 & -a_3 & 0 & 0 & 0 \\ a_3 s\theta_4 s\theta_5 - d_5 s\theta_5 & a_4 + a_3 c\theta_4 & 0 & 0 & 0 & 0 \\ \hdashline c\theta_4 s\theta_5 & -s\theta_4 & 0 & 0 & s\theta_3 & -s\theta_2 c\theta_3 \\ s\theta_4 s\theta_5 & c\theta_4 & 0 & 0 & c\theta_3 & s\theta_2 s\theta_3 \\ c\theta_5 & 0 & 1 & 1 & 0 & c\theta_2 \end{array}\right] \quad (5.30) $$

5.1.5. Singularity Analysis

Singularities of a serial manipulator occur when it is configured to a posture for which the Jacobian matrix loses its full rank. Physically, the manipulator loses one or more DOFs, which prevents it from moving in some directions of the end-effector space [142]. Because singularities correspond to manipulator posture, it does not matter that the Jacobian developed in the previous section was based on a reverse-order observation of the manipulator; regardless of the Jacobian considered, the conditions that cause a manipulator to become singular are the same. Therefore, the serial manipulator's singular configurations can be determined by evaluating the ${}^{3}\mathbf{J}_{w}^{\text{LEG}}*$ for rank deficiency (i.e., solving for the joint displacements that cause ${}^{3}\mathbf{J}_{w}^{\text{LEG}}*$ to be

singular). This process is achieved by equating the ${}^{3}\mathbf{J}_{w}^{\text{LEG}}*$ matrix's determinant to zero. Because the upper-right 3-by-3 submatrix of ${}^{3}\mathbf{J}_{w}^{\text{LEG}}*$ contains all zero elements, the determinant of the Jacobian can be determined as follows:

$$\left|{}^{3}\mathbf{J}_{w}^{\text{LEG}}*\right| = \left|A_{3\times3}\right|\left|C_{3\times3}\right| = 0 \text{, where } {}^{3}\mathbf{J}_{w}^{\text{LEG}}* = \left[\begin{array}{c:c} A_{3\times3} & 0_{3\times3} \\ \hdashline B_{3\times3} & C_{3\times3} \end{array}\right] \tag{5.31}$$

$$\begin{aligned} \therefore,\ \left|A_{3\times3}\right| &= \left|\begin{bmatrix} d_4 s\theta_4 s\theta_5 + c\theta_5\left(a_4 s\theta_4 + d_5 c\theta_4\right) & d_4 c\theta_4 & 0 \\ -d_4 c\theta_4 s\theta_5 + c\theta_5\left(d_5 s\theta_4 - a_4 c\theta_4 - a_3\right) & d_4 s\theta_4 & -a_3 \\ a_3 s\theta_4 s\theta_5 - d_5 s\theta_5 & a_4 + a_3 c\theta_4 & 0 \end{bmatrix}\right| = 0 \text{ and/or} \\ \left|C_{3\times3}\right| &= \left|\begin{bmatrix} 0 & s\theta_3 & -s\theta_2 c\theta_3 \\ 0 & c\theta_3 & s\theta_2 s\theta_3 \\ 1 & 0 & c\theta_2 \end{bmatrix}\right| = 0 \end{aligned} \tag{5.32}$$

where $\left|\ \right|$ signifies the matrix determinant.

'Main-Arm' Singularities

The determinant of $A_{3\times3}$ provides the 'main-arm' singularities when equated to zero and factorized as follows:

$$\left|A_{3\times3}\right| = -a_3\left(a_4 s\theta_4 + d_5 c\theta_4\right)\left(-d_4 s\theta_5 + \left(-a_4 - a_3 c\theta_4\right)c\theta_5\right) = 0 \tag{5.33}$$

Note that in practice, it is infeasible for a_3 to be zero, because this condition only occurs when the knee axis intersects the hip joint (i.e., a zero-length thigh). Therefore, Equation (5.33) is only realistically satisfied when:

$$a_4 s\theta_4 + d_5 c\theta_4 = 0 \text{ and/or } -d_4 s\theta_5 + \left(-a_4 - a_3 c\theta_4\right)c\theta_5 = 0 \tag{5.34}$$

The first case is fulfilled when θ_4 takes on a value of:

$$\theta_4 = \operatorname{atan2}\left(\pm d_5, \mp a_4\right) \tag{5.35}$$

which corresponds the boundary singularities that occur when the manipulator is fully-extended or folded-back. As shown in the left image of Figure 5.3, these configurations align frame origins O_1^{LEG} through O_6^{LEG} onto a common plane, so the only possible direction of end-effector motion is the tangential of the limb; radial motion is not possible, which is typical of boundary singularities [142]. The second singularity condition of Equation (5.34) occurs when:

$$\theta_5 = \operatorname{atan2}\left(\pm\left(a_4 + a_3 c\theta_4\right), \mp d_4\right) \tag{5.36}$$

The loci defined by Equation (5.36) represent interior singularities for which the axes of joints $\mathrm{J}_1^{\text{LEG}}$, $\mathrm{J}_2^{\text{LEG}}$, $\mathrm{J}_3^{\text{LEG}}$, and $\mathrm{J}_6^{\text{LEG}}$ all intersect at the hip COR, as depicted by one

example on the right side of Figure 5.3. The end-effector loses a DOF in these configurations because the combined rotations of joints $J_1^{LEG} - J_3^{LEG}$ may be exactly canceled by a counterrotation of J_6^{LEG}. That is, the end-effector may remain stationary despite motions of intermediate links, and J_6^{LEG} loses its ability to transmit a unique motion to the end-effector. It is apparent that the knee angle, θ_4, influences the values of θ_5 that cause such an intersection of joint axes.

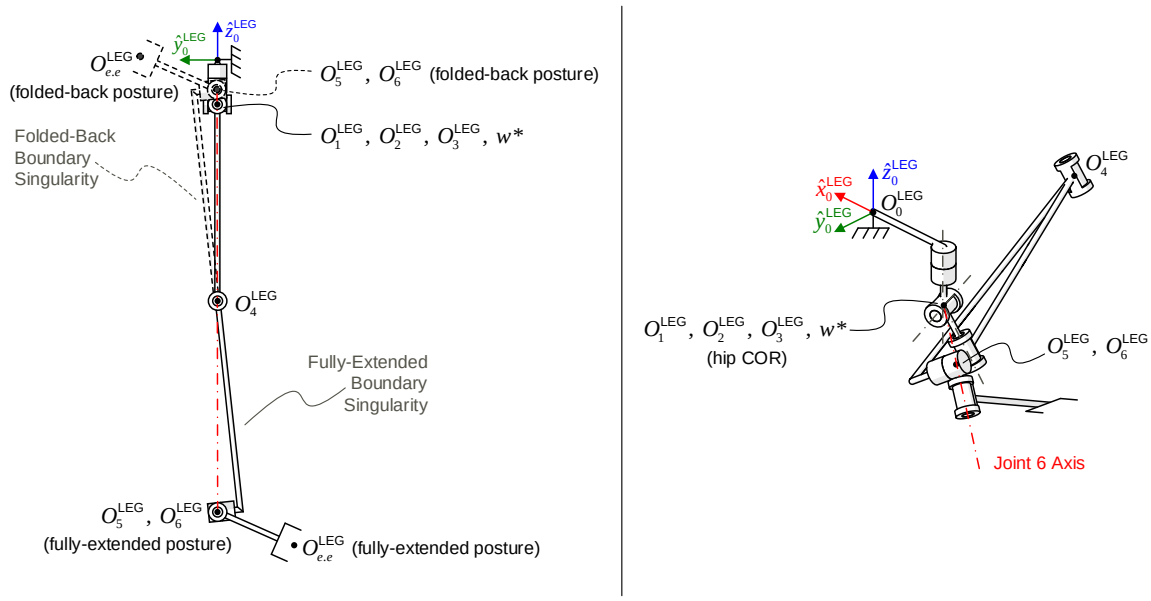

Figure 5.3. Example boundary (left) and interior (right) 'main-arm' singularities associated with the 6R kinematic model of the human lower limb

'Wrist' Singularities

Setting the determinant of the ${}^3\mathbf{J}_w^{LEG}*$ matrix's $C_{3\times3}$ submatrix to zero yields the singularities associated with the manipulator wrist:

$$\left|C_{3\times3}\right| = s\theta_2 s\theta_3^{\,2} + s\theta_2 c\theta_3^{\,2} = s\theta_2 = 0 \text{ and } \therefore,\ \theta_2 = m180° \tag{5.37}$$

where m is any integer. Physically, this singularity represents a situation in which the J_1^{LEG} and J_3^{LEG} axes are coincident. As a consequence of Equation (5.37), the 6R model of the human lower limb is singular in its zero-displacement configuration, for which m = 0 (see Figure 5.2).

6R Manipulator Singularities respecting the Workspace of the Human Leg

The motivation to find the singular configurations of the kinematic model for the lower limb is to check if these postures exist within the human leg's normal biomechanical workspace, as reported at the beginning of Chapter 5. As a manipulator

approaches a singular configuration, its Jacobian matrix becomes ill-conditioned and may lose its invertibility [142]. In practice, a manipulator's control may become unstable and, in simulation, the model configuration may become erroneous near the singular postures. Therefore, if singular configurations do exist within the workspace, they should be avoided during the manipulator trajectory planning process, which potentially limits the utility of the chosen kinematic model. Note that Denavit and Hartenberg parameters associated with the human right leg are used in this subsection (see Subsection 5.1.1), but singularity configurations for the left leg would be mirrored from right leg singularities with respect to the body's sagittal plane.

Before the kinematic model's singular configurations can be compared with biological limb postures, the joint angle values from the two representations must be made commensurate. In a biomechanical sense, human leg joint angles are generally measured relative to a neutral-standing posture. For the proposed 6R model of the leg, joint angles are measured relative to the zero-displacement configuration, as shown on the right side of Figure 5.2, as established per the Craig convention of link-frame attachments. A neutral-standing posture may vary from person-to-person depending on one's individual morphology. However, this thesis assumes that a neutral-standing posture is achieved in the kinematic model when $\hat{z}_0^{\text{LEG}}$, $\hat{z}_1^{\text{LEG}}$, $\hat{x}_2^{\text{LEG}}$, $\hat{x}_3^{\text{LEG}}$, $\hat{x}_4^{\text{LEG}}$, and $\hat{x}_5^{\text{LEG}}$ are all parallel (i.e., when the knee center is directly below the hip center, and the knee is fully-extended straight), as shown on the left side of Figure 5.2. Moreover, the $\hat{x}_6^{\text{LEG}}$ axis is directed 30 degrees below the horizontal in the neutral-standing posture, such that the end-effector tip is positioned inferior and anterior to the ankle (e.g., at the toes). This detail is not critical, because the singular configurations are not influenced by θ_6. By this assumption, the 6R joint variable values that correspond to a neutral-standing posture are:

$$\theta_1 = 0°,\ \theta_2 = 90°,\ \theta_3 = 0°,\ \theta_4 = 0°,\ \theta_5 = 0°,\ \text{and}\ \theta_6 = -60° \tag{5.38}$$

Table 5.2 presents the normal biomechanical joint limits associated with the human leg [99], along with the correlation between anatomical rotations and model-joint rotations.

Table 5.2. Typical upper-biomechanical limits associated with the human leg joints and their correspondence to the 6R kinematic model joints

Joint Motion	Max. Angle	Model Joint	Joint Motion	Max. Angle	Model Joint
Hip			*Ankle*		
Internal Rotation	30°	J_1^{LEG} (+)	Pronation	27.5°	J_5^{LEG} (+)
External Rotation	60°	J_1^{LEG} (–)	Supination	50°	J_5^{LEG} (–)
Abduction	45°	J_2^{LEG} (+)	Plantarflexion	40°	J_6^{LEG} (+)
Adduction	45°	J_2^{LEG} (–)	Dorsiflexion	25°	J_6^{LEG} (–)
Extension	20°	J_3^{LEG} (+)	Adduction	40°	N/A
Flexion	120°	J_3^{LEG} (–)	Abduction	40°	N/A
Knee			*Knee*		
Flexion	120°	J_4^{LEG} (+)	Extension	0°	J_4^{LEG} (–)

Note: The positive (+) and negative (–) labels attached to model J_i^{LEG} indicate whether the corresponding joint motion is positive or negative, respectively, about the $\hat{z}_i^{LEG}$ axis in accordance with the right-hand rule.

Given the information provided in Table 5.2 and Equation (5.38), the biological joint limits map to the following ranges for J_2^{LEG}, J_4^{LEG}, and J_5^{LEG} of the kinematic model:

$$\theta_2 \in [45° \quad 135°],\ \theta_4 \in [0° \quad 120°], \text{ and } \theta_5 \in [-50° \quad 27.5°] \tag{5.39}$$

where θ_2, θ_4, and θ_5 are the joint variables that have a role in singular configuration development. To start, the θ_2 angle range does not include $m180°$, where m is any integer, so the 'wrist' singularity of the kinematic model is well outside of its intended workspace. Next, the singular configuration values associated with θ_4 and θ_5 are dependent on the value selections for a_3, a_4, d_4, and d_5, as per Equations (5.35) and (5.36). Therefore, the following example values for each of these parameters are adopted to allow a quantitative indication of whether the kinematic model's singularities are included in its intended workspace:

$$a_3 = 378.4\text{mm},\ a_4 = 401.6\text{mm},\ d_4 = 41.32\text{mm}, \text{ and } d_5 = 43.33\text{mm} \tag{5.40}$$

These values are approximated from a CAD model based on the 50th-percentile man.

Using Equation (5.40) numbers, the 'main-arm' boundary singularities occur at:

$$\theta_4 = \text{atan2}(\pm d_5, \mp a_4) = \text{atan2}(\pm 43.33, \mp 401.6) = 173.8°,\ -6.158° \notin [0° \quad 120°] \tag{5.41}$$

Thus, the θ_4 joint angles associated with singular configurations do not belong to the range that defines the manipulators workspace for the selected link lengths. Generally, the lower-limb model's boundary singularity is not included in its intended workspace as long as d_5 is greater than zero and within reasonable biomechanical limits for the offset

between the knee and ankle CORs. Physically, the boundary singularities tend to require hyperextension or hyperflexion of the knee joint (see the left-side image of Figure 5.3). Finally, the joint variable range for θ_4 from Equation (5.39) restricts the values for θ_5 that can produce interior singularities to the following ranges:

$$\left.\begin{aligned}\theta_5 &= \operatorname{atan2}\left(\left(a_4 + a_3 c\theta_4\right), -d_4\right) \rightarrow \left[93.03^\circ \quad 101.0^\circ\right] \\ \theta_5 &= \operatorname{atan2}\left(-\left(a_4 + a_3 c\theta_4\right), d_4\right) \rightarrow \left[-86.97^\circ \quad -78.99^\circ\right]\end{aligned}\right\} \notin \left[-50^\circ \quad 27.5^\circ\right] \tag{5.42}$$

As indicated in the equations, both of these singularity loci do not exist within the intended θ_5 workspace limits. Moreover, the ranges that could cause singularity are well outside of the intended workspace range. Thus, it is unlikely for these ranges to overlap for wide range of design parameter selections, within the practical limits of human morphology. This is reasonable, because it is difficult and unusual for a person to align their ankle's plantarflexion/dorsiflexion axis to intersect the hip joint on the same leg. Overall, none of the singularity configurations associated with the proposed 6R model for the human leg occur within the limits of its intended, anatomically-motivated workspace, so it is a valid model for simulation use.

5.2. Kinematic Considerations for the Exoskeleton-Human System

With the kinematic formulations completed for the isolated human lower-limb model in Section 5.1 above, this section brings these together with the kinematic analyses for the selected orientation manipulator and motion-transfer manipulator to provide a complete kinematic description of the exoskeleton-human system. Subsection 5.2.1 does so with the 6R model for the human leg, which is useful for kinematic simulations, while Subsection 5.2.2 considers a modified human-leg model that has utility for motion-capture (MoCap) experimentation with a physical exoskeleton.

5.2.1. Complete System Kinematics with the 6R Simulation Model for the Human Lower Limb

Figure 5.4 presents a schematic illustration of the complete manipulator system, in which the Simplified Agile Eye (SAE) is chosen for the orientation manipulator subsystem, the PU scheme is selected for the motion-transfer manipulator, and the human leg is represented by the 6R model. In the figure, the relative sizes of the

subsystem's links are intentionally disproportionate to promote visual clarity; as a spherical manipulator, note that the SAE's links can be scaled without changing the manipulator's kinematic performance.

Before the kinematic formulations from each of the subsystems can be combined, a common reference frame must be established. As mentioned in Subsection 5.1.1, the human lower limb's reference frame, affixed to the innominate bone of the pelvis, is chosen as the global reference frame for the complete exoskeleton-limb system. Anatomically, the innominate bone contains the acetabulum socket, relative to which the hip joint undergoes its articulations [99]. Therefore, the kinematic model does not neglect any human body joints between the global reference frame and hip joint. In addition to a global reference frame, any frame rotations that exist between the SAE's local reference frame and its active spherical joint representation in the PU must be considered. Likewise, any rotation between the target joint frame in the PU scope and the corresponding joint frame in the 6R model must be taken into account. Essentially, a set of constant rotations must be introduced such that the orientation pairings between the spherical joints (i.e., orientation manipulator and target body joint) and PU local reference frame are consistent with the frame definitions in the complete-system context.

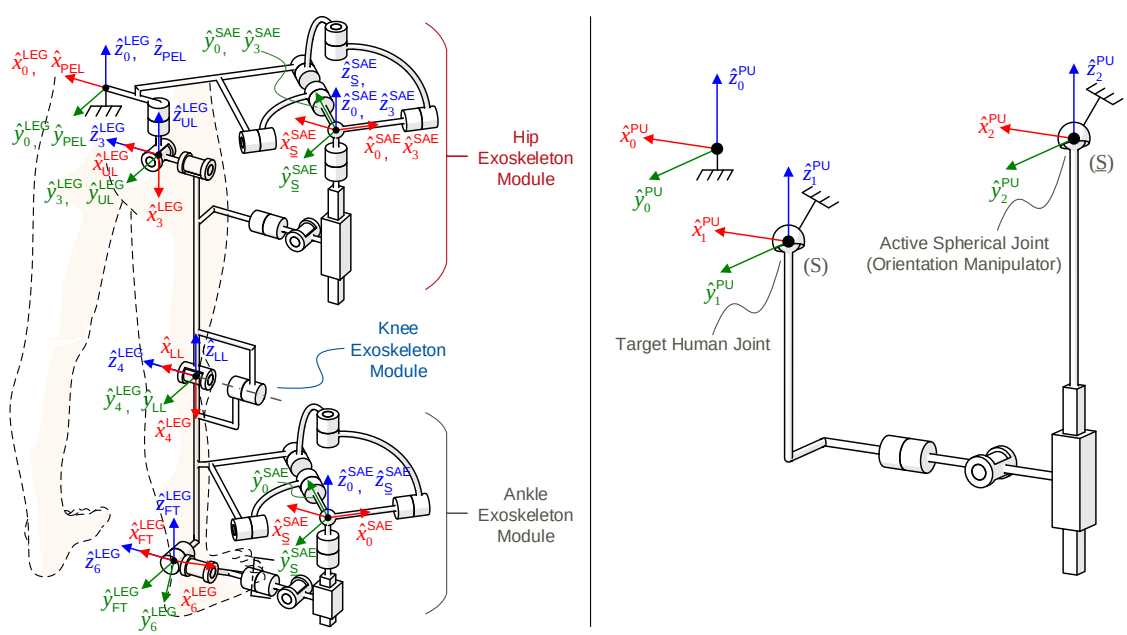

Figure 5.4. Schematic of the complete exoskeleton-limb system with frame labels (left) and recap image of the PU subsystem (right)

Note: The $\{3\}^{SAE}$ frame is not shown within the ankle exoskeleton module to reduce visual complexity. Also, the 6R model for the human lower limb is adopted here.

To achieve the desired consistency, several new frames are introduced in the scope of the complete exoskeleton-limb system as shown in Figure 5.4. First, a {PEL} frame is attached to the pelvis with its *z*-axis normal to the transverse plane, *y*-axis normal to the coronal plane, and *x*-axis normal to the sagittal plane of the body. This happens to be the same orientation as the $\{0\}^{\text{LEG}}$ frame:

$$ {}^{\text{PEL}}_{0}\mathbf{R}^{\text{LEG}} = \begin{bmatrix} 1 & 0 & 0 \\ 0 & 1 & 0 \\ 0 & 0 & 1 \end{bmatrix} = \mathbf{I}_{3\times 3} \tag{5.43} $$

Although it is not strictly necessary to differentiate these two frames, the new {PEL} frame is introduced in the interest of generality (i.e., if the $\{0\}^{\text{LEG}}$ frame was defined differently). As shown in the figure for the hip exoskeleton module, the SAE base link is rigidly attached to the pelvis such that the $\hat{z}_0^{\text{SAE}}$ axis is normal to the transverse plane of the body and a 135-degree rotation exists between the $\hat{x}_0^{\text{SAE}}$ and $\hat{x}_{\text{PEL}}$ axes:

$$ {}^{\text{PEL}}_{0}\mathbf{R}^{\text{SAE}} = \mathbf{R}_Z\left(-135°\right) = \begin{bmatrix} \cos\left(-135°\right) & -\sin\left(-135°\right) & 0 \\ \sin\left(-135°\right) & \cos\left(-135°\right) & 0 \\ 0 & 0 & 1 \end{bmatrix} \tag{5.44} $$

Next, a $\{\text{UL}\}^{\text{LEG}}$ frame is rigidly attached to the upper-leg link of the lower-limb manipulator. When the leg is configured to a neutral-standing posture, this frame is oriented with respect to the body frames in the same manner as the {PEL} frame. Therefore, a constant *y*-axis rotation exists between the $\{3\}^{\text{LEG}}$ and $\{\text{UL}\}^{\text{LEG}}$ frames:

$$ {}^{3}_{\text{UL}}\mathbf{R}^{\text{LEG}} = \mathbf{R}_Y\left(-90°\right) = \begin{bmatrix} 0 & 0 & -1 \\ 0 & 1 & 0 \\ 1 & 0 & 0 \end{bmatrix} \tag{5.45} $$

A $\{\underline{\text{S}}\}^{\text{SAE}}$ frame is also introduced here. It is fixed to the SAE's end-effector link and is oriented with its axes parallel to the exoskeleton module's universal joint axes (i.e., just as frame $\{2\}^{\text{PU}}$ is oriented within the scope of the PU manipulator). For the right-leg exoskeleton shown in the left-side schematic of Figure 5.4, this is:

$$ {}^{3}_{\underline{\text{S}}}\mathbf{R}^{\text{SAE}} = \mathbf{R}_Z\left(135°\right) = \begin{bmatrix} \cos\left(135°\right) & -\sin\left(135°\right) & 0 \\ \sin\left(135°\right) & \cos\left(135°\right) & 0 \\ 0 & 0 & 1 \end{bmatrix} \tag{5.46} $$

This applies for both the hip and ankle exoskeleton modules.

At the lower-leg, a {LL} frame is attached to the shank such that it is oriented with the body frames equivalent to {PER} and {UL}^{LEG} when the leg is in its neutral-standing posture. Therefore, the {LL} frame relates to {4}^{LEG} in accordance with:

$$ {}^{\text{LL}}_{4}\mathbf{R}^{\text{LEG}} = \mathbf{R}_Y\left(90°\right) = \begin{bmatrix} 0 & 0 & 1 \\ 0 & 1 & 0 \\ -1 & 0 & 0 \end{bmatrix} \tag{5.47} $$

Like the hip exoskeleton's attachment to the pelvis, the ankle exoskeleton module is oriented with respect to the {LL} frame as follows:

$$ {}^{\text{LL}}_{0}\mathbf{R}^{\text{SAE}} = \mathbf{R}_Z\left(-135°\right) = \begin{bmatrix} \cos\left(-135°\right) & -\sin\left(-135°\right) & 0 \\ \sin\left(-135°\right) & \cos\left(-135°\right) & 0 \\ 0 & 0 & 1 \end{bmatrix} \tag{5.48} $$

Similarly, a {FT}^{LEG} frame is attached to the foot link of the lower-limb manipulator, and is oriented to match the {PER}, {UL}^{LEG}, and {LL} frames when the leg achieves its neutral-standing posture. Since the {6}^{LEG} frame is also attached to the foot link, and θ_6 is defined to equal 60 degrees when the leg assumes its neutral posture, the relationship between {FT}^{LEG} and {6}^{LEG} is given by:

$$ {}^{6}_{\text{FT}}\mathbf{R}^{\text{LEG}} = \mathbf{R}_Z\left(60°\right)\mathbf{R}_Y\left(-90°\right) = \begin{bmatrix} 0 & -\sin\left(60°\right) & -\cos\left(60°\right) \\ 0 & \cos\left(60°\right) & -\sin\left(60°\right) \\ 1 & 0 & 0 \end{bmatrix} \tag{5.49} $$

Now, upon comparing the left- and right-side images of Figure 5.4, it is apparent that ${}^{\text{PEL}}_{\text{UL}}\mathbf{R}^{\text{LEG}}$ and ${}^{\text{PEL}}_{\underline{\text{S}}}\mathbf{R}^{\text{SAE}}$ represent ${}^{0}_{1}\mathbf{R}^{\text{PU}}$ and ${}^{0}_{2}\mathbf{R}^{\text{PU}}$, respectively, with regard to the hip exoskeleton module. That is, the former two matrices provide the appropriate conversion constants to transition from the complete-system scope to the PU subsystem scope. Similarly, ${}^{\text{LL}}_{\text{FT}}\mathbf{R}^{\text{LEG}}$ and ${}^{\text{LL}}_{\underline{\text{S}}}\mathbf{R}^{\text{SAE}}$ represent ${}^{0}_{1}\mathbf{R}^{\text{PU}}$ and ${}^{0}_{2}\mathbf{R}^{\text{PU}}$ for the ankle exoskeleton module. The ${}^{3}_{\underline{\text{S}}}\mathbf{R}^{\text{SAE}}$ matrix then provides the mapping between the PU scope and SAE scope, and the remaining rotations from Equations (5.43)–(5.49) provide connections between the subsystem levels (i.e., SAE, PU, and LEG) and high-level complete system. Furthermore, the proposed knee exoskeleton module simply comprises an active revolute joint that is coaxial with the single-DOF knee. Therefore, the knee exoskeleton joint directly measures the human knee's angular position, assuming the exoskeletal joint is appropriately zeroed (i.e., set to zero when the lower limb is configured to its neutral posture). Note that the {PEL} and {LL} frames do not have superscripts because they are used in both the SAE and LEG scopes. Furthermore, the origin positions of the

frames introduced to the complete-system scope are not significant in the high-level kinematic analyses to follow.

Complete System Inverse Kinematic Analysis

Within the context of the complete exoskeleton-limb system, the inverse kinematics problem involves a known target position and orientation for the human foot, and the corresponding angles for the exoskeleton's active joints must be solved. This analysis is thereby an essential component of trajectory planning for the complete manipulator system. From a practical standpoint, the inverse kinematics solution is imperative in the control of an actuated exoskeleton; some form of user interface would define a target posture for the leg based on the user's intended motion, so the system controller would then aim to align the exoskeleton's active joints to angular positions that achieve the desired leg posture.

To start the inverse kinematics analysis for the complete system, the inverse kinematics solution for the 6R serial manipulator is performed, as outlined in Subsection 5.1.3. This process produces values for each of the lower-limb model joints, θ_i for i = 1, 2, 3, 4, 5, and 6. This permits computation of the ${}^{0}_{3}\mathbf{R}^{\text{LEG}}_{\mathbf{N}}$ and ${}^{4}_{6}\mathbf{R}^{\text{LEG}}_{\mathbf{N}}$ rotation matrices, which are obtained as the upper-left 3×3 matrices of the following homogeneous transforms, after the appropriate joint variable substitutions are made:

$$ {}^{0}_{3}\mathbf{T}^{\text{LEG}} = {}^{0}_{1}\mathbf{T}^{\text{LEG}}\,{}^{1}_{2}\mathbf{T}^{\text{LEG}}\,{}^{2}_{3}\mathbf{T}^{\text{LEG}} \text{ and } {}^{4}_{6}\mathbf{T}^{\text{LEG}} = {}^{4}_{5}\mathbf{T}^{\text{LEG}}\,{}^{5}_{6}\mathbf{T}^{\text{LEG}} \tag{5.50} $$

Note that the matrix elements for each of the transforms multiplied above are specified in Equation (5.2). Proceeding with the inverse kinematic analysis of the hip exoskeleton module, ${}^{\text{PEL}}_{\text{UL}}\mathbf{R}^{\text{LEG}}_{\mathbf{N}}$ is evaluated as:

$$ {}^{\text{PEL}}_{\text{UL}}\mathbf{R}^{\text{LEG}}_{\mathbf{N}} = {}^{\text{PEL}}_{0}\mathbf{R}^{\text{LEG}}\,{}^{0}_{3}\mathbf{R}^{\text{LEG}}_{\mathbf{N}}\,{}^{3}_{\text{UL}}\mathbf{R}^{\text{LEG}} \tag{5.51} $$

where Equations (5.43) and (5.45) provide the constant rotations associated with ${}^{\text{PEL}}_{0}\mathbf{R}^{\text{LEG}}$ and ${}^{3}_{\text{UL}}\mathbf{R}^{\text{LEG}}$, respectively. Recall that ${}^{\text{PEL}}_{\text{UL}}\mathbf{R}^{\text{LEG}}_{\mathbf{N}}$ represents ${}^{0}_{1}\mathbf{R}^{\text{PU}}_{\mathbf{N}}$ in the context of the hip exoskeleton module. Hence, the two matrices are equated, and the inverse kinematics procedure outlined in Subsection 4.2.2 is carried out for the hip's motion-transfer manipulator. This process yields ${}^{0}_{2}\mathbf{R}^{\text{PU}}_{\mathbf{N}}$, which corresponds to ${}^{\text{PEL}}_{\underline{\text{S}}}\mathbf{R}^{\text{SAE}}_{\mathbf{N}}$ for the hip exoskeleton. So, the orientation of the SAE's end-effector with respect to its local reference frame can now be found as:

$$ {}^{0}_{3}\mathbf{R}^{\text{SAE}}_{\mathbf{N}} = \left({}^{\text{PEL}}_{0}\mathbf{R}^{\text{SAE}}\right)^{\text{T}}\,{}^{\text{PEL}}_{\underline{\text{S}}}\mathbf{R}^{\text{SAE}}_{\mathbf{N}}\left({}^{3}_{\underline{\text{S}}}\mathbf{R}^{\text{SAE}}\right)^{\text{T}} \tag{5.52} $$

where expressions for ${}^{\text{PEL}}_{0}\mathbf{R}^{\text{SAE}}$ and ${}^{3}_{\underline{S}}\mathbf{R}^{\text{SAE}}$ are provided in Equations (5.44) and (5.46). Finally, the inverse kinematics solution for the SAE, as presented in Subsection 3.4.2, yields the θ_1^{SAE}, θ_2^{SAE}, and θ_3^{SAE} active joint states for the hip exoskeleton module.

The process for the ankle exoskeleton module continues in a parallel manner to the hip exoskeleton. First, ${}^{\text{LL}}_{\text{FT}}\mathbf{R}^{\text{LEG}}_{\mathbf{N}}$ is computed as:

$$ {}^{\text{LL}}_{\text{FT}}\mathbf{R}^{\text{LEG}}_{\mathbf{N}} = {}^{\text{LL}}_{4}\mathbf{R}^{\text{LEG}}\,{}^{4}_{6}\mathbf{R}^{\text{LEG}}_{\mathbf{N}}\,{}^{6}_{\text{FT}}\mathbf{R}^{\text{LEG}} \tag{5.53} $$

where ${}^{\text{LL}}_{4}\mathbf{R}^{\text{LEG}}$ and ${}^{6}_{\text{FT}}\mathbf{R}^{\text{LEG}}$ are matrices of constant elements, as given in Equations (5.47) and (5.49). Next, because ${}^{\text{LL}}_{\text{FT}}\mathbf{R}^{\text{LEG}}_{\mathbf{N}}$ represents ${}^{0}_{1}\mathbf{R}^{\text{PU}}_{\mathbf{N}}$ for the ankle exoskeleton module, the PU inverse kinematics is conducted to produce ${}^{0}_{2}\mathbf{R}^{\text{PU}}_{\mathbf{N}}$, which in turn represents ${}^{\text{LL}}_{\underline{S}}\mathbf{R}^{\text{SAE}}_{\mathbf{N}}$. Subsequently, ${}^{0}_{3}\mathbf{R}^{\text{SAE}}_{\mathbf{N}}$ for the ankle exoskeleton's SAE can be computed as per:

$$ {}^{0}_{3}\mathbf{R}^{\text{SAE}}_{\mathbf{N}} = \left({}^{\text{LL}}_{0}\mathbf{R}^{\text{SAE}}\right)^{\text{T}}\,{}^{\text{LL}}_{\underline{S}}\mathbf{R}^{\text{SAE}}_{\mathbf{N}}\left({}^{3}_{\underline{S}}\mathbf{R}^{\text{SAE}}\right)^{\text{T}} \tag{5.54} $$

where the pre- and post-multiplier matrices are given in Equations (5.48) and (5.46), respectively. The inverse kinematics solution for the SAE then yields the ankle exoskeleton module's active joint angles in accordance with the formulations prepared in Subsection 3.4.2. Lastly, the angular position of the knee exoskeleton's active joint, θ^{KNEE}, is given directly from θ_4, which is obtained after the initial 6R inverse kinematic computations. In summary, Figure 5.5 provides a block diagram illustrating the inverse kinematics procedure for the complete exoskeleton-limb system. In the diagram, note that $f_{\text{I.K.}}^{\text{ABC}}(\ )$ denotes the inverse kinematic algorithm for the ABC subsystem (i.e., where ABC is either LEG, PU, or SAE).

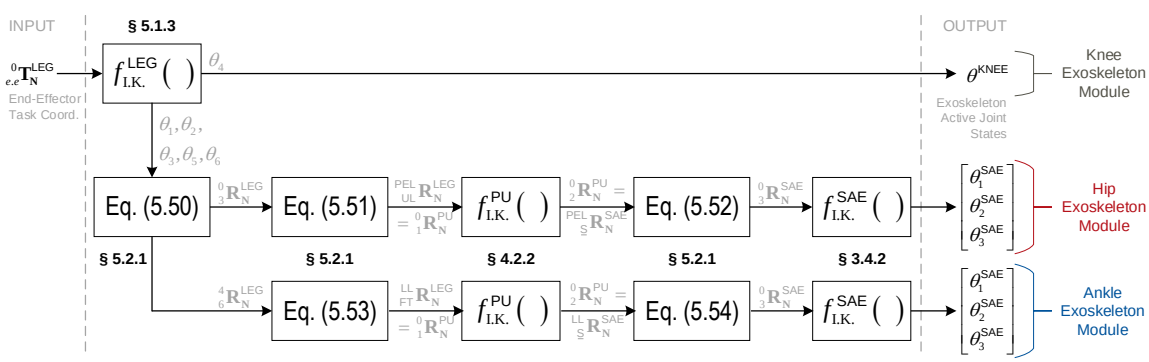

Figure 5.5. Block diagram for the complete-system inverse kinematic analysis

Complete System Forward Kinematic Analysis

The generalized forward kinematics problem associated with a manipulator is to determine the position and orientation of the end-effector in terms of a known set of joint variable values. For the complete exoskeleton-limb system, the end-effector is the leg model's foot link, and the known joint variables are those associated with the exoskeleton's active joints. In a simulation context, the forward kinematic solution is necessary for animating each system link with the appropriate position and orientation with respect to the global reference frame. In practice, motion capture applications use the exoskeleton as a tool for tracking the anatomical joint angle trajectories, which in turn relies on the forward kinematic solution. That is, the forward kinematics solution provides the means of mapping sensed exoskeleton joint angles to anatomical joint angle measurements. Additionally, the forward kinematic solution may be used to predict leg posture for controller feedback in fully-actuated exoskeletons. In these contexts, inverse kinematic procedures are only used to obtain joint angle values from rotation matrices.

The high-level forward kinematics procedure for the complete exoskeleton-limb system is essentially completed by carrying out the inverse kinematics process step-by-step in reverse order. Starting with the hip exoskeleton module, the θ_1^{SAE}, θ_2^{SAE}, and θ_3^{SAE} active joint angles are known, so the SAE forward kinematics presented in Subsection 3.4.3 can be effectuated to produce ${}^{0}_{3}\mathbf{R}_{\mathbf{N}}^{\text{SAE}}$. The ${}^{\text{PEL}}_{\underline{\text{S}}}\mathbf{R}_{\mathbf{N}}^{\text{SAE}}$ can then be obtained by rearranging Equation (5.52) as follows:

$$ {}^{\text{PEL}}_{\underline{\text{S}}}\mathbf{R}_{\mathbf{N}}^{\text{SAE}} = {}^{\text{PEL}}_{0}\mathbf{R}^{\text{SAE}}\, {}^{0}_{3}\mathbf{R}_{\mathbf{N}}^{\text{SAE}}\, {}^{3}_{\underline{\text{S}}}\mathbf{R}^{\text{SAE}} \tag{5.55} $$

Since ${}^{\text{PEL}}_{\underline{\text{S}}}\mathbf{R}_{\mathbf{N}}^{\text{SAE}}$ represents ${}^{0}_{2}\mathbf{R}_{\mathbf{N}}^{\text{PU}}$ for the hip exoskeleton module when projected into the PU subsystem scope, the PU forward kinematics are then performed as per the developments in Subsection 4.2.3. This results in a numerical rotation matrix for ${}^{0}_{1}\mathbf{R}^{\text{PU}}$, which corresponds to ${}^{\text{PEL}}_{\text{UL}}\mathbf{R}_{\mathbf{N}}^{\text{LEG}}$ in the full-system context. Subsequently, the orientation of the lower-limb model's thigh with respect to the pelvis can be determined by isolating for the ${}^{0}_{3}\mathbf{R}_{\mathbf{N}}^{\text{LEG}}$ matrix in Equation (5.51):

$$ {}^{0}_{3}\mathbf{R}_{\mathbf{N}}^{\text{LEG}} = \left({}^{\text{PEL}}_{0}\mathbf{R}^{\text{LEG}}\right)^{\text{T}}\, {}^{\text{PEL}}_{\text{UL}}\mathbf{R}_{\mathbf{N}}^{\text{LEG}} \left({}^{3}_{\text{UL}}\mathbf{R}^{\text{LEG}}\right)^{\text{T}} \tag{5.56} $$

Now, from Equation (5.4) in the 6R manipulator's forward kinematic analysis, the numerical ${}^{0}_{3}\mathbf{T}_{\mathbf{N}}^{\text{LEG}}$ homogeneous transform can be populated as follows:

$$ {}^{0}_{3}\mathbf{T}_{\mathbf{N}}^{\text{LEG}} = \left[\begin{array}{c:c} {}^{0}_{3}\mathbf{R}_{\mathbf{N}}^{\text{LEG}} & \begin{matrix} -a_0 \\ 0 \\ -d_1 \end{matrix} \\ \hdashline \bar{0}_{3\times1} & 1 \end{array}\right] \tag{5.57} $$

Recall from Subsection 5.1.1 that a_0 and d_1 are constant design parameters associated with the lower limb's kinematic model.

Now considering the ankle exoskeleton module, the θ_1^{SAE}, θ_2^{SAE}, and θ_3^{SAE} active joint angles are again known for the forward kinematics problem. Therefore, the SAE forward kinematic solution for ${}^{0}_{3}\mathbf{R}_{\mathbf{N}}^{\text{SAE}}$ can ultimately be obtained from the formulations in Subsection 3.4.3. Upon rearranging Equation (5.54), in which ${}^{\text{LL}}_{0}\mathbf{R}^{\text{SAE}}$ and ${}^{3}_{\underline{S}}\mathbf{R}^{\text{SAE}}$ are constant rotations defined earlier, the ${}^{\text{LL}}_{\underline{S}}\mathbf{R}_{\mathbf{N}}^{\text{SAE}}$ matrix is found:

$$ {}^{\text{LL}}_{\underline{S}}\mathbf{R}_{\mathbf{N}}^{\text{SAE}} = {}^{\text{LL}}_{0}\mathbf{R}^{\text{SAE}}\, {}^{0}_{3}\mathbf{R}_{\mathbf{N}}^{\text{SAE}}\, {}^{3}_{\underline{S}}\mathbf{R}^{\text{SAE}} \tag{5.58} $$

Given that ${}^{\text{LL}}_{\underline{S}}\mathbf{R}_{\mathbf{N}}^{\text{SAE}}$ represents ${}^{0}_{2}\mathbf{R}_{\mathbf{N}}^{\text{PU}}$ at the PU subsystem level, the motion-transfer manipulator forward kinematics given in Subsection 4.2.3 can be used to obtain ${}^{0}_{1}\mathbf{R}_{\mathbf{N}}^{\text{PU}}$. In turn, the ${}^{0}_{1}\mathbf{R}_{\mathbf{N}}^{\text{PU}}$ matrix is equal to ${}^{\text{LL}}_{\text{FT}}\mathbf{R}_{\mathbf{N}}^{\text{LEG}}$ in the ankle-exoskeleton context. The numerical matrix relating the 6R model's fifth link to its end-effector can then be extracted from a rearranged version of Equation (5.53):

$$ {}^{4}_{6}\mathbf{R}_{\mathbf{N}}^{\text{LEG}} = \left({}^{\text{LL}}_{4}\mathbf{R}^{\text{LEG}}\right)^{\text{T}}\, {}^{\text{LL}}_{\text{FT}}\mathbf{R}_{\mathbf{N}}^{\text{LEG}} \left({}^{6}_{\text{FT}}\mathbf{R}^{\text{LEG}}\right)^{\text{T}} \tag{5.59} $$

Next, using the information from Equation (5.2), a numerical ${}^{4}_{6}\mathbf{T}_{\mathbf{N}}^{\text{LEG}}$ homogeneous transform can be arranged:

$$ {}^{4}_{6}\mathbf{T}_{\mathbf{N}}^{\text{LEG}} = \left[\begin{array}{c:c} {}^{4}_{6}\mathbf{R}_{\mathbf{N}}^{\text{LEG}} & \begin{matrix} a_4 \\ d_5 \\ 0 \end{matrix} \\ \hdashline \bar{0}_{3\times1} & 1 \end{array}\right] \tag{5.60} $$

Moreover, a numerical ${}^{3}_{4}\mathbf{T}_{\mathbf{N}}^{\text{LEG}}$ transform can also be obtained, because the knee exoskeleton module directly provides the θ_4 joint angle:

$$ {}^{3}_{4}\mathbf{T}_{\mathbf{N}}^{\text{LEG}} = \begin{bmatrix} c\theta_4 & -s\theta_4 & 0 & a_3 \\ s\theta_4 & c\theta_4 & 0 & 0 \\ 0 & 0 & 1 & -d_4 \\ 0 & 0 & 0 & 1 \end{bmatrix}, \text{ where } \theta_4 = \theta^{\text{KNEE}} \tag{5.61} $$

In the previous two equations, note that a_3, a_4, d_4, and d_5 are all constants. Furthermore, ${}^{6}_{e.e}\mathbf{T}^{\text{LEG}}$ is always a matrix of constant elements, so the complete-system forward

kinematic solution is realized by successive ascending-order multiplication of the numerical transforms from Equations (5.57), (5.60), and (5.61):

$$ {}^{0}_{e.e}\mathbf{T}^{\text{LEG}}_{\mathbf{N}} = {}^{0}_{3}\mathbf{T}^{\text{LEG}}_{\mathbf{N}}\ {}^{3}_{4}\mathbf{T}^{\text{LEG}}_{\mathbf{N}}\ {}^{4}_{6}\mathbf{T}^{\text{LEG}}_{\mathbf{N}}\ {}^{6}_{e.e}\mathbf{T}^{\text{LEG}} \tag{5.62} $$

Figure 5.6 summarizes the complete-system forward kinematics procedure in the form of a block diagram. In the figure, $f^{\text{ABC}}_{\text{F.K.}}(\ )$ denotes the forward kinematic algorithm for the ABC subsystem (i.e., where ABC is either LEG, PU, or SAE).

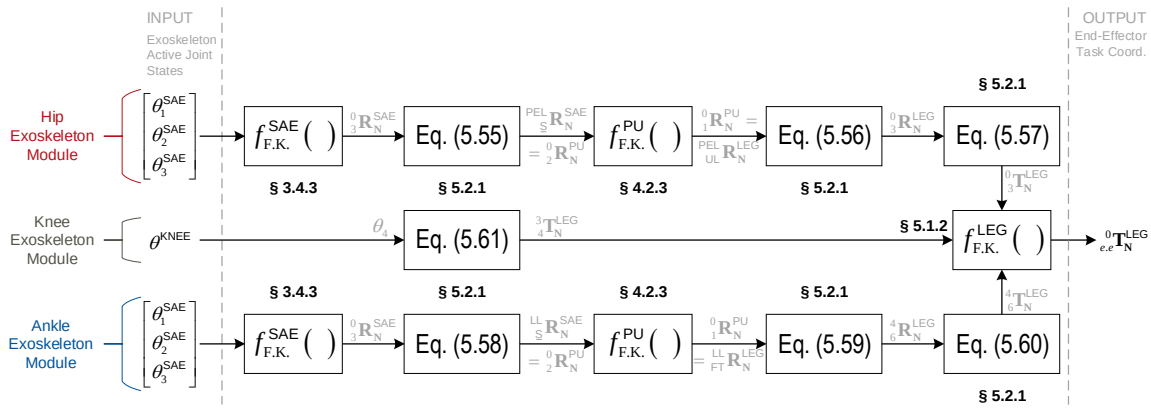

Figure 5.6. Block diagram for the complete-system forward kinematic analysis

Walking Gait Simulation based on the 6R Lower-Limb Model

To provide an indication of the correctness of the complete-system kinematic analysis, a walking gait simulation was developed. To start, SolidWorks models for the exoskeleton and human limb were developed, where the latter was based on 3D scans of a custom-articulated lower-body mannequin. These models were saved in stereolithography (STL) format to facilitate simulation within the MATLAB environment. A trajectory for the foot was then generated using data obtained from a walking gait simulation available in the open-source biomechanical simulation software, OpenSim [82], [182]. The complete-system inverse kinematics procedure was then performed to generate joint angle trajectories for 6R manipulator joints and the exoskeleton's active joints. Subsequently, the complete-system forward kinematics was used to determine the positions and orientations of all the system links relative to the global reference frame throughout the gait-motion cycle. This information was then applied to graphically animate the system motions. Figure 5.7 shows the starting configuration of the simulation model overlaid with a 3D plot of the end-effector path. Figure 5.8 shows a sequence of screens captured during the gait simulation for the exoskeleton-limb system. Note that the exoskeleton is mounted to the left leg in the simulation, so

adjustments to the 6R kinematic analyses and rotation constants of Equations (5.43)–(5.49) were made accordingly. Moreover, the ankle exoskeleton module was placed posteriorly instead of laterally from the shank, so the rotation values used in Equations (5.47)–(5.49) were correspondingly modified. Note that the simulation model also features a simple RPR/R planar parallel manipulator at the knee exoskeleton-body interface; the analysis of this manipulator is not discussed here because it was not implemented in the final exoskeleton design. Table 5.3 provides a listing of the DH parameter values associated with the 6R simulation model.

Figure 5.7. Overlay 3D plot of the complete-system model and the end-effector path for the walking gait simulation

Table 5.3. DH parameter values for the 6R manipulator in the simulation model

Parameter	a_0	d_1	a_3	d_4	a_4	d_5	a_6	$d_{e.e}$
Value (mm)	98.02	175.9	426.7	23.42	426.7	20.00	199.4	0.2497

Note: The lower-body mannequin on which the 6R model for the simulation is based is not representative of a typical human morphology. So, different values are used in Equation (5.40) to evaluate 6R singularities.

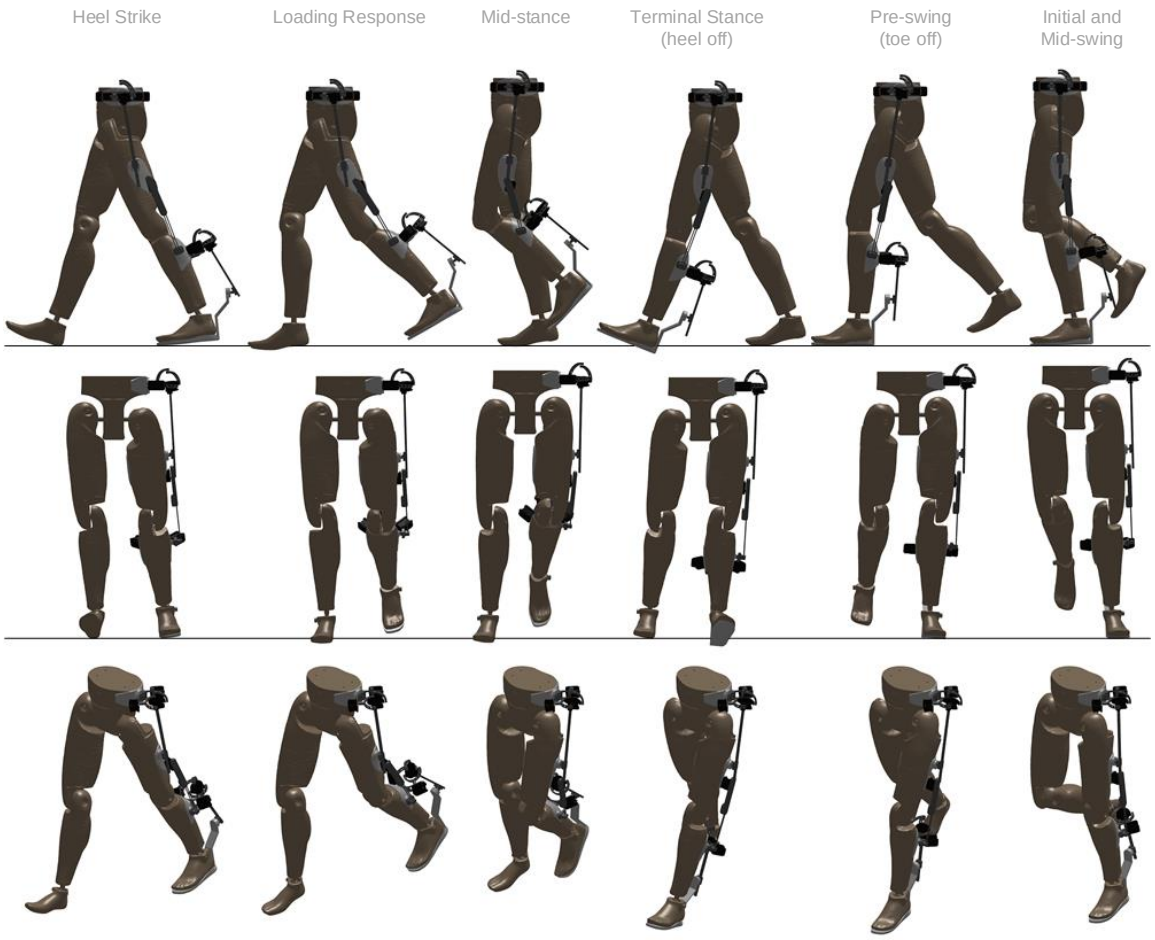

Figure 5.8. Side (top), front (middle), and isometric (bottom) views of the complete-system simulation model performing walking gait motions

5.2.2. Complete System Forward Kinematics with a SRS Experimentation Model for the Human Lower Limb

To facilitate the presentation of experimental results obtained from a prototype exoskeleton system, as is done in Chapter 6, a second model for the human lower limb is considered here. This model comprises a serial chain of a spherical joint, revolute joint, and another spherical joint, producing a SRS manipulator structure. By preserving the link lengths and offsets from the 6R model, the experimentation model is functionally equivalent, except the adduction/abduction capability of anatomical ankle is now taken into consideration. This DOF was excluded from the first model because its movements are limited in the context of general human mobility, and its inclusion would produce an infinity of solutions to the inverse kinematics problem. However, exoskeletal motion-capture only makes use of the forward kinematics solution, which is trivial for an open-

chain serial manipulator, so the third DOF of the ankle is taken into consideration for the added generality it provides. Moreover, the new model makes full use of the ankle exoskeleton module's 3-DOF sensing capability. Figure 5.9 shows a schematic illustration of the complete exoskeleton-limb system with the SRS model for the human lower limb.

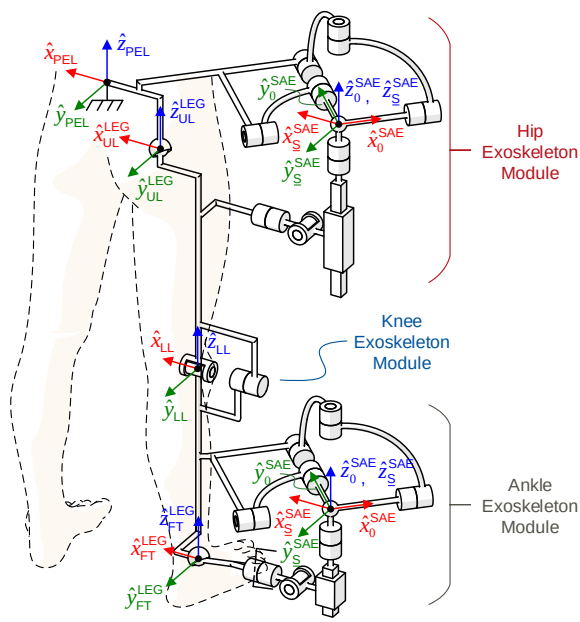

Figure 5.9. Schematic of the complete exoskeleton-limb system with a SRS model for the human lower limb and important frame labels

Note: Like in Figure 5.4, the various systems links are intentionally disproportionate to facilitate visualization of the manipulator and frame attachments.

Experimentation Model Forward Kinematic Analysis

In the literature, anatomical limb posture measurements are typically reported as the corresponding joint angles relative to a neutral-standing posture. To achieve this form of presentation for the forward kinematics results, the complete system with the SRS leg model makes use of the same {PEL}, $\{UL\}^{LEG}$, {LL}, $\{FT\}^{LEG}$, and $\{S\}^{SAE}$ frames as introduced in Subsection 5.2.1. Note the visibility of these frames in Figure 5.9. Furthermore, the forward kinematics solution for this experimentation model proceeds in the same manner as presented in Subsection 5.2.1. However, the process is truncated at the points that ${}^{PEL}_{UL}\mathbf{R}^{LEG}_{N}$ and ${}^{LL}_{FT}\mathbf{R}^{LEG}_{N}$ are obtained. That is, Equations (5.56), (5.57), (5.59), and (5.60), as well as the 6R model's forward kinematic algorithm from Subsection 5.1.2, are not used here.

Instead, anatomical joint angle measurements are taken directly from the ${}^{\text{PEL}}_{\text{UL}}\mathbf{R}_{\mathbf{N}}^{\text{LEG}}$ and ${}^{\text{LL}}_{\text{FT}}\mathbf{R}_{\mathbf{N}}^{\text{LEG}}$ matrices using the Tait-Bryan roll-pitch-yaw convention. This method can be interpreted as an intrinsic *Z-Y'-X"* ordering of rotations, such that the two rotation matrices are represented symbolically as:

$$
{}^{\text{PEL}}_{\text{UL}}\mathbf{R}_{\mathbf{S}}^{\text{SRS}} = \mathbf{R}_Z\left(\theta_1^{\text{SRS}}\right)\mathbf{R}_{Y'}\left(\theta_2^{\text{SRS}}\right)\mathbf{R}_{X''}\left(\theta_3^{\text{SRS}}\right) =
$$

$$
\begin{bmatrix} c\theta_1^{\text{SRS}}c\theta_2^{\text{SRS}} & c\theta_1^{\text{SRS}}s\theta_2^{\text{SRS}}s\theta_3^{\text{SRS}} - s\theta_1^{\text{SRS}}c\theta_3^{\text{SRS}} & c\theta_1^{\text{SRS}}s\theta_2^{\text{SRS}}c\theta_3^{\text{SRS}} + s\theta_1^{\text{SRS}}s\theta_3^{\text{SRS}} \\ s\theta_1^{\text{SRS}}c\theta_2^{\text{SRS}} & s\theta_1^{\text{SRS}}s\theta_2^{\text{SRS}}s\theta_3^{\text{SRS}} + c\theta_1^{\text{SRS}}c\theta_3^{\text{SRS}} & s\theta_1^{\text{SRS}}s\theta_2^{\text{SRS}}c\theta_3^{\text{SRS}} - c\theta_1^{\text{SRS}}s\theta_3^{\text{SRS}} \\ -s\theta_2^{\text{SRS}} & c\theta_2^{\text{SRS}}s\theta_3^{\text{SRS}} & c\theta_2^{\text{SRS}}c\theta_3^{\text{SRS}} \end{bmatrix} \tag{5.63}
$$

and ${}^{\text{LL}}_{\text{FT}}\mathbf{R}_{\mathbf{S}}^{\text{SRS}} = \mathbf{R}_Z\left(\theta_5^{\text{SRS}}\right)\mathbf{R}_{Y'}\left(\theta_6^{\text{SRS}}\right)\mathbf{R}_{X''}\left(\theta_7^{\text{SRS}}\right) =$

$$
\begin{bmatrix} c\theta_5^{\text{SRS}}c\theta_6^{\text{SRS}} & c\theta_5^{\text{SRS}}s\theta_6^{\text{SRS}}s\theta_7^{\text{SRS}} - s\theta_5^{\text{SRS}}c\theta_7^{\text{SRS}} & c\theta_5^{\text{SRS}}s\theta_6^{\text{SRS}}c\theta_7^{\text{SRS}} + s\theta_5^{\text{SRS}}s\theta_7^{\text{SRS}} \\ s\theta_5^{\text{SRS}}c\theta_6^{\text{SRS}} & s\theta_5^{\text{SRS}}s\theta_6^{\text{SRS}}s\theta_7^{\text{SRS}} + c\theta_5^{\text{SRS}}c\theta_7^{\text{SRS}} & s\theta_5^{\text{SRS}}s\theta_6^{\text{SRS}}c\theta_7^{\text{SRS}} - c\theta_5^{\text{SRS}}s\theta_7^{\text{SRS}} \\ -s\theta_6^{\text{SRS}} & c\theta_6^{\text{SRS}}s\theta_7^{\text{SRS}} & c\theta_6^{\text{SRS}}c\theta_7^{\text{SRS}} \end{bmatrix} \tag{5.64}
$$

Therefore, if the numerical elements of the ${}^{\text{PEL}}_{\text{UL}}\mathbf{R}_{\mathbf{N}}^{\text{LEG}}$ and ${}^{\text{LL}}_{\text{FT}}\mathbf{R}_{\mathbf{N}}^{\text{LEG}}$ matrices are defined by:

$$
{}^{\text{PEL}}_{\text{UL}}\mathbf{R}_{\mathbf{N}}^{\text{LEG}} = \begin{bmatrix} q_{11} & q_{12} & q_{13} \\ q_{21} & q_{22} & q_{23} \\ q_{31} & q_{32} & q_{33} \end{bmatrix} \text{ and } {}^{\text{LL}}_{\text{FT}}\mathbf{R}_{\mathbf{N}}^{\text{LEG}} = \begin{bmatrix} r_{11} & r_{12} & r_{13} \\ r_{21} & r_{22} & r_{23} \\ r_{31} & r_{32} & r_{33} \end{bmatrix} \tag{5.65}
$$

then the solutions for θ_1^{SRS}, θ_2^{SRS}, θ_3^{SRS}, θ_5^{SRS}, θ_6^{SRS}, and θ_7^{SRS} are:

$$
\theta_2^{\text{SRS}} = \operatorname{atan2}\left(-q_{31}, \pm\sqrt{q_{11}^2 + q_{21}^2}\right),\ \theta_1^{\text{SRS}} = \operatorname{atan2}\left(\frac{q_{21}}{c\theta_2^{\text{SRS}}}, \frac{q_{11}}{c\theta_2^{\text{SRS}}}\right),
$$

$$
\theta_3^{\text{SRS}} = \operatorname{atan2}\left(\frac{q_{32}}{c\theta_2^{\text{SRS}}}, \frac{q_{33}}{c\theta_2^{\text{SRS}}}\right) \tag{5.66}
$$

$$
\theta_6^{\text{SRS}} = \operatorname{atan2}\left(-r_{31}, \pm\sqrt{r_{11}^2 + r_{21}^2}\right),\ \theta_5^{\text{SRS}} = \operatorname{atan2}\left(\frac{r_{21}}{c\theta_6^{\text{SRS}}}, \frac{r_{11}}{c\theta_6^{\text{SRS}}}\right), \text{ and}
$$

$$
\theta_7^{\text{SRS}} = \operatorname{atan2}\left(\frac{r_{32}}{c\theta_6^{\text{SRS}}}, \frac{r_{33}}{c\theta_6^{\text{SRS}}}\right) \tag{5.67}
$$

The selection of the positive square root terms for θ_2^{SRS} and θ_6^{SRS} is appropriate and robust; it produces hip adduction/abduction and ankle pronation/supination measurements within [–90 90] degrees, which completely encompasses the anatomical ranges-of-motion for these DOFs. Finally, the forward kinematics solution is completed by equating the knee exoskeleton's active joint measurement to the anatomical knee-joint angle:

$$
\theta_4^{\text{SRS}} = \theta^{\text{KNEE}} \tag{5.68}
$$

Table 5.4 provides the correspondence between the experimentation model's lower-limb joint angles and the anatomical motions outlined in Figure 2.7.

Table 5.4. Correlation between experimentation model joint rotations and anatomical motions for the human right-side lower limb

	Hip			*Knee*	*Ankle*		
Model Joint Rotation:	$+\theta_1^{\text{SRS}}$	$+\theta_2^{\text{SRS}}$	$+\theta_3^{\text{SRS}}$	$+\theta_4^{\text{SRS}}$	$+\theta_5^{\text{SRS}}$	$+\theta_6^{\text{SRS}}$	$+\theta_7^{\text{SRS}}$
Anatomical Motion:	Int. Rot.	Abd.	Ext.	Flex.	Add.	Pro.	Pla.
Model Joint Rotation:	$-\theta_1^{\text{SRS}}$	$-\theta_2^{\text{SRS}}$	$-\theta_3^{\text{SRS}}$	$-\theta_4^{\text{SRS}}$	$-\theta_5^{\text{SRS}}$	$-\theta_6^{\text{SRS}}$	$-\theta_7^{\text{SRS}}$
Anatomical Motion:	Ext. Rot.	Add.	Flex.	Ext.	Abd.	Sup.	Dor.

Note: The anatomical motion abbreviations are clarified in the List of Acronyms.

5.2.3. Practical Considerations for the Complete System

When the exoskeleton system moves from the computer-based simulation environment towards physical implementation, there are a few characteristics of the system model and design that demand particular attention.

Exoskeleton-Limb Connections

To start, the models depicted in Figure 5.4 and Figure 5.9 show rigid connections between the human limb segments and the adjacent base and output links of the exoskeleton modules. In practice, these connections should be realized in a non-invasive manner that closely approximates a rigid attachment without causing undue discomfort to the human subject. The chosen approach is to utilize orthotics that fit tightly to the subject's pelvis, thigh, shank, and foot. In fitting these orthotics to the subject's body, care should be taken to align the exoskeleton modules with the body planes, as intended by the experimentation model. Specifically, since they are treated as known design parameters, the attachment orientations of the hip exoskeleton module relative to the pelvis and the ankle module relative to the shank should be made mindfully. The base links of these modules are designed to support a proper alignment, so this only involves wearing the orthotics to appropriately align with the subject's transverse, coronal, and sagittal planes. The relative positions of the SAE COR and target body joint must then be measured with respect to the body frames, as these coordinates are taken to be known constants in the kinematic analyses of the motion-transfer manipulator. Additionally, the knee exoskeleton's active joint axis should be fitted with respect to the flexion/extension axis of the subject's knee such that axial misalignments are minimized (i.e., insofar as is possible, given the translational nature of the anatomical knee axis). Anatomical landmarks on the subject's lower limb (e.g., bony prominences of the greater trochanter external surface at the hip, medial epicondyle and

lateral epicondyle at the knee, etc.) are used to facilitate these joint position measurements and axial alignments.

Zero-Angle Establishment at the Neutral-Standing Posture

Another important consideration is that, in practice, the subject's leg generally does not achieve its neutral-standing posture when the exoskeleton subsystems are posed in their home configurations. One might erroneously assume this is the case based on the schematic of Figure 5.9, for which attachments and alignments are exact. The adopted approach for handling this issue is to instruct the motion-capture subject to assume a neutral-standing posture for the first several seconds of each capture session. From within this period of steady neutral posture, the exoskeleton's active joint angles are used in the complete-system forward kinematic algorithm to produce neutral-standing orientation measurements for the hip and ankle joints: ${}^{\text{PEL}}_{\text{UL}}\mathbf{R}^{\text{LEG}}_{\text{N}}\left(\vec{q}_{\text{NEUTRAL}}\right)$ and ${}^{\text{LL}}_{\text{FT}}\mathbf{R}^{\text{LEG}}_{\text{N}}\left(\vec{q}_{\text{NEUTRAL}}\right)$. Here, $\vec{q}_{\text{NEUTRAL}}$ is a vector containing the angular position states of each active joint in the exoskeleton when the subject's lower limb is posed in its neutral-standing posture. These matrices are then treated as constant rotations for the remainder of a motion capture session. By post-multiplying each subsequent ${}^{\text{PEL}}_{\text{UL}}\mathbf{R}^{\text{LEG}}_{\text{N}}$ measurement by $\left({}^{\text{PEL}}_{\text{UL}}\mathbf{R}^{\text{LEG}}_{\text{N}}\left(\vec{q}_{\text{NEUTRAL}}\right)\right)^{\text{T}}$ and ${}^{\text{LL}}_{\text{FT}}\mathbf{R}^{\text{LEG}}_{\text{N}}$ measurement by $\left({}^{\text{LL}}_{\text{FT}}\mathbf{R}^{\text{LEG}}_{\text{N}}\left(\vec{q}_{\text{NEUTRAL}}\right)\right)^{\text{T}}$, the resulting values for θ_i^{SRS}, i = 1, 2, 3, 5, 6, and 7, are relative to the recorded neutral-standing posture. For example, when this neutral posture is achieved, the post-multiplication yields $\mathbf{I}_{3\times3}$, which in turn produces a set of anatomical joint angles with all zero values; this is the desired result for the neutral-standing posture.

Exoskeleton-Limb Workspace in Relation to the Leg's Anatomical Motions

Next, it is important to consider the target-anatomical-joint range-of-motion permitted by the workspace of the SAE-PU exoskeleton module when it is interfaced with a human subject. Ideally, the exoskeleton should allow the user to move through their complete ranges-of-motion for each target-joint DOF without reaching or coming into close proximity of an SAE singular configuration. Recall from Section 3.6 that singular conditions are met when either $\theta_1^{\text{SAE}} = 90° + d180°$ or $\theta_2^{\text{SAE}} = 90° + d180°$, where d is an integer. To facilitate a workspace check for the proposed exoskeleton design and to prepare for system prototyping, a detailed SolidWorks model of the exoskeleton-human system was developed. The design parameters associated with the model's hip exoskeleton module are listed in Table 5.5.

Table 5.5. Hip-exoskeleton-module design-parameter selections for the workspace and singularity considerations

Design Parameter (from Section 4.2)	Value Used for Workspace/Singularity Investigations (mm)
$x_{1\to 2}$	–134.02
$y_{1\to 2}$	–9.99
$z_{1\to 2}$	118.34
l_o	22.06
l_r	263.72

To begin an evaluation of the exoskeleton's workspace in relation to the human leg, the model's lower limb was configured to each of the hip's individual DOF limits (see Figure 2.7 in Section 2.1.2). Table 5.6 provides the corresponding angular positions of the hip exoskeleton's active joints, as measured within the SolidWorks model. During this set of pure body-plane rotations, the closest proximity to a singular condition in the SAE occurs when the model's hip joint is flexed to 120 degrees, which corresponds with a 76.23-degree angle for θ_1^{SAE}. The other hip motions cause θ_1^{SAE} and θ_2^{SAE} values to remain well within the [–90 90] degree range, the limits of which represent singularities. This provides a preliminary indication that the proposed exoskeleton supports the lower limb's full range-of-motion without encountering a singular configuration.

Table 5.6. Hip-exoskeleton-module active-joint angles associated with the individual rotational limits of each anatomical hip DOF when Table 5.5 parameters are asserted

Hip DOF Limit	J_1^{SAE} Angle, θ_1^{SAE} (deg)	J_2^{SAE} Angle, θ_2^{SAE} (deg)	J_3^{SAE} Angle, θ_3^{SAE} (deg)
Extension = 20 deg	–17.03	–8.96	2.25
Flexion = 120 deg	76.23	17.59	35.20
Abduction = 45 deg	–37.45	16.40	–10.98
Adduction = 45 deg	14.15	–19.33	0.18
Int. Rot. = 30 deg	3.79	8.46	29.91
Ext. Rot. = 60 deg	–10.93	–25.41	–54.18

Note: The J_3^{SAE} joint angle does not contribute to the development of singular configurations in the SAE.

To further investigate whether the exoskeleton design should be expected to accurately track target-joint angles through their complete range-of-motion without restriction, a reachable workspace plot is developed for the hip exoskeleton module. To start, this analysis applies limits on each of the module's active joints as follows:

$$\theta_1^{\text{SAE}} \in [-85° \quad 85°],\ \theta_2^{\text{SAE}} \in [-85° \quad 85°] \text{ and } \theta_3^{\text{SAE}} \in [-150° \quad 150°] \tag{5.69}$$

The selected ranges for θ_1^{SAE} and θ_2^{SAE} ensure that the workspace does not include any SAE singularities, while the that for θ_3^{SAE} is based on the approximate range of the revolute sensors employed in the prototype system, to be discussed further in Chapter 6.

The analysis proceeds by iteratively conducting the complete-system forward kinematic algorithm (i.e., to the point at which ${}^{\text{PEL}}_{\text{UL}}\mathbf{R}_{\mathbf{N}}^{\text{SAE}}$ is solved) for each pairing of the active-joint angles within their Equation (5.69) ranges and using 1-degree incrementation. Next, assuming the knee center lies at a point of unit-length distance directly below the hip, the partial-sphere surface of attainable knee positions is given by the collection of points:

$$\vec{\mathrm{p}}_{knee} = {}^{\text{PEL}}_{\text{UL}}\mathbf{R}_{\mathbf{N}}^{\text{SAE}}\begin{bmatrix}0 & 0 & -1\end{bmatrix}^{\mathrm{T}} \text{ for each } {}^{\text{PEL}}_{\text{UL}}\mathbf{R}_{\mathbf{N}}^{\text{SAE}} \tag{5.70}$$

The left side of Figure 5.10 shows the benchmark range-of-motion for a healthy human hip reported by Turley et al. in [189]; that study considers similar hip-motion limits as those assumed in this thesis. The middle image of Figure 5.10 presents a 3D scatterplot of the results from the workspace analysis described above overlaid with the benchmark. Note that the middle image's exoskeleton-hip workspace surface offers a visualization of the extents of hip extension/flexion and abduction/adduction, but the extent of hip rotation cannot be depicted in this 3D-plot format (i.e., the orientation of the knee is not specified). Therefore, to help clarify the workspace, the right-side image of Figure 5.10 shows the system workspace after removing data points that are only attainable with a hip-rotation angle beyond the normal limits depicted in Figure 2.7; clearly, atypical ranges in the other DOFs are still considered here in the right-side plot. As expected, this restriction removes data points from the edges of the workspace surface, which correspond to the most extreme-angle postures. Also, the hip-rotation angles were computed using an order of rotations consistent with [189] to facilitate comparison with the range-of-motion benchmark.

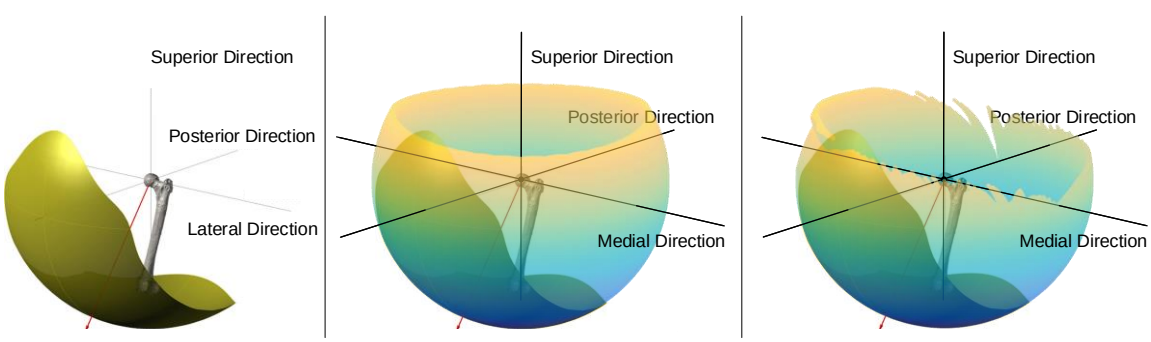

Figure 5.10. Healthy range-of-motion benchmark for the human hip (left), hip workspace permitted by the exoskeleton when Table 5.5 parameters and Equation (3.19) active-joint ranges are asserted (middle), and the permitted workspace after removing atypical hip rotations (right)

Note: The range-of-motion benchmark considers the left hip while the hip exoskeleton module workspace considers the right hip, so lateral and medial directions are swapped. However, the benchmark displays mirror-symmetry about the sagittal plane, so the comparison is still valid.

Upon comparing the considered exoskeleton-hip workspace with the benchmark, it is apparent that the hip exoskeleton module permits the vast majority of healthy-hip postures, along with many postures outside of the healthy range, without encountering a singular configuration. However, the benchmark range extends beyond the computed exoskeleton-hip workspace in both the middle- and right-side images for some postures near the upper-limit of hip flexion. This finding does not indicate that the hip exoskeleton module restricts joint motions to those postures, because the range of the revolute sensors constituting J_1^{SAE} and J_2^{SAE} is larger than that asserted to the joints during the workspace computation. Although, this lack of workspace overlap with the benchmark does suggest that the SAE requires a closer proximity to a singular configuration before those high-flexion postures are attainable. Note the discrepancy between the Figure 5.10 results and those of Table 5.6, which predicts that the exoskeleton can attain 120 degrees of hip flexion without exceeding the ±85-degree thresholds for J_1^{SAE} or J_2^{SAE}. This disagreement arises despite consistent use of design parameters because the SolidWorks model inherently incorporates a rotational offset in the SAE when the human achieves neutral-standing posture (i.e., $\vec{q}_{NEUTRAL}$), whereas the reachable workspace analysis does not take this into account. This difference in approach between the two workspace investigations is intentional, because it helps highlight why these analyses have limited ability to predict the actual workspace of a physical human-interfaced system. These limitations are further elaborated after the discussion on SAE singularities in relation to lower-limb postures in the next low-level subsection.

The ankle joint has smaller ranges-of-motion than the hip, especially in the sagittal-plane DOF (i.e., plantarflexion/dorsiflexion – see Figure 2.7). Thus, the proposed exoskeleton design is likely to support its complete ranges-of-motion given the large exoskeleton-module workspace demonstrated in Figure 5.10. So, in the interest of brevity, a workspace analysis for the ankle exoskeleton module is not included here. Additionally, as the knee exoskeleton module simply involves a sensor aligned coaxially with the anatomical joint, provision of a complete range-of-motion is ensured by the selection of a sensor with equal or greater rotation range than the knee. Ultimately, the main takeaways from these workspace-analysis exercises are that the exoskeleton is expected to provide kinematic compliance with the human lower limb through the complete range-of-motion in each of its DOFs, but the hip exoskeleton module may approach a singular configuration in its SAE when the hip is flexed to large angles. The

next paragraphs explore this further by considering how hip-exoskeleton singularities map to postures in the anatomical joint.

SAE Singularities in Relation to Lower-Limb Postures

Recall from Section 3.6 that singular conditions in the SAE materialize as either an inverse kinematic singularity if $\theta_2^{\text{SAE}} = 90° + d180°$ or a combined singularity when $\theta_1^{\text{SAE}} = 90° + d180°$ and $\theta_2^{\text{SAE}} = d180°$, d is an integer. Starting with the former, Figure 5.11 illustrates two example postures that occur when θ_2^{SAE} is set to ±90 degrees within the SolidWorks model developed for the exoskeleton-human system. As shown in the figure, both postures involve significantly exceeding at least one of the rotational limits among the hip joint's DOFs. Note that these are only two of an infinite number of postures associated with the inverse kinematic singularity in the hip exoskeleton module's SAE, because the orientation manipulator's J_1^{SAE} and J_3^{SAE} active joints may assume any angular position within their respective ranges without affecting the singular condition. However, these maintained DOFs in the SAE tend to only influence rotations about the thigh's longitudinal axis. So, the system is expected to avoid the hip exoskeleton module's inverse kinematic singularities throughout the anatomical hip joint's healthy range-of-motion.

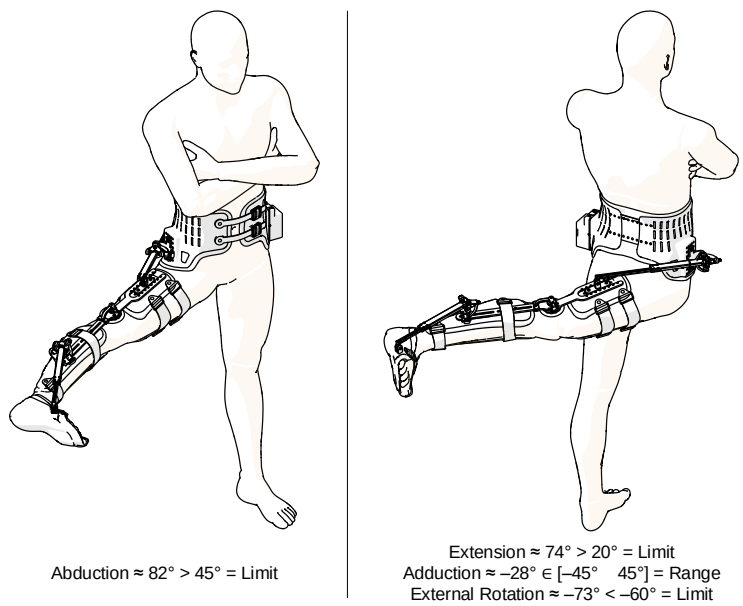

Figure 5.11. Example lower-limb postures associated with the inverse kinematic singularities of the hip exoskeleton module's SAE for θ_2^{SAE} = 90 degrees (left) and θ_2^{SAE} = –90 degrees (right)

Note: The hip rotation angles corresponding to both images and their relation to the anatomical upper limits or ranges from Figure 2.7 are indicated.

Next, Figure 5.12 presents a series of thigh postures associated with the combined singularity in the hip exoskeleton module's SAE. Although this condition causes the J_2^{SAE} active joint to become locked, it introduces an unsensed DOF about $\hat{y}_2^{SAE}$ to the manipulator's end-effector and permits J_3^{SAE} rotations as well. As such, there again exists an infinity of thigh postures associated with the singularity. These postures are generally limited to those outside of the hip's typical range-of-motion. Considering the leftmost image in Figure 5.12, the hyper-abducted thigh can rotate towards the posterior about the vertical while maintained the SAE's combined singularity; however, such postures are well outside of the hip's normal motions. Alternatively, the thigh can move anteriorly as shown in the right three images of Figure 5.12. Although the hip tends to remain hyper-flexed and/or hyper-rotated in these loci of the combined singularity, it approaches or possibly encroaches on the hip's anatomical workspace near the postures illustrated in the middle two images. Note that the introduced DOF within the SAE for the combined singularity results in no significant differences between the +90-degree and –90-degree cases for θ_1^{SAE} (i.e., the rotational difference can be counteracted by the free rotation about $\hat{y}_2^{SAE}$).

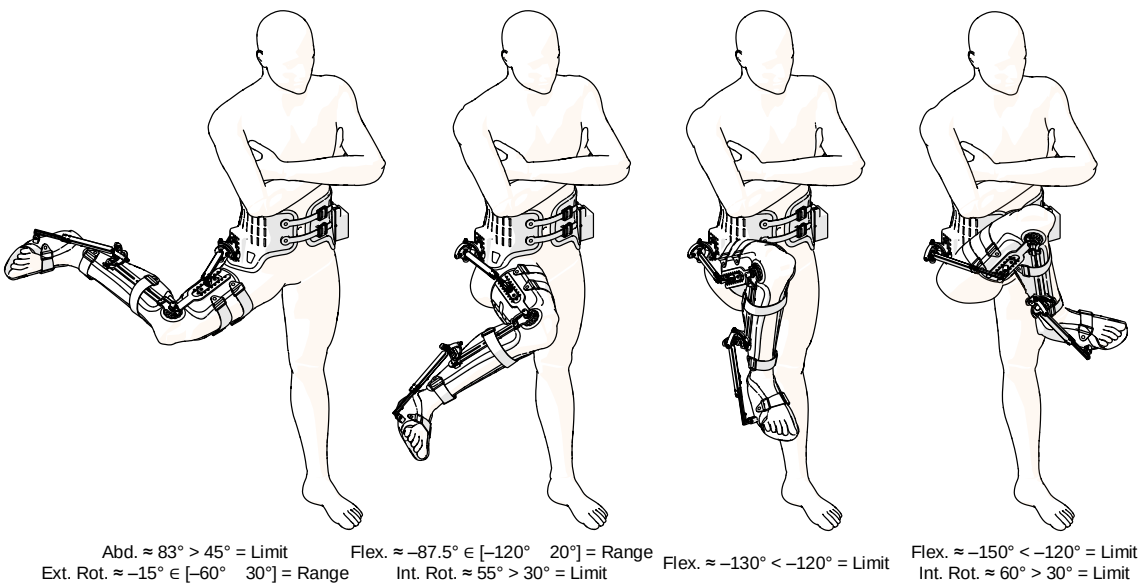

Figure 5.12. Example lower-limb postures associated with the combined singularities of the hip exoskeleton module's SAE

Note: The hip rotation angles corresponding to each image and their relation to the anatomical upper limits or ranges from Figure 2.7 are indicated.

In agreement with the results from the workspace analyses above, the Figure 5.12 findings provide further evidence that the proposed exoskeleton may approach a

singular configuration during movements involving large hip flexion. Since the ankle exoskeleton module oriented with respect to its target joint in the same manner as the hip module and ankle plantarflexion/dorsiflexion has a significantly reduced range relative to hip flexion/extension, this issue is not expected for the ankle exoskeleton module. However, although their considerations are important, the practical utility of the specific results obtained during these workspace and singularity analyses is limited. The numeric values obtained are dependent on the design parameters listed in Table 5.5 as well as the SAE orientation that corresponds with a neutral-standing posture of the subject. In practice, all these quantities vary on an intra- and inter-subject basis and are ultimately determined by the wearer's individual morphology and orthotic attachment decisions. Thus, aside from brevity and its reduced ranges-of-motion relative to the hip, another reason for excluding the ankle joint from the workspace and singularity analyses is the limited usefulness associated with the specific numerical results. Also note that singularities are not applicable for the single-joint knee exoskeleton module.

In the end, the workspace and singularity evaluations suggest that the exoskeleton manipulator is expected to offer complete kinematic compliance with each major DOF of the lower limb and not impose restrictions on their full ranges-of-motions. Additionally, the hip exoskeleton module may approach a singular configuration when the hip is flexed to great extents; proximity to such a singular condition is expected to diminish the exoskeleton's MoCap-measurement accuracy, but the severity of the degradation is unclear. The ultimate test of the exoskeleton's functionality in these aspects is to construct a physical prototype of the proposed design and evaluate its performance in the presence of the various nuances associated with real-world application that the system models overlook.

With the sum of these practical considerations in mind, a physical prototype of the exoskeleton system was developed. Its efficacy as a motion capture device was then tested in an experimentation setting, using the complete-system forward kinematic solution for the experimentation model to process the exoskeleton's sensor data. The relevant materials on these matters are presented next in Chapter 6.

Chapter 6.

Prototype Development and Efficacy Study of a Hybrid-Manipulator Exoskeleton as a Lower-Limb Motion-Capture System

To verify the forward kinematic accuracy of the selected exoskeleton manipulator in an applied scenario, a prototype system was developed and tested alongside an optical motion capture (MoCap) system. The experiment was designed to evaluate the efficacy of the exoskeleton as a motion capture device. Recall from Chapters 1 and 2 that such a passive (i.e., non-motorized) motion-capturing exoskeleton is a beneficial precursor to an active one, because it provides a low-cost assessment of the exoskeleton's ability to accurately detect the wearer's lower-limb posture; the ability of an active-exoskeleton counterpart to control fine movements and maintain balance during mobility assistance depends on this accurate detection of limb posture. Aside from assistive applications, the exoskeleton's inherent mechanical connection to the human body also yields the opportunity for a low-power active version to provide haptic feedback functionality in virtual reality or augmented reality applications. Moreover, a sufficiently accurate passive exoskeleton that can track all rotations of multi-DOF joints may be an attractive alternative to other MoCap solutions in its own right. Sections 6.1 and 6.2 respectively detail the prototype system development and the experimental proceedings for verifying its proper functionality and measurement accuracy.

6.1. Novel Motion Capture Exoskeleton Prototyping

6.1.1. Mechanical Design

The prototype's mechanical design can be considered modularly as the combination of hip exoskeleton, knee exoskeleton, and ankle exoskeleton subsystems. As depicted in the SolidWorks model of Figure 6.1, the hip and ankle exoskeleton module designs are based on the hybridized Simplified Agile Eye (SAE) manipulator selected in Chapter 3 and the PU motion-transfer manipulator discussed in Chapter 4. Consequentially, the overall mechanism architecture for these modules is (<u>R</u>R-<u>R</u>RR)<u>R</u>PU/S, where the underlines identify joints with position sensors and '/S' indicates

the spherical constraint asserted on the exoskeleton module by its connection to the anatomical spherical joint. This connection is formed by mechanical attachments to orthotics worn by the subject on body segments superiorly and inferiorly surrounding the targeted joints. That is, for the hip module, the SAE base is attached to a pelvis orthotic and the PU transfer manipulator's end-effector is attached to a thigh orthotic; meanwhile, the SAE base and PU end-effector attach to a shank orthotic and foot orthotic, respectively, for the ankle module. Next, the knee exoskeleton module simply consists of a sensed revolute joint with its axis of rotation coincident to that of the biological knee joint. Recall from Chapter 5 that the biological knee is considered here as a single degree-of-freedom joint.

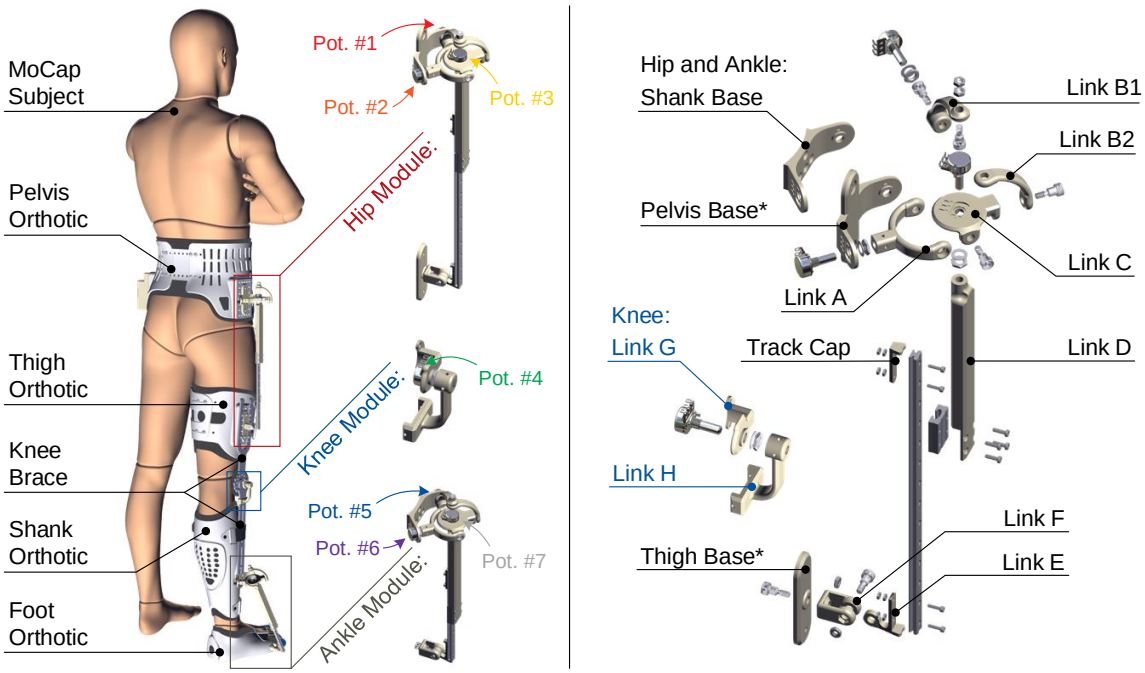

Figure 6.1. SolidWorks model of the MoCap exoskeleton's mechanical design with potentiometer numbering convention (left) and exploded view of module components (right)

Note: Components in the right-side image marked with an asterisk (*) are included in the hip module but not in the ankle module; the Shank Base is only used in the ankle module.

In terms of component composition, all the exoskeleton linkages are 3D-printed from ABSplus thermoplastic filament using the uPrint machine at Simon Fraser University's Mechatronic Machining and Testing Centre. The sensed exoskeleton joints are composed of Mode Electronics rotary potentiometers with linear 10kΩ resistance. At one end, each potentiometer housing is fastened to its proximal linkage by way of a nut tightened to the fixed and threaded portion its shaft; at the other end, the joint's distal

linkage is press-fitted to the rotating portion of the potentiometer shaft. The left side of Figure 6.1 shows the numbering convention applied to the potentiometers. All unmeasured rotary joints are realized using concentric contact surfaces between the distal linkage and a nylon shoulder screw press-fitted to the proximal linkage. The hip and ankle exoskeleton's prismatic joints are made from a sleeve bearing carriage mounted to a 9mm-wide anodized aluminum guide rail. Finally, the orthotics to which the exoskeleton modules attach are taken from an Ober leg brace; originally, the shank and foot orthotics were combined, so the piece was cut to separate it into two orthotics.

Each exoskeleton module is attached to the orthotics surrounding its target joint using bolts, except for the knee exoskeleton which is respectively bolted and press-fitted to the upper and lower portions of the Ober knee brace pieces. Additionally, the knee brace is bolted to the thigh and shank orthotics at its upper and lower ends, respectively. Bolts are also used within the hip and ankle exoskeletons to fix adjacent 3D-printed parts to the prismatic joint's carriage and track; this includes a cap part on the top of the track to prevent it from passing completely through the carriage and separating the module. Table 6.1 provides a bill of materials and summary of costs for the MoCap exoskeleton prototype at the time of purchase in May 2017, including electrical components [190]–[203]. The right side of Figure 6.1 specifies the 3D-printed part naming convention used in the bill of materials, excluding the electrical housing case. Note that the expense of most of these items would be reduced for a hypothetical marketable version of the MoCap exoskeleton, because the components would be sourced in bulk quantities. Moreover, 3D-print prototyping, leg-brace orthotics, and precision sleeve-bearings, the latter two of which comprise 70.5% of the prototype cost, would be replaced with more cost-effective alternatives to help reduce the expense.

6.1.2. Electrical Design

As shown in the electrical schematic of Figure 6.2, the core electrical components of the MoCap exoskeleton are: the seven rotary potentiometers, a microcontroller unit (MCU) board, a microSD shield, a normally-open pushbutton, a manual rocker switch, and a 9V power source. Each potentiometer provides voltage readings proportional to the angle of the joint that it mechanically comprises, as detailed in the previous subsection. The high and low voltage pins of each potentiometer are wired to the 5V and ground pins of the MCU board, respectively; the potentiometers'

wiper pins are sequentially wired to the A0–A6 analog input ports of the MCU in ascending numeric order. An Arduino Mega was selected for the MCU to digitize the potentiometer readings through analog-to-digital conversion (ADC) and transfer this raw data to a computer for processing. This board was chosen primarily for its sufficient number of on-board analog input ports (i.e., 16) to measure all 14 of the assumed DOFs associated with two human lower limbs, although the prototype only measures 7 DOFs of one lower limb. A secondary reason for this board's selection was familiarity and ease of use with the Arduino integrated development environment.

Two options are established for MCU-to-personal computer (PC) data transfer: direct communication via Universal Serial Bus (USB) or microSD card storage and later transfer. The former caters to real-time applications and circumstances permitting wired PC connection, while the latter allows more mobility from the PC. For both methods, a normally-open pushbutton is used to trigger the start and end of a data recording session when activated and deactivated, respectively. The record pushbutton is wired to the MCU's 5V port at one end and a general-purpose input/output (GPIO) port at the other end. A 1kΩ pull-down resistor connects the GPIO line to ground to ensure the logical value near zero is read at the GPIO port when the pushbutton is deactivated (i.e., to prevent the open button terminal from acting as an antenna). The second data transfer method necessitates the inclusion of a circuit board dedicated to SD card data storage in the circuit design. An OSEPP-MSDS-01 microSD shield board was selected due to its availability at a local electronics vendor and suitably low cost. This board is appropriately wired to the Arduino Mega such that the latter sends the digitized potentiometer readings for SD card storage and power (i.e., via 3.3V connection) to the former. More specifically, the Arduino's Slave Select (SS), Master Out Slave In (MOSI), Master In Slave Out (MISO), and System Clock (SCK) pins respectively connect to the microSD shield's corresponding pins [204], [205]. Note that the SD card-based data-transfer method was ultimately used to perform the experiments described in Subsection 6.1.5. Finally, a 9V battery is wired between the input voltage and ground ports of the MCU board to provide mobile power when the second data collection method is used; a manual on/off switch is serially connected on the battery line, so the electronics can be deenergized when not in use. Moreover, as the PC provides power during the tethered scheme, the on/off switch should be off when that method is used to prevent any possible current backflow and subsequent damage to the circuit or PC.

Table 6.1. Bill of materials and costs associated with the MoCap-exoskeleton prototype

Category/Item		Qty.	Unit Vol./Lgth.	Unit Cost	Cost (CAD)
Orthotics/Knee Brace					
Ober Leg Brace		1	-	$381.23/unit	$381.23
3D-Printed Linkages					
Set-Up Fee		1	-	$20.00/print	$20.00
Pelvis Base	Hip Module	1	0.98 in.^{3}	$5.00/in.^{3}	$4.90
Thigh Base	Hip Module	1	0.57 in.^{3}	$5.00/in.^{3}	$2.87
Shank Base	Ankle Module	1	0.66 in.^{3}	$5.00/in.^{3}	$3.29
Link A	Hip and Ankle Modules	2	0.40 in.^{3}	$5.00/in.^{3}	$4.05
Link B1	Hip and Ankle Modules	2	0.29 in.^{3}	$5.00/in.^{3}	$2.90
Link B2	Hip and Ankle Modules	2	0.22 in.^{3}	$5.00/in.^{3}	$2.24
Link C	Hip and Ankle Modules	2	0.38 in.^{3}	$5.00/in.^{3}	$3.81
Link D	Hip and Ankle Modules	2	1.44 in.^{3}	$5.00/in.^{3}	$14.42
Link E	Hip and Ankle Modules	2	0.09 in.^{3}	$5.00/in.^{3}	$0.93
Link F	Hip and Ankle Modules	2	0.22 in.^{3}	$5.00/in.^{3}	$2.23
Track Cap	Hip and Ankle Modules	2	0.06 in.^{3}	$5.00/in.^{3}	$0.56
Link G	Knee Module	1	0.17 in.^{3}	$5.00/in.^{3}	$0.84
Link H	Knee Module	1	0.46 in.^{3}	$5.00/in.^{3}	$2.32
Electrical Housing Case Bottom		1	1.33 in.^{3}	$5.00/in.^{3}	$6.64
Electrical Housing Case Top		1	3.04 in.^{3}	$5.00/in.^{3}	$15.21
Unmeasured Joints/Fasteners					
Sleeve-Bearing Carriage		2	-	$49.90/unit	$99.79
Sleeve-Bearing Track (155mm)		1	-	$29.99/unit	$29.99
Sleeve-Bearing Track (275mm)		1	-	$49.67/unit	$49.67
10-24 Thread Nylon Shoulder Screw		12	-	$0.32/unit	$3.80
10-24 Thread Hex Nut		12	-	$0.07/unit	$0.85
M3 Thread Socket Cap Screw		10	-	$0.14/unit	$1.36
M3 Thread Hex Nut		2	-	$0.09/unit	$0.18
M2.5 Thread Socket Cap Screw		8	-	$0.15/unit	$1.20
M2.5 Thread Hex Nut		16	-	$0.06/unit	$0.97
Sensed Joints/Electrical Components					
Potentiometer		7	-	$2.80/unit	$19.60
Arduino Mega 2560 Rev. 2		1	-	$59.26/unit	$59.26
OSEPP-MSDS-01 MicroSD Shield		1	-	$13.95/unit	$13.95
On/Off Rocker Switch		1	-	$4.20/unit	$4.20
Record Push Button		1	-	$10.40/unit	$10.40
9V Battery		1	-	$5.99/unit	$5.99
9V Battery Clips		1	-	$0.75/unit	$0.75
1kΩ Resistor		1	-	$0.15/unit	$0.15
MicroSD Card with Adapter for PC		1	-	$10.99/unit	$10.99
22 AWG Wire		1	38 ft.	$0.22/ft.	$8.36
Braided Wrap Sleeving (1/2")		1	6.4 ft.	$0.93/ft.	$5.94
PROTOTYPE GROSS TOTAL					**$795.83 CAD**

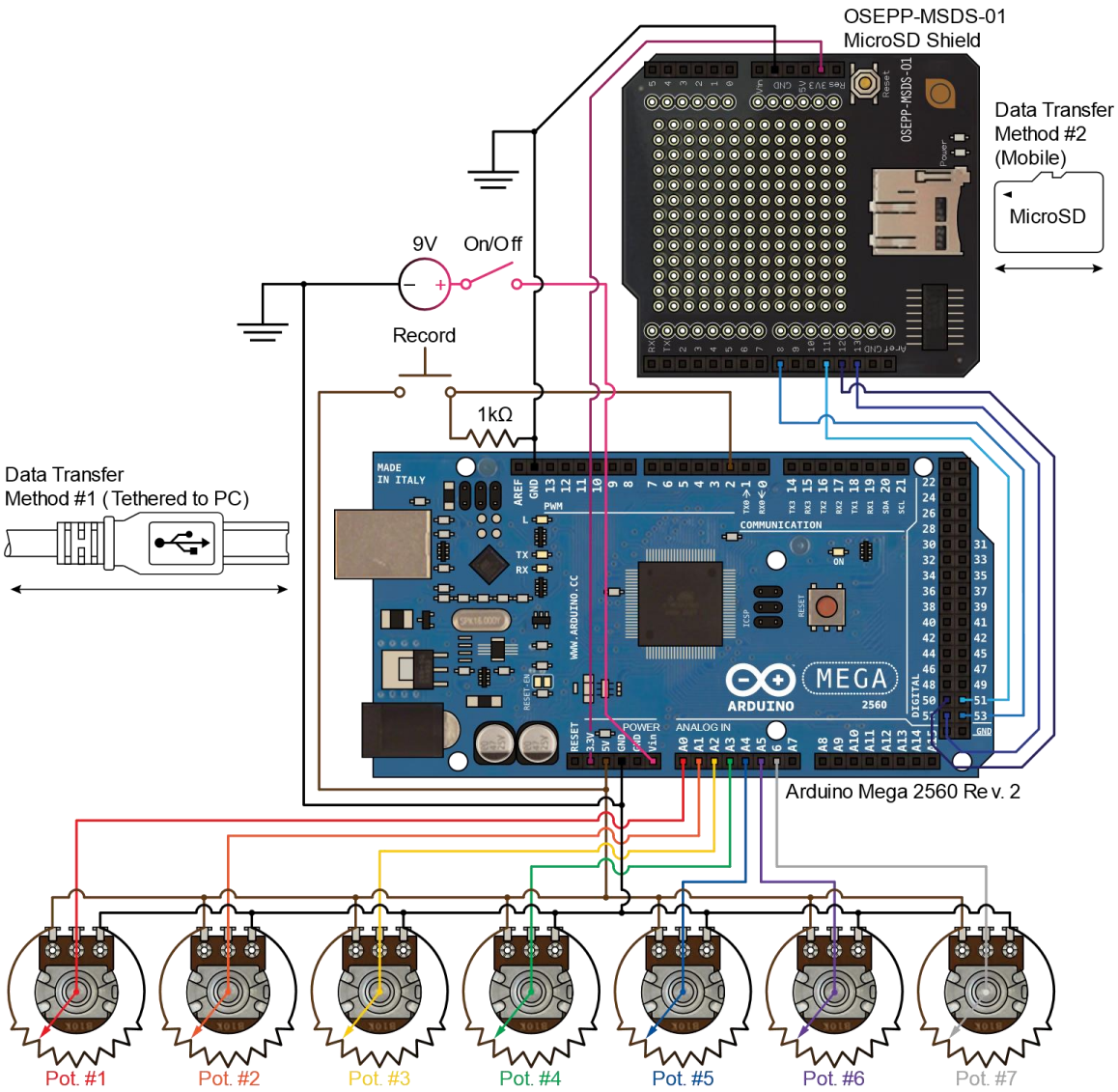

Figure 6.2. Schematic of the MoCap exoskeleton's electrical subsystem
Note: Each potentiometer (i.e. 'Pot.') has a 10kΩ linear resistance.

6.1.3. Software Design

In order for the MCU board to appropriately sample and log the measured potentiometer data, it has to be programmed to do so. The software uploaded to the Arduino MCU is based on open-source code called "AnalogBinLogger.ino" by Bill Greiman [206]. This program samples the targeted analog pins during interrupt routines (i.e., based on time elapsed from the system clock) to establish a regular sampling interval, the value for which is set in the code. The program's author reports conducting a reliability test by sampling five analog pins at a 5kHz rate, which resulted in zero

dropped values on the Arduino Uno board after logging 512MB of data [207]. A buffer is also used in the program to overcome possible sampling delays due to SD card writing latency. Furthermore, this software saves multiple MoCap recording sessions as separate files on the SD card. However, to suit the needs of the MoCap exoskeleton, the "AnalogBinLogger.ino" code required some adjustments; these included: establishing the record pushbutton activation as the log trigger, setting the pushbutton release as the condition for ending a log session, and automatically converting the recorded data from binary to comma-separated values (CSV) file format at the end of each record session; originally, the program would perform these actions based on serial input from a connected PC. Figure 6.3 shows a high-level logic diagram of the modified "AnalogBinLogger.ino" program including, a lower-level diagram for the data-logging function used within the main program.

6.1.4. Preparatory Procedures for Data Conversion and Zeroing

The measured potentiometer angles are interpreted by the ADC process on the Arduino board as an integer value on the range 0-1023, inclusive (i.e., from 10-bit digitization). A value of 0 corresponds to the potentiometer wiper contacting the grounded lead, whereas a value of 1023 is achieved when the wiper contacts the high voltage lead. Before the digitized value can be used by the exoskeleton mechanism's kinematic algorithm, they must be converted into physically-meaningful values with angular units of either degrees or radians. To determine the appropriate conversion factors, the total angular range swept by each potentiometer wiper between its two physical limits was measured. The measuring apparatus comprised: fixing each potentiometer to a tracing surface with temporary adhesive, fitting a 3D-printed measurement arm to the potentiometer wiper, and attaching a pencil lead to the distal face of the measurement arm such that the graphite contacted the tracing surface. The potentiometer wiper was then rotated through its range, leaving a pencil tracing on the tracing surface. The range was then measured using a protractor. Once the physical ranges were measured for each potentiometer, the conversion factors were obtained by dividing each of those angular ranges by the digitized value range (i.e., 1023). Table 6.2 provides the range, conversion factor, and zeroing offset (discussed later) for each potentiometer. Figure 6.4 shows the measuring apparatus with an example tracing, as well as an indication of the rotation-vector direction associated with the potentiometers.

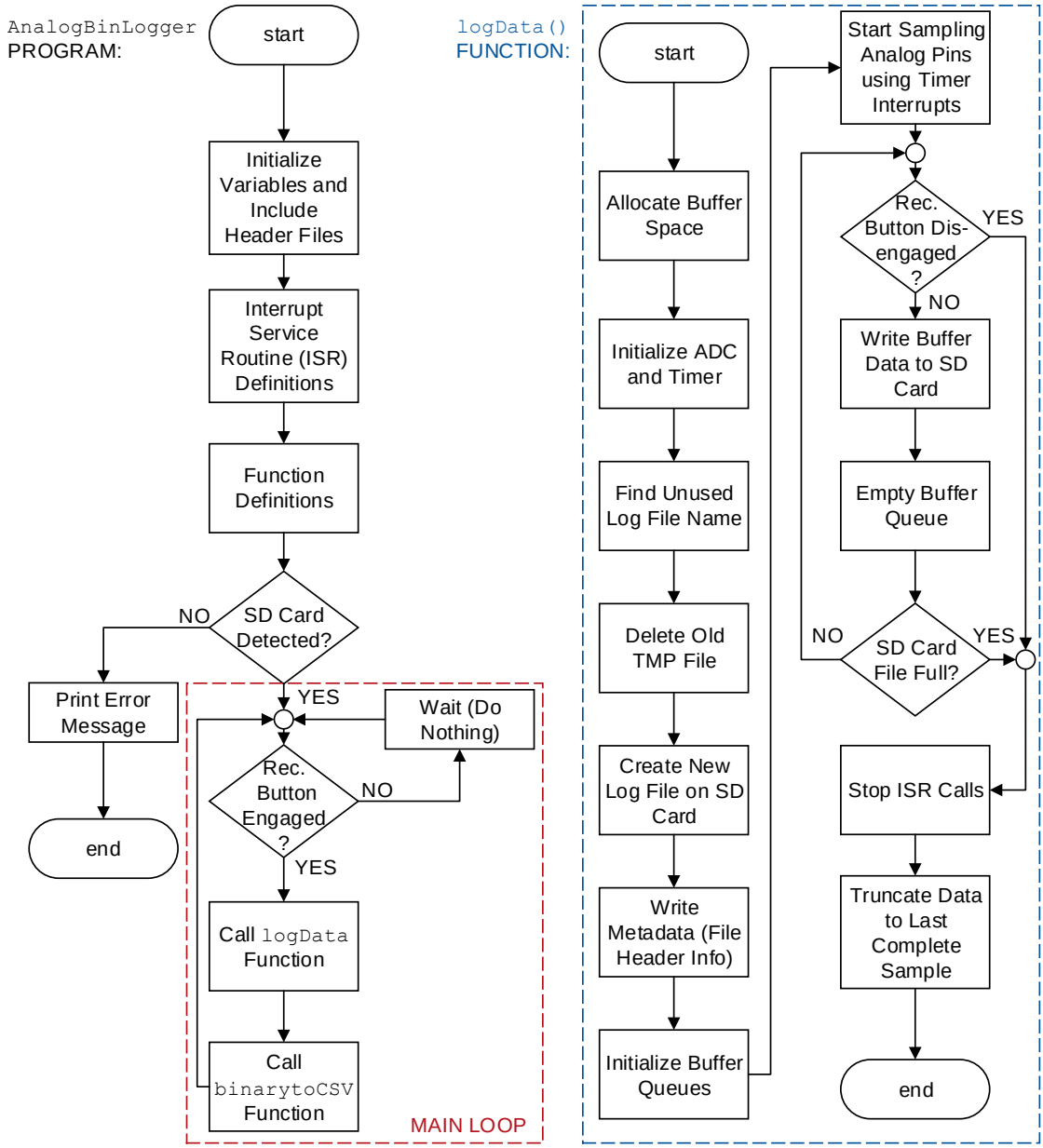

Figure 6.3. Logic diagram of MCU program used for logging data from the MoCap exoskeleton's potentiometers

Note: 'Rec. Button' denotes the normally-open pushbutton for recording MoCap sessions.

Table 6.2. Angular range, ADC value-to-angle conversion factor, and zeroing offset (as a 10-bit ADC value) for each exoskeleton potentiometer

	Pot. #1	Pot. #2	Pot. #3	Pot. #4	Pot. #5	Pot. #6	Pot. #7
Angular Range:	302.0°	302.0°	300.0°	301.2°	297.5°	301.0°	300.0°
Conversion Factor:	$\frac{302.0°}{1023}$	$\frac{302.0°}{1023}$	$\frac{300.0°}{1023}$	$\frac{301.2°}{1023}$	$\frac{297.5°}{1023}$	$\frac{301.0°}{1023}$	$\frac{300.0°}{1023}$
Zeroing Offset:	542	376	429	889	661	550	651

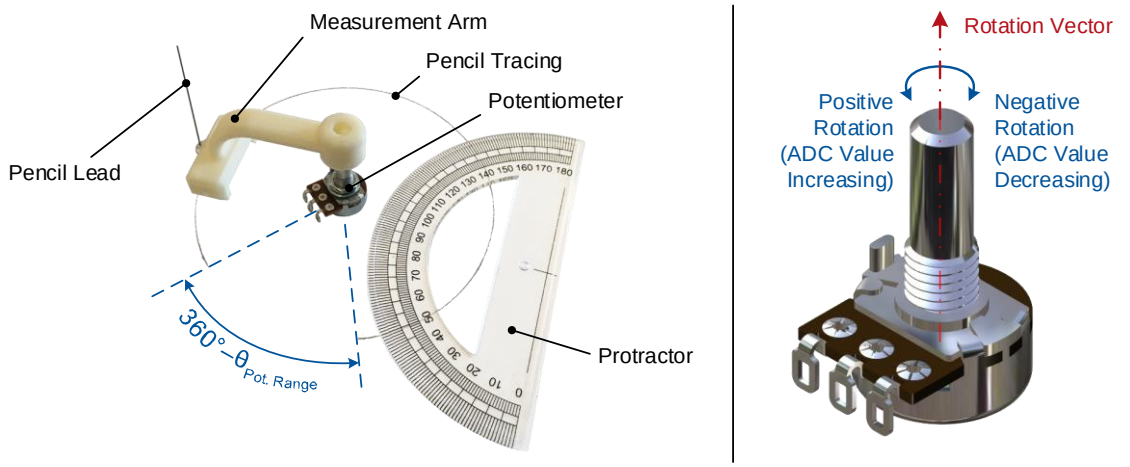

Figure 6.4. Potentiometer angular range-measuring apparatus with example range tracing (left) and rotation vector for the potentiometers (right)

The reported conversion factors are only valid if the potentiometers are linear and repeatable. Although they are advertised as such, a verification test was developed and executed to confirm these characteristics. This procedure involved rigidly mounting both a Dynamixel RX-28 servo actuator and test potentiometer to a wooden frame such that the actuator and sensor axes were collinear. Additionally, a 3D-printed interfacing piece was bolted to the actuator's output shaft at one end and press-fitted to the potentiometer shaft at the other end. Finally, a simple electric circuit was wired to record the potentiometer measurements with 16-bit digitization, and the actuator was driven to ramp up and down at a constant rate across the potentiometer's rotation range. Figure 6.5 shows the test rig and three overlaid sample results from one of the potentiometers. The plotted result sets are closely aligned, demonstrating repeatability, and the measurements occur on a straight line, demonstrating sensor linearity.

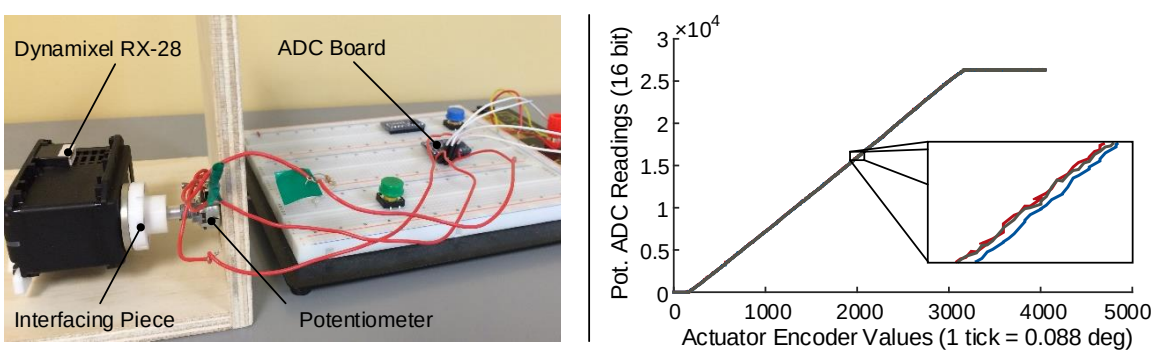

Figure 6.5. Test rig (left) and sample results (right) for three trials of potentiometer linearity and repeatability tests

Note: The flattened sections on either end of the line indicate rotations beyond the pot.'s range (i.e., the actuator continued to rotate but the potentiometer did not).

In addition to converting the potentiometer readings into values in degrees, the angles must also be represented with respect to their installation on the exoskeleton mechanism. As described in the kinematic analysis of the hybrid SAE mechanism (see Subsection 3.4.1), a home configuration is established for which all active-joint angles are zero. Thus, to match the physical angle measurements with this convention, thereby facilitating the kinematic analysis process, the hip and ankle exoskeleton potentiometer angles were measured after aligning these exoskeleton modules to their home configurations. Figure 6.6 shows a photograph and SolidWorks model of a hip-exoskeleton module in its home configuration. As for the knee exoskeleton, a zeroed potentiometer angle is taken to occur when the knee brace to which it attaches is aligned straight (i.e., all flat knee brace side faces are parallel as shown on the left side of Figure 6.1). With the potentiometer angles obtained from each exoskeleton module's home configuration, hereafter called the 'offset values', each potentiometer measurement is properly zeroed by subtracting its corresponding offset value. In its final row, Table 6.2 lists the offset value for each potentiometer of the prototype exoskeleton.

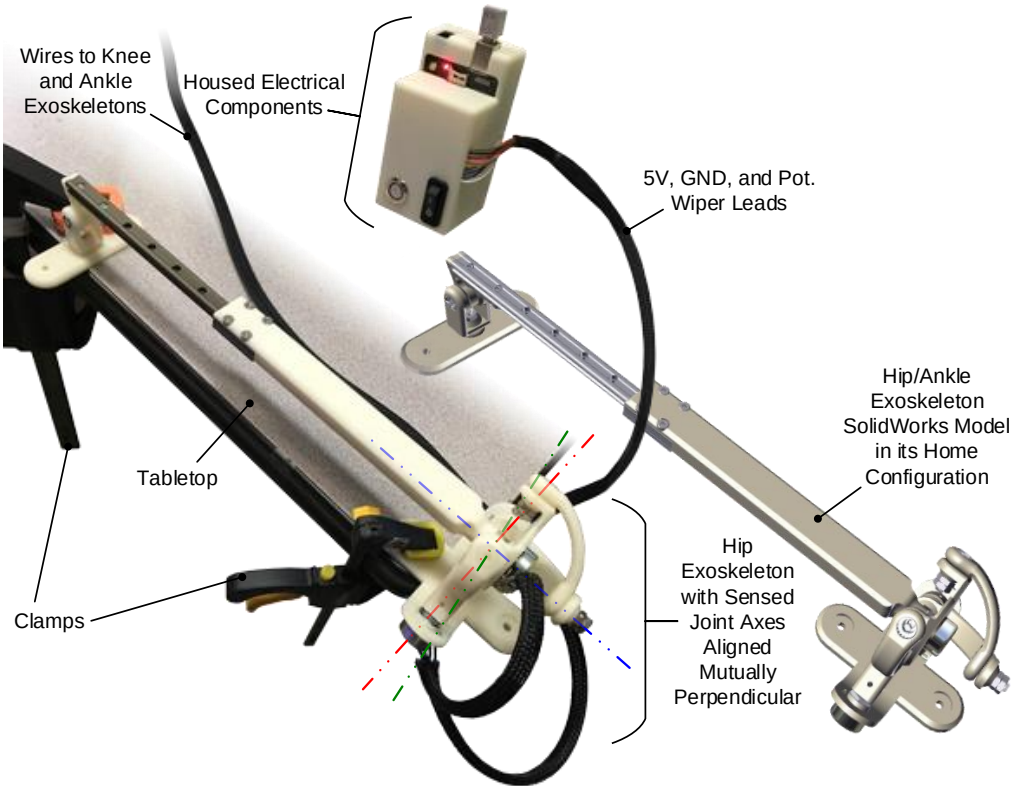

Figure 6.6. Photograph and SolidWorks model of the hip exoskeleton module in its home configuration

Note: The ankle exoskeleton module's home configuration is identical. Also, a square tool was used to achieve orthogonal-axis alignments before clamping base components to the tabletop.

6.1.5. System Integration and Final Design

After verifying the functionality of the electrical and software designs and assembling the mechanical components, these subsystems were integrated into a cohesive system. The electrical components were compactly encased in a 3D-printed housing, which was then bolted to the pelvis orthotic to allow the user to easily start and stop an untethered motion-capturing session. The potentiometer leads were soldered to the MCU board from their respective mechanical installation points via 22 AWG wire. Whereas each wiper lead had its own wire and port connection, the ground and high-voltage leads daisy chained from sensor to sensor ending with Pot. #2, which was soldered to the GND and 5V ports. All the wire was sheathed in sleeving to minimize interference with the user's movements. Figure 6.7 shows a photo of the completed prototype, highlighting the electrical housing, alongside a SolidWorks model. Although the electrical subsystem remained unchanged throughout the prototype's development, the mechanical and software subsystems each had one preliminary iteration prior to the final forms described in Subsections 6.1.1 and 6.1.3, respectively. Appendix C details these initial designs, which did not achieve the desired level of functionality.

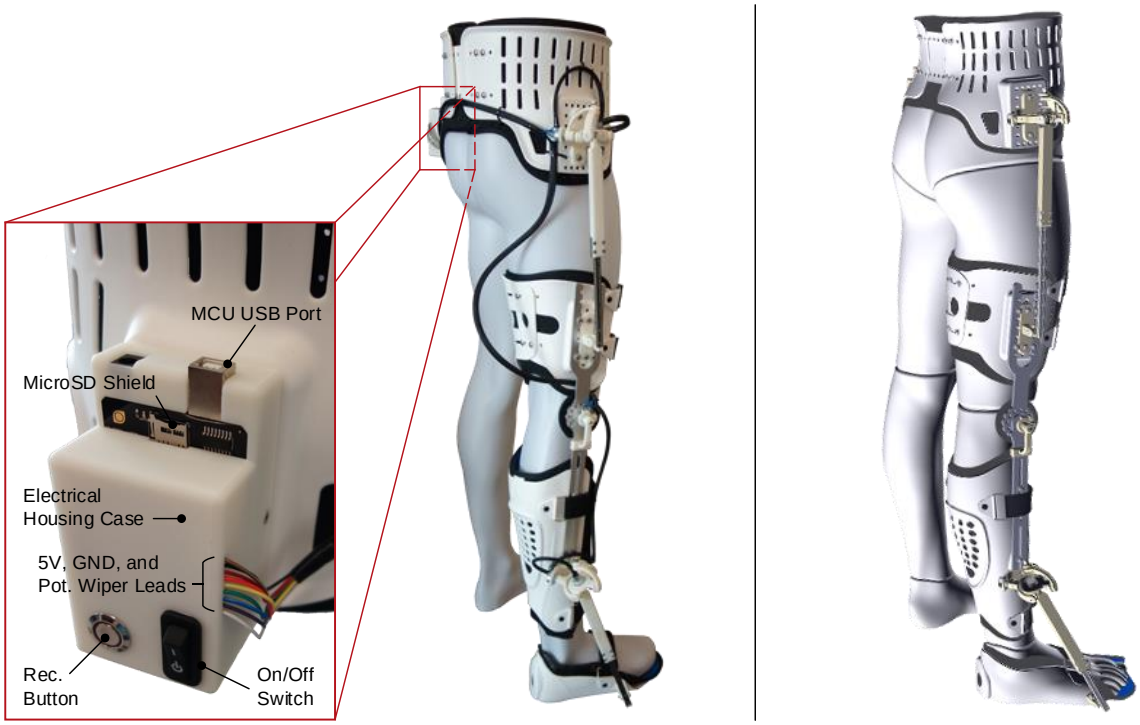

Figure 6.7. Photograph of MoCap exoskeleton prototype mounted on a mannequin with a callout of the electrical housing (left) and its SolidWorks design reference (right)

6.2. Motion Capture Experiment with a Stereophotogrammetrical Reference

6.2.1. Experimental Setup

To evaluate the efficacy of the proposed MoCap exoskeleton, the prototype system was worn and tested during various lower-limb movements with simultaneous data capture from a Qualisys optical system for reference and comparison. Xsens MTw inertial measurement units (IMUs) were also worn as a secondary reference, but their results were ultimately disregarded, as will be explained later. The two reference systems were chosen on the basis that optical- and inertial-based systems are the most commonly-used techniques for MoCap. Moreover, since optical MoCap is widely considered the gold standard for this type of technology, the data obtained from the Qualisys system are considered the correct results. Finally, as most human motion occurs on a frequency range between 3Hz and 26Hz [73], [208], [209], a sufficiently rapid data-sampling rate of 100Hz was used for each MoCap system.

Exoskeleton System's Setup and Calibration

The setup and calibration procedure associated with the proposed exoskeleton system began with the MoCap subject placing the exoskeleton's orthotics against their corresponding leg segments and then securing them in place via the orthotics' hook-and-loop-fastener straps. To achieve comfort and maximal accuracy of the knee exoskeleton module, care was taken to approximately align the exoskeleton's knee brace rotational axis with the flexion/extension axis of the knee. Moreover, to facilitate data processing, effort was made to align the hip and ankle exoskeletons such that the orthotic-attachment faces of the pelvis and shank base components were parallel to the body's sagittal plane and orthogonal to the transverse plane (i.e., such that the $\hat{x}_0^{\text{SAE}}$ and $\hat{y}_0^{\text{SAE}}$ axes had a 135-degree offset from those axes of the subject's body frame per the Figure 5.9 design). Once the exoskeleton was properly fitted to the subject's body, a calibration procedure involving several distance measurements was necessary. As illustrated in Figure 6.8, the required measurements for the hip and ankle are the three-dimensional coordinates of the anatomical-joint center-of-rotation (COR) to the corresponding exoskeleton-module COR, and the length from the anatomical-joint COR to the exoskeleton-module universal-joint center. Note that the universal joint occurs at

the axes-intersection of the two revolute joints between the prismatic joint and inferior orthotic. Also, recall from Subsection 4.2.1 that the distances correspond to variables of known value in the kinematic analyses of the exoskeleton-limb manipulator. Table 6.3 lists the calibration measurements made prior to the experiment. The final steps of the exoskeleton system setup were to insert a microSD card into the accessible slot of the SD card shield and switch on the power. Overall, the setup and calibration of the exoskeleton system required about 5–10 minutes.

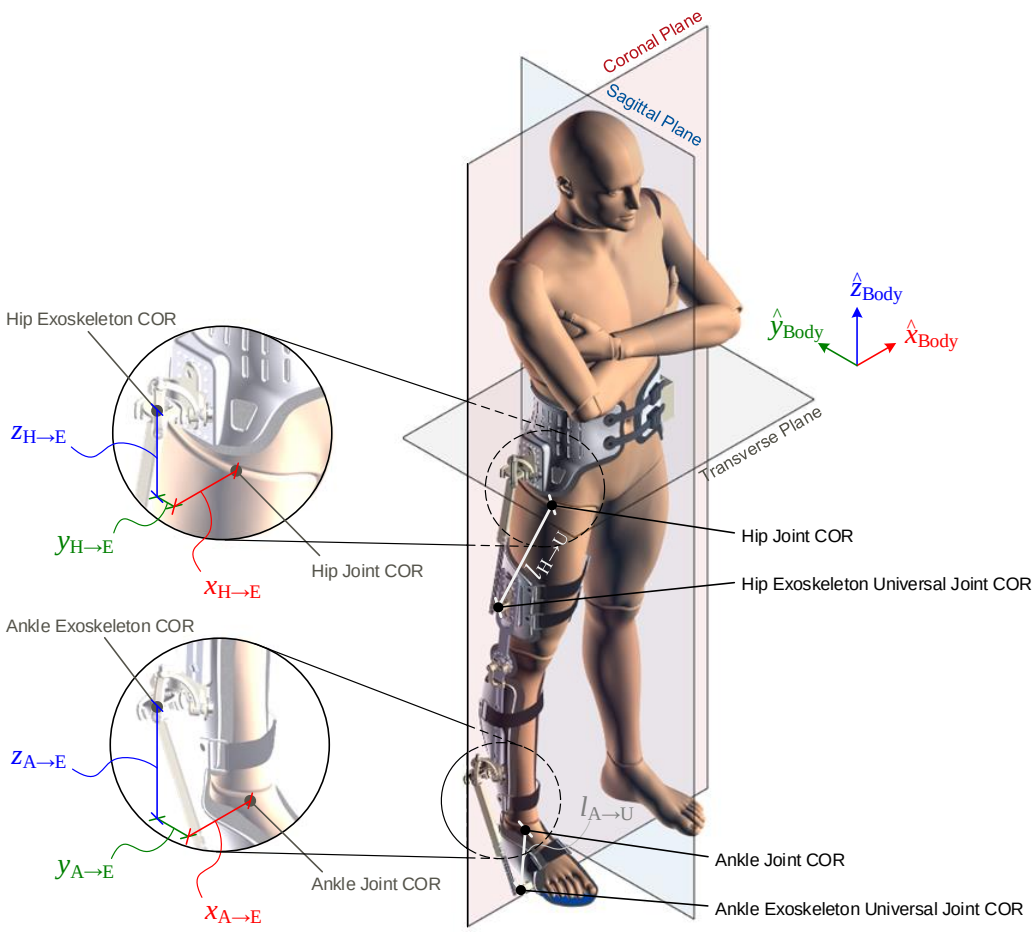

Figure 6.8. Variables requiring measurement for MoCap exoskeleton calibration

Table 6.3. Experimental calibration parameters for the MoCap exoskeleton

Hip Parameter	Value (mm)	Ankle Parameter	Value (mm)	Variable Name in Section 4.2
$x_{H\to E}$	–115	$x_{A\to E}$	–102	$x_{1\to 2}$
$y_{H\to E}$	–2	$y_{A\to E}$	22	$y_{1\to 2}$
$z_{H\to E}$	37	$z_{A\to E}$	137	$z_{1\to 2}$
$l_{H\to U}$	295	$l_{A\to U}$	169	l_r

Note: Parameter measurements were made using digital calipers (i.e., for absolute values <150mm) or a ruler (i.e., for greater lengths); also note that l_o = 22.1mm in the prototype, where the value is set by the design of Link E.

Qualisys and Xsens Systems' Setup Summary

Since the exoskeleton prototype only tracks motions of the hip, knee, and ankle joints of the subject's right leg, four groups of optical system's passive markers and four Xsens MTw sensors were attached to surround each of these joints. Each marker group consisted of four markers, which allowed for orientation computation with one redundant marker to be considered in case of an occlusion. Moreover, the markers for limb segments superior to each target joint were attached to flat surfaces in common with the exoskeleton-module attachment sites to facilitate the development of shared local reference frames between these two MoCap systems. As for the inertial system, sensors were also attached on the pelvis, thigh, shank, and foot. Their placements were chosen to avoid proximity with the exoskeleton's ferromagnetic components, which could interfere with the IMUs' magnetometer readings. Also, because the IMUs were fitted with a hook-fastener surface, they were attached to the orthotics' straps for the thigh, shank, and foot; the pelvis MTw sensor was secured in place between the pelvis orthotic's plastic shell and subject's body with its hook-fastener side against the orthotic fabric. Figure 6.9 illustrates the passive-marker and MTw placements used for the experiment.

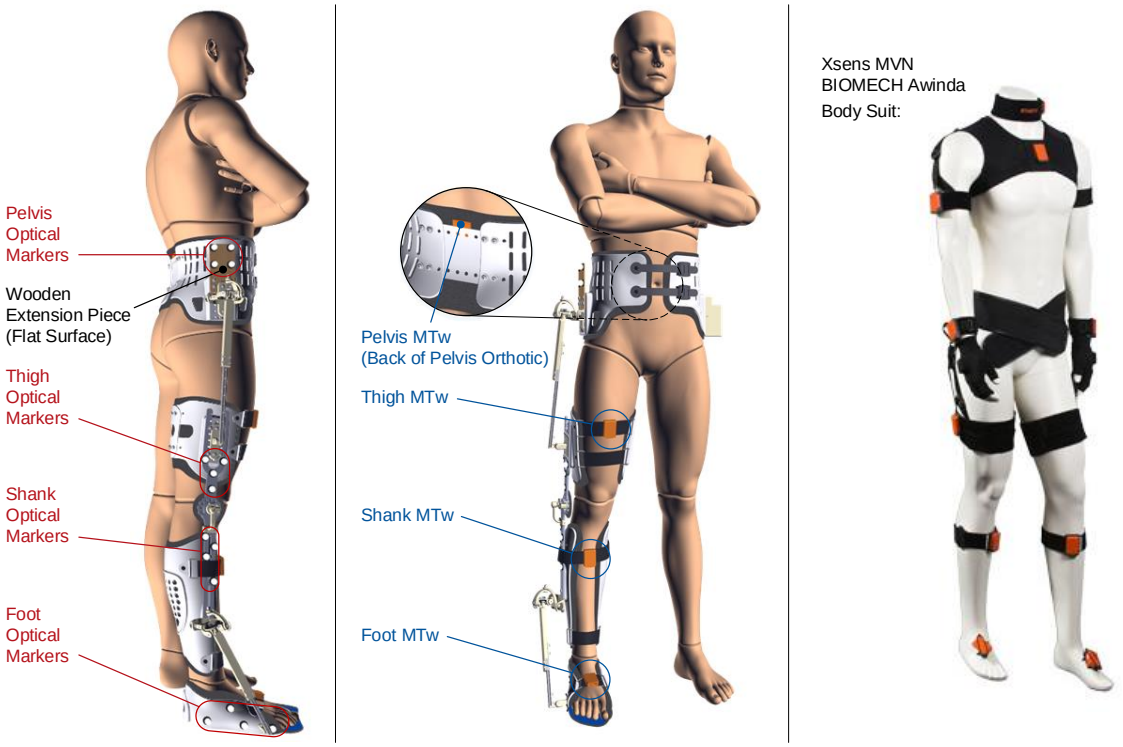

Figure 6.9. Experimental attachments for Qualisys markers (left) and Xsens sensors (middle), along with a photo of the Xsens MVN suit (right)

Note: The chosen MTw placements resemble those recommended for the Xsens suit [210].

In addition to the retroreflective-marker attachments, the Qualisys system setup required positioning and calibrating MoCap cameras on tripods to establish a 3D measurement space. For a preliminary experiment, a semicircular arrangement of five high-speed Oqus cameras was employed, as shown in schematic illustration of Figure 6.10. However, upon reviewing the marker trajectories captured by the optical system, it was discovered that 25 of 29 movement trials had discontinuous trajectory detections for one or more markers, most often from the pelvis group. Thus, if the data were to be processed, manual interpolation for those markers would be necessary, which would significantly increase processing complexity and severely degrade the accuracy of motion data. There are several likely causes for this loss of data. First, during the calibration procedure, all cameras were oriented such that the lab-room frame-reference object placed on the floor was in their field-of-view, per the Qualisys user manual's recommendation. Therefore, the pelvis markers were systematically undetected because they would occasionally move above the downward-oriented fields-of-view. Another factor was the initial placement of pelvis markers was directly on the curvature of the pelvis orthotic. The resulting recessed positions of these markers potentially made them more susceptible to occlusion, prompting the subsequent inclusion of the wooden extension piece shown in Figure 6.9. Moreover, no redundant markers were used in the preliminary experiment, so any instance of occlusion would prevent the orientation computation for the affected marker group. Lastly, the experiment subject generally kept his arms crossed to avoid blocking the pelvis markers from the cameras' fields-of-view, but he may have temporarily lapsed from this posture.

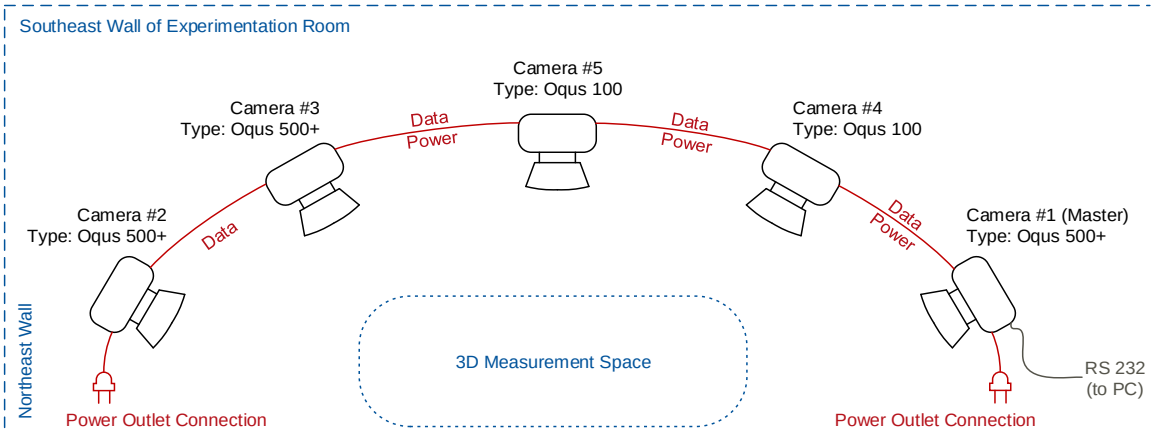

Figure 6.10. Qualisys camera setup for the preliminary experiment
Note: The camera numbering was done automatically by the Qualisys software and does not necessarily follow the order of camera connection.

In addition to adding a redundant marker to each marker group and preparing the wooden extension piece for the pelvis orthotic, three more MoCap cameras were used during the final experiment procedures to reduce the likelihood of occlusions. As shown in Figure 6.11, the direction of the cameras within the lab room was also reversed from that during the preliminary experiment just in case ambient lighting was also a factor in the initial occlusions. Moreover, a mock experiment was conducted during the Qualisys system setup, prior to camera calibration. This mock experiment involved attaching markers on the studied body segments in roughly the same positions as planned for the actual experiment, and then performing the protocol movements while observing the camera's video images on the lab-PC screen. If any marker was detected by less than two cameras at any point in the mock movements, the position and orientation of the camera(s) that lost detection of the marker were adjusted. Once a suitable arrangement of cameras was achieved for all trials, tape was placed on the lab-room floor to mark the allowable space for each movement (i.e., limits of measurement workspace were roughly identified). The final camera arrangement had alternating downward orientations (i.e., to capture the lower markers and the lab-room frame-reference object during calibration) and approximately horizontal orientations (i.e., to capture higher markers).

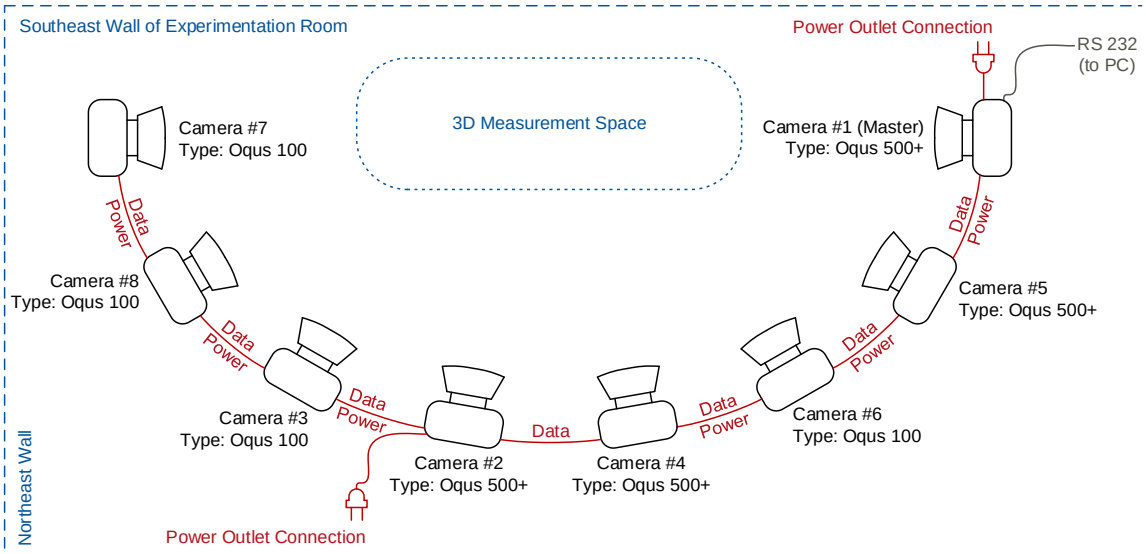

Figure 6.11. Qualisys camera setup for the final experiment
Note: The camera numbering was done automatically by the Qualisys software and does not necessarily follow the order of camera connection.

As for the Xsens IMUs, one of the MTw sensors dropped all its data packets for one of the preliminary trials. This meant that one of the body joints had no motion

captured for that trial. The most likely reason for this loss of data is that the system's Awinda wireless receiver became too far away from the MTw sensor during the subject's movements. Therefore, the receiver was placed closer to the measurement space during the final experiments. The issues experienced with the Qualisys and Xsens systems exemplify some of the common shortcomings associated optical and inertial MoCap technologies, respectively. For the reader's reference, Appendix D provides greater details regarding the calibration process for the optical system as well as the setup for the software accompanying the Qualisys and Xsens systems. Ultimately, the setup and calibration of the Qualisys system required between two and three hours, whereas the Xsens system required about 5–10 minutes. A photograph of the final experimental setup is shown in Figure 6.12.

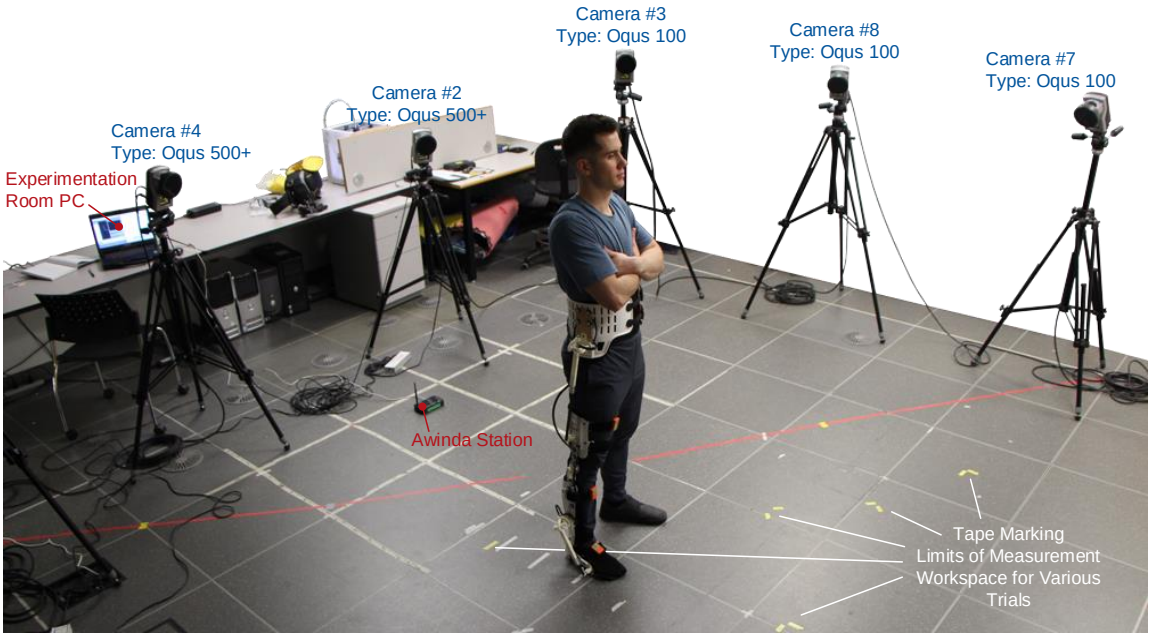

Figure 6.12. Photograph of the final experiment setup
Note: Three of the Qualisys system's Oqus cameras are outside of the photographed area.

6.2.2. Experimental Protocol

The protocol for subject motion-tracking tests considered three categories of human movement: joint range-of-motion, general mobility, and extended mobility. Table 6.4 lists the set of individual movements studied during the MoCap experiment as well as the number of trials conducted for each movement; duplicate trials were performed to verify the repeatability of exoskeleton system measurements. The range-of-motion tests were designed to demonstrate the hip and ankle exoskeleton modules' non-restrictive

compliance with its corresponding body joints' ranges-of-motion. The latter two categories of tests were included to respectively demonstrate MoCap competency for lower-limb motions associated with daily tasks and more dynamic activities. These respectively reflect the general requirements of mobility-assisting exoskeletons and those used for augmentation or virtual-reality applications. Each trial began with a few seconds of standing still to provide a zero-angle reference posture; body-joint angles were ultimately measured relative to this neutral-standing posture for each movement (see the discussion on practical considerations in Subsection 5.2.3 for more details). After the standing period, the knee joint was quickly flexed and then extended to provide an identifiable motion peak with which to time-synchronize the data obtained from each MoCap system. The experiment was a proof-of-concept study, so only a single subject performed the experimental procedures: an able-bodied 25-year-old male with height and body mass of 175cm and 75kg, respectively. The experimental protocol was approved by the Research Ethics Board of Simon Fraser University (reference no. 2013s0750).

Table 6.4. Protocol for subject movements during the experimental study

Movement	No. of Trials
Category 1: Joint Range-of-Motion Tests	
1.1. Hip Flexion/Extension	8
1.2. Hip Abduction/Adduction	8
1.3. Hip Internal/External Rotations	8
1.4. Knee Flexion/Extension	8
1.5. Ankle Dorsiflexion/Plantarflexion	8
1.6. Ankle Supination/Pronation	8
Category 2: General Mobility Tests	
2.1. Walking Gait	8
2.2. Walking with Left/Right Turn (~90 degrees)	3
2.3. Lateral Walking (Leftward/Rightward)	3
2.4. Bending at the Waist	3
2.5. Standing Still	3
2.6. Stair Ascending/Descending	3
2.7. Standing-to-Sitting/Sitting-to-Standing	3
2.8. Squatting	3
Category 3: Extended Mobility Tests	
3.1. Fast Walking Gait	3
3.2. Double-Leg Horizontal Jumping	3
3.3. Walking Lunges	3
3.4. Kneeling (Left Leg/Right Leg)	3

6.2.3. Data Processing

Exoskeleton System's Data Processing

During the experiment, the mobile method of data collection was employed, as described in Subsection 6.1.2. So, the digitally-converted potentiometer readings from each movement trial were stored in CSV files on a microSD card. After transferring the MoCap files onto a processing PC and importing the data into Matlab, the first processing action was to two-way filter the potentiometer readings using a fourth-order Butterworth low-pass filter with 10Hz cut-off frequency. This removed noise from the raw potentiometer readings without affecting the underlying signal. Afterwards, the corresponding zeroing offset was subtracted from each potentiometer reading trajectory, and the result was multiplied by the appropriate conversion factor (see Table 6.1). This produced time sequences for each potentiometer with appropriate zero values and units of degrees. Next, the initial peak in the knee angle trajectory was identified in each trial for synchronization with other systems' data. Finally, the forward kinematic algorithm outlined in Subsection 5.2.2 was used to convert the potentiometer angles to body joint angles. Note that if any potentiometer was installed with a rotation vector (see Figure 6.4) aligned in the opposite direction as assumed in the forward kinematic algorithm, the zeroed and converted potentiometer readings were negated. The exoskeleton calibration parameters (see Table 6.3) were also mandatory inputs for the exoskeleton's forward kinematic algorithm. Additionally, an extra calibration factor, named k_{Factor} and equal to 0.86, was applied to the exoskeleton's detected knee angle data to compensate for any systematic differences with the Qualisys measurements. Figure 6.13 shows a block diagram summarizing the data processing procedures for the exoskeleton MoCap data.

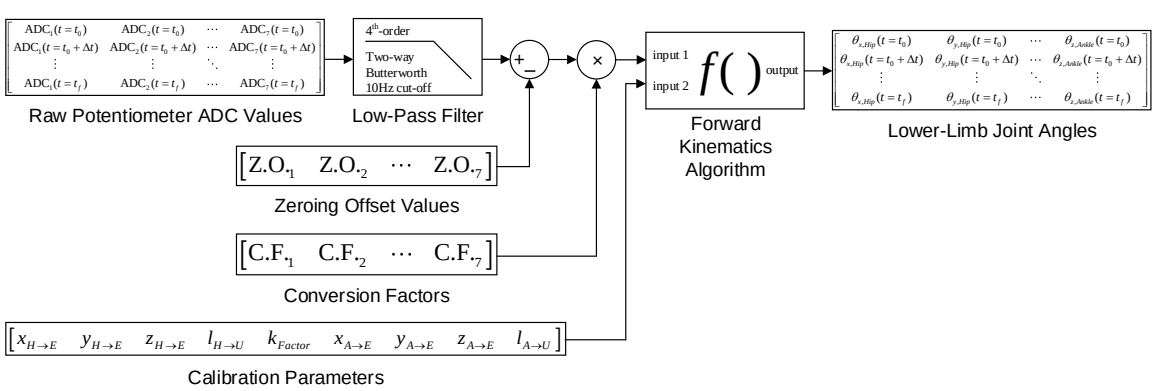

Figure 6.13. Block diagram of the data processing method for the MoCap exoskeleton

Qualisys and Xsens Systems' Data Processing Summary

As for the Qualisys system, the 3D positional data of the marker clusters on each limb segment were converted into segment orientation data (i.e., in the form of a rotation matrix) using the strategy outlined in [211]. That is, for each limb segment's marker cluster, one marker's position was chosen as the origin for that segment's orientation frame. Next, the normalized vector from that origin marker position to another marker's position was taken as one of the three axes in the segment's frame. The frame axis normal to the plane of the marker cluster was then determined by the normalized cross-product of the first established axis and the vector from the origin position to a third marker's position. The limb segment's third frame axis was finally established by the cross-product of the first two axes. Overall, this orientation frame-development process required three marker positions for each limb segment and guaranteed the mutual orthogonality of the frame axes. However, the resulting frame is arbitrarily oriented with respect to the underlying bony segment; oftentimes a calibration with markers at anatomical landmarks (e.g., bony prominences of the greater trochanter external surface at the hip, medial epicondyle and lateral epicondyle at the knee, etc.) is undergone to define anatomical frames that can be created with intra- and inter-subject repeatability [211]. For this proof-of-concept study, such an anatomical calibration procedure was foregone because the current prototype design made many bony prominences inaccessible to marker placements or susceptible to occlusion. Efforts were instead focused on aligning optical system frames with those of the exoskeleton. Note that the roll-pitch-yaw angle computations from the Qualisys frames were also subjected to a 4th-order two-way Butterworth low-pass filter with 10Hz cut-off frequency.

The Xsens system can directly log MoCap data in the form of rotation matrix entries. Thus, the only processing tasks were to multiply the captured orientations by a set of constant rotation matrices to establish the same common reference frame for each limb segment as used by the other systems, and then filter the associated rotation angles (i.e., using the same filter parameters as for the other systems). However, upon attempting to process the Xsens-captured data in this way, strong evidence of measurement distortion due to magnetic interference from the exoskeleton's ferromagnetic components was unveiled. Appendix E details the processing attempts and distortion evidence for the Xsens data along with further processing details for the

Qualisys data. Because of its corruption, the Xsens data is excluded from the results presented in the next subsection.

6.2.4. Experimental Results and Discussion

Results Sample and Summary

To highlight some key results from the Category 1: Joint Range-of-Motion Tests, Figure 6.14 presents photograph sequences and result plots for hip abduction/adduction and hip internal/external rotation movements. These results demonstrate that the exoskeleton does not restrict those degrees-of-freedom (DOFs) of hip joint rotations within their normal ranges. From Category 2, the left side of Figure 6.15 presents results associated with a normal-walking-gait trial, which is showcased here because it illustrates the exoskeleton's ability to track the independent motions of each target joint DOF during this routine movement. Next, the MoCap results and a photographic sequence for a double-leg horizontal-jump trial is also included in Figure 6.15 to illustrate the exoskeleton's performance in tracking highly dynamic movements. Additionally, the results of Figure 6.15 demonstrate that the hip exoskeleton module permits a full range-of-motion in hip flexion/extension movements. Within the joint trajectory plots, note that the movement associated with increasing/positive angle values is listed before the movement associated with decreasing/negative angles (e.g., hip extension has a positive value whereas hip flexion is associated with negative values). These joint rotation directions correspond to the forward kinematic model for the human right leg developed in Subsection 5.2.2 (see Table 5.4).

In the interest of brevity, result plots for each of the studied movements are not presented in this subsection. Instead, one trial's result plots for each of the remaining movements are attached to Appendix F; moreover, Table 6.5 summarily lists the root mean square error (RMSE) and standard deviation (STD) of error associated with the exoskeleton measurements relative to the Qualisys measurements for all movements performed by the motion capture subject. These statistics were computed across two cycles of all Category 1: Joint Range-of-Motion, standing-to-sitting/sitting-to-standing, and squatting movements; one motion cycle was considered for all other movements. Note that only the positive joint motion abbreviation is used to identify results in the figure box plots and Table 6.5, although the complete motion signal is considered.

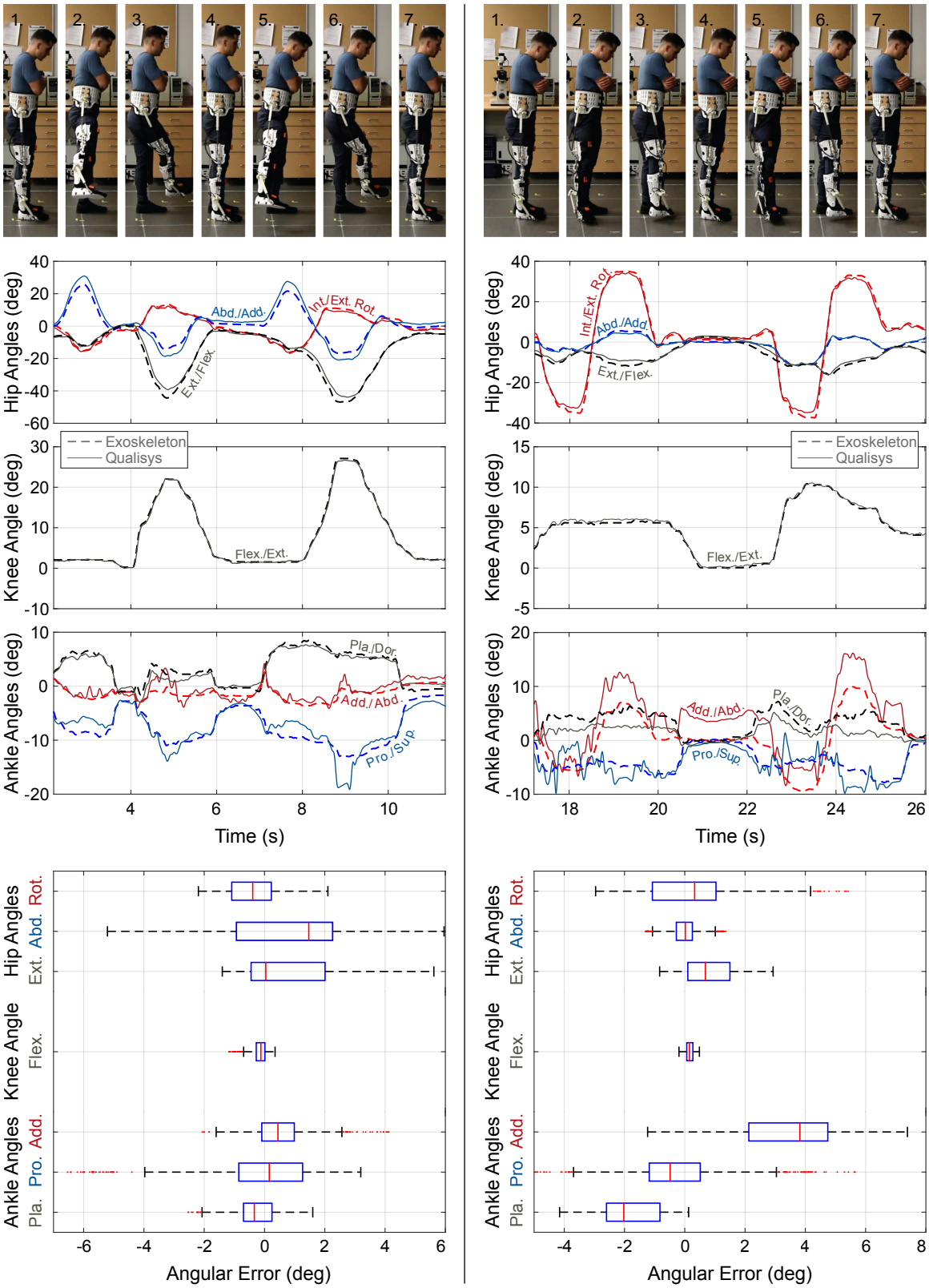

Figure 6.14. Photo sequence, joint trajectories, and box plots of angular errors in the exoskeleton's measurements associated with two cycles of hip abduction/adduction (left) and hip rotation (right) movements

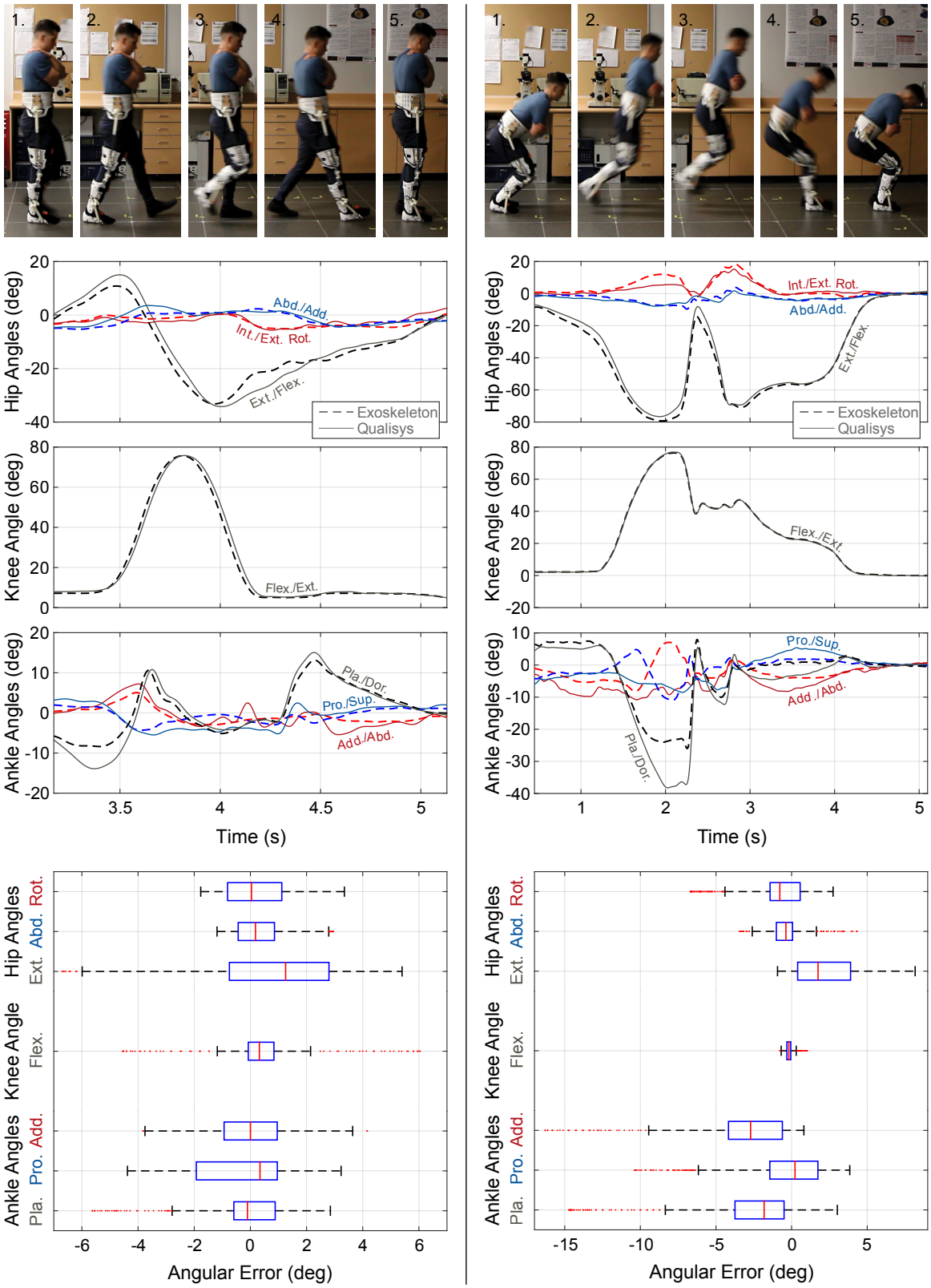

Figure 6.15. Photo sequence, joint trajectories, and box plots of angular errors in the exoskeleton's measurements associated with one cycle of walking (left) and double-leg horizontal jumping (right) movements

Table 6.5. Mean and standard deviation of error in exoskeleton measurements for lower-limb joint angles during the experimental movements

	Joint Angle RMSE±STD (deg)						
	Hip			*Knee*	*Ankle*		
Trial Movement	Rot.	Abd.	Ext.	Flex.	Add.	Pro.	Pla.
Category 1: Joint Range-of-Motion Tests							
1.1. Hip Ext./Flex.	4.0±3.7	2.6±2.3	1.3±1.3	0.7±0.7	1.3±1.3	1.3±0.8	1.2±0.9
1.2. Hip Abd./Add.	1.0±0.9	3.1±3.0	2.0±1.8	0.3±0.3	1.0±0.9	1.8±1.8	0.8±0.8
1.3. Hip Int./Ext. Rot.	1.6±1.5	0.5±0.5	1.3±1.0	0.2±0.1	3.9±1.8	1.7±1.7	2.1±1.1
1.4. Knee Flex./Ext.	1.9±1.2	0.9±0.8	3.2±2.8	1.1±1.1	1.3±0.7	1.5±1.1	1.8±0.7
1.5. Ankle Pla./Dor.	1.3±0.5	1.1±0.8	1.3±1.3	0.7±0.5	2.3±1.5	4.3±4.2	3.1±3.1
1.6. Ankle Pro./Sup.	2.0±0.9	1.2±1.2	1.2±1.2	0.2±0.2	3.1±3.1	3.4±2.4	3.9±2.4
Averages: Category 1	2.0±1.5	1.6±1.4	1.7±1.6	0.5±0.5	2.2±1.6	2.3±2.0	2.2±1.5
Category 2: General Mobility Tests							
2.1. Normal Walk	1.4±1.4	1.2±1.2	3.2±3.1	2.2±2.2	1.5±1.5	1.9±1.8	2.1±2.1
2.2.a. L Turn Walk	2.2±1.3	1.8±1.4	3.3±2.5	0.4±0.3	1.7±1.7	1.7±1.6	3.6±2.4
2.2.b. R Turn Walk	2.0±2.0	1.5±1.5	2.9±2.8	0.7±0.3	2.7±2.2	3.1±2.9	2.9±2.2
2.3.a. Lateral Walk L	2.0±1.4	1.4±1.3	2.3±1.6	0.2±0.2	2.7±1.9	2.0±1.5	1.0±1.0
2.3.b. Lateral Walk R	1.6±1.5	1.8±1.7	2.7±1.7	0.5±0.3	1.4±1.4	1.8±1.8	1.6±0.8
2.4. Bend at Waist	1.7±1.7	1.1±1.1	0.8±0.7	0.2±0.1	0.6±0.6	0.6±0.5	0.9±0.8
2.5. Stand Still*	0.3±0.2	0.1±0.1	0.3±0.2	0.1±0.1	0.1±0.1	0.1±0.1	0.3±0.2
2.6.a. Ascend Stairs	1.1±0.9	1.4±1.4	2.8±2.2	0.3±0.3	2.3±2.2	2.0±1.6	3.6±1.9
2.6.b. Descend Stairs	1.3±0.9	1.1±1.1	4.5±3.5	0.8±0.8	4.3±4.0	2.8±2.8	3.8±2.7
2.7. Sit/Stand	30.2±25.4	3.4±2.2	5.7±5.6	0.6±0.6	5.0±1.9	1.1±0.6	1.0±0.8
2.8. Squat	11.1±10.0	2.1±1.4	1.6±1.4	0.6±0.2	1.9±1.8	0.7±0.7	1.0±0.9
Averages: Category 2	5.5±4.6	1.7±1.4	3.0±2.5	0.6±0.5	2.4±1.9	1.8±1.6	2.1±1.6
Category 3: Extended Mobility Tests							
3.1. Fast Walk	1.7±1.7	1.1±1.0	2.7±2.7	0.9±0.9	1.9±1.5	3.3±2.9	3.1±3.1
3.2. Dbl.-Leg Jump	2.5±2.3	1.3±1.2	3.3±2.3	0.3±0.3	4.6±3.4	3.3±3.3	4.6±3.7
3.3. Lunge Walk	2.3±2.1	1.1±1.0	5.4±4.0	0.7±0.4	5.4±5.4	4.6±4.6	5.1±4.8
3.4.a. L Leg Kneel	4.9±4.2	2.2±2.0	3.4±2.2	0.6±0.5	17.2±17.2	7.3±7.3	5.4±5.2
3.4.b. R Leg Kneel	1.4±1.2	1.7±0.9	7.4±4.5	0.2±0.2	5.2±3.6	2.8±1.3	4.2±4.2
Averages: Category 3	2.6±2.3	1.5±1.2	4.4±3.1	0.5±0.5	4.3±3.5	3.5±3.0	4.2±3.9
Overall Averages:	3.8±3.2	1.6±1.4	3.0±2.4	0.6±0.5	3.4±2.8	2.5±2.2	2.7±2.2

*Note: The Category 2 and overall averages do not include the stand-still trial results, as doing so could be interpreted as skewing these values. The standing trial was intended to demonstrate the exoskeleton's immunity from measurement drift and potentially reveal the Xsens IMUs' susceptibility to it.

Discussion of the Results

Considering only the hip and ankle DOFs from the results above and excluding the standing-still trial, 90.5% of the exoskeleton-based measurements have RSME values within 5 degrees relative to the Qualisys system's reference measurements. Regarding the same result subset, 83.3% and 68.3% of the exoskeleton-captured values have RSMEs within 4 degrees and 3 degrees, respectively. This level of accuracy is comparable to that achieved using MoCap systems based on Xsens inertial

measurement units, as reported in [212] and [213]. Note that both of those studies aimed to benchmark the Xsens MVN MoCap system against an optical MoCap reference by considering independent anatomical-frame calibrations from the evaluated systems, although the latter did eliminate potential soft tissue artifact differences by placing optical marker clusters atop the Xsens sensors. Conversely, this study focuses on verifying the accuracy of the prototype exoskeleton system by using an optical system as a measurement reference. Table 6.6 shows a comparison in RMSE and STD between exoskeleton system results from this experiment and Xsens system results from similar movements in the experiment conducted using the same Qualisys reference [212]. Because the exoskeleton prototype can measure lower-limb joint angles with a similar magnitude of RMSE and STD in error as the commercially-available and widely-adopted Xsens MVN system, the efficacy of the proposed exoskeleton system is confirmed.

Table 6.6. Average RMSE and STD of error in the exoskeleton's and Xsens MTw's joint angle measurements during walking/stair-climbing and jumping/fast-walking trials

Subject Movement	Average RMSE ± Average STD of Error Relative to Qualisys (deg)	
Joint DOF	**Exoskeleton (Current Experiment)**	**Xsens (Data from [212])**
Walking Gait/Stair Ascent		
Hip Abd./Add.	1.3±1.3	2.9±1.5
Hip Flex.Ext.	3.0±2.7	2.7±1.7
Knee Flex./Ext.	1.3±1.2	3.5±1.1
Ankle Dorsi./Plant.	2.9±2.0	1.4±0.5
Jumping/Fast-Walking		
Hip Abd./Add.	1.2±1.1	3.7±1.8
Hip Flex.Ext.	3.0±2.5	3.4±2.1
Knee Flex./Ext.	0.6±0.6	4.5±1.3
Ankle Dorsi./Plant.	3.8±3.4	2.1±0.9

Although the MoCap results obtained from the exoskeleton are suitably accurate, sources of its systematic errors should be investigated and understood in order to improve the system design in the future. Considering the hip exoskeleton module, it generally tracked the motion trends with sufficient accuracy except for some localized regions of increased error. The motion results with notably greater error, particularly in the hip's internal/external rotation DOF, are: the standing-to-sitting/sitting-to-standing and squatting trials, and to a lesser extent the hip-flexion/extension, left-leg-kneeling, and walking-lunge trials. A common feature amongst all these movements is their inclusion of large hip-flexion angles. For the body-interfacing arrangement employed by the prototype system, large hip flexions cause the Simplified Agile Eye (SAE) in the hip

exoskeleton module to approach the combined singularity occurring when $\theta_1^{\text{SAE}} = 90° + d180°$ and $\theta_2^{\text{SAE}} = d180°$ (d is an integer; see Section 3.6). As discussed in Subsection 3.2.6, when a parallel manipulator nears a singular configuration, its local dexterity correspondingly approaches zero. Figure 6.16 shows a plot of the SAE's dexterity in terms of its J_1^{SAE} and J_2^{SAE} active joint angles. The physical implication for the hip exoskeleton is that errors in potentiometer readings are amplified to greater errors at the forward kinematic function output. Near the singularity under consideration, there is very little difference in sensed joint angles between a hip rotation associated with flexion/extension and one associated with internal/external rotation, hence the prominence of large errors in the latter DOF. The possibility of approaching a singularity was predicted in Subsection 5.2.3, although its practical ramifications could not be fully understood until the experimental study was completed. Ultimately, the hip exoskeleton's approach towards a singular configuration is the primary cause for increased measurement errors for movements involving large angles of hip flexion.

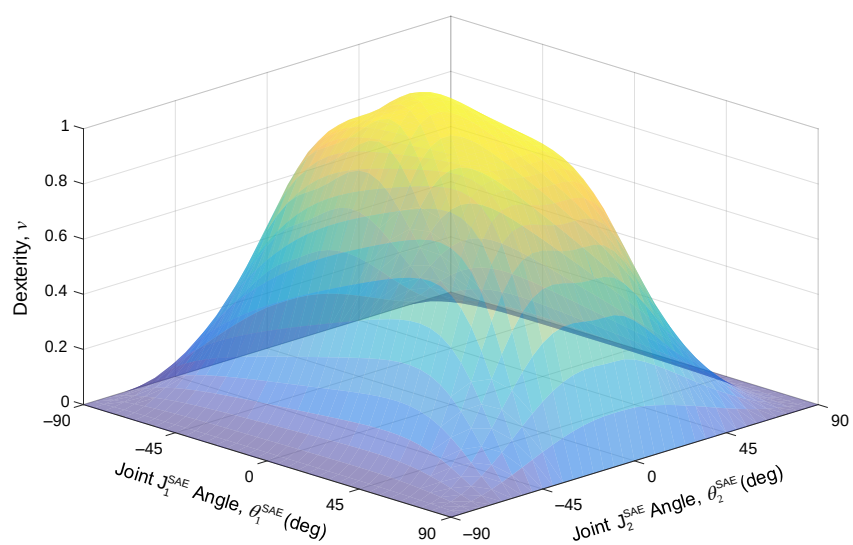

Figure 6.16. Dexterity of the SAE versus active joint angles θ_1^{SAE} and θ_2^{SAE}
Note: Dexterity reaches a value of zero (i.e., singular condition) when either $\theta_1^{\text{SAE}} = 90° + d180°$ or $\theta_2^{\text{SAE}} = 90° + d180°$, as expected from the singularity analysis results of Section 3.6.

Another limitation of the exoskeleton prototype worth noting is that its knee brace at least partially restricts adduction/abduction movements of the foot, which occur along the length of the shank's longitudinal axis and can only naturally occur when the knee is flexed [99]. However, this constraint did not obstruct the subject's ability to perform any of the experimental movements, and the knee brace helped impose the assumption of a

single-DOF knee. Also, note that both exoskeleton and Qualisys systems detected nonnegligible movements in the foot adduction/abduction DOF due to the lack of a precise anatomical-alignment procedure in this study, as described in Section 6.2.3 regarding Qualisys data processing. Because it does not improve upon the current state-of-the-art, the knee exoskeleton module is not a focus in this results discussion; however, note that it achieves accurate measurements with error generally within one degree relative to the optical reference system.

Such a clear trend in localized error as observed for the hip exoskeleton does not exist in the ankle exoskeleton results. In fact, some of the distinctly larger errors in the ankle exoskeleton's MoCap measurements seem to stem from erroneous reference-system results. The Qualisys system generally produced noisy measurements at the ankle and occasionally struggled to properly detect and track the markers placed on the foot orthotic, perhaps due to their proximity to the ankle exoskeleton components and the floor. An illuminating example of this occurs during the left-leg-kneeling trial, for which the optical system measured an instance of foot abduction exceeding 150 degrees. Obviously, the subject did not actually carry out this motion, so the large corresponding error reported in Table 6.5 may not actually reflect inaccurate ankle exoskeleton measurements. Another possible occurrence of Qualisys error occurs around the two-second mark in the double-leg horizontal jumping results. As can be observed in the ankle angles versus time plot on the right side of Figure 6.15, the Qualisys measurement of dorsiflexion diverges from the exoskeleton near this time, which roughly corresponds to the first image in photo sequence. It is likely that the Qualisys measurement magnitude is greater than the true value around this time, because during the ankle-dorsiflexion/plantarflexion trials, the extent of dorsiflexion range was approximately 10 degrees less than maximum magnitude measured by Qualisys in the jumping trial. Further evidence is that the maximum dorsiflexion angle captured by Qualisys during double-leg jumping exceeds the typical range for this joint DOF [99]. In this case, it is possible that the foot orthotic's heel lost contact with the subject's heel. This would have a greater affect on Qualisys measurements than exoskeleton measurements, because optical markers were placed directly onto the foot orthotic whereas the loss-of-contact may only attribute to a passive-joint rotation in the ankle module (i.e., in the universal joint adjacent to the foot orthotic).

It is also important to mention that, in addition to the protocollary movements of Table 6.4, the subject performed running-gait movements. This is differentiated from the fast-walking gait by the inclusion of an aerial stage (i.e., in which both feet do not contact the floor). However, the Qualisys system failed to provide continuous marker trajectories for at least three pelvis markers during each trial of this movement. As a result, none of these trials' reference data could be processed, so the associated results cannot be reported. Visible in the photographs of Figure 6.14, Figure 6.15, and Appendix F, the experiment's subject was instructed to maintain an arms-crossed upper-body posture during MoCap movements to deter optical-system occlusions caused by the upper limbs. The likely cause of the Qualisys' missing data is the subject's inability to completely maintain this unnatural posture while performing the running movements. This exemplifies one of the major disadvantages of marker-based optical-MoCap technology. Further issues encountered with the Qualisys system and noteworthy discrepancies between the exoskeleton and reference measurements are included alongside the remaining result plots in Appendix F.

Chapter 7.

Conclusions and Future Work

7.1. Summary of Thesis and Contributions

The prominent high-level applications of lower-limb exoskeletons are motion capture; strength augmentation or energy conservation for muscularly weakened persons; rehabilitation for victims of relevant injury or disease; and personal-mobility assistance for those with ongoing ambulatory disablements. Utilization of the technology in these contexts has the propensity to improve the quality of life for many people by providing a means to improve competency in independent walking and perform valid, reliable clinical assessments. The demographics that could benefit most include individuals living with the effects of stroke, spinal cord injury, Parkinson's disease, or multiple sclerosis, along with members of the elderly population. In serving these functions, it is fundamental that an exoskeleton offer kinematic compliance with the primary leg-joint movements associated with walking and daily activity. However, most of the existing lower-limb exoskeletons restrict several of these degrees-of-freedom (DOFs). Moreover, the current state-of-the-art mostly requires coaxial joint alignments in the exoskeleton-human interface, which is prone to inducing undesired interaction forces; it also generally neglects to employ parallel manipulators, which provide pertinent performance advantages over serial-manipulator alternatives. Considering these motivating factors and current-system shortcomings, the main objectives of this work have been to design, prototype, and test a novel lower-limb exoskeleton with advanced kinematic characteristics in the above-mentioned areas. Correspondingly, the principal contributions of this thesis can be summarized as follows.

7.1.1. Contributions from Chapter 3

In the development of the proposed exoskeleton's orientation manipulator component, a novel parallel manipulator with 3-<u>R</u>US architecture is presented. Inverse kinematic, forward kinematic, and Jacobian analyses for the manipulator are conducted, and its manipulability, dexterity, and rotational sensitivity performance indices are formulated. Moreover, a global manipulability index is derived in order to determine

optimal design parameters for maximizing that performance criterion. The same kinematic analyses are then performed for Gosselin's and Caron's Simplified Agile Eye (SAE) along with a hybridized 3-DOF form, which are both new contributions to the best of the author's knowledge. The SAE's manipulability, dexterity, and rotational sensitivity are evaluated, but a global performance index is irrelevant because the manipulator's Jacobian is not dependent on any design parameters (e.g., link lengths). The 3-RUS and SAE are then compared alongside Gosselin's and Hamel's original Agile Eye spherical manipulator. The SAE is deemed superior in terms of the three considered performance indices as well as smallest joint count, which is beneficial in terms of system simplicity, size, and minimal backlash. So, this manipulator is selected for use in the proposed exoskeleton design, and its singular configurations are identified based on an evaluation of its Jacobian matrix.

7.1.2. Contributions from Chapter 4

Two possible design schemes for the motion-transfer manipulator of the proposed exoskeleton system are described: a SRRP/S architecture and a SPU/S architecture. Both are novel contributions, as corroborated by an affirmative examination by the World Intellectual Property Organization and their successful inclusion in Patent Cooperation Treaty publication. The manipulators' inverse and forward kinematic analyses are formulated. The SPU/S is selected for inclusion in the proposed exoskeleton design due to the alternative's proneness to backlash and bulkiness.

7.1.3. Contributions from Chapter 5

Chapter 5 puts the selected developments from Chapter 3 together with those from Chapter 4 and then describes how the complete exoskeleton system interacts with two models for the human lower limb. The first model is a 6R serial manipulator suited for simulations of the exoskeleton-limb system; the manipulator's singular postures are confirmed to be outside of its anatomically-inspired intended workspace for expected design parameter selections. The second model considers the hip and ankle as spherical joints and the knee as a revolute joint to comprise a SRS structure. This latter model is used to interpret the experimental data described in Chapter 6. To support these simulation and experimentation functions, the forward and inverse kinematics are evaluated for the exoskeleton-6R system, whereas only the forward kinematics solution

is formulated when the human leg is modeled as a SRS manipulator. This latter solution represents the data-processing algorithm for a physical construction of the motion-capture (MoCap) exoskeleton.

7.1.4. Contributions from Chapter 6

A low-cost method of prototyping the lower-limb exoskeleton design is outlined. Experimental results obtained from the prototype and its data-processing algorithm reveal average root mean square errors and standard deviations of error to be: 3.8±3.2 degrees for hip rotations; 1.6±1.4 degrees for hip abduction/adduction; 3.0±2.4 degrees for hip extension/flexion; 0.6±0.5 degrees for knee flexion/extension; 3.4±2.8 degrees for ankle adduction/abduction; 2.5±2.2 degrees for ankle pronation/supination; and 2.7±2.2 degrees for ankle plantarflexion/dorsiflexion (i.e., in RMSE±STD format). The averages are taken across three categories of movement tests: joint range-of-motion, general mobility (e.g., walking, sitting, and ascending/descending stairs), and extended mobility (e.g., fast walking, double-leg horizontal jumping, and lunging). Also, a Qualisys optical MoCap system with passive markers was used as the reference from which errors were computed.

7.2. Concluding Remarks

In the end, this work fulfills its primary objectives, with one minor deviation. First, as demonstrated by its ability to independently track 3-DOF rotations at the hip, 1-DOF rotation at the knee, and 3-DOF rotations at the ankle, the exoskeleton design achieves kinematic compliance with all seven of the main human-leg articulations. The experimentation subject also reports being able to move through his full range-of-motion in each of these DOFs while wearing the exoskeleton, with the exception of ankle adduction/abduction. This movement ability is partially sacrificed to exploit the flat reference surface and limb attachment rigidity offered by the knee bracing component included with the off-the-shelf orthotics; since ankle adduction/abduction occurs along the length of the shank, the shank orthotic would need to be limited to a narrow attachment surface immediately below the knee to minimize the restriction on the DOF. This trade-off is justified by the negligible role of ankle adduction/abduction in normal ambulatory and general-mobility movements.

The proposed exoskeleton design is also developed without any requirement for coaxial alignments between the exoskeleton and human at the hip and ankle joints, per the thesis objectives. Moreover, the exoskeleton design includes the SAE as a parallel manipulator with two active joints in its hip and ankle modules. Lastly, the prototype successfully achieves a level of MoCap accuracy comparable to that of the inertial-based Xsens MVN system during similar subject movements. Thus, the proposed exoskeleton design shows promising potential for use in motion capture applications. Not only does the developed system resolve the primary shortcomings of current exoskeleton MoCap systems by satisfying this work's core objectives, but it also maintains the various electromechanical advantages over other MoCap system types; these include freedom from a limited measurement volume, low cost, quick setup and calibration, and immunity from occlusions and magnetic disturbances.

7.3. Future Work

The following subsections suggest several application-specific research directions that would constitute a continuation of the work presented in this thesis.

7.3.1. Unactuated Exoskeleton Applications (Motion Capture)

The presented exoskeleton design provides satisfactorily accurate results on average. However, the appearance of localized high-error regions should be eliminated from any measurements made within the operating workspace, which is defined by the upper extremes of human capability in joint mobility. These high-error regions have been observed to coincide with postures of close proximity to SAE singularities, which is consistent with the concept of manipulator dexterity. That is, as a parallel manipulator approaches a singular configuration, its Jacobian matrix becomes ill-conditioned and its kinematic accuracy declines. Therefore, a hypothetical approach to resolve this issue is to formulate an optimization procedure that identifies the orientation(s) of the SAE base with respect to the human body planes that maximizes its dexterity throughout the largest possible joint workspace. Perhaps this optimization routine could apply heavier weighting to the human joint angles associated with the most common MoCap movements or in a task-specific manner. The study could also investigate the effects of

employing revolute sensors with higher accuracy and precision on the overall accuracy in MoCap measurements.

Other recommendations for future work are to investigate the efficacy of adding sensors to the hip and ankle modules (i.e., at motion-transfer manipulator's revolute joints) in eliminating the need for parameter inputs in the data-processing algorithm. This would be beneficial because the act of measuring the required parameters is currently a potential source of error and a factor in system-setup time. Also, due to the wearable nature of the exoskeleton system, intra-subject measurement repeatability could be promoted by recording the states of the mechanical adjustments made upon interfacing with the system (e.g., strap-attachment lengths) or affixing the system to clothing; systematic inter- and intra-subject comparisons could then consider the differences in these adjustment states between MoCap sessions (e.g., for standardization in clinical assessments). The knee exoskeleton module should also be replaced with a design that does not require coaxial joint alignment nor restrict foot abduction/adduction movements. Next, since the prototype's orthotics and prismatic joints represent the most expensive components, cheaper and potentially more practical options for these items should be explored (e.g., mechanism integration with clothing instead of orthotics). Finally, additional exoskeleton modules should be subsequently developed for the capture of primary upper-body joint movements. In doing so, the selected motion-transfer manipulator should be tested and potentially modified for measuring the motions of multi-DOF joints in the human upper body. The attendant increase in sensors would likely necessitate adjustment or the addition of multiplexing to the MCU board in the electrical design of the system.

7.3.2. Actuated Exoskeleton Applications

After the dexterity optimization work outlined above is completed, the resulting design could also be fitted with actuators at its active joints in preparation for haptic feedback, strength augmentation, energy conservation, rehabilitation, or daily assistive applications. To start, application-specific expectations for human inertial properties and joint torques should be established, and a dynamic analysis of the exoskeleton-human system should be performed (e.g., by Newton-Euler or Lagrangian Formulation). This would provide a sense of appropriate actuator selections. Thereafter, the various actuated-exoskeleton applications are complex, each with their own set of numerous

considerations that will not be elaborated here. Notwithstanding, the author expects that the applications involve some form of sensory input based on user intention and/or environmental interaction that can be mapped to a desired lower-limb posture; following that, the present work provides a method of translating the desired posture to actuated joint position targets (i.e., the exoskeleton-limb system's inverse kinematic solution). In the pursuit of efficient and optimized power consumption, the author suggests consideration of the force-length relationship in skeletal muscle for an assist-as-needed approach to strength augmentation applications; moreover, the concept of passive dynamics should be explored and implemented in the exoskeleton control scheme during repetitive movements (e.g., level-ground gait or stair descent) if deemed appropriate and safe for strength augmentation or daily mobility-assistance applications.

References

[1] J. L. Pons, R. Ceres, and L. Calderón, “Introduction to wearable robotics,” in *Wearable Robots: Biomechatronic Exoskeletons*, 1st ed., J. L. Pons, Ed. Hoboken, NJ: John Wiley & Sons, 2008, pp. 1–16.

[2] J. Starck and A. Hilton, “Surface Capture for Performance-Based Animation,” *IEEE Comput. Graph. Appl.*, vol. 27, no. 3, pp. 21–31, May 2007.

[3] J. Gall, C. Stoll, E. de Aguiar, C. Theobalt, B. Rosenhahn, and H.-P. Seidel, “Motion capture using joint skeleton tracking and surface estimation,” in *2009 IEEE Conference on Computer Vision and Pattern Recognition*, 2009, pp. 1746–1753.

[4] M. Tejera, D. Casas, and A. Hilton, “Animation Control of Surface Motion Capture,” *IEEE Trans. Cybern.*, vol. 43, no. 6, pp. 1532–1545, Dec. 2013.

[5] S. Maggioni, A. Melendez-Calderon, E. van Asseldonk, V. Klamroth-Marganska, L. Lünenburger, R. Riener, and H. van der Kooij, “Robot-aided assessment of lower extremity functions: a review.,” *J. Neuroeng. Rehabil.*, vol. 13, no. 1, p. 72, 2016.

[6] R. Camicioli, D. Howieson, B. Oken, G. Sexton, and J. Kaye, “Motor slowing precedes cognitive impairment in the oldest old.,” *Neurology*, vol. 50, no. 5, pp. 1496–8, May 1998.

[7] N. T. Aggarwal, R. S. Wilson, T. L. Beck, J. L. Bienias, and D. A. Bennett, “Motor Dysfunction in Mild Cognitive Impairment and the Risk of Incident Alzheimer Disease,” *Arch. Neurol.*, vol. 63, no. 12, p. 1763, Dec. 2006.

[8] J. Verghese, M. Robbins, R. Holtzer, M. Zimmerman, C. Wang, X. Xue, and R. B. Lipton, “Gait Dysfunction in Mild Cognitive Impairment Syndromes,” *J. Am. Geriatr. Soc.*, vol. 56, no. 7, pp. 1244–1251, Jul. 2008.

[9] A. Akl, B. Taati, and A. Mihailidis, “Autonomous Unobtrusive Detection of Mild Cognitive Impairment in Older Adults,” *IEEE Trans. Biomed. Eng.*, vol. 62, no. 5, pp. 1383–1394, May 2015.

[10] M. D. Hurd, P. Martorell, A. Delavande, K. J. Mullen, and K. M. Langa, “Monetary Costs of Dementia in the United States,” *N. Engl. J. Med.*, vol. 368, no. 14, pp. 1326–1334, Apr. 2013.

[11] I. Bautmans, B. Jansen, B. Van Keymolen, and T. Mets, “Reliability and clinical correlates of 3D-accelerometry based gait analysis outcomes according to age and fall-risk,” *Gait Posture*, vol. 33, no. 3, pp. 366–372, Mar. 2011.

[12] M. Terroso, N. Rosa, A. Torres Marques, and R. Simoes, “Physical consequences

of falls in the elderly: a literature review from 1995 to 2010," *Eur. Rev. Aging Phys. Act.*, vol. 11, no. 1, pp. 51–59, Apr. 2014.

[13] M. Prince, R. Bryce, E. Albanese, A. Wimo, W. Ribeiro, and C. P. Ferri, "The global prevalence of dementia: a systematic review and metaanalysis.," *Alzheimers. Dement.*, vol. 9, no. 1, p. 63–75.e2, Jan. 2013.

[14] Statistics Canada, "Population by broad age groups and sex, 2016 counts for both sexes, Canada, provinces and territories, 2016 Census – 100% Data," *Age and Sex Highlight Tables, 2016 Census*, 2017. [Online]. Available: http://www12.statcan.gc.ca/census-recensement/2016/dp-pd/hlt-fst/as/Table.cfm?Lang=E&T=11. [Accessed: 05-Feb-2018].

[15] Statistics Canada, "Age and sex, and type of dwelling data: Key results from the 2016 Census," *The Daily*, 2017. [Online]. Available: http://www.statcan.gc.ca/daily-quotidien/170503/dq170503a-eng.htm. [Accessed: 05-Feb-2018].

[16] W. He, D. Goodkind, and P. Kowal, "An Aging World: 2015," Washington, DC, 2016.

[17] J. E. Graham, G. V. Ostir, S. R. Fisher, and K. J. Ottenbacher, "Assessing walking speed in clinical research: a systematic review," *J. Eval. Clin. Pract.*, vol. 14, no. 4, pp. 552–562, Aug. 2008.

[18] D. Fitzgerald, J. Foody, D. Kelly, T. Ward, C. Markham, J. McDonald, and B. Caulfield, "Development of a wearable motion capture suit and virtual reality biofeedback system for the instruction and analysis of sports rehabilitation exercises," in *2007 29th Annual International Conference of the IEEE Engineering in Medicine and Biology Society*, 2007, vol. 2007, pp. 4870–4874.

[19] A. Menache, *Understanding motion capture for computer animation and video games*. Morgan Kaufmann, 2000.

[20] Heart and Stroke Foundation of Canada, "2016 Stroke Report," Ottawa, 2016.

[21] E. J. Benjamin, M. J. Blaha, S. E. Chiuve, M. Cushman, S. R. Das, R. Deo, S. D. de Ferranti, and J. Floyd, "Heart Disease and Stroke Statistics—2017 Update: A Report from the American Heart Association," 2017.

[22] P. Poli, G. Morone, G. Rosati, and S. Masiero, "Robotic technologies and rehabilitation: new tools for stroke patients' therapy.," *Biomed Res. Int.*, vol. 2013, p. 153872, Nov. 2013.

[23] K. Y. Nam, H. J. Kim, B. S. Kwon, J.-W. Park, H. J. Lee, and A. Yoo, "Robot-assisted gait training (Lokomat) improves walking function and activity in people with spinal cord injury: a systematic review," *J. Neuroeng. Rehabil.*, vol. 14, no. 1, p. 24, Dec. 2017.

[24] C. Fisahn, M. Aach, O. Jansen, M. Moisi, A. Mayadev, K. T. Pagarigan, J. R. Dettori, and T. A. Schildhauer, “The Effectiveness and Safety of Exoskeletons as Assistive and Rehabilitation Devices in the Treatment of Neurologic Gait Disorders in Patients with Spinal Cord Injury: A Systematic Review,” *Glob. Spine J.*, vol. 6, no. 8, pp. 822–841, Dec. 2016.

[25] S. L. Wong, H. Gilmour, and P. L. Ramage-Morin, “Parkinson’s disease: Prevalence, diagnosis and impact,” 2015.

[26] Multiple Sclerosis Society of Canada, “About MS.” [Online]. Available: https://mssociety.ca/about-ms. [Accessed: 07-Feb-2018].

[27] V. K. Noonan, M. Fingas, A. Farry, D. Baxter, A. Singh, M. G. Fehlings, and M. F. Dvorak, “Incidence and Prevalence of Spinal Cord Injury in Canada: A National Perspective,” *Neuroepidemiology*, vol. 38, no. 4, pp. 219–226, 2012.

[28] National Spinal Cord Injury Statistical Center (NSCISC), “Spinal Cord Injury Facts and Figures at a Glance,” *2017 SCI Data Sheet*, 2017. [Online]. Available: https://www.nscisc.uab.edu/Public/Facts and Figures - 2017.pdf. [Accessed: 06-Feb-2018].

[29] S. L. Kowal, T. M. Dall, R. Chakrabarti, M. V. Storm, and A. Jain, “The current and projected economic burden of Parkinson’s disease in the United States,” *Mov. Disord.*, vol. 28, no. 3, pp. 311–318, Mar. 2013.

[30] P. Dilokthornsakul, R. J. Valuck, K. V Nair, J. R. Corboy, R. R. Allen, and J. D. Campbell, “Multiple sclerosis prevalence in the United States commercially insured population.,” *Neurology*, vol. 86, no. 11, pp. 1014–21, Mar. 2016.

[31] F. Ferrati, R. Bortoletto, E. Menegatti, and E. Pagello, “Socio-economic impact of medical lower-limb Exoskeletons,” in *2013 IEEE Workshop on Advanced Robotics and its Social Impacts*, 2013, pp. 19–26.

[32] H. Kawamoto, K. Kamibayashi, Y. Nakata, K. Yamawaki, R. Ariyasu, Y. Sankai, M. Sakane, K. Eguchi, and N. Ochiai, “Pilot study of locomotion improvement using hybrid assistive limb in chronic stroke patients,” *BMC Neurol.*, vol. 13, no. 1, p. 141, Dec. 2013.

[33] J. L. Contreras-Vidal, N. A Bhagat, J. Brantley, J. G. Cruz-Garza, Y. He, Q. Manley, S. Nakagome, K. Nathan, S. H. Tan, F. Zhu, and J. L. Pons, “Powered exoskeletons for bipedal locomotion after spinal cord injury,” *J. Neural Eng.*, vol. 13, no. 3, p. 31001, Jun. 2016.

[34] E. Y. Y. Cheung, T. K. W. Ng, K. K. K. Yu, R. L. C. Kwan, and G. L. Y. Cheing, “Robot-Assisted Training for People With Spinal Cord Injury: A Meta-Analysis,” *Arch. Phys. Med. Rehabil.*, vol. 98, no. 11, p. 2320–2331.e12, Nov. 2017.

[35] M. Pohl, C. Werner, M. Holzgraefe, G. Kroczek, I. Wingendorf, G. Hoölig, R. Koch, and S. Hesse, “Repetitive locomotor training and physiotherapy improve

walking and basic activities of daily living after stroke: a single-blind, randomized multicentre trial (DEutsche GAngtrainerStudie, DEGAS)," *Clin. Rehabil.*, vol. 21, no. 1, pp. 17–27, Jan. 2007.

[36] J. Mehrholz, S. Thomas, C. Werner, J. Kugler, M. Pohl, and B. Elsner, "Electromechanical-assisted training for walking after stroke," *Cochrane Database Syst. Rev.*, May 2017.

[37] A. C. Lo, V. C. Chang, M. A. Gianfrancesco, J. H. Friedman, T. S. Patterson, and D. F. Benedicto, "Reduction of freezing of gait in Parkinson's disease by repetitive robot-assisted treadmill training: a pilot study," *J. Neuroeng. Rehabil.*, vol. 7, no. 1, p. 51, Oct. 2010.

[38] A. Picelli, C. Melotti, F. Origano, A. Waldner, A. Fiaschi, V. Santilli, and N. Smania, "Robot-Assisted Gait Training in Patients With Parkinson Disease," *Neurorehabil. Neural Repair*, vol. 26, no. 4, pp. 353–361, May 2012.

[39] A. Picelli, C. Melotti, F. Origano, A. Waldner, R. Gimigliano, and N. Smania, "Does robotic gait training improve balance in Parkinson's disease? A randomized controlled trial.," *Parkinsonism Relat. Disord.*, vol. 18, no. 8, pp. 990–3, Sep. 2012.

[40] P. Sale, M. F. De Pandis, D. Le Pera, I. Sova, V. Cimolin, A. Ancillao, G. Albertini, M. Galli, F. Stocchi, and M. Franceschini, "Robot-assisted walking training for individuals with Parkinson's disease: a pilot randomized controlled trial," *BMC Neurol.*, vol. 13, no. 1, p. 50, Dec. 2013.

[41] M. Galli, V. Cimolin, M. F. De Pandis, D. Le Pera, I. Sova, G. Albertini, F. Stocchi, and M. Franceschini, "Robot-assisted gait training versus treadmill training in patients with Parkinson's disease: a kinematic evaluation with gait profile score.," *Funct. Neurol.*, vol. 31, no. 3, pp. 163–70, 2016.

[42] A. Furnari, R. S. Calabrò, M. C. De Cola, M. Bartolo, A. Castelli, A. Mapelli, G. Buttacchio, E. Farini, P. Bramanti, and R. Casale, "Robotic-assisted gait training in Parkinson's disease: a three-month follow-up randomized clinical trial," *Int. J. Neurosci.*, vol. 127, no. 11, pp. 996–1004, Nov. 2017.

[43] S. Beer, B. Aschbacher, D. Manoglou, E. Gamper, J. Kool, and J. Kesselring, "Robot-assisted gait training in multiple sclerosis: a pilot randomized trial," *Mult. Scler. J.*, vol. 14, no. 2, pp. 231–236, Mar. 2008.

[44] A. C. Lo and E. W. Triche, "Improving Gait in Multiple Sclerosis Using Robot-Assisted, Body Weight Supported Treadmill Training," *Neurorehabil. Neural Repair*, vol. 22, no. 6, pp. 661–671, Nov. 2008.

[45] I. Schwartz, A. Sajin, E. Moreh, I. Fisher, M. Neeb, A. Forest, A. Vaknin-Dembinsky, D. Karusis, and Z. Meiner, "Robot-assisted gait training in multiple sclerosis patients: a randomized trial," *Mult. Scler. J.*, vol. 18, no. 6, pp. 881–890, Jun. 2012.

[46] E. Swinnen, D. Beckwée, D. Pinte, R. Meeusen, J.-P. Baeyens, and E. Kerckhofs, “Treadmill Training in Multiple Sclerosis: Can Body Weight Support or Robot Assistance Provide Added Value? A Systematic Review,” *Mult. Scler. Int.*, vol. 2012, pp. 1–15, May 2012.

[47] S. Straudi, M. G. Benedetti, E. Venturini, M. Manca, C. Foti, and N. Basaglia, “Does robot-assisted gait training ameliorate gait abnormalities in multiple sclerosis? A pilot randomized-control trial,” *NeuroRehabilitation*, vol. 33, no. 4, pp. 555–563, Jan. 2013.

[48] M. Gandolfi, C. Geroin, A. Picelli, D. Munari, A. Waldner, S. Tamburin, F. Marchioretto, and N. Smania, “Robot-assisted vs. sensory integration training in treating gait and balance dysfunctions in patients with multiple sclerosis: a randomized controlled trial,” *Front. Hum. Neurosci.*, vol. 8, p. 318, May 2014.

[49] M. Hubli and V. Dietz, “The physiological basis of neurorehabilitation - locomotor training after spinal cord injury,” *J. Neuroeng. Rehabil.*, vol. 10, no. 1, p. 5, Jan. 2013.

[50] N. Hajela, C. K. Mummidisetty, A. C. Smith, and M. Knikou, “Corticospinal reorganization after locomotor training in a person with motor incomplete paraplegia.,” *Biomed Res. Int.*, vol. 2013, p. 516427, Dec. 2013.

[51] R. S. Calabrò, A. Naro, A. Leo, and P. Bramanti, “Usefulness of robotic gait training plus neuromodulation in chronic spinal cord injury: a case report,” *J. Spinal Cord Med.*, vol. 40, no. 1, pp. 118–121, Jan. 2017.

[52] J. Kressler, C. K. Thomas, E. C. Field-Fote, J. Sanchez, E. Widerström-Noga, D. C. Cilien, K. Gant, K. Ginnety, H. Gonzalez, A. Martinez, K. D. Anderson, and M. S. Nash, “Understanding Therapeutic Benefits of Overground Bionic Ambulation: Exploratory Case Series in Persons With Chronic, Complete Spinal Cord Injury,” *Arch. Phys. Med. Rehabil.*, vol. 95, no. 10, p. 1878–1887.e4, Oct. 2014.

[53] E. Swinnen, S. Duerinck, J. Baeyens, R. Meeusen, and E. Kerckhofs, “Effectiveness of robot-assisted gait training in persons with spinal cord injury: A systematic review,” *J. Rehabil. Med.*, vol. 42, no. 6, pp. 520–526, 2010.

[54] P. Sale, M. Franceschini, A. Waldner, and S. Hesse, “Use of the robot assisted gait therapy in rehabilitation of patients with stroke and spinal cord injury.,” *Eur. J. Phys. Rehabil. Med.*, vol. 48, no. 1, pp. 111–21, Mar. 2012.

[55] M. Arazpour, S. W. Hutchins, and M. Ahmadi Bani, “The efficacy of powered orthoses on walking in persons with paraplegia,” *Prosthet. Orthot. Int.*, vol. 39, no. 2, pp. 90–99, Apr. 2015.

[56] R. Teasell and N. Hussein, “Background Concepts in Stroke Rehabilitation,” London, Canada, 2016.

[57] J. D. Walston, “Sarcopenia in older adults.,” *Curr. Opin. Rheumatol.*, vol. 24, no.

6, pp. 623–7, Nov. 2012.

[58] C. J. Brown and K. L. Flood, “Mobility Limitation in the Older Patient,” *J. Am. Med. Assoc.*, vol. 310, no. 11, pp. 1168–1177, Sep. 2013.

[59] Lockheed Martin, “Relief for the Daily Grind: Industrial Exoskeletons at Work,” 2014. [Online]. Available: https://www.lockheedmartin.com/us/news/features/2014/mfc-103114-relief-daily-grind-industrial-exoskeletons-work.html. [Accessed: 02-Feb-2018].

[60] A. Yassi, “Repetitive strain injuries,” *Lancet*, vol. 349, no. 9056, pp. 943–947, Mar. 1997.

[61] C. J. Walsh, K. Endo, and H. Herr, “A Quasi-Passive Leg Exoskeleton For Load-Carrying Augmentation,” *Int. J. Humanoid Robot.*, vol. 4, no. 3, pp. 487–506, Sep. 2007.

[62] C. Bizier, G. Fawcett, and S. Gilbert, “Canadian Survey on Disability, 2012: Mobility disabilities among Canadians aged 15 years and older, 2012,” 2016.

[63] E. A. Courtney-Long, D. D. Carroll, Q. C. Zhang, A. C. Stevens, S. Griffin-Blake, B. S. Armour, and V. A. Campbell, “Morbidity and Mortality Weekly Report: Prevalence of Disability and Disability Type Among Adults — United States, 2013,” 2015.

[64] Eunice Kennedy Shriver National Institute of Child Health and Human Development, “How many people use assistive devices?,” 2016. [Online]. Available: https://www.nichd.nih.gov/health/topics/rehabtech/conditioninfo/people. [Accessed: 08-Feb-2018].

[65] E. M. Smith, E. M. Giesbrecht, W. B. Mortenson, and W. C. Miller, “Prevalence of Wheelchair and Scooter Use Among Community-Dwelling Canadians,” *Phys. Ther.*, vol. 96, no. 8, pp. 1135–1142, Aug. 2016.

[66] V. Lajeunesse, C. Vincent, F. Routhier, E. Careau, and F. Michaud, “Exoskeletons’ design and usefulness evidence according to a systematic review of lower limb exoskeletons used for functional mobility by people with spinal cord injury,” *Disabil. Rehabil. Assist. Technol.*, vol. 11, no. 7, pp. 535–547, Oct. 2016.

[67] A. Esquenazi, M. Talaty, and A. Jayaraman, “Powered Exoskeletons for Walking Assistance in Persons with Central Nervous System Injuries: A Narrative Review,” *PM&R*, vol. 9, no. 1, pp. 46–62, Jan. 2017.

[68] M. Arazpour, M. A. Bani, S. W. Hutchins, and R. K. Jones, “The physiological cost index of walking with mechanical and powered gait orthosis in patients with spinal cord injury,” *Spinal Cord*, vol. 51, no. 5, pp. 356–359, May 2013.

[69] L. E. Miller, A. K. Zimmermann, and W. G. Herbert, “Clinical effectiveness and

safety of powered exoskeleton-assisted walking in patients with spinal cord injury: systematic review with meta-analysis.," *Med. Devices (Auckl).*, vol. 9, pp. 455–66, 2016.

[70] T. Platz, A. Gillner, N. Borgwaldt, S. Kroll, and S. Roschka, "Device-Training for Individuals with Thoracic and Lumbar Spinal Cord Injury Using a Powered Exoskeleton for Technically Assisted Mobility: Achievements and User Satisfaction," *Biomed Res. Int.*, vol. 2016, pp. 1–10, Aug. 2016.

[71] G. Zeilig, H. Weingarden, M. Zwecker, I. Dudkiewicz, A. Bloch, and A. Esquenazi, "Safety and tolerance of the ReWalk™ exoskeleton suit for ambulation by people with complete spinal cord injury: a pilot study.," *J. Spinal Cord Med.*, vol. 35, no. 2, pp. 96–101, Mar. 2012.

[72] P. Allard, I. A. F. Stokes, and J.-P. Blanchi, *Three-Dimensional Analysis of Human Movement*. Champaign, IL: Human Kinetics, 1995.

[73] D. G. E. Robertson, G. E. Caldwell, J. Hamill, G. Kamen, and S. N. Whittlesey, *Research methods in biomechanics*. Champaign, IL: Human Kinetics, 2004.

[74] B. Rosenhahn, R. Klette, and D. Metaxas, *Human Motion: Understanding, Modelling, Capture and Animation*, vol. 36. Dordrecht: Springer Netherlands, 2008.

[75] M. Field, D. Stirling, F. Naghdy, and Z. Pan, "Motion capture in robotics review," in *2009 IEEE International Conference on Control and Automation*, 2009, pp. 1697–1702.

[76] T. Everett and C. Kell, *Human movement: an introductory text.*, 6th ed. Edinburgh, NY: Elsevier, 2010.

[77] L. Chèze, *Kinematic Analysis of Human Movement*. Wiley-ISTE, 2014.

[78] J. Hamill, K. M. Knutzen, and T. R. Derrick, *Biomechanical Basis of Human Movement*, 4th ed. Philadelphia, PA: Wolters Kluwer Health, 2015.

[79] L. Chiari, U. Della Croce, A. Leardini, and A. Cappozzo, "Human movement analysis using stereophotogrammetry: Part 2. Instrumental errors," *Gait Posture*, vol. 21, no. 2, pp. 197–211, Feb. 2005.

[80] OptiTrack, "OSU Dancers," 2013. [Online]. Available: https://www.facebook.com/OptiTrack/photos/a.186641774811383.49931.111685218973706/186998188109075/?type=3&theater. [Accessed: 30-Jan-2018].

[81] PTI Phoenix Technologies, "VZ4050 3D Motion Capture Systems." [Online]. Available: http://www.ptiphoenix.com/products/trackers/VZ4050. [Accessed: 15-Aug-2017].

[82] F. C. Anderson and M. G. Pandy, “A Dynamic Optimization Solution for Vertical Jumping in Three Dimensions.,” *Comput. Methods Biomech. Biomed. Engin.*, vol. 2, no. 3, pp. 201–231, Jan. 1999.

[83] A. Fern’ndez-Baena, A. Susin, and X. Lligadas, “Biomechanical Validation of Upper-Body and Lower-Body Joint Movements of Kinect Motion Capture Data for Rehabilitation Treatments,” in *2012 Fourth International Conference on Intelligent Networking and Collaborative Systems*, 2012, pp. 656–661.

[84] Xsens, “Xsens MVN.” [Online]. Available: https://www.xsens.com/products/xsens-mvn/?gclid=CM3NpJSo19UCFQ5Efgod9HcAyA. [Accessed: 14-Aug-2017].

[85] Metamotion, “Gypsy 7 Motion Capture System.” [Online]. Available: http://metamotion.com/gypsy/gypsy-motion-capture-system.htm. [Accessed: 13-Aug-2017].

[86] Biometrics Ltd, “Goniometers (Electrogoniometers) and Torsiometers for Joint Movement Analysis.” [Online]. Available: http://www.biometricsltd.com/gonio.htm. [Accessed: 15-Aug-2017].

[87] S. G. Kim, K. W. Jang, W. J. Yoo, S. H. Shin, S. Cho, and B. Lee, “Feasibility study on fiber-optic goniometer for measuring knee joint angle,” *Opt. Rev.*, vol. 21, no. 5, pp. 694–697, Sep. 2014.

[88] M. L. RAWES, J. B. RICHARDSON, and J. J. DIAS, “A New Technique for The Assessment of Wrist Movement using a Biaxial Flexible Electrogoniometer,” *J. Hand Surg. Am.*, vol. 21, no. 5, pp. 600–603, Oct. 1996.

[89] A. Gmiterko and T. Lipták, “Motion Capture of Human for Interaction with Service Robot,” *Am. J. Mech. Eng.*, vol. 1, no. 7, pp. 212–216, 2013.

[90] Metamotion, “Magnetic Motion Capture Systems.” [Online]. Available: http://metamotion.com/motion-capture/magnetic-motion-capture-1.htm. [Accessed: 13-Aug-2017].

[91] O. Gabai and H. Primo, “Acoustic motion capture,” WO2009072126 A2, 2008.

[92] M. Cenciarini and A. M. Dollar, “Biomechanical considerations in the design of lower limb exoskeletons.,” *IEEE Int. Conf. Rehabil. Robot.*, vol. 2011, p. 5975366, Jan. 2011.

[93] I. Díaz, J. J. Gil, and E. Sánchez, “Lower-Limb Robotic Rehabilitation: Literature Review and Challenges,” *J. Robot.*, vol. 2011, pp. 1–11, 2011.

[94] S. Sargsyan, V. Arakelian, and S. Briot, “Robotic Rehabilitation Devices of Human Extremities: Design Concepts and Functional Particularities,” in *Volume 3: Advanced Composite Materials and Processing; Robotics; Information Management and PLM; Design Engineering*, 2012, p. 245.

[95] M. Dzahir and S. Yamamoto, “Recent Trends in Lower-Limb Robotic Rehabilitation Orthosis: Control Scheme and Strategy for Pneumatic Muscle Actuated Gait Trainers,” *Robotics*, vol. 3, no. 4, pp. 120–148, Apr. 2014.

[96] T. Yan, M. Cempini, C. M. Oddo, and N. Vitiello, “Review of assistive strategies in powered lower-limb orthoses and exoskeletons,” *Rob. Auton. Syst.*, vol. 64, pp. 120–136, 2015.

[97] B. Chen, H. Ma, L.-Y. Qin, F. Gao, K.-M. Chan, S.-W. Law, and W.-H. Liao, “Recent developments and challenges of lower extremity exoskeletons,” *J. Orthop. Transl.*, vol. 5, pp. 26–37, 2016.

[98] A. J. Young and D. P. Ferris, “State of the Art and Future Directions for Lower Limb Robotic Exoskeletons,” *IEEE Trans. Neural Syst. Rehabil. Eng.*, vol. 25, no. 2, pp. 171–182, Feb. 2017.

[99] N. Palastanga and R. W. Soames, *Anatomy and Human Movement: Structure and function*. Elsevier Health Sciences UK, 2011.

[100] H. Kazerooni and R. Steger, “The Berkeley Lower Extremity Exoskeleton,” *J. Dyn. Syst. Meas. Control*, vol. 128, no. 1, p. 14, Mar. 2006.

[101] Berkeley Robotics & Human Engineering Laboratory, “ExoHiker™.” [Online]. Available: http://bleex.me.berkeley.edu/research/exoskeleton/exohiker/. [Accessed: 03-Oct-2016].

[102] Berkeley Robotics & Human Engineering Laboratory, “ExoClimber™.” [Online]. Available: http://bleex.me.berkeley.edu/research/exoskeleton/exoclimber/. [Accessed: 03-Oct-2016].

[103] Berkeley Robotics & Human Engineering Laboratory, “HULC™.” [Online]. Available: http://bleex.me.berkeley.edu/research/exoskeleton/hulc/. [Accessed: 03-Oct-2016].

[104] S. Marcheschi, F. Salsedo, M. Fontana, and M. Bergamasco, “Body Extender: Whole body exoskeleton for human power augmentation,” in *2011 IEEE International Conference on Robotics and Automation*, 2011, pp. 611–616.

[105] G. Mone, “Building the Real Iron Man,” *Popular Science*, 2008. [Online]. Available: https://www.popsci.com/scitech/article/2008-04/building-real-iron-man. [Accessed: 02-Feb-2018].

[106] K. H. Low, X. Liu, and H. Yu, “Design and implementation of NTU wearable exoskeleton as an enhancement and assistive device,” *Appl. Bionics Biomech.*, vol. 3, no. 3, pp. 209–225, Jan. 2006.

[107] A. Valiente, “Design of a Quasi-Passive Parallel Leg Exoskeleton to Augment Load Carrying for Walking,” Massachusetts Institute of Technology, 2005.

[108] J. C. Selinger and J. M. Donelan, “Myoelectric Control for Adaptable Biomechanical Energy Harvesting,” *IEEE Trans. Neural Syst. Rehabil. Eng.*, vol. 24, no. 3, pp. 364–373, Mar. 2016.

[109] G. Colombo, M. Joerg, R. Schreier, and V. Dietz, “Treadmill training of paraplegic patients using a robotic orthosis,” *J. Rehabil. Res. Dev.*, vol. 37, no. 6, pp. 693–700, Jan. 2000.

[110] G. Colombo, M. Wirz, and V. Dietz, “Driven gait orthosis for improvement of locomotor training in paraplegic patients.,” *Spinal Cord*, vol. 39, no. 5, pp. 252–5, May 2001.

[111] R. G. West, “Powered gait orthosis and method of utilizing same,” US 6,689,075 B2, 10-Feb-2004.

[112] J. F. Veneman, R. Kruidhof, E. E. G. Hekman, R. Ekkelenkamp, E. H. F. Van Asseldonk, and H. van der Kooij, “Design and Evaluation of the LOPES Exoskeleton Robot for Interactive Gait Rehabilitation,” *IEEE Trans. Neural Syst. Rehabil. Eng.*, vol. 15, no. 3, pp. 379–386, Sep. 2007.

[113] D. J. Reinkensmeyer, D. Aoyagi, J. L. Emken, J. A. Galvez, W. Ichinose, G. Kerdanyan, S. Maneekobkunwong, K. Minakata, J. A. Nessler, R. Weber, R. R. Roy, R. de Leon, J. E. Bobrow, S. J. Harkema, and V. R. Edgerton, “Tools for understanding and optimizing robotic gait training.,” *J. Rehabil. Res. Dev.*, vol. 43, no. 5, pp. 657–70, 2006.

[114] S. K. Banala, S. K. Agrawal, and J. P. Scholz, “Active Leg Exoskeleton (ALEX) for Gait Rehabilitation of Motor-Impaired Patients,” in *2007 IEEE 10th International Conference on Rehabilitation Robotics*, 2007, pp. 401–407.

[115] D. Zanotto, P. Stegall, and S. K. Agrawal, “ALEX III: A novel robotic platform with 12 DOFs for human gait training,” in *2013 IEEE International Conference on Robotics and Automation*, 2013, pp. 3914–3919.

[116] P. Beyl, M. Van Damme, R. Van Ham, R. Versluys, B. Vanderborght, and D. Lefeber, “An exoskeleton for gait rehabilitation: Prototype design and control principle,” in *2008 IEEE International Conference on Robotics and Automation*, 2008, pp. 2037–2042.

[117] P. Beyl, “Design and control of a knee exoskeleton powered by pleated pneumatic artificial muscles for robot-assisted gait rehabilitation,” Vrije Universiteit Brussel, 2010.

[118] R. Ronsse, T. Lenzi, N. Vitiello, B. Koopman, E. van Asseldonk, S. M. M. De Rossi, J. van den Kieboom, H. van der Kooij, M. C. Carrozza, and A. J. Ijspeert, “Oscillator-based assistance of cyclical movements: model-based and model-free approaches,” *Med. Biol. Eng. Comput.*, vol. 49, no. 10, pp. 1173–1185, Oct. 2011.

[119] RObotics And Rehabilitation (ROAR) Laboratory, “ALEX,” *Columbia University*.

[Online]. Available: https://roar.me.columbia.edu/content/alex. [Accessed: 02-Feb-2018].

[120] P. Beyl, M. Van Damme, R. Van Ham, B. Vanderborght, and D. Lefeber, “Design and control of a lower limb exoskeleton for robot-assisted gait training,” *Appl. Bionics Biomech.*, vol. 6, no. 2, pp. 229–243, Jul. 2009.

[121] A. Goffer, “Gait-locomotor apparatus,” US 7153242 B2, 2001.

[122] H. Kawamoto, S. Suwoong Lee, S. Kanbe, and Y. Sankai, “Power assist method for HAL-3 using EMG-based feedback controller,” in *SMC’03 Conference Proceedings. 2003 IEEE International Conference on Systems, Man and Cybernetics. Conference Theme - System Security and Assurance (Cat. No.03CH37483)*, 2003, vol. 2, pp. 1648–1653.

[123] Berkeley Robotics & Human Engineering Laboratory, “eLEGS™.” [Online]. Available: http://bleex.me.berkeley.edu/research/exoskeleton/elegs™/. [Accessed: 03-Oct-2016].

[124] Berkeley Robotics & Human Engineering Laboratory, “Austin.” [Online]. Available: http://bleex.me.berkeley.edu/research/exoskeleton/medical-exoskeleton/. [Accessed: 03-Oct-2016].

[125] SuitX, “Phoenix.” [Online]. Available: http://www.suitx.com/phoenix. [Accessed: 04-Feb-2018].

[126] ReWalk Robotics, “ReWalk - More Than Walking.” [Online]. Available: http://rewalk.com/. [Accessed: 03-Oct-2016].

[127] Cyberdyne, “Cyberdyne.” [Online]. Available: http://www.cyberdyne.jp/english/. [Accessed: 03-Oct-2016].

[128] Ekso Bionics, “Ekso Bionics.” [Online]. Available: http://eksobionics.com/. [Accessed: 03-Oct-2016].

[129] H. A. Quintero, R. J. Farris, and M. Goldfarb, “Control and implementation of a powered lower limb orthosis to aid walking in paraplegic individuals,” in *2011 IEEE International Conference on Rehabilitation Robotics*, 2011, pp. 1–6.

[130] P. D. Neuhaus, J. H. Noorden, T. J. Craig, T. Torres, J. Kirschbaum, and J. E. Pratt, “Design and evaluation of Mina: A robotic orthosis for paraplegics,” in *2011 IEEE International Conference on Rehabilitation Robotics*, 2011, pp. 1–8.

[131] Institute for Human and Machine Cognition, “IHMC Robotics - Cybathlon Team.” [Online]. Available: http://robots.ihmc.us/cybathlon/. [Accessed: 04-Feb-2018].

[132] GOGOA Mobility Robots, “HANK Exoskeleton Design.” [Online]. Available: http://gogoa.eu/technology/hank-exoskeleton-design/. [Accessed: 04-Feb-2018].

[133] D. Salisbury, “FDA approves Indego exoskeleton for clinical and personal use,” 2016. [Online]. Available: https://phys.org/news/2016-03-fda-indego-exoskeleton-clinical-personal.html. [Accessed: 02-Feb-2018].

[134] ExoAtlet, “For home.” [Online]. Available: https://www.exoatlet.com/en/for-home. [Accessed: 02-Feb-2018].

[135] G. Barbareschi, R. Richards, M. Thornton, T. Carlson, and C. Holloway, “Statically vs dynamically balanced gait: Analysis of a robotic exoskeleton compared with a human,” in *2015 37th Annual International Conference of the IEEE Engineering in Medicine and Biology Society (EMBC)*, 2015, pp. 6728–6731.

[136] REX Bionics, “REX P.” [Online]. Available: https://www.rexbionics.com/rex-for-home-use/. [Accessed: 02-Feb-2018].

[137] S. Kizir and Z. Bingul, “Position Control and Trajectory Tracking of the Stewart Platform,” in *Serial and Parallel Robot Manipulators - Kinematics, Dynamics, Control and Optimization*, S. Kucuk, Ed. InTech, Chapters published under CC BY 3.0 license, 2012, pp. 179–202.

[138] C. M. Gosselin and E. Lavoie, “On the Kinematic Design of Spherical Three-Degree-of- Freedom Parallel Manipulators,” *Int. J. Rob. Res.*, vol. 12, no. 4, pp. 394–402, Aug. 1993.

[139] D. Zanotto, Y. Akiyama, P. Stegall, and S. K. Agrawal, “Knee Joint Misalignment in Exoskeletons for the Lower Extremities: Effects on User’s Gait,” *IEEE Trans. Robot.*, vol. 31, no. 4, pp. 978–987, Aug. 2015.

[140] M. Pan and D. Zhang, “Analysis of a Novel Design of a Three-Degree of Freedom Hip Exoskeleton Based on Biomimetic Parallel Structure,” in *2011 First International Conference on Robot, Vision and Signal Processing*, 2011, pp. 6–9.

[141] E. Singla, B. Dasgupta, K. Kondak, C. Fleischer, and G. Hommel, “Optimal design of an exoskeleton hip using three-degrees-of-freedom spherical mechanism,” Kanpur, India, 2014.

[142] L. Tsai, “Robot Analysis: The Mechanics of Serial and Parallel Manipulators,” *New York, NY: J. Wiley and Sons, ISBN 0-471-32593-7*, 1999. [Online]. Available: http://ca.wiley.com/WileyCDA/WileyTitle/productCd-0471325937.html. [Accessed: 17-Nov-2015].

[143] Jean-Pierre Merlet, *Parallel Robots*, Second Edi. Sophia-Antipolis, France: Springer, 2006.

[144] S. Sadeqi, S. Bourgeois, E. J. Park, and S. Arzanpour, “Performance Analysis of 6-UPS Parallel Manipulators for Hip Exoskeleton Applications,” in *Proceedings of the CSME International Congress*, 2016, pp. 1–6.

[145] C. M. Gosselin and J. F. Hamel, “The agile eye: a high-performance three-degree-of-freedom camera-orienting device,” in *Proceedings of the 1994 IEEE International Conference on Robotics and Automation*, pp. 781–786.

[146] C. M. Gosselin, E. St. Pierre, and M. Gagne, “On the development of the Agile Eye,” *IEEE Robot. Autom. Mag.*, vol. 3, no. 4, pp. 29–37, 1996.

[147] C. M. Gosselin and E. St-Pierre, “Development and Experimentation of a Fast 3-DOF Camera-Orienting Device,” *Int. J. Rob. Res.*, vol. 16, no. 5, pp. 619–630, Oct. 1997.

[148] S. Bai, M. R. Hansen, and J. Angeles, “A robust forward-displacement analysis of spherical parallel robots,” *Mech. Mach. Theory*, vol. 44, no. 12, pp. 2204–2216, Dec. 2009.

[149] Y. Jian and J. Angeles, “Kinematics simulation and control design of the Agile Wrist in a Dual-arm robotic mechanical systems,” in *2012 IEEE International Conference on Computer Science and Automation Engineering (CSAE)*, 2012, vol. 3, pp. 39–42.

[150] A. Niyetkaliyev and A. Shintemirov, “An approach for obtaining unique kinematic solutions of a spherical parallel manipulator,” in *2014 IEEE/ASME International Conference on Advanced Intelligent Mechatronics*, 2014, pp. 1355–1360.

[151] J. Gallardo-Alvarado, M. A. García-Murillo, and L. Pérez-González, “Kinematics of the 3RRRS+S Parallel Wrist: A Parallel Manipulator Free of Intersecting Revolute Axes #,” *Mech. Based Des. Struct. Mach.*, vol. 41, no. 4, pp. 452–467, Oct. 2013.

[152] C. Wang, Y. Fang, S. Guo, and Y. Chen, “Design and Kinematical Performance Analysis of a 3- R US/ R RR Redundantly Actuated Parallel Mechanism for Ankle Rehabilitation,” *J. Mech. Robot.*, vol. 5, no. 4, p. 41003, Jul. 2013.

[153] G. Cui, H. Zhou, H. Zhang, D. Zhang, and Y. Zhang, “Robust Design Optimization of a 4-UPS-S Parallel Manipulator for Orientation-Regulating Control System of Solar Gather Panels,” *J. Ind. Eng.*, vol. 2015, p. 10, 2015.

[154] J. Enferadi and A. Shahi, “On the position analysis of a new spherical parallel robot with orientation applications,” *Robot. Comput. Integr. Manuf.*, vol. 37, pp. 151–161, Feb. 2016.

[155] A. Mueller, “Redundant Actuation of Parallel Manipulators,” in *Parallel Manipulators, towards New Applications*, I-Tech Education and Publishing, 2008.

[156] S. Sadeqi, “Design of a hybrid spherical manipulator for lower limb exoskeleton applications,” Simon Fraser University, 2017.

[157] M. W. Spong, S. Hutchinson, and M. Vidyasagar, *Robot Dynamics and Control*, 2nd ed. John Wiley & Sons, 2004.

[158] I. Mansouri and M. Ouali, “The power manipulability – A new homogeneous performance index of robot manipulators,” *Robot. Comput. Integr. Manuf.*, vol. 27, no. 2, pp. 434–449, Apr. 2011.

[159] T. Yoshikawa, “Manipulability of Robotic Mechanisms,” *Int. J. Rob. Res.*, vol. 4, no. 2, pp. 3–9, Jun. 1985.

[160] P. Cardou, S. Bouchard, and C. Gosselin, “Kinematic-sensitivity indices for dimensionally nonhomogeneous jacobian matrices,” *IEEE Trans. Robot.*, vol. 26, no. 1, pp. 166–173, Feb. 2010.

[161] J. Angeles and C. S. Lopez-Cajun, “Kinematic Isotropy and the Conditioning Index of Serial Robotic Manipulators,” *Int. J. Rob. Res.*, vol. 11, no. 6, pp. 560–571, Dec. 1992.

[162] M. H. Abedinnasab, Y.-J. Yoon, and H. Zohoor, “Exploiting Higher Kinematic Performance - Using a 4-Legged Redundant PM Rather than Gough-Stewart Platforms,” in *Serial and Parallel Robot Manipulators - Kinematics, Dynamics, Control and Optimization*, S. Kucuk, Ed. InTech, 2012, pp. 43–66.

[163] R. S. Stoughton and T. Arai, “Modified Stewart platform manipulator with improved dexterity,” *IEEE Trans. Robot. Autom.*, vol. 9, no. 2, pp. 166–172, Apr. 1993.

[164] K. H. Pittens and R. P. Podhorodeski, “A family of stewart platforms with optimal dexterity,” *J. Robot. Syst.*, vol. 10, no. 4, pp. 463–479, Jun. 1993.

[165] A. B. K. Rao, P. V. M. Rao, and S. K. Saha, “Workspace and dexterity analyses of hexaslide machine tools,” in *Robotics and Automation, 2003. Proceedings. ICRA ’03. IEEE International Conference on*, 2003, vol. 3, pp. 4104–4109 vol.3.

[166] C. M. Gosselin, “The optimum design of robotic manipulators using dexterity indices,” *Rob. Auton. Syst.*, vol. 9, no. 4, pp. 213–226, Jan. 1992.

[167] C. Gosselin, “Kinematic Analysis Optimization and Programming of Parallel Robotic Manipulators.pdf,” McGill University, Montreal, 1985.

[168] S. Sadeqi, S. P. Bourgeois, E. J. Park, and S. Arzanpour, “Design and performance analysis of a 3-RRR spherical parallel manipulator for hip exoskeleton applications,” *J. Rehabil. Assist. Technol. Eng.*, vol. 4, pp. 1–11, Jan. 2017.

[169] C. M. Gosselin and M. Gagné, “A Closed-Form Solution for the Direct Kinematics of a Special Class of Spherical Three-Degree-of-Freedom Parallel Manipulators,” in *Computational Kinematics ’95*, 1995, pp. 231–240.

[170] C. M. Gosselin and F. Caron, “Two degree-of-freedom spherical orienting device,” US5966991, 1998.

[171] D. Chablat and P. Wenger, “A Six Degree-Of-Freedom Haptic Device Based On The Orthoglide And A Hybrid Agile Eye,” Jul. 2007.

[172] “The Agile Eye.” [Online]. Available: http://robot.gmc.ulaval.ca/en/research/research-thrusts/parallel-mechanisms/the-agile-eye/. [Accessed: 10-Nov-2016].

[173] E. Samson, D. Laurendeau, M. Parizeau, S. Comtois, J.-F. Allan, and C. Gosselin, “The Agile Stereo Pair for active vision,” *Mach. Vis. Appl.*, vol. 17, no. 1, pp. 32–50, Apr. 2006.

[174] C. H. Chiang, *Kinematics of spherical mechanisms*. New York: Cambridge University Press, 1988.

[175] C. Gosselin and J. Angeles, “The Optimum Kinematic Design of a Spherical Three-Degree-of-Freedom Parallel Manipulator,” *J. Mech. Transm. Autom. Des.*, vol. 111, no. 2, pp. 202–207, Jun. 1989.

[176] S. Arzanpour, S. Sadeqi, S. Bourgeois, and J. W. Park, “System and Device for Guiding and Detecting Motions of 3-DOF Rotational Target Joint,” WO/2017/120680, 21-Jul-2017.

[177] P. V. Loubert, J. T. Zipple, M. J. Klobucher, E. D. Marquardt, and M. J. Opolka, “In Vivo Ultrasound Measurement of Posterior Femoral Glide During Hip Joint Mobilization in Healthy College Students,” *J. Orthop. Sport. Phys. Ther.*, vol. 43, no. 8, pp. 534–541, Aug. 2013.

[178] F. Ruiz-Diaz, A. Altamirano-Altamirano, and G. Valentino-Orozco, “External knee prosthesis with four bar linkage mechanism,” in *2016 13th International Conference on Electrical Engineering, Computing Science and Automatic Control (CCE)*, 2016, pp. 1–6.

[179] B. Baldisserri and V. Parenti-Castelli, “A New 3D Mechanism for Modeling the Passive Motion of the Tibia–Fibula–Ankle Complex,” *J. Mech. Robot.*, vol. 4, no. 2, p. 21004, May 2012.

[180] E. Sung, A. H. Slocum, R. Ma, J. F. Bean, and M. L. Culpepper, “Design of an Ankle Rehabilitation Device Using Compliant Mechanisms,” *J. Med. Device.*, vol. 5, no. 1, p. 11001, Mar. 2011.

[181] M. Dettwyler, A. Stacoff, I. A. Kramers-de Quervain, and E. Stüssi, “Modelling of the ankle joint complex. Reflections with regards to ankle prostheses,” *Foot Ankle Surg.*, vol. 10, no. 3, pp. 109–119, Jan. 2004.

[182] S. L. Delp, J. P. Loan, M. G. Hoy, F. E. Zajac, E. L. Topp, and J. M. Rosen, “An interactive graphics-based model of the lower extremity to study orthopaedic surgical procedures,” *IEEE Trans. Biomed. Eng.*, vol. 37, no. 8, pp. 757–767, 1990.

[183] J. A. Saglia, N. G. Tsagarakis, J. S. Dai, and D. G. Caldwell, “A High-performance Redundantly Actuated Parallel Mechanism for Ankle Rehabilitation,” *Int. J. Rob. Res.*, vol. 28, no. 9, pp. 1216–1227, Sep. 2009.

[184] S. H. Scott and D. A. Winter, “Talocrural and talocalcaneal joint kinematics and kinetics during the stance phase of walking.,” *J. Biomech.*, vol. 24, no. 8, pp. 743–52, 1991.

[185] J. J. Craig, “Manipulator kinematics,” in *Introduction to Robotics: Mechanics and Control*, 3rd ed., Upper Saddle River, NJ: Pearson, 2005, pp. 62–100.

[186] M. Raghavan and B. Roth, “Kinematic analysis of the 6r manipulator of general geometry,” in *International Symposium on Robotics Research*, 1989, pp. 314–320.

[187] D. L. Pieper, “The Kinematics of Manipulators Under Computer Control,” Stanford University, 1968.

[188] D. L. Pieper and B. Roth, “The Kinematics of Manipulators Under Computer Control,” in *Proceedings of the Second International Congress on Theory of Machines and Mechanisms*, 1969, pp. 159–169.

[189] G. A. Turley, M. A. Williams, R. M. Wellings, and D. R. Griffin, “Evaluation of range of motion restriction within the hip joint.,” *Med. Biol. Eng. Comput.*, vol. 51, no. 4, pp. 467–77, Apr. 2013.

[190] AliExpress, “Hip knee Ankle Foot Adjustable Orthotics Fracture Holder Brace.” [Online]. Available: https://www.aliexpress.com/item/Hip-knee-Ankle-Foot-Adjustable-Orthotics-fracture-Holder-brace-free-shipping/32708810173.html?spm=2114.40010308.4.197.LRf8Sx. [Accessed: 12-Jul-2017].

[191] Mechatronic Systems Engineering - Simon Fraser University, “Rates & Equipment List.” [Online]. Available: https://www.sfu.ca/mechatronics/services-and-training/rates-and-equipment-list.html. [Accessed: 12-Jul-2017].

[192] McMaster-Carr, “Current Order.” [Online]. Available: https://www.mcmaster.com/#orders/=18gw9o9. [Accessed: 12-Jul-2017].

[193] RP Electronics, “62-244-1 | Potentiometer - 10K Linear.” [Online]. Available: http://www.rpelectronics.com/62-244-1-1-2-watt-10k-linear.html. [Accessed: 12-Jul-2017].

[194] Arduino, “Arduino Mega 2560 Rev3.” [Online]. Available: https://store.arduino.cc/usa/arduino-mega-2560-rev3. [Accessed: 12-Jul-2017].

[195] RP Electronics, “MSDS-01 | Micro SD Shield.” [Online]. Available: http://www.rpelectronics.com/msds-01.html. [Accessed: 12-Jul-2017].

[196] RP Electronics, “457-116-1 | Rocker Switch - DPST 8A, ON-OFF, Black.” [Online]. Available: https://www.rpelectronics.com/457-116-1-dpst-8a-on-off-black.html. [Accessed: 12-Jul-2017].

[197] RP Electronics, “AF-916 | Push Button Switch - SPDT 6A, ON-ON, Red LED Ring, Metal.” [Online]. Available: http://www.rpelectronics.com/af-916-push-button-switch-spdt-6a-on-on-red-led-ring-metal.html. [Accessed: 12-Jul-2017].

[198] Canadian Tire, “Duracell Copper Top Alkaline 9V Battery.” [Online]. Available: http://www.canadiantire.ca/en/pdp/duracell-copper-top-alkaline-9v-battery-0653017p.html#srp. [Accessed: 12-Jul-2017].

[199] RP Electronics, “150-901-2 | 9V Battery Clip "I"- 24 AWG Wire Leads, Pkg/2.” [Online]. Available: http://www.rpelectronics.com/150-901-2-9v-battery-clip-i-24-awg-wire-leads-pkg-2.html. [Accessed: 12-Jul-2017].

[200] DigiKey, “Through Hole Resistors | CFR-50JB-52-1K Yageo.” [Online]. Available: https://www.digikey.ca/product-detail/en/yageo/CFR-50JB-52-1K/1.0KH-ND/95. [Accessed: 12-Jul-2017].

[201] Dell Canada, “8GB microSDHC Class 4 Flash Memory Card (SDC4/8GB).” [Online]. Available: http://www.dell.com/en-ca/shop/accessories/apd/a2278354?c=ca&l=en&s=dhs&cs=cadhs1&sku=A2278354&cid=3852&st=&pdv=c&lid=5635587&VEN1=sHHr5mmXm,82727171957,901mtv7630,c,&VEN2=,&dgc=ST&DGSeg=DHS&acd=1230881379501410&VEN3=113003959132242666. [Accessed: 12-Jul-2017].

[202] RP Electronics, “10-HS22-BL-25 | 22AWG Solid Wire - Blue, 25ft.” [Online]. Available: https://www.rpelectronics.com/10-hs22-bl-25.html. [Accessed: 12-Jul-2017].

[203] RP Electronics, “PET-1/2-BK-7 | Clean Cut Braided Wrap Sleeving 1/2" x 7ft, Black.” [Online]. Available: http://www.rpelectronics.com/pet-1-2-bk-7-clean-cut-braided-sleeving.html. [Accessed: 12-Jul-2017].

[204] “ATmega2560-Arduino Pin Mapping.” [Online]. Available: https://www.arduino.cc/en/Hacking/PinMapping2560. [Accessed: 18-Jul-2017].

[205] OSEPP, “micro SD Shield,” 2017. [Online]. Available: https://www.osepp.com/electronic-modules/shields/47-micro-sd-shield. [Accessed: 18-Jul-2017].

[206] B. Greiman, “AnalogBinLogger.ino,” 2017. [Online]. Available: https://github.com/greiman/SdFat/blob/master/examples/AnalogBinLogger/AnalogBinLogger.ino. [Accessed: 18-Jul-2017].

[207] fat16lib, “Try this super fast analog pin logger,” 2014. [Online]. Available: https://forum.arduino.cc/index.php?topic=228549.0. [Accessed: 18-Jul-2017].

[208] J. Wosk and A. Voloshin, “Wave attenuation in skeletons of young healthy persons,” *J. Biomech.*, vol. 14, no. 4, pp. 261–263, 265–267, 1981.

[209] G. A. Wood, “Data smoothing and differentiation procedures in biomechanics,” *Exerc. Sport Sci. Rev.*, vol. 10, pp. 308–362, 1982.

[210] Xsens, “Xsens launches MVN Awinda and MVN BIOMECH Awinda featuring fully wireless motion trackers,” 2013. [Online]. Available: https://www.xsens.com/news/xsens-launches-mvn-awinda-mvn-biomech-awinda-featuring-fully-wireless-motion-trackers/. [Accessed: 26-Jul-2017].

[211] A. Cappozzo, U. Della Croce, A. Leardini, and L. Chiari, “Human movement analysis using stereophotogrammetry: Part 1. Theoretical background,” *Gait Posture*, vol. 21, no. 2, pp. 186–196, Feb. 2005.

[212] S. Zihajehzadeh and E. J. Park, “A Novel Biomechanical Model-Aided IMU/UWB Fusion for Magnetometer-Free Lower Body Motion Capture,” *IEEE Trans. Syst. Man, Cybern. Syst.*, vol. 47, no. 6, pp. 927–938, Jun. 2017.

[213] J.-T. Zhang, A. C. Novak, B. Brouwer, and Q. Li, “Concurrent validation of Xsens MVN measurement of lower limb joint angular kinematics,” *Physiol. Meas.*, vol. 34, no. 8, pp. N63–N69, Aug. 2013.

[214] T. Igoe, “Using the SD library to log data,” 2015. [Online]. Available: https://www.arduino.cc/en/Tutorial/Datalogger. [Accessed: 18-Jul-2017].

[215] Qualisys, “QTM Qualisys Track Manager User Manual,” Gothenburg, Sweden, 2011.

[216] G. Zhao and A. Seyfarth, “Contributions of Stance and Swing Leg Movements to Human Walking Dynamics,” in *International Conference on Climbing and Walking Robots and Support Technologies for Mobile Machines*, 2015, pp. 224–231.

[217] J. Sinclair, P. J. Taylor, and S. J. Hobbs, “Digital filtering of three-dimensional lower extremity kinematics: an assessment.,” *J. Hum. Kinet.*, vol. 39, pp. 25–36, Dec. 2013.

[218] Xsens, “MTi and MTx User Manual and Technical Documentation: Document MT0100P, Revision O,” 2010.

.

Appendix A.

Performance Analysis of 6-UPS Parallel Manipulators for Hip Exoskeleton Applications

The work attached to the following six pages is reproduced with permission from CSME. The original source of the work is provided in reference [144].

Proceedings of The Canadian Society for Mechanical Engineering International Congress 2016
CSME International Congress 2016
June 26-29, 2016, Kelowna, BC, Canada

PERFORMANCE ANALYSIS OF 6-UPS PARALLEL MANIPULATORS FOR HIP EXOSKELETON APPLICATIONS

Soheil Sadeqi, Shaun Bourgeois, Edward J. Park, Siamak Arzanpour
School of Mechatronic Systems Engineering
Simon Fraser University
Surrey, Canada
ssadeqi@sfu.ca, shaunb@sfu.ca, ed_park@sfu.ca, arzanpour@sfu.ca

Abstract—*This paper presents a kinematical performance analysis of the 6-UPS parallel manipulator in the context of hip exoskeleton applications. The inverse kinematics derivation and Jacobian development procedures are first reviewed to facilitate the subsequent evaluation of manipulability, dexterity, and rotational sensitivity performance indices. These studies consider two methods for interfacing the 6-UPS device to a human user, as well as three different robotic limb arrangement possibilities. A global conditioning index is then evaluated, leading to the formulation of a design-optimization equation for maximizing manipulability. Finally, a preferable combination of bodily interfacing scheme, robotic limb arrangement, and dimensional parameter settings that correspond to a superior-performing hip exoskeleton are proposed.*

Keywords- hip exoskeleton; Stewart-Gough platform; parallel manipulator; Jacobian; kinematic performance indices

I. INTRODUCTION

An exoskeleton is a wearable robotic device intended to augment the abilities of the human body segment to which is attached. Common motivations for exoskeleton use are energy conservation for limbs that are otherwise functional or strength augmentation for limbs that have weakened or complete loss of functionality. One significant challenge associated with either of these goals arises when the targeted limb contains a joint with multiple active degrees-of-freedom (DOFs) that must be supported by an external robotic structure.

One candidate robot that may be used to overcome this challenge is the 6-UPS parallel manipulator, which is also commonly referred to as the Stewart-Gough platform. This manipulator has been extensively analyzed and proposed for use in a number of different technology applications. First, Stewart introduced the mechanism and suggested application as a flight simulator for pilot training in [1]. Later, Merlet and Tsai among others revisit the device and discuss its kinematical and Jacobian matrix analyses [2, 3]. Additionally, Gosselin presents a method of inverse kinematics development and workspace analysis for the Stewart-Gough platform in [4]. Abedinnasab and Vossoughi also present a performance analysis of the mechanism when the device is limited to planar translational motions in [5]. More recently, Takaiwa *et al.* discuss the use of a pneumatically-actuated Stewart-Gough platform for use in wrist rehabilitation [6], while Onodera *et al.* propose an assistive device incorporating a Stewart-Gough platform for ankle-foot rehabilitation [7].

This paper explores the use of the 6-UPS manipulator within a hip exoskeleton system. Specifically, this paper revisits the inverse kinematics and Jacobian development processes for the Stewart-Gough platform and then analyzes its performance for two different body attachment schemes and three different intra-device limb arrangements.

II. KINEMATIC ANALYSIS & GEOMETRY CONSIDERATIONS

A. Structure Description

Fig. 1 shows a geometrical schematic of a 6-UPS parallel manipulator. As shown in the schematic, six identical limbs connect a moving platform to a fixed base via spherical joint connections to the fixed base at points A_i and universal joint connections to the moving platform at points B_i, for $i = 1,2, \ldots, 6$. Each limb consists of an upper member and a lower member connected by an active prismatic joint. Actuated ball screws, hydraulic jacks, or other linear actuators can be used to vary the lengths of the prismatic joints and thereby control the position and orientation of the moving platform.

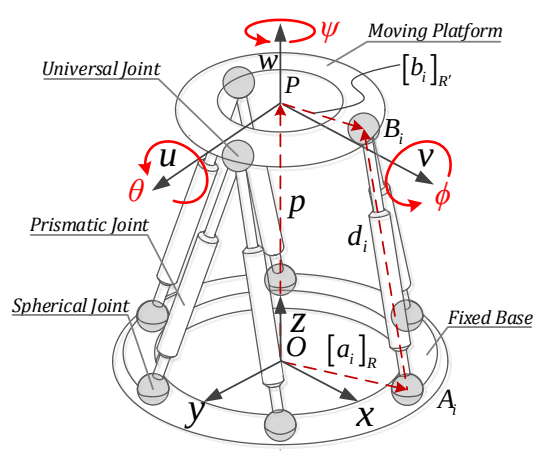

Figure 1. Schematic model of a 6-UPS parallel manipulator

This work was supported by the Natural Sciences and Engineering Research Council of Canada.

Stewart-Gough platforms can have various different manifestations depending on how the joints on the moving platform and fixed base are configured. This paper considers three common design schemes of the Stewart-Gough platform (see Fig. 2) as possible candidates for utilization in a lower extremity exoskeleton hip joint.

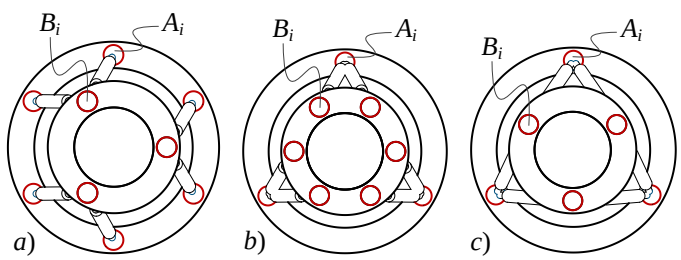

Figure 2. Top view of a) 6-3, b) 3-6, and c) 3-3 Stewart-Gough platforms

B. *Inverse Kinematics*

The inverse kinematics analysis for the 6-UPS manipulator has been extensively studied previously by a number of academics [2–4]. However, the procedure is briefly outlined here again for the sake of completeness and to familiarize the reader with the notations and naming conventions used in subsequent sections of this paper. First, consider two Cartesian coordinate systems: frame R attached to the base with axes x, y, and z, and frame R' attached to the moving platform with axes u, v, and w, as shown in Fig. 1. Note that the origin of frame R', denoted P, is located on the central axis of the moving platform and lies in the plane defined by the universal joint attachment points.

Vectors $\boldsymbol{a_i}$ and $\boldsymbol{b_i}$ respectively designate the positions of each spherical and universal joint, where the subscript i differentiates the six limbs (i.e. i = 1, 2, …, 6). Because the spherical joints and frame R are both attached to the fixed base structure, vectors $\boldsymbol{a_i}$ are constant when expressed in frame R. Similarly, vectors $\boldsymbol{b_i}$ are constant with respect to frame R'.

Furthermore, Q is the transformation matrix describing the orientation of R' with respect to fixed frame R. This transformation is uniquely defined by roll, pitch, and yaw rotation angles. Specifically, Q is produced by a rotation of θ about the fixed x-axis, followed by a rotation of ϕ about the fixed y-axis, and then a final rotation of ψ about the fixed z-axis. Mathematically, it follows that the orientation of the moving platform frame with respect to the base platform frame is obtained as shown in Eq. (1):

$$\boldsymbol{Q} = \boldsymbol{Q}_z\boldsymbol{Q}_y\boldsymbol{Q}_x = \begin{bmatrix} C\psi C\phi & C\psi S\phi S\theta - S\psi C\theta & C\psi S\phi C\theta + S\psi S\theta \\ S\psi C\phi & S\psi S\phi S\theta + C\psi C\theta & S\psi S\phi C\theta - C\psi S\theta \\ -S\psi & C\phi S\theta & C\phi C\theta \end{bmatrix} \quad (1)$$

If the position of point P with respect to the origin of the fixed coordinate frame R is denoted by vector $[\boldsymbol{r}]_R = [x_r, y_r, z_r]^T$, each vector $\mathbf{b}_i$ can be expressed in frame R as follows:

$$[\boldsymbol{b}_i]_R = [\boldsymbol{r}]_R + \boldsymbol{Q}[\boldsymbol{b}_i]_{R'} \qquad i = 1,\ldots,6 \quad (2)$$

where the subscript outside of the brackets indicates the coordinate frame in which the associated vector is expressed. Now, subtracting $\boldsymbol{a_i}$ from both sides of Eq. (2) provides a vector directed along the ith limb, connecting point A_i to B_i:

$$[\boldsymbol{b}_i - \boldsymbol{a}_i]_R = [\boldsymbol{r}]_R + \boldsymbol{Q}[\boldsymbol{b}_i]_{R'} - [\boldsymbol{a}_i]_R \qquad i = 1,\ldots,6 \quad (3)$$

Thus, the Euclidean norm of each side of Eq. (3) produces

$$d_i = \|\boldsymbol{b}_i - \boldsymbol{a}_i\| = \|[\boldsymbol{r}]_R + \boldsymbol{Q}[\boldsymbol{b}_i]_{R'} - [\boldsymbol{a}_i]_R\| \qquad i = 1,\ldots,6 \quad (4)$$

where d_i is a scalar measure of the ith limb's length. Note that an alternative form of Eq. (4) is as follows:

$$d_i = \sqrt{(x_r - u_i)^2 + (y_r - v_i)^2 + (z_r - w_i)^2} \qquad i = 1,\ldots,6 \quad (5)$$

for which the scalar quantities u_i, v_i, and w_i are given as:

$$\begin{aligned} u_i &= x_{ai} - q_{11}x_{bi} - q_{12}y_{bi} - q_{13}z_{bi} \\ v_i &= y_{ai} - q_{21}x_{bi} - q_{22}y_{bi} - q_{23}z_{bi} \qquad i = 1,\ldots,6 \\ w_i &= z_{ai} - q_{31}x_{bi} - q_{32}y_{bi} - q_{33}z_{bi} \end{aligned} \quad (6)$$

In Eq. (6), q_{ij} is the ith row – j^{th} column element of the transformation matrix Q.

Eqs. (4–6) represent the solution to the inverse kinematics problem for the 6-UPS manipulator because they provide the required active joint states, d_i, necessary to achieve a desired position and orientation of the moving platform end-effector. That is, once each element of Q and $\boldsymbol{r}$ are established as inputs, associated lengths for the prismatic actuators can be identified.

C. *Body Interfacing and Geometric Considerations*

Depending on how the 6-UPS is interfaced with the human body for application as a hip joint exoskeleton, a number of geometric considerations are introduced that may influence the manipulator's preferred method of operation. Fig. 3 illustrates two proposed schemes for interfacing the 6-UPS to the body.

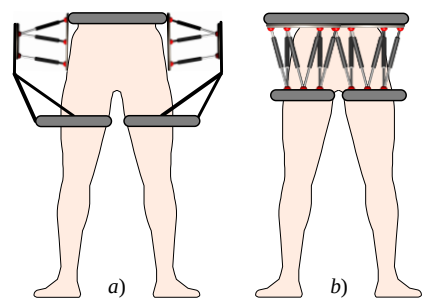

Figure 3. The two body interfacing schemes considered for the 6-UPS

For scheme *a*), it is assumed that the position of point P remains constant with respect to frame R. That is, the 6-UPS acts as a 3-DOF rotational joint with center-of-rotation located at point P. Mathematically, $\boldsymbol{r}$ then becomes a vector of constant values as follows:

$$[\boldsymbol{r}]_R = \begin{bmatrix} x_r \\ y_r \\ z_r \end{bmatrix} = \begin{bmatrix} 0 \\ 0 \\ P_z \end{bmatrix} \quad (7)$$

where P_z is the z-axis coordinate of point P's position. Fig. 4 *a*) shows examples of moving platform orientations and positions attainable given this motion restriction. Note that for this example scenario, additional mechanisms would be required to prevent forces acting to dislocate the hip joint when transferring the 6-UPS manipulator's motions to the upper leg. These mechanisms are not discussed here.

Meanwhile, for interfacing scheme *b*) in Fig. 3, it is assumed that the hip joint's center-of-rotation coincides with the origin *O* of frame *R*. A further assumption that no additional mechanisms are used to guide hip motions (i.e. the moving platform is fixed directly to the upper leg) requires that point *P* only move along a spherical surface centered at *O* and that the *w*-axis always pass through point *O*. Fig. 4 *b*) provides an illustration of this geometrical constraint on the 6-UPS' motions. Furthermore, the position of *P* in terms of frame *R* is expressed as follows for this interfacing case:

$$[\boldsymbol{r}]_R = \begin{bmatrix} x_r \\ y_r \\ z_r \end{bmatrix} = \begin{bmatrix} q_{11}P_x + q_{12}P_y + q_{13}P_z \\ q_{21}P_x + q_{22}P_y + q_{23}P_z \\ q_{31}P_x + q_{32}P_y + q_{33}P_z \end{bmatrix} \tag{8}$$

where q_{ij} is the ith row – j^{th} column term in the *Q* matrix of Eq. (1). Additionally, P_k is the *k*-coordinate of *P* expressed in the *R* frame when the manipulator is fitted on the upper leg and it is in its starting position. Note that Fig. 4 *b*) shows the case for which $P_x = 0$ and $P_y = 0$ in Eq. (8).

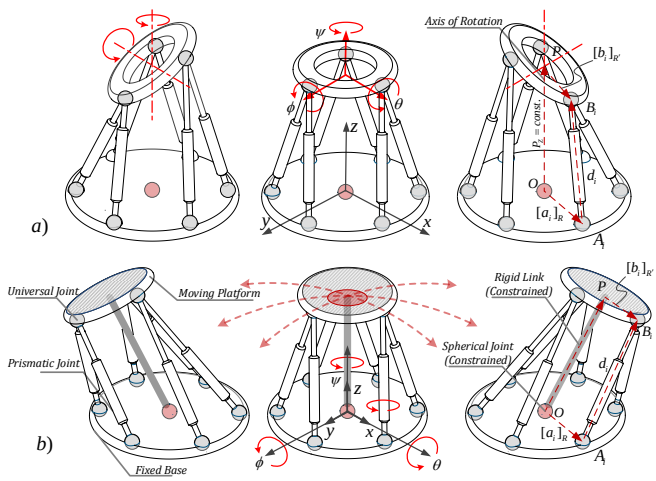

Figure 4. Example 6-UPS motions for two considered methods of operation

III. Jacobian Analysis of the 6-UPS manipulator

A number of indices are commonly used to compare the performance of different parallel manipulator mechanisms [2]. These indices are generally acquired from a manipulator's Jacobian matrix and often have physical significance that lends itself for use as an objective function for design optimization [8]. Therefore, the 6-UPS manipulator's Jacobian is discussed before performance indices are introduced and analyzed in Sections IV and V. Note that Merlet and Tsai also present Jacobian studies for the 6-UPS manipulator in [2, 3], among others.

To start, a vector **q** is assigned to describe the active articular variables, and vector **x** is set to denote the moving platform position. It follows that Eq. (9) represents the kinematic constraints asserted by the manipulator's limbs in general form:

$$f(\mathbf{x},\mathbf{q}) = \mathbf{0} \tag{9}$$

where *f* is an *n*-dimensional implicit function of **q** and **x**, and *n* is the device's active joint count (i.e. *n* = 6 for the 6-UPS). Time-differentiation of Eq. (9) yields the following relationship between the input joint rates and the end-effector output velocity:

$$\frac{\partial \mathbf{f}}{\partial \mathbf{x}}\dot{\mathbf{X}} + \frac{\partial \mathbf{f}}{\partial \mathbf{q}}\dot{\mathbf{q}} = 0 \rightarrow \mathrm{J}_x\dot{\mathbf{X}} = \mathrm{J}_q\dot{\mathbf{q}} \tag{10}$$

The J_x and J_q components in the above equation are then combined into the complete Jacobian matrix:

$$\dot{\mathbf{q}} = \mathrm{J}_q^{-1}\mathrm{J}_x\dot{\mathbf{X}} = \mathrm{J}\dot{\mathbf{X}} \tag{11}$$

Note that the Jacobian of a parallel manipulator is inverted compared to that of a serial manipulator [3].

Next, the velocity vector-loop closure method is used to analyze the Jacobian matrix. Each loop includes points on the fixed base, moving platform, and all links of a limb, as follows:

$$\overline{OP} + \overline{PB_i} = \overline{OA_i} + \overline{A_iB_i} \tag{12}$$

The velocities associated with passive joints are eliminated by taking a dot product of the velocity vector-loop equation above with an appropriate vector normal to all vectors representing passive joint rates. Lastly, the resulting equations are combined to create a Jacobian matrix.

The input vector for the 6-UPS is given by $\dot{q} = [\dot{d}_1, \dot{d}_1, ..., \dot{d}_6]$, whereas the output vector is described by the velocity of centroid *P* and angular velocity of the moving platform. These terms are obtained by differentiating Eq. (12) with respect to time:

$$\mathrm{v}_p + \omega_B \times b_i = d_i\omega_i \times s_i + \dot{d}_i s_i, \tag{13}$$

where b_i and s_i denote the vector $\overline{PB_i}$ and a unit vector along $\overline{A_iB_i}$ respectively. Furthermore, ω_i denotes the angular velocity of the ith limb with respect to the fixed frame *R*. Both sides of Eq. (13) are dot-multiplied by s_i in order to eliminate ω_i as follows:

$$s_i.\mathbf{v}_p + (b_i \times s_i).\boldsymbol{\omega}_B = \dot{d}_i \tag{14}$$

When written six times (i.e. once for each limb), Eq. (14) yields six scalar equations, which can be assembled into matrix form as shown below:

$$\begin{bmatrix} s_1^T & (b_1 \times s_1)^T \\ s_2^T & (b_2 \times s_2)^T \\ \vdots & \vdots \\ s_6^T & (b_6 \times s_6)^T \end{bmatrix} \dot{\mathbf{X}} = I_{6\times 6}\dot{\mathbf{q}} \tag{15}$$

IV. Performance Indices

As mentioned above, the Jacobian matrix's development enables evaluation of the 6-UPS manipulator's performance indices. However, before the performance indices are computed for a specific set of 6-UPS designs and operating methods, the following subsections provide a brief overview of the indices to be considered in this study.

A. *Manipulability*

Articular forces in parallel robots can reach large magnitudes near singular configurations [2]. Therefore, the ability to measure proximity to a singular configuration is useful for analyzing parallel manipulator design. Manipulability is a performance index used to achieve this

quantification. As given in Eq. (16), this index is calculated as the absolute value of the Jacobian determinant [10]:

$$\mu = \sqrt{\left|\mathrm{J}^T \mathrm{J}\right|} \tag{16}$$

Physically, manipulability is an indicator of a manipulator's ability to transmit a desired velocity to its end-effector [11]. The isotropy index for manipulability is an indication of how uniformly velocity can be transferred to the end-effector across all directions of motion [12]. The isotropy index for manipulability is defined as:

$$\mu_{iso} = \sigma_{min} / \sigma_{max} \tag{17}$$

where σ_{max} and σ_{min} are respectively the maximum and minimum singular values of the Jacobian matrix, and μ_{iso} therefore ranges in value from 0 to 1. An isotropy index of one indicates that the manipulator is oriented such that it is able to transmit velocity uniformly from its actuators to its end-effector along all directions. Contrarily, when the isotropy index is equal to zero, the manipulator is oriented in a singular configuration and is therefore unable to transmit velocity to the end-effector.

B. Dexterity (Condition Number)

Because a parallel manipulator is generally controlled using the position coordinates of its joints, any errors in these coordinates will cause error in the moving platform position and/or orientation [2]. This end-effector error is obtained as the product of the errors in the articular coordinates and an amplification factor, called the condition number, k [13]. Consequentially, the accuracy of a parallel manipulator is dependent on its condition number, which is defined in terms of the Jacobian matrix as follows [13–15]:

$$k\left(\mathrm{J}\right) = \|\mathrm{J}\| \|\mathrm{J}^{-1}\| \tag{18}$$

where J is the Jacobian matrix and $\|\mathrm{J}\|$ denotes its Euclidean norm:

$$\|\mathrm{J}\| = \sqrt{tr\left(\frac{1}{n}\mathrm{J}\mathrm{J}^T\right)} \tag{19}$$

It follows that Gosselin [16] has defined the local dexterity, v, as the inverse of the condition number and characterized it as a criterion for measuring the kinematical accuracy of a manipulator. Local dexterity is the second performance index considered in this paper:

$$v = \frac{1}{\|\mathrm{J}\| \|\mathrm{J}^{-1}\|} \tag{20}$$

Again, values for v are limited to the range [0, 1]. A value of zero indicates that the Jacobian matrix is singular, whereas higher values indicate more accurate motion generation for a given device configuration.

C. Rotational Sensitivity

Rotational sensitivity is a measure of how severe actuator displacements affect the orientation of a parallel manipulator's end-effector. Cardou *et al.* define τ_r as the index for rotational sensitivity in [17]; technically, it is the maximum-magnitude rotation of the end-effector under a unit-norm actuator displacement. Therefore, the sensitivity index is mathematically represented as:

$$\tau_r = \|\mathrm{J}\| \tag{21}$$

for which it is recommended that either a 2–norm or ∞–norm is used to normalize the Jacobian.

V. Comparison of the Performance Indices

Upon evaluating the three performance indices introduced above for the 6-U<u>P</u>S manipulator, the two body interfacing arrangements shown in Fig. 3 are considered. Furthermore, each of the three joint configurations depicted in Fig. 2 are addressed for both interfacing schemes. Further still, two major motions of the hip joint [9] are taken into account: flexion/extension and abduction/adduction, while the third DOF of the hip joint (i.e. rotation) is assumed to be relaxed and unchanging. As can be deduced from Figs. 1 and 3, the manipulator's ψ angle corresponds to flexion/extension motions for interfacing scheme *a*), while ϕ is associated with these motions in interfacing scheme *b*); for both cases, θ corresponds to abduction/adduction motions. Moreover, the workspace considered for the manipulator during these performance studies is the range of [-0.2 0.2] radians in both flexion/extension and abduction/adduction.

In addition to the study conditions described above, a number of device parameter values or ratios are assumed before specific performance results can be obtained. To start, a 6-U<u>P</u>S manipulator with a base radius of $r_b = 1$ and a moving platform radius of $r_m = 0.5r_b$ is considered. It is also assumed that the moving platform is initially oriented parallel to the base platform and positioned at a distance of $P_z = 0.75r_b$ from it for each study; this is considered the 'zeroed' state for the manipulator hereafter.

Given the above parameter specifications, Fig. 5 and Fig. 6 show the performance analysis results for both body-manipulator interfacing schemes shown in Fig. 3. These surface plots demonstrate a general trend that greatest manipulability, greatest dexterity, and least sensitivity can be achieved at the 'zeroed' state, with each of these performance index values degrading as the manipulator moves towards the edges of its considered workspace.

Comparatively, the 3-3 limb configuration for the 6-U<u>P</u>S device has an observably greater isotropy index for manipulability and local dexterity than the 3-6 and 6-3 configurations for both interfacing schemes; meanwhile, the 3-6 and 6-3 arrangements display relatively similar average values for both manipulability and dexterity indices. In terms of rotational sensitivity, Fig. 5 and Fig. 6 suggest that the 3-3 limb configuration has the smallest magnitude average, whereas 3-6 and 6-3 arrangements have similar greater magnitude averages. For interfacing scheme *a*) the 3-3 limb configuration has the least performance deviation across the device's workspace for all indices, followed by 3-6 and then 6-3. Contrarily, when the 6-U<u>P</u>S is attached to the body via interfacing scheme *b*), the 3-6 limb arrangement has the least associated deviation across its workspace for each index, while the 3-3 and 6-3 structures have similar greater deviations.

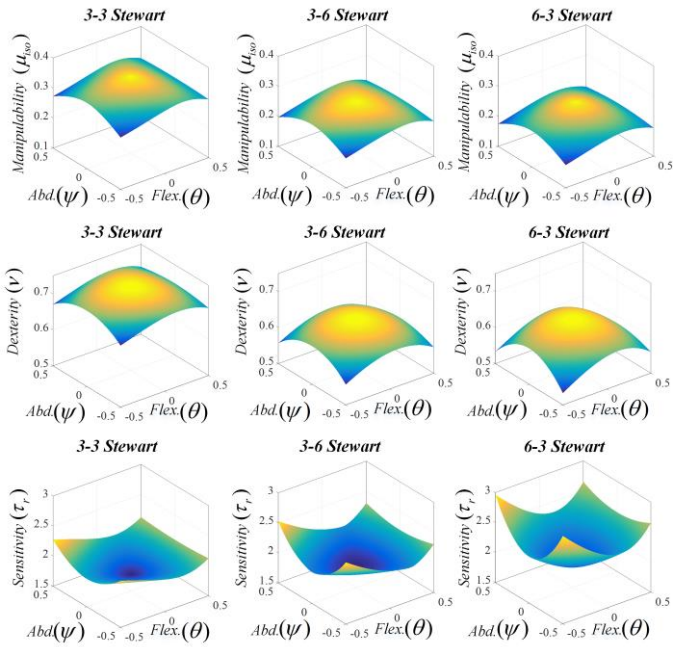

Figure 5. Performance analysis results for interfacing scheme a)

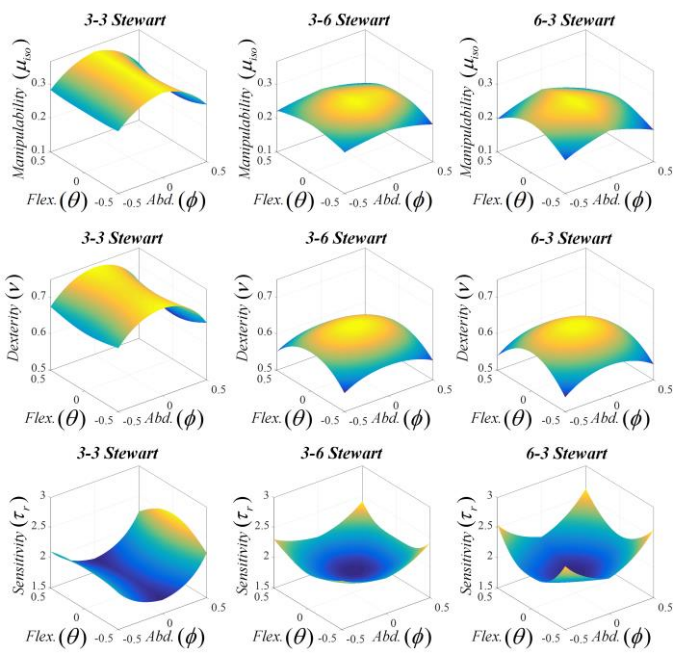

Figure 6. Performance analysis results for interfacing scheme b)

VI. Design Optimization of the 6-UPS Manipulator

The above performance index results are considered local evaluations for the 6-UPS device because they only apply when the aforementioned device parameter values and ratios are selected. To evaluate the performance of a parallel manipulator over a given workspace for a varying set of design parameters, Gosselin proposes a global performance index (*GPI*) in [18] as follows:

$$GPI = \frac{\int (PI)\, dW}{\int dW} \tag{21}$$

where *PI* represents any performance index of interest and *W* indicates the manipulator's considered workspace. Thus, the above equation provides the average value of a given performance index for all considered workspace orientations; these average values may then be evaluated for a set of device parameters as a means of comparing performance for various designs. This concept lends itself to design optimization for parallel manipulators because the average value of any performance index is an important design factor.

The design variables chosen for the optimization process are the ratio of moving platform radius to base platform radius, r_m/r_b, and the distance between the moving and base platform, h. The optimization procedure is accomplished by finding the *GPI* value for different combinations of height and platform radii ratio. For this study, manipulability was selected as the performance index under evaluation, and the corresponding graphical results are shown in Fig. 7. From this surface plot, it is apparent that there is an optimal combination of r_m/r_b and h that produces maximum manipulability for the 6-UPS device; Table I summarizes the optimal selections for these parameters.

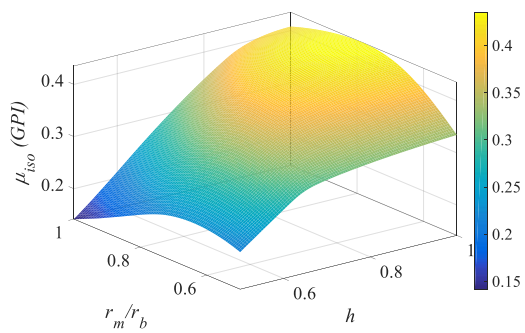

Figure 7. Global manipulability analysis of the 6-UPS manipulator

TABLE I. Optimal Parameter Selections for 6-UPS Manipulability

Interfacing Scheme	Equation for Optimal Value	
	r_m	h
a)	$r_m = 0.8r_b$	$h = r_b$
b)	$r_m = 0.8r_b$	$h = r_b$

VII. Conclusions & Future Work

This paper proposes application of the well-established 6-UPS Stewart-Gough platform as a robotic hip within an exoskeleton system. Inverse kinematics and Jacobian development for the manipulator were revisited, which in turn enabled the analysis of three commonly-studied performance indices: manipulability, dexterity, and rotational sensitivity. These indices were explored for two possible interfacing schemes with the human hip and three different robotic limb connection arrangements.

In general, the 3-3 limb structure provided the most preferable average index values for either body interfacing

scheme. However, the 3-6 arrangement generally provided the most uniform index values across the device's considered workspace. Therefore, the ideal selection of 6-UPS limb arrangement is application dependent. That is, if the application does not require an extensive workspace and is centered on the 'zeroed' state, the 3-3 configuration offers superior performance indices and would therefore likely be the preferred selection. Alternatively, if a significant workspace must be covered, the 3-6 limb arrangement may be preferable because consistency in performance across the workspace could result in ease of control.

In terms of the method for connecting the robot to the user's body, interfacing scheme *a*) is preferable in terms of performance. This is because the exoskeleton application requires a sufficiently large workspace and the performance indices associated with scheme *a*) tend to have greater uniformity across the studied workspace.

After studying the 6-UPS performance for the specific parameter values and ratios considered, a global performance evaluation was conducted for manipulability. This GPI provides an indication of optimal parameter selections to achieve the greatest possible manipulability in the device. Overall, we propose that a 3-3 Stewart-Gough platform attached to its user via interfacing scheme *a*) and having $r_m = 0.8r_b$ and $h = r_b$ would provide the best performance for a 6-UPS-based hip exoskeleton.

Future work includes singularity, dynamic, and workspace analyses, and design and analysis of a 6-UPS-based prototype system with bodily interfacing details considered.

REFERENCES

[1] D. Stewart, "A platform with Six Degrees of Freedom," *Proc. Inst. Mech. Eng. Part C-Journal Mech. Eng. Sci.*, vol. 180, no. 15, pp. 371–386, 1965.

[2] Jean-Pierre Merlet, *Parallel Robots*, Second Edi. Sophia-Antipolis, France: Springer, 2006.

[3] L. Tsai, "Robot Analysis: The Mechanics of Serial and Parallel Manipulators," *New York, NY: J. Wiley and Sons, ISBN 0-471-32593-7*, 1999. [Online]. Available: http://ca.wiley.com/WileyCDA/WileyTitle/productCd-0471325937.html. [Accessed: 17-Nov-2015].

[4] C. Gosselin, "Determination of the Workspace of 6-DOF Parallel Manipulators," *J. Mech. Des.*, vol. 112, no. 3, p. 331, Sep. 1990.

[5] M. H. Abedinnasab and G. R. Vossoughi, "Analysis of a 6-DOF redundantly actuated 4-legged parallel mechanism," *Nonlinear Dyn.*, vol. 58, no. 4, pp. 611–622, Apr. 2009.

[6] M. Takaiwa, T. Noritsugu, N. Ito, and D. Sasaki, "Wrist Rehabilitation Device Using Pneumatic Parallel Manipulator Based on EMG Signal," *Int. J. Autom. Technol.*, vol. 5, no. 4, pp. 472–477, 2011.

[7] T. Onodera, M. Ding, H. Takemura, and H. Mizoguchi, "Design and development of Stewart platform-type assist device for ankle-foot rehabilitation," in *2012 First International Conference on Innovative Engineering Systems*, 2012, pp. 1–6.

[8] S. Kucuk and Z. Bingul, "Comparative study of performance indices for fundamental robot manipulators," *Rob. Auton. Syst.*, vol. 54, no. 7, pp. 567–573, Jul. 2006.

[9] N. Palastanga and R. W. Soames, *Anatomy and Human Movement: Structure and function*. Elsevier Health Sciences UK, 2011.

[10] T. Yoshikawa, "Manipulability of Robotic Mechanisms," *Int. J. Rob. Res.*, vol. 4, no. 2, pp. 3–9, Jun. 1985.

[11] I. Mansouri and M. Ouali, "The power manipulability – A new homogeneous performance index of robot manipulators," *Robot. Comput. Integr. Manuf.*, vol. 27, no. 2, pp. 434–449, Apr. 2011.

[12] J. Angeles and C. S. Lopez-Cajun, "Kinematic Isotropy and the Conditioning Index of Serial Robotic Manipulators," *Int. J. Rob. Res.*, vol. 11, no. 6, pp. 560–571, Dec. 1992.

[13] R. S. Stoughton and T. Arai, "Modified Stewart platform manipulator with improved dexterity," *IEEE Trans. Robot. Autom.*, vol. 9, no. 2, pp. 166–172, Apr. 1993.

[14] K. H. Pittens and R. P. Podhorodeski, "A family of stewart platforms with optimal dexterity," *J. Robot. Syst.*, vol. 10, no. 4, pp. 463–479, Jun. 1993.

[15] A. B. K. Rao, P. V. M. Rao, and S. K. Saha, "Workspace and dexterity analyses of hexaslide machine tools," in *Robotics and Automation, 2003. Proceedings. ICRA '03. IEEE International Conference on*, 2003, vol. 3, pp. 4104–4109 vol.3.

[16] C. M. Gosselin, "The optimum design of robotic manipulators using dexterity indices," *Rob. Auton. Syst.*, vol. 9, no. 4, pp. 213–226, Jan. 1992.

[17] P. Cardou, S. Bouchard, and C. Gosselin, "Kinematic-sensitivity indices for dimensionally nonhomogeneous jacobian matrices," *IEEE Trans. Robot.*, vol. 26, no. 1, pp. 166–173, Feb. 2010.

[18] C. Gosselin, "Kinematic Analysis Optimization and Programming of Parallel Robotic Manipulators.pdf," McGill University, Montreal, 1985.

Appendix B.

Design and Performance Analysis of a 3-RRR Spherical Parallel Manipulator for Hip Exoskeleton Applications

The work attached to the following eleven pages is reproduced in accordance with the terms of the Creative Commons Attribution-NonCommercial 4.0 License (http://www.creativecommons.org/licenses/by-nc/4.0/). The original source of the work is provided in reference [168].

Original Article

RATE

Journal of Rehabilitation and Assistive Technologies Engineering
Volume 4: 1–11

DOI: 10.1177/2055668317697596
journals.sagepub.com/home/jrt

Design and performance analysis of a 3-RRR spherical parallel manipulator for hip exoskeleton applications

Soheil Sadeqi, Shaun P Bourgeois, Edward J Park and Siamak Arzanpour

Abstract

This paper presents the design and performance analysis and experimental study of a 3-RRR spherical parallel manipulator in the context of hip exoskeleton applications. First, the mechanism's inverse kinematics analysis and Jacobian matrix development are revisited. Manipulability, dexterity, and rotational sensitivity indices are then evaluated for two different methods of attachment to the human body. The superior attachment method in terms of these performance measures is indicated, and an experimental study based on the selected method is conducted; the experiment involves testing the capability of a 3-RRR manipulator's end-effector in tracking the motions experienced by a human hip joint during normal gait cycles. Finally, the results of the experimental study indicate that the manipulator represents a feasible hip exoskeleton solution providing total kinematic compliance with the human hip joint's 3-degree-of-freedom motion capabilities.

Keywords

Hip exoskeleton, spherical parallel manipulator, inverse kinematics, Jacobian, dexterity, manipulability, rotational sensitivity, experimental data

Date received: 27 October 2016; accepted: 30 January 2017

Introduction

An exoskeleton is a wearable robot designed to supplement one or more abilities of the human body part to which it is connected. Exoskeleton usage is often motivated by energy conservation for functional bodily limbs or strength assistance for limbs that have weakened or total loss of functionality. These capabilities stand to improve the quality of life for people suffering from mobility disablements, which have been reported to affect approximately 20,639,200 non-institutionalized individuals in the United States (7.1% of the total US population) in 2013[1] and 2,512,800 Canadians (7.2% of the total Canadian population) in 2012.[2]

The presence of one or more joints with multiple active degrees-of-freedom (DOFs) in the pertinent limb complicates the design of an exoskeleton with complete kinematic compliance. One method to address this challenge is to restrict the motions that the exoskeleton supports about the multi-DOF joint, instead of providing total kinematic compliance. This is the common design method for current exoskeleton research and technologies.[3–6] Consequently, most present-day exoskeletons are composed of kinematic open chains: serially connected single-DOF rotary or prismatic joints between rigid linkages. However, Kizir and Bingul conclude that closed-chain parallel manipulators (PMs) have better performance than their serial manipulator counterparts with regard to positioning accuracy, speed, force application, and payload-to-weight ratio.[7] Thus, in order to improve the robotic performance and kinematic functionality of exoskeletons, we propose the use of parallel robots paired with a mechanical structure that transmits motions to the targeted body part in a comfortable,

School of Mechatronic Systems Engineering, Simon Fraser University, Surrey, British Columbia, Canada

Corresponding author:
Siamak Arzanpour, Simon Fraser University, 250-13450 102 Ave, Surrey, British Columbia V3T 0A3, Canada.
Email: arzanpour@sfu.ca

non-restrictive way. One parallel robotic structure that has potential for use in such an application is the 3-RRR spherical parallel manipulator. Among previous works in the literature, Gosselin and Angeles present an inverse kinematics analysis, along with discussions of design optimization and singularities, for this manipulator.[8] Gosselin and Lavoie further discuss the kinematic design and Jacobian derivation for the mechanism.[9] Gosselin and Hamel have gone on to present a specific embodiment of the manipulator, the Agile Eye;[10] Gosselin and St-Pierre have further developed its kinematic description and experimentation.[11] More recently, Bai *et al.* have revisited the forward displacement analysis of the 3-RRR manipulator and introduced a new embodiment, called the Agile Wrist.[12] Wang *et al.* have conceptualized, analyzed (i.e. kinematic performance), and completed experiments (i.e. torque study) on the use of a redundantly actuated 3-RUS/RRR manipulator for 3-DOF ankle rehabilitation.[13] Most recently, Niyetkaliyev and Shintemirov detail one method of obtaining forward and inverse kinematics solutions for the Agile Wrist design, including simulation results and numerical examples for verification.[14]

This paper investigates the performance of the 3-RRR in the context of exoskeleton applications. Specifically, manipulability, dexterity, and rotational sensitivity performance indices are evaluated for two different body-interfacing schemes of the manipulator when it is applied as a hip exoskeleton device; here it is assumed that the manipulator supports 3-DOF rotational motions of the upper leg with respect to the pelvis. Our findings suggest that a 3-RRR manipulator can be employed as the hip actuator in an exoskeleton system; this represents an original contribution to the field of exoskeleton research.

Kinematic considerations for the 3-RRR manipulator

Kinematic architecture

Figure 1 shows a geometrical schematic of a generalized 3-RRR manipulator. This device is considered a 3-DOF spherical mechanism because all of its moving linkages perform spherical motions about a common point, O, which is stationary with respect to its base structure.[15,16] That is, all particles' motions within the system can be unambiguously described by radial projections on the surface of a unit sphere centered at the aforementioned stationary point. Consequently, the only permissible lower-pair joint within a spherical mechanism's limbs is a revolute joint; furthermore, all joint axes must intersect at the common stationary point mentioned above. In Figure 1, linkages are

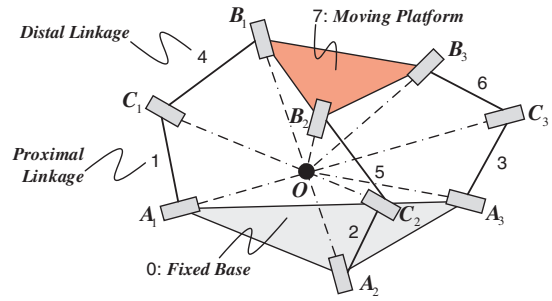

Figure 1. Schematic illustration of a generalized 3-RRR manipulator.[16]

labeled 0–7, where 0 indicates the fixed base structure and 7 corresponds to the manipulator's end-effector (i.e. the moving platform). A_i, B_i, and C_i denote the three revolute joints of each limb i, where $i = 1, 2, 3$ and only A_i joints are active.

Note that two notable embodiments of the 3-RRR manipulator are the Agile Eye and Agile Wrist, as mentioned in the previous section and shown in Figure 2(a) and (b), respectively. Although mechanically distinct, these two embodiments have the same inverse kinematics procedure, which is reviewed in the subsection that follows.

Inverse kinematics derivation

Inverse kinematics analysis for the 3-RRR manipulator has been examined extensively.[8,9,11,12] One approach is briefly revisited here for the sake of completeness and to acclimatize the reader to the notations and naming conventions used subsequently in this paper.

To start, direction vectors $\mathbf{u_1}$, $\mathbf{u_2}$, and $\mathbf{u_3}$ specify the rotational axes of the system's three active A_i joints, as shown in Figure 3. These vectors have constant values with respect to the global frame (with origin O) because they correspond to fixed joints. Next, input scalar variables θ_1, θ_2, and θ_3 define the angular states of the respective active joints. Direction vectors $\mathbf{w_1}$, $\mathbf{w_2}$, and $\mathbf{w_3}$ in turn specify the rotational axes of the joints between the three proximal–distal link pairs (i.e. the C_i joints). These vectors vary in element values with respect to the global frame because they correspond to free joints. The final set of direction vectors, $\mathbf{v_1}$, $\mathbf{v_2}$, and $\mathbf{v_3}$, specify the rotational axes of the joints between the three connection points of the distal links to the end effector (i.e. the B_i joints). Again, these vectors vary with respect to the global frame because they correspond to free joints.

Scalar constant α_1 specifies the angle between each actuated A_i joint and the corresponding proximal C_i joint within the plane containing both of these joints as well as the global origin, O. The value of α_1 used for the 3-RRR design analyzed here is 90°. The second

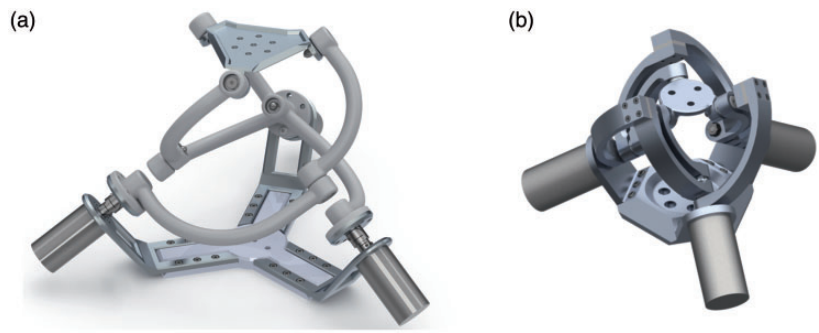

Figure 2. (a) Agile Eye and (b) Agile Wrist embodiments of the 3-RRR manipulator.

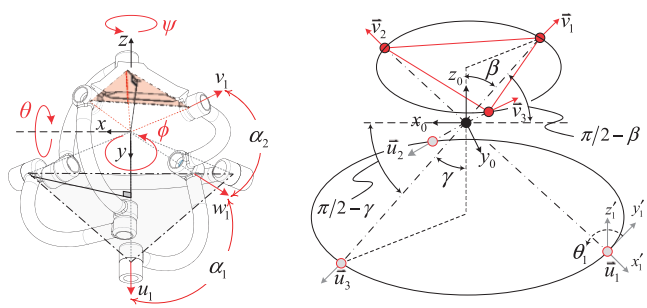

Figure 3. 3-RRR schematics with parameters and direction vectors labelled.

scalar constant, α_2, specifies the angle between each proximal C_i joint and the corresponding distal B_i joint within the plane containing both of these joints as well as the global origin. The value of α_2 used for the 3-RRR design considered here is also 90°. Third, scalar constant β indicates the angle between the $\mathbf{v}_i$ direction vectors and the global z-axis when the device is in its 'home' position (i.e. when the plane created by A_i joint positions is parallel to that defined by the B_i points). The value of β used here is 54.75°. Fourth, scalar constant γ indicates the angle between the $\mathbf{u}_i$ direction vectors and the vertical axis (i.e. the global z-axis). Unlike β, this value is constant for all mechanism states because the joints corresponding to the $\mathbf{u}_i$ direction vectors are fixed relative to the global frame. The value of γ used in this analysis is also 54.75°.

Finally, scalar constants η_1, η_2, and η_3 are used to specify the locations of the active joints associated with direction vectors $\mathbf{u_1}$, $\mathbf{u_2}$, and $\mathbf{u_3}$ and 'home-positioned' distal passive joints associated with $\mathbf{v_1}$, $\mathbf{v_2}$, and $\mathbf{v_3}$ within the global x-y plane. Measured with respect to the positive y-axis, the values of η_1, η_2, and η_3 are 0°, 120°, and 240°, respectively. Using this convention, η_i directly specifies the directions $\mathbf{u}_i$ in the global x-y plane and specifies the directions $\mathbf{v}_i$ in the global x-y plane when added to 60° and the mechanism is in its 'home' position. Note that the above parameter values are not independent, as they are related through geometry.

Equations for the $\mathbf{u}_i$ direction vectors can be derived in terms of the η_i and γ parameters discussed above. This derivation involves the following fixed-frame rotation process: rotation of a local frame F_1 (i.e. originally identical to the global frame) by (90°–η) about the global ${}^0y$-axis and then rotation of F_1 by η_i about the ${}^0z$-axis. This overall transformation is represented mathematically in Kucuk and Bingul.[17] Note that a superscript '0' indicates an axis or vector expressed with respect to the global frame.

$$R_{01} = R_z(\eta_i + 90^\circ)R_y(90^\circ - \gamma) = \begin{bmatrix} -S\eta_i S\gamma & -C\eta_i & -S\eta_i C\gamma \\ C\eta_i S\gamma & -S\eta_i & C\eta_i C\gamma \\ -C\gamma & 0 & S\gamma \end{bmatrix} \tag{1}$$

It follows that the x-axis of the resulting R_{01} orientation frame is equal to the direction vector $\mathbf{u}_i$.

$$\mathbf{u}_i = \begin{bmatrix} -S\eta_i S\gamma \\ C\eta_i S\gamma \\ -C\gamma \end{bmatrix}^T \tag{2}$$

Direction vectors $\mathbf{w}_i$ are in turn related to the corresponding $\mathbf{u}_i$ vectors through a fixed rotation by α_1 within the plane containing O, A_i, and C_i, along with a variable rotation dependent on actuator angle θ_i.

The parameterization of this transformation can be considered as a set of current frame rotations: first a rotation of θ_i about the local ${}^1x$-axis and then a rotation of α_1 about the updated local z-axis. In matrix format, an expression for this is as follows.

$$R_x(\theta_i)R_z(\alpha_1) = \begin{bmatrix} C\alpha_1 & -S\alpha_1 & 0 \\ -S\theta_i S\alpha_1 & -S\theta_i C\alpha_1 & -C\theta_i \\ C\theta_i S\alpha_1 & C\theta_i C\alpha_1 & -S\theta_i \end{bmatrix} \quad (3)$$

Now, to obtain expression in terms of the global coordinate system, the set of rotations described above must be pre-multiplied by R_{01}. Finally, the set of direction vectors $\mathbf{w_i}$ is obtained from the resulting matrix set as the x-axes for each i, as shown below.

$$\mathbf{w_i} = \begin{bmatrix} (-S\eta_i C\gamma C\theta_i + C\eta_i S\theta_i)S\alpha_1 - S\eta_i S\gamma C\alpha_1 \\ (C\eta_i C\gamma C\theta_i + S\eta_i S\theta_i)S\alpha_1 + C\eta_i S\gamma C\alpha_1 \\ -C\gamma C\alpha_1 + S\gamma C\theta_i S\alpha_1 \end{bmatrix}^T \quad (4)$$

Similarly to the derivation for $\mathbf{u_i}$ vectors summarized in equations (1) and (2), the $\mathbf{v_i}$ vectors can be established via two spatial rotations as follows when the device is in its 'home' position.

$$R_{03} = R_z(\eta_i)R_y(\beta) \quad (5)$$

Again, $\mathbf{v_i}$ is given as the x-axis component of the orientation matrix shown in equation (5). To determine the $\mathbf{v_i}$ directions after the mechanism's end-effector has undergone roll, pitch, and/or yaw rotations, R_{03} must be pre-multiplied by another transformation.

$$R_{04} = R_{rpy}R_{03} \quad (6)$$

where R_{rpy} represents the orientation of the end-effector with respect to the global frame. If it is assumed that R_{rpy} is expressed as fixed-frame rotations about the global x-axis by θ, y-axis by ϕ, and z-axis by ψ, respectively, then the $\mathbf{v_i}$ vector can be explicitly derived as follows.

$$\begin{bmatrix} v_{ix} \\ v_{iy} \\ v_{iz} \end{bmatrix} = \begin{bmatrix} 1 \\ 0 \\ 0 \end{bmatrix} \cdot R_z(\psi)R_y(\phi)R_x(\theta)R_{03} \quad (7)$$

Given that all direction vectors $\mathbf{w_i}$ and $\mathbf{v_i}$ are of unit length, the angle between corresponding $\mathbf{w_i}$ and $\mathbf{v_i}$ vectors is α_2 (by the parameter's definition), and the geometric definition of the vector dot product, the following equation relates the two sets of direction vectors.

$$\mathbf{w_i} \cdot \mathbf{v_i} = \cos\alpha_2 \quad i = 1, 2, 3 \quad (8)$$

Now, through substitution of equations (4) and (7) into equation (8), a set of relationships between the system inputs and outputs is obtained. Upon performing this substitution and simplifying the result, the following equation is produced.

$$A \times \tan^2(\theta_i/2) + B \times \tan(\theta_i/2) + C = 0 \quad i = 1, 2, 3 \quad (9)$$

where

$$\begin{aligned} A = {} & (-C\eta_i C\gamma S\alpha_1 + C\eta_i S\gamma C\alpha_1)v_{iy} \\ & + \ldots (S\eta_i C\gamma S\alpha_1 - S\eta_i S\gamma C\alpha_1)v_{ix} \\ & + \ldots (-C\gamma C\alpha_1 - S\alpha_1 S\gamma)v_{iz} - c\alpha_2 \end{aligned} \quad (10)$$

$$B = 2S\eta_i S\alpha_1 v_{iy} + 2C\eta_i S\alpha_1 v_{ix} \quad (11)$$

$$\begin{aligned} C = {} & (-S\eta_i C\gamma S\alpha_1 - S\eta_i S\gamma C\alpha_1)v_{ix} \\ & + (-C\gamma C\alpha_1 + S\alpha_1 S\gamma)v_{iz} \\ & + (C\eta_i C\gamma S\alpha_1 + C\eta_i S\gamma C\alpha_1)v_{iy} - c\alpha_2 \end{aligned} \quad (12)$$

It follows that the input angle required to achieve a desired end-effector positional output can be found with the following equation.

$$\theta_i = 2atan2\left(\frac{-B \pm \sqrt{B^2 - 4AC}}{2A}\right) \quad i = 1, 2, 3 \quad (13)$$

Equations (10)–(13) represent the solution to the inverse kinematics problem for the 3-$\underline{\text{R}}$RR manipulator because they provide the required active joint states, θ_i, necessary to achieve a desired orientation of the end-effector. That is, once end-effector rotations θ, ϕ, and ψ are established, the associated angular states of the active revolute joints can be identified.

Jacobian analysis

A number of generally accepted performance indices for parallel manipulators are often published as a method for comparing various robotic manipulators.[16] The values of these indices usually have physical significance and applications for design optimization.[17] The three indices considered in this paper, which are manipulability, dexterity, and rotational sensitivity, all derive from the Jacobian matrix of a manipulator. Thus, the 3-$\underline{\text{R}}$RR device's Jacobian development is discussed in this section, before the performance indices are examined in the next section.

To start, a vector $\mathbf{q}$ is assigned to represent active joint variables while $\mathbf{x}$ is used to characterize the end-effector's position. The kinematic constraints associated

with the device's limbs can be expressed as follows.

$$f(\mathbf{x},\mathbf{q}) = \mathbf{0} \tag{14}$$

where f is an n-dimensional implicit function of $\mathbf{q}$ and $\mathbf{x}$, and n is the active joint count within the mechanism. Now, time-differentiating equation (14) yields the following relationship between input joint rates and end-effector velocity.

$$\frac{\partial \mathbf{f}}{\partial \mathbf{x}}\dot{\mathbf{X}} + \frac{\partial \mathbf{f}}{\partial \mathbf{q}}\dot{\mathbf{q}} = 0 \rightarrow \mathrm{J}_x\dot{\mathbf{X}} = \mathrm{J}_q\dot{\mathbf{q}} \tag{15}$$

As shown above, two components of the Jacobian are produced: J_x and J_q. The combination of these components yields the complete Jacobian matrix.

$$\dot{\mathbf{q}} = \mathrm{J}_q^{-1}\mathrm{J}_x\dot{\mathbf{X}} = \mathrm{J}\dot{\mathbf{X}} \tag{16}$$

It is important to note that the Jacobian associated with a parallel manipulator, as in equation (16), is derived as the inverse of a serial manipulator's Jacobian.[15]

when equation (15) is written once for each of $i = 1$, 2, and 3, three scalar equations are produced. These can be arranged in matrix form as follows.

$$\begin{bmatrix} (\mathbf{w_1} \times \mathbf{v_1})^T \\ (\mathbf{w_2} \times \mathbf{v_2})^T \\ (\mathbf{w_3} \times \mathbf{v_3})^T \end{bmatrix} \omega_b = -\begin{bmatrix} \mathbf{w_1} \times \mathbf{u_1}.\mathbf{v_1} & 0 & 0 \\ 0 & \mathbf{w_2} \times \mathbf{u_2}.\mathbf{v_2} & 0 \\ 0 & 0 & \mathbf{w_3} \times \mathbf{u_3}.\mathbf{v_3} \end{bmatrix} \dot{\mathbf{q}} \tag{17}$$

Combining equations (16) and (17) yields a complete form of the 3-RRR manipulator's Jacobian matrix.

$$\mathrm{J} = \mathrm{J}_q^{-1}\mathrm{J}_x = -\begin{bmatrix} \mathbf{w_1} \times \mathbf{u_1}.\mathbf{v_1} & 0 & 0 \\ 0 & \mathbf{w_2} \times \mathbf{u_2}.\mathbf{v_2} & 0 \\ 0 & 0 & \mathbf{w_3} \times \mathbf{u_3}.\mathbf{v_3} \end{bmatrix}^{-1} \times \begin{bmatrix} (\mathbf{w_1} \times \mathbf{v_1})^T \\ (\mathbf{w_2} \times \mathbf{v_2})^T \\ (\mathbf{w_3} \times \mathbf{v_3})^T \end{bmatrix} \tag{18}$$

Recall that vectors $\mathbf{u}_i$, $\mathbf{w}_i$, and $\mathbf{v}_i$ can be computed from equations (2), (4), and (7), respectively.

Hip exoskeleton design based on performance indices

With the 3-RRR manipulator's Jacobian matrix derived, it is now possible to evaluate several of the device's performance indices. In doing so, two methods for attaching the device to the human body are considered, as shown in Figure 4. Furthermore, only flexion-extension and abduction-adduction motions are considered; the final major DOF of the hip joint (i.e. internal/external rotation) is assumed to be constant and oriented such that the knee's axis of rotation is perpendicular to the sagittal plane of the body. As can be deduced from Figure 3, the device's ψ angle corresponds to flexion/extension motions for Attachment Method 1, while ϕ is associated with those motions in Attachment Method 2; for both cases, θ corresponds to abduction/adduction motions. Additionally, a workspace range of [–0.2 0.2] radians for both flexion-extension and abduction-adduction motions was considered for all local performance studies. Finally, the results below are only applicable when the parameter values (i.e. for α_1, α_2, β, γ, η_1, η_2, and η_3) are selected as per the discussion in Kinematic architecture section.

Manipulability

Forces experienced by joints within parallel manipulators tend to become large when such a device nears singular configurations.[16] Thus, the ability to quantify a manipulator's nearness to singular configurations is useful. Manipulability is a common performance index used to accomplish this quantification. It is defined as the absolute value of the Jacobian's determinant,[18] as given in equation (19). Alternatively, this index can be interpreted as the Jacobian matrix's minimum-magnitude eigenvalue.

$$\mu = \sqrt{|\mathrm{J}^T\mathrm{J}|} \tag{19}$$

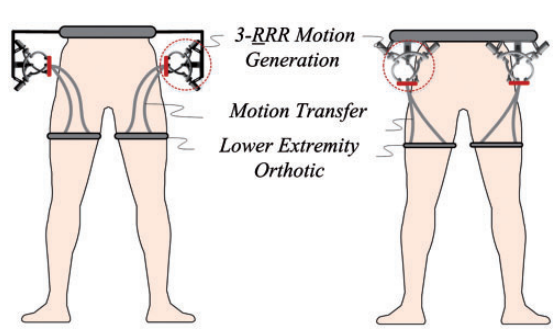

Figure 4. Considered 3-RRR attachment methods as a hip exoskeleton. (a) Interfacing scheme 1; (b) interfacing scheme 2.

In mechanical terms, manipulability represents a manipulator's ability to successfully create a desired velocity at its end-effector.[19] Alternatively, this index can be understood as the ellipsoid volume resulting when a unit sphere is mapped from the manipulator's n-dimensional joint space into Cartesian space through its Jacobian matrix and a constant proportionality factor;[20] recall that n represents the active joint count for the manipulator. It follows that a manipulator achieves greater manipulability performance if its ellipsoid has a greater uniformity, or isotropy, characteristic.[21] Such an isotropy index for manipulability can be quantified as follows.

$$\mu_{iso} = \sigma_{\min}/\sigma_{\max} \tag{20}$$

where $\sigma_{\min}$ and $\sigma_{\max}$ are the minimum and maximum singular values of the Jacobian matrix, respectively. The μ_{iso} value in equation (20) is limited to the range [0, 1], where 0 indicates inability to transmit velocity to the end-effector (i.e. a singular configuration) and 1 indicates ability to transmit velocity to the end-effector uniformly in all directions. Figure 5 shows the 3-RRR device's manipulability deviation and statistical distribution within the considered workspace for the two attachment methods depicted in Figure 4.

According to the surface plots, the manipulability of the 3-RRR is greatest when operating near its 'home' configuration and least near the boundaries of the considered workspace for both attachment methods. Comparatively, Attachment Method 1 achieves a greater average value for manipulability than Attachment Method 2. Furthermore, Method 1 achieves less variance in performance within the workspace considered. Therefore, Method 1 is superior to Method 2 in terms of manipulability.

Dexterity (condition number)

Because a manipulator's control scheme generally relies on its joint position coordinates, any errors between the expected and actual joint coordinates cause errors in the end-effector's position and orientation.[16] This end-effector error can be determined through multiplication of the errors in the joint coordinates by a scaling factor: the condition number, k.[22] A manipulator's condition number is obtained from the Jacobian matrix as follows.[22–25]

$$k(\mathrm{J}) = \|\mathrm{J}\|\|\mathrm{J}^{-1}\| \tag{21}$$

where J is the Jacobian matrix. Here, ||J|| denotes the Jacobian's Euclidean norm.

$$\|\mathrm{J}\| = \sqrt{tr\left(\frac{1}{n}\mathrm{J}\mathrm{J}^T\right)} \tag{22}$$

Gosselin proposes that the condition number's inverse be used to quantify a manipulator's kinematic accuracy;[24] this criterion is called the local dexterity index, denoted by ν.

$$\nu = \frac{1}{\|\mathrm{J}\|\|\mathrm{J}^{-1}\|} \tag{23}$$

Again, allowable values for ν are constrained between 0 and 1; zero indicates a singularity, and

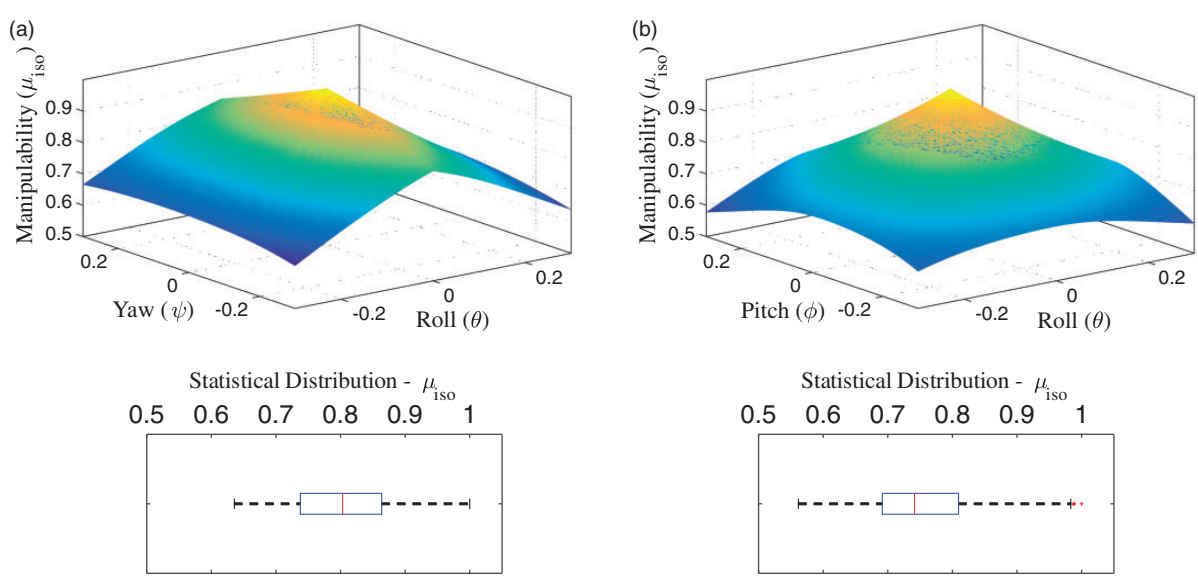

Figure 5. 3-RRR manipulability for (a) Attachment Method 1 and (b) Attachment Method 2.

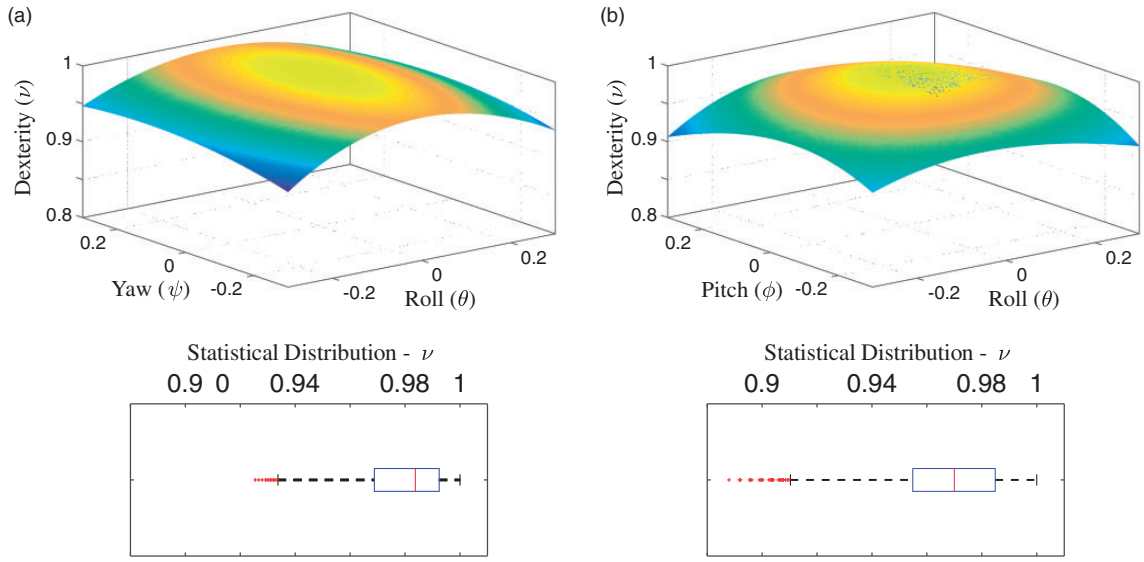

Figure 6. 3-RRR dexterity for (a) Attachment Method 1 and (b) Attachment Method 2.

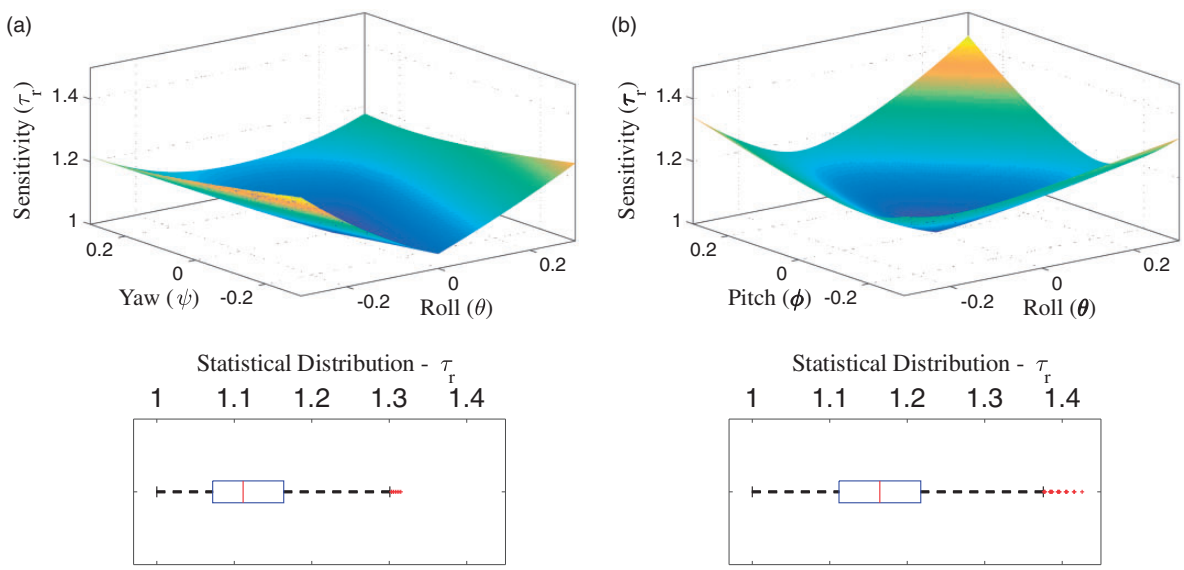

Figure 7. 3-RRR rotational sensitivity for (a) Attachment Method 1 and (b) Attachment Method 2.

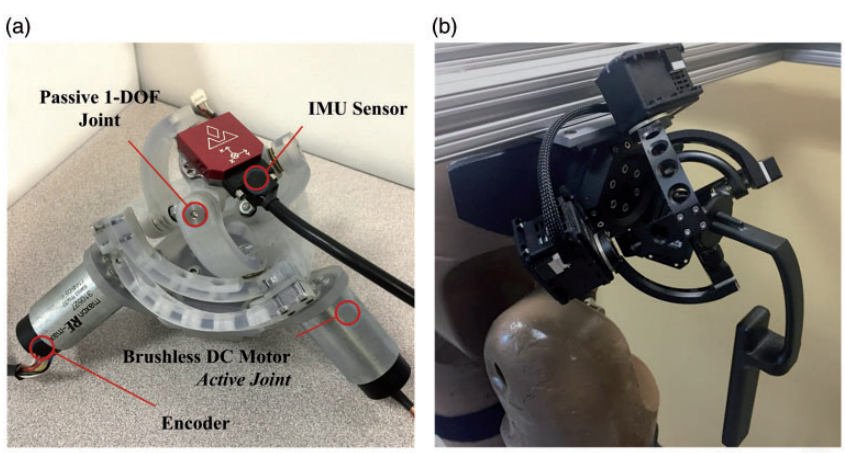

Figure 8. (a) Experimental prototype of the 3-RRR manipulator and (b) 3-RRR manipulator mounted on the Hip mannequin.

greater values correspond to increasingly accurate motion generation at the end-effector.

Figure 6 depicts dexterity index surface plots and statistical box plots for both body-attachment arrangements of the 3-RRR manipulator across its considered workspace. Similarly to manipulability, these plots suggest that the mechanism's dexterity is greatest when configured in close proximity to its 'home' orientation and that it decreases as the device moves towards the boundaries of its considered workspace. Additionally, greater average dexterity and less dexterity variation are achieved when the 3-RRR robot is interfaced with the human body according to Attachment Method 1 as opposed to Method 2, which makes the former preferable.

Rotational sensitivity

The rotational sensitivity index of a manipulator indicates how reactive its end-effector is to changes in active joint states. More specifically, it is the maximum-magnitude rotation of the end-effector under a unit-norm actuator displacement;[20] it is given by either the 2–norm or the ∞–norm of the Jacobian matrix as follows.

$$\tau_r = \|\mathrm{J}\| \tag{24}$$

Figure 7 shows the sensitivity results for the 3-RRR manipulator when subject to the body-interfacing schemes of Figure 4 and constrained to the [–0.2 0.2] radian workspace range in both flexion-extension and abduction-adduction motions. Again, Attachment Method 1 demonstrates preferable performance to that of Method 2 because the former possesses the smaller-magnitude average and variance range in sensitivity index value. Furthermore, sensitivity performance is optimal for both arrangements near the device's 'home' orientation and degrades as the workspace limits are approached.

Experimental study on the 3-RRR manipulator

Mechanism fabrication details

In preparation for experimental tests on the 3-RRR manipulator design proposed in this paper, a prototype system was fabricated. As shown in Figure 8, all linkage components of the device are 3D-printed, including the base structure, proximal and distal links, and end-effector platform. The prototype's passive revolute joints are composed of off-the-shelf shoulder screws, rotary ball bearings, and thrust bearings. Meanwhile, the active revolute joints are prototyped with Maxon RE-max 29 brushed DC motors. Lastly, a VectorNAV VN-100 Rugged inertial measurement unit (IMU) is attached to the end-effector platform for capturing orientation data during system operation.

Experimental results

The purpose of our experimental study on the 3-RRR prototype is to confirm its end-effector's ability to perform the 3-DOF motions experienced by the human hip joint during normal gait cycles. In order to complete this test, the prototype's motors are controlled with a simple proportional-integral (PI) scheme; angular feedback is provided by the actuator's attached encoders.

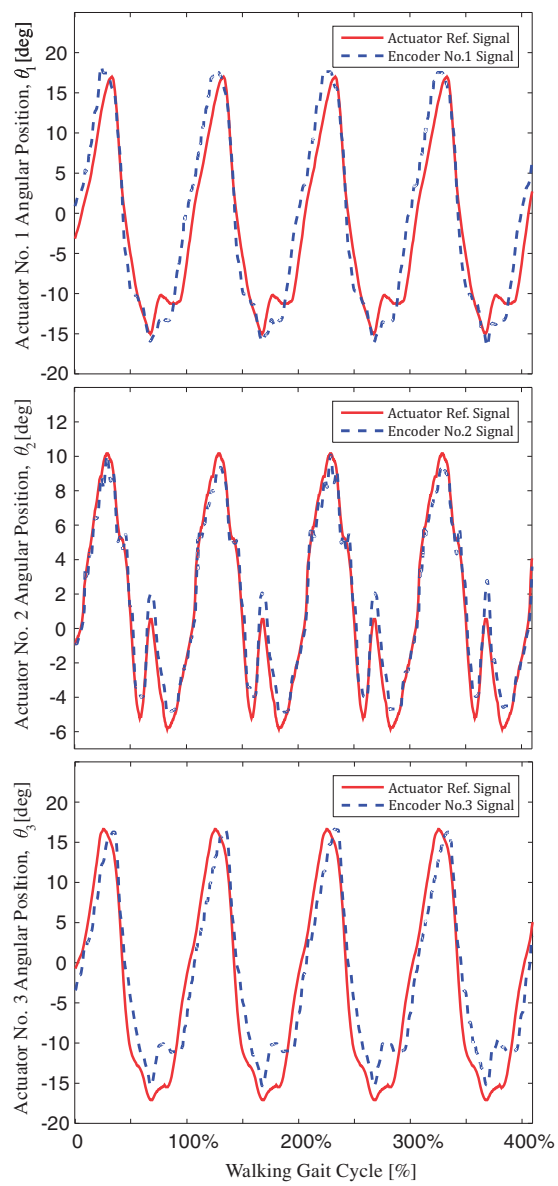

Figure 9. Comparison of reference signal and encoder feedback from each actuator during gait motion tracking.

In terms of test execution, reference signals for the end-effector to track are provided by Stanford University's OpenSim software.[26,27] Subsequently, motor reference signals are obtained by applying the inverse kinematics algorithm discussed in Kinematic architecture section to the OpenSim angular motion signals. Because Attachment Method 1 is expected to provide manipulability, dexterity, and sensitivity performance that are superior to those of Method 2, the motion strategy associated with Method 1 is utilized. That is, the prototype's ψ motions are matched to hip flexion-extension motions, θ to abduction-adduction, and ϕ to internal/external rotations.

The experimental results of Figure 9 depict the reference and response signals associated with the individual system motors. These are the motions required by the selected design and body-attachment scheme to achieve the hip motions associated with normal gait cycles at the end-effector, as determined by the inverse kinematics algorithm. In turn, Figure 10 presents an

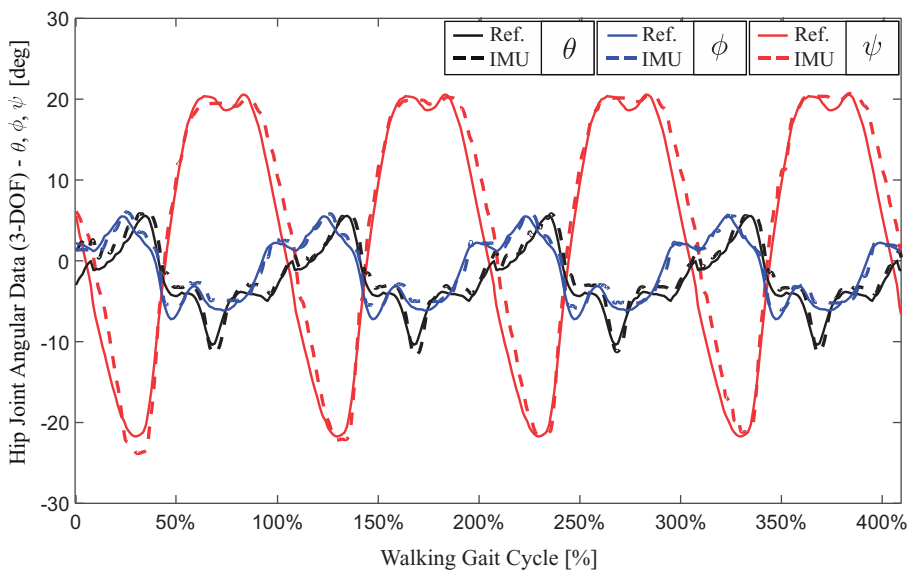

Figure 10. Comparison of desired end-effector orientation and IMU-measured value during gait motion tracking.

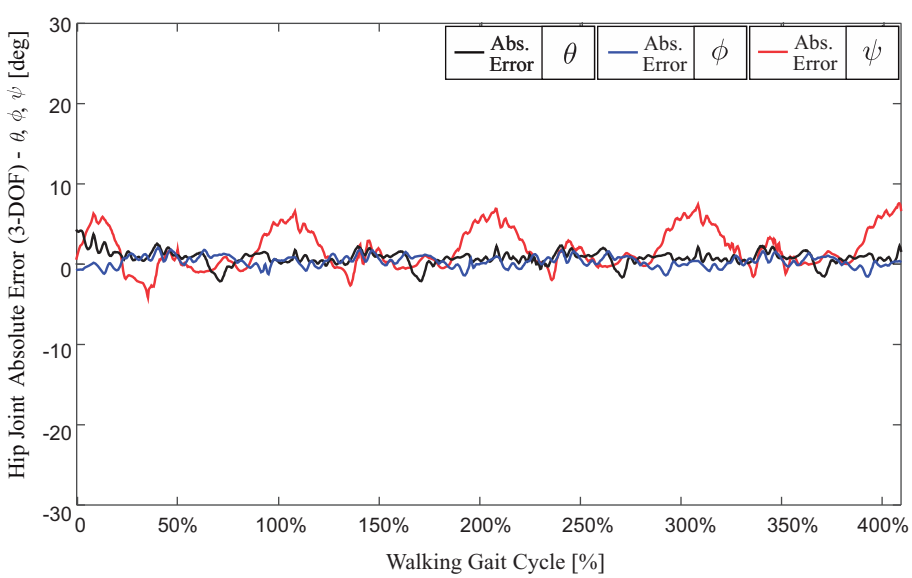

Figure 11. Absolute error between desired end-effector orientation and IMU-measured value during gait motion tracking.

overlay of the resulting end-effector orientation angles, as captured by the system IMU, and the desired angles, as provided by the OpenSim software.

The results shown in Figures 9 and 10 indicate that the 3-RRR manipulator can achieve the same motion ranges as the human hip during normal gait cycles. Furthermore, the plots suggest that the mechanism can complete these motions with a similar rate to that of the human hip. The maximum absolute error between a single desired end-effector angle and the measured angle is 7.6°, and it applies to ψ (i.e. flexion-extension motions); the root mean squared error values for θ, ϕ, and ψ are 1.2°, 0.7°, and 3.1°, respectively.

As shown in the absolute error plots of Figure 11, the error in ψ rises periodically during a rapid extension motion of the hip joint. This systematic error can be primarily attributed to the experiment's non-optimal control method, which does not account for inherent nonlinearities of the device's dynamics and inhibits the device from adequately tracking its reference signal. Therefore, the development of a more effective control algorithm would likely reduce the end-effector's orientation errors. Given this solution and the otherwise small magnitudes of error, it is feasible that the 3-RRR manipulator could be used within a hip exoskeleton system.

Conclusion and future work

This paper proposes the use of the well-established 3-RRR manipulator as a robotic component within a hip exoskeleton system. Before investigating the mechanism's performance for two different body-attachment methods and presenting the results of a motion-tracking experiment, the device's inverse kinematics and Jacobian matrix development procedures were revisited.

The performance study results indicate that the body-interfacing arrangement that orients the manipulator's x-y plane parallel to the body's sagittal plane is superior in terms of average value and variability for manipulability, dexterity, and rotational sensitivity indices. As can be expected, the manipulator's performance is optimal when configured at its initial 'home' orientation and degrades as the end-effector moves away from this state.

For the experimental study, a prototype manipulator's end-effector was controlled to track the motions experienced by a human hip joint during normal gait cycles. In summary, the general agreement between input and output signals depicted in the resulting figures suggests that application of this 3-RRR design as a hip exoskeleton is feasible. Furthermore, this application poses a motion assistance solution with total kinematic compliance for multi-DOF body joints. Future work includes singularity, dynamic, and workspace analyses, design and analysis of the complete exoskeleton system with bodily interfacing details considered, and development of an effective closed-loop control algorithm for the 3-RRR manipulator.

Declaration of Conflicting Interests

The author(s) declared no potential conflicts of interest with respect to the research, authorship, and/or publication of this article.

Funding

The author(s) disclosed receipt of the following financial support for the research, authorship, and/or publication of this article: This work was supported by the Natural Sciences and Engineering Research Council of Canada (NSERC).

References

1. W. Erickson, C. Lee and S. von Schrader. *Disability statistics from the 2013 American Community Survey (ACS)*. Ithaca, NY: Cornell university, 2015.
2. Statistics Canada. *Disability in Canada: Initial findings from the Canadian Survey on Disability*. Ottawa: Canadian Survey on disability.
3. Li Z, Xie H, Li W, et al. Proceeding of human exoskeleton technology and discussions on future research. *Chin J Mech Eng* 2014; 27: 437–447.
4. Cenciarini M and Dollar AM. Biomechanical considerations in the design of lower limb exoskeletons. *IEEE Int Conf Rehabil Robot* 2011; 2011: 1–6.
5. Esquenazi A, Talaty M, Packel A, et al. The ReWalk powered exoskeleton to restore ambulatory function to individuals with thoracic-level motor-complete spinal cord injury. *Am J Phys Med Rehabil* 2012; 91: 911–921.
6. Ambrose RO, Aldridge H, Askew RS, et al. Robonaut: NASA's space humanoid. *IEEE Intell Syst Appl* 2000; 15: 57–63.
7. Kizir S and Bingul Z. Position control and trajectory tracking of the Stewart platform. In: Kucuk S (ed.) *Serial and parallel robot manipulators - kinematics, dynamics, control and optimization*. Istanbul, Turkey: InTech, Chapters published under CC BY 3.0 license, 2012, 179–202.
8. Gosselin C and Angeles J. The optimum kinematic design of a spherical three-degree-of-freedom parallel manipulator. *J Mech Transm Autom Des* 1989; 111: 202–207.
9. Gosselin CM and Lavoie E. On the kinematic design of spherical three-degree-of-freedom parallel manipulators. *Int J Rob Res* 1993; 12: 394–402.
10. Gosselin CM and Hamel J-F. The agile eye: A high-performance three-degree-of-freedom camera-orienting device. In: *Proceedings of the 1994 IEEE International Conference on Robotics and Automation*, San Diego, pp.781–786.
11. Gosselin CM and St-Pierre E. Development and experimentation of a fast 3-DOF camera-orienting device. *Int J Robot Res* 1997; 16: 619–630.

12. Bai S, Hansen MR and Angeles J. A robust forward-displacement analysis of spherical parallel robots. *Mech Mach Theory* 2009; 44: 2204–2216.
13. Wang C, Fang Y, Guo S, et al. Design and kinematical performance analysis of a 3-RUS/RRR redundantly actuated parallel mechanism for ankle rehabilitation. *J Mechanisms Robotics* 2013; 5: 1–11.
14. Niyetkaliyev A and Shintemirov A. An approach for obtaining unique kinematic solutions of a spherical parallel manipulator. In: *2014 IEEE/ASME International Conference on Advanced Intelligent Mechatronics*, Besançon, France, 2014, 1355–1360.
15. Tsai L. *Robot analysis: The mechanics of serial and parallel manipulators*. New York, NY: J. Wiley and Sons, 1999.
16. Merlet J-P. *Parallel Robots*, 2nd ed. Sophia-Antipolis, France: Springer, 2006.
17. Kucuk S and Bingul Z. Comparative study of performance indices for fundamental robot manipulators. *Rob Auton Syst* 2006; 54: 567–573.
18. Yoshikawa T. Manipulability of robotic mechanisms. *Int J Robot Res* 1985; 4: 3–9.
19. Mansouri L and Ouali M. The power manipulability – A new homogeneous performance index of robot manipulators. *Robot Comput Integr Manuf* 2011; 27: 434–449.
20. Cardou P, Bouchard S and Gosselin C. Kinematic-sensitivity indices for dimensionally nonhomogeneous Jacobian matrices. *IEEE Trans Robot* 2010; 26: 166–173.
21. Angeles J and Lopez-Cajun CS. Kinematic isotropy and the conditioning index of serial robotic manipulators. *Int J Robot Res* 1992; 11: 560–571.
22. Stoughton RS and Arai T. Modified Stewart platform manipulator with improved dexterity. *IEEE Trans Robot Autom* 1993; 9: 166–172.
23. Pittens KH and Podhorodeski RP. A family of Stewart platforms with optimal dexterity. *J Robot Syst* 1993; 10: 463–479.
24. Rao ABK, Rao PVM and Saha SK. Workspace and dexterity analyses of hexaslide machine tools. In: *Proceedings of ICRA '03, IEEE International Conference on Robotics and Automation*, Vol. 3, Taipei, Taiwan, 2003, pp.4104–4109.
25. Gosselin CM. The optimum design of robotic manipulators using dexterity indices. *Rob Auton Syst* 1992; 9: 213–226.
26. Delp SL, Loan JP, Hoy MG, et al. An interactive graphics-based model of the lower extremity to study orthopaedic surgical procedures. *IEEE Trans Biomed Eng* 1990; 37: 757–767.
27. Anderson FC and Pandy MG. A dynamic optimization solution for vertical jumping in three dimensions. *Comput Methods Biomech Biomed Engin* 1999; 2: 201–231.

Appendix C.

Initial Mechanical and Software Designs for the Prototype Motion-Capture Exoskeleton

Initial Mechanical Design

The initial design for the prototype motion capture (MoCap) exoskeleton had the ankle module attached to the back side of the shank orthotic, as shown in Figure C.1. However, after the initial system construction was complete, several preliminary MoCap tests revealed a flaw with the ankle exoskeleton module functionality: large plantarflexion and dorsiflexion motions of the ankle only registered very small angular displacements at the exoskeleton module's potentiometers. As illustrated in the callouts of Figure C.1, the reason for this insensitivity is that large and plantarflexion/dorsiflexion rotations would move the prismatic joint's carriage along a path very nearly tangent to the prismatic track, thus imposing large translations of the prismatic joint but very little rotation in any sensed joint.

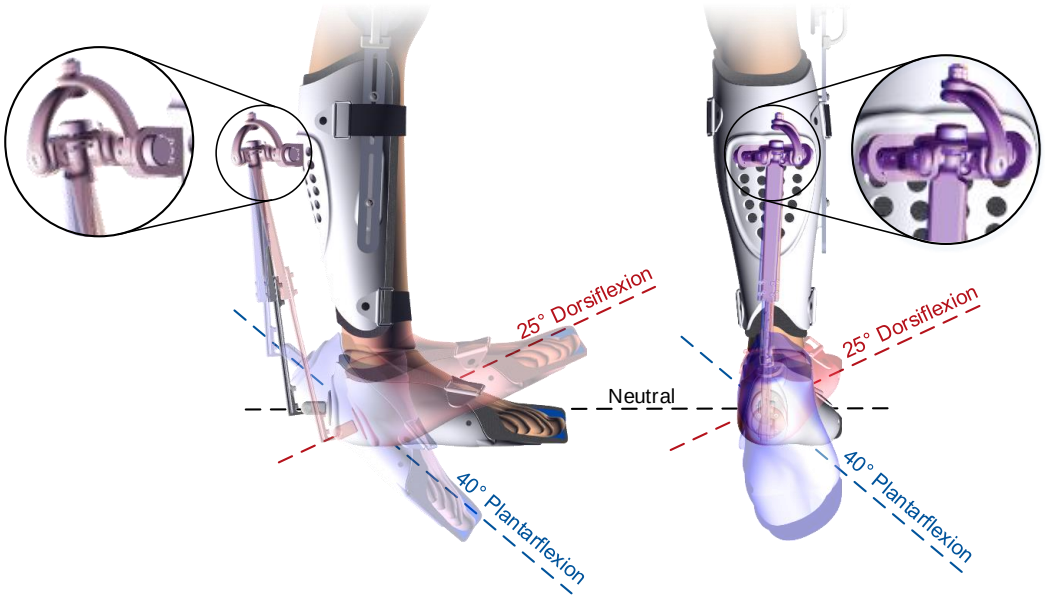

Figure C.1. Illustration of the small orientation change in the SAE corresponding to the ankle's full plantarflexion/dorsiflexion range for the prototype MoCap exoskeleton's initial mechanical design

Note: The plantarflexion image has blue-colored highlights and the dorsiflexion image has red-colored highlights.

One solution to this problem is to include sensing capability on the prismatic joint (e.g., replace the passive slider with a linear potentiometer or linear encoder). However, the somewhat arbitrary orientation of the Simplified Agile Eye's (SAE's) base component for this construction also made it difficult to determine accurate kinematic parameters (i.e., the SAE base frame orientation with respect to the shank frame). Therefore, the ankle exoskeleton was instead removed and reinstalled on the outside face of the shank orthotic, as shown in the final mechanical design of Chapter 5 and Subsection 6.1.1. Not only did this adjustment provide a more easily-measured SAE base orientation with respect to the lower component of the knee brace, which is used to define the shank frame, but it also proved to make the ankle exoskeleton more sensitive to ankle motions in subsequent test trials.

Initial Software Design

The software uploaded to the prototype system's Arduino microcontroller unit (MCU) was initially a version of the open-source SD-card datalogger code developed by Tom Igoe [214]. This code was modified to match the electrical design associated with the MoCap exoskeleton, as detailed in Subsection 6.1.2. Figure C.2 shows a logic diagram of the modified code. However, a shortcoming associated with this program is its use of hard-coded delays to establish the potentiometer data sampling rate; because this method does not consider the MCU clock cycles required to execute sampling and other program tasks, the actual sampling rate is not precisely that specified by the delay. Even if the total system clock cycles between each delay command is determined and accounted for, which is not the case in this program, any unexpected interrupt routines or delays caused by hardware results in an inconsistent data sampling rate. This inconsistent sample rate was observed during preliminary system trials, in which the time between samples (i.e., as determined via the system clock) was nonuniformly greater than the desired period. To address the inconsistent sampling rate, the initial MCU program was replaced by the code described in Subsection 6.1.3.

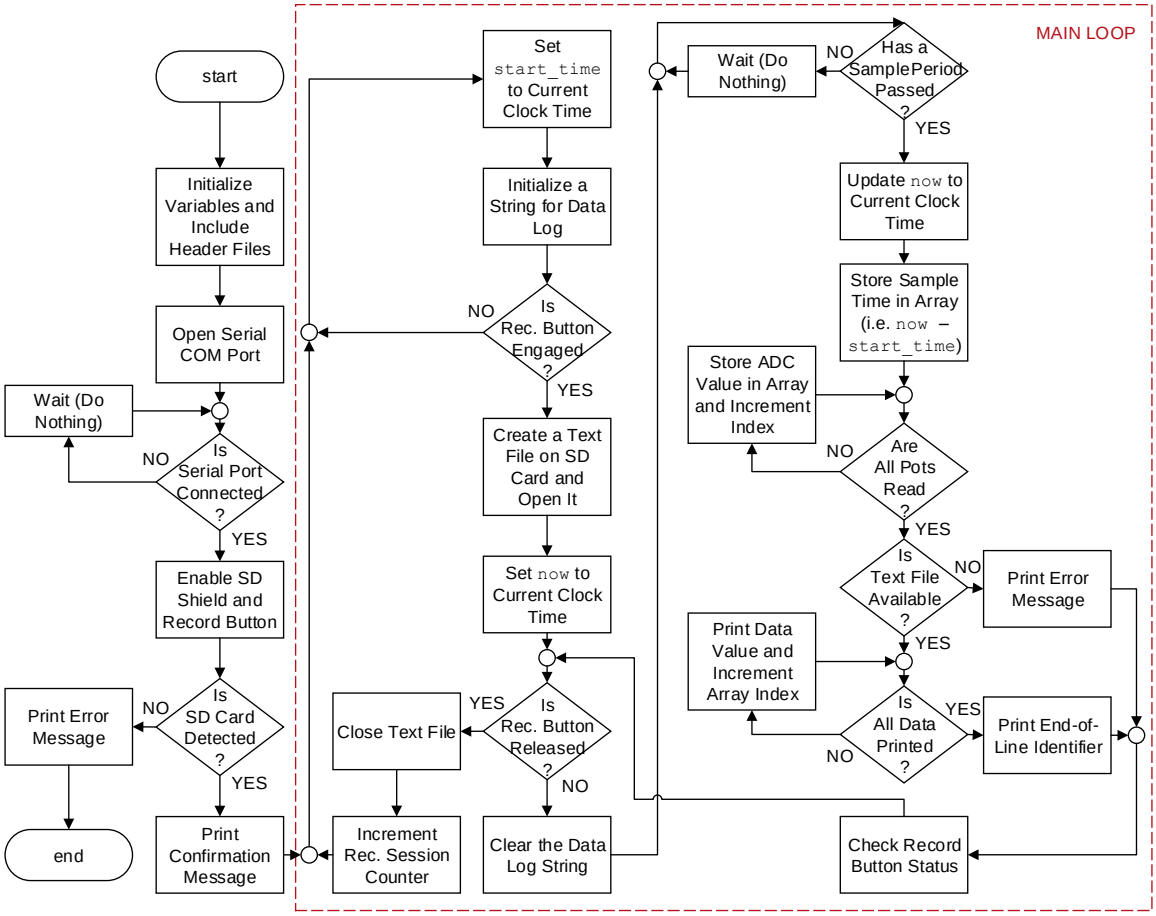

Figure C.2. Logic diagram of initial MCU program used for logging data from the MoCap exoskeleton's potentiometers

Appendix D.

Setup and Calibration Procedures for the Qualisys and Xsens Systems prior to Experimentation

Qualisys System Setup

Per the Qualisys Track Manager (QTM) user manual [215], the setup procedure for the Qualisys system started with placing the Oqus cameras within the experimentation room surrounding an empty area on the floor that would be the motion capture (MoCap) workspace; this designated the spatial region in which all motion tests had to be performed. As described in Subsection 6.2.1, one experiment was conducted using five cameras and another with eight cameras. The MCU of one camera, assigned as the 'master camera', was then connected to a PC with the QTM software installed via an RS232 host cable. Considering this master camera as first in the series of cameras, data cables were then connected between each successive camera. The first and fifth cameras were connected to electrical outlets, and power cables were connected to adjacent cameras to supply power to the whole camera system. Taken from the QTM user manual, Figure D.1 shows a diagram of an appropriate camera connection scheme.

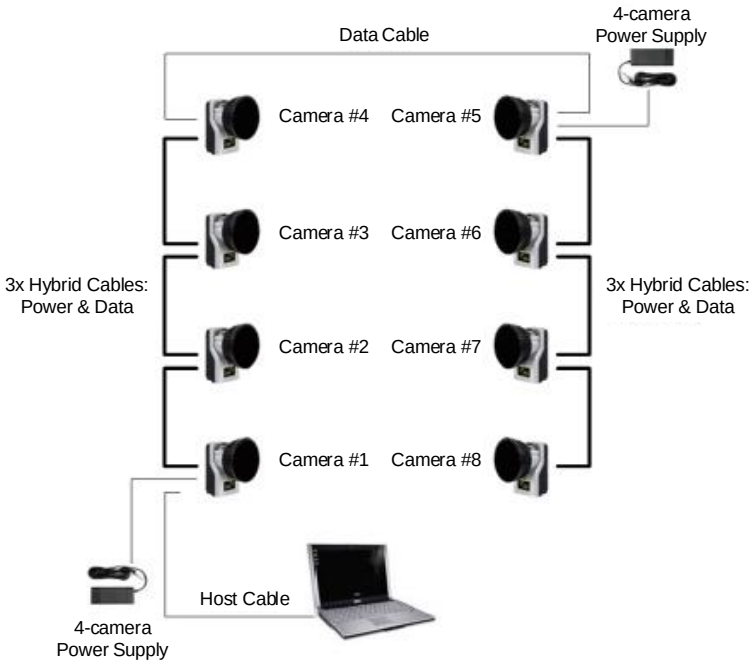

Figure D.1. Oqus camera cable-connection setup for the Qualisys system [215]

Once the Qualisys system's camera-cable connections were made, the QTM software was launched on the connected PC. The program's first prompt inquires the user about opening a new Qualisys project (i.e., folder and setting option files) or loading an existing one; for the initial experiment conducted during this study, a new project was created with default settings, and for the main experiment, a new project was created with the same settings as established for the initial project. After the project was specified, the QTM main window opened automatically. In order to identify and connect the Oqus cameras with the QTM software, the 'Connection' menu was accessed from the 'Input Devices' and 'Camera System' branches of the 'Project Options' window, which was opened from the main window's 'Tools' dropdown list. The 'Locate System' button was then pressed and the RS232 serial connection method for searching was selected. After doing this, the QTM software was able to obtain and display the data captured for each camera. Figure D.2 shows a screenshot of the 'Connection' menu after locating the 8-camera system during the main experiment.

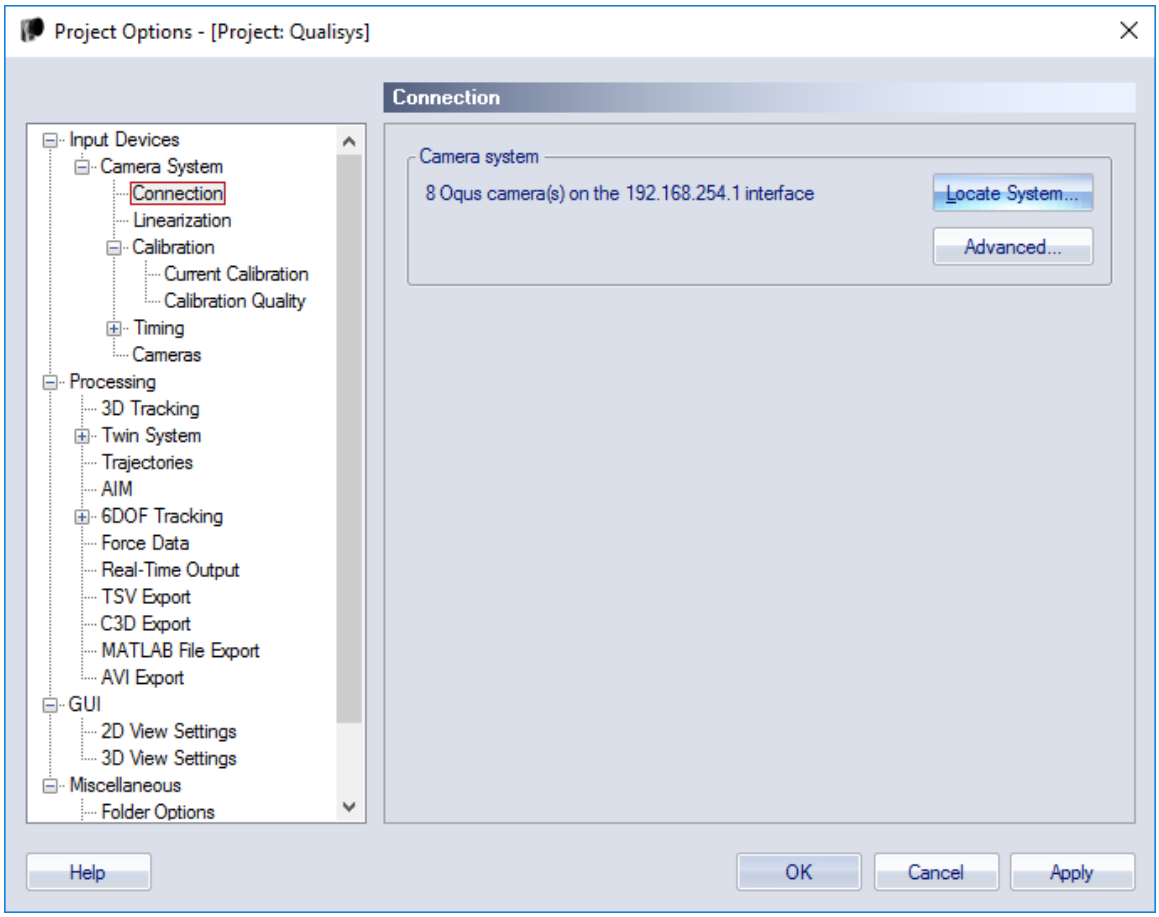

Figure D.2. The QTM 'Connection' menu with 8 cameras located

The next setup activity for the Qualisys system was the camera aperture and focus adjustments. Following the camera connection process, it was possible to switch the cameras to video mode in QTM and observe the video images obtained from each camera. This was done by selecting the capture button from the QTM main window and selecting ‘Stop on button only’ for the ‘Capture period’ option. Since the camera calibration procedure was not yet completed, the software provided a message indicating that calibration was necessary before any MoCap data could be saved; this message was acknowledged and closed. At this point, the video images from each camera became visible from the QTM main window. In order to appropriately adjust each camera’s aperture and focus, retroreflective markers were placed or held within the intended measurement volume. The lens of each camera was then accessed by turning the strobe part of the camera counter-clockwise. Subsequently, the aperture and focus dials on each camera were adjusted until the markers were as small and sharp as possible within their observation windows in QTM. After each camera’s aperture and focus were appropriately set, the strobe part of the camera was closed to conceal the lens from infrared strobing interference originating from its own camera unit. Figure D.3 shows an Oqus camera with strobe part opened to reveal the aperture and focus dials as well as an example screenshot of properly-detected retroreflective markers in the field-of-view of three cameras in QTM.

Figure D.3. Opened Oqus camera revealing aperture and focus dials (left) and video images from three cameras in the QTM main window (right) [215]

The next stage of setup for the Qualisys system involved calibrating and finalizing the camera position and orientation arrangement. The goal of this calibration

procedure is for the processing software to determine the spatial position and orientation of each camera so that detected marker positions can be properly interpreted. First, an L-shaped reference object was placed on the experimentation room floor. This object creates the cartesian global-reference frame for the Qualisys data and consists of two perpendicular axis lines, identified by two markers for the *y*-axis and three markers for the *x*-axis (the *z*-axis is determined by the cross-product of the other two axes. If fewer than two of the cameras could detect all the reference frame markers, it was necessary to adjust the position and/or orientation of the cameras until this requirement was met; otherwise, the calibration processes would be unable to develop the data's reference frame and, ultimately, the calibration would fail.

Next, the Qualisys calibration wand was assembled by screwing the wand head to a handle shaft. On the wand head are two markers attached at a fixed distance from each other. Within the QTM software, the wand head marker distance, accurate to a tenth of a millimeter, was entered into the 'Calibration' menu. This was accessed from the 'Input Devices' and 'Camera System' branches of the 'Project Options' window. As shown in the screenshot of Figure D.4, this step ensured that the software could appropriately process the calibration data and generate accurate MoCap data during subsequent record sessions. The calibrate button was then selected from the QTM main window, and an appropriate calibration session time was designated in a resulting prompt window. A 2-minute calibration session was used here.

Lastly, while the QTM software was recording the calibration session, the calibration wand was moved throughout the intended measurement volume, with efforts to orient the wand parallel to all three of the reference axes at the various positions covered and to focus data point collection at locations where markers would move during MoCap record sessions. After the calibration session was complete, a calibration quality report was generated and shown in the QTM software, either indicating success or prompting the user to redo the calibration session. Since calibration determines camera positions and orientations, the process must be repeated if any camera moves after the calibration is completed. Once the camera arrangement was finalized and calibrated, masks could be applied to any of the camera's views that included erroneous marker detections (e.g., from another camera's strobe lights or reflections from shiny surfaces in the experimentation room).

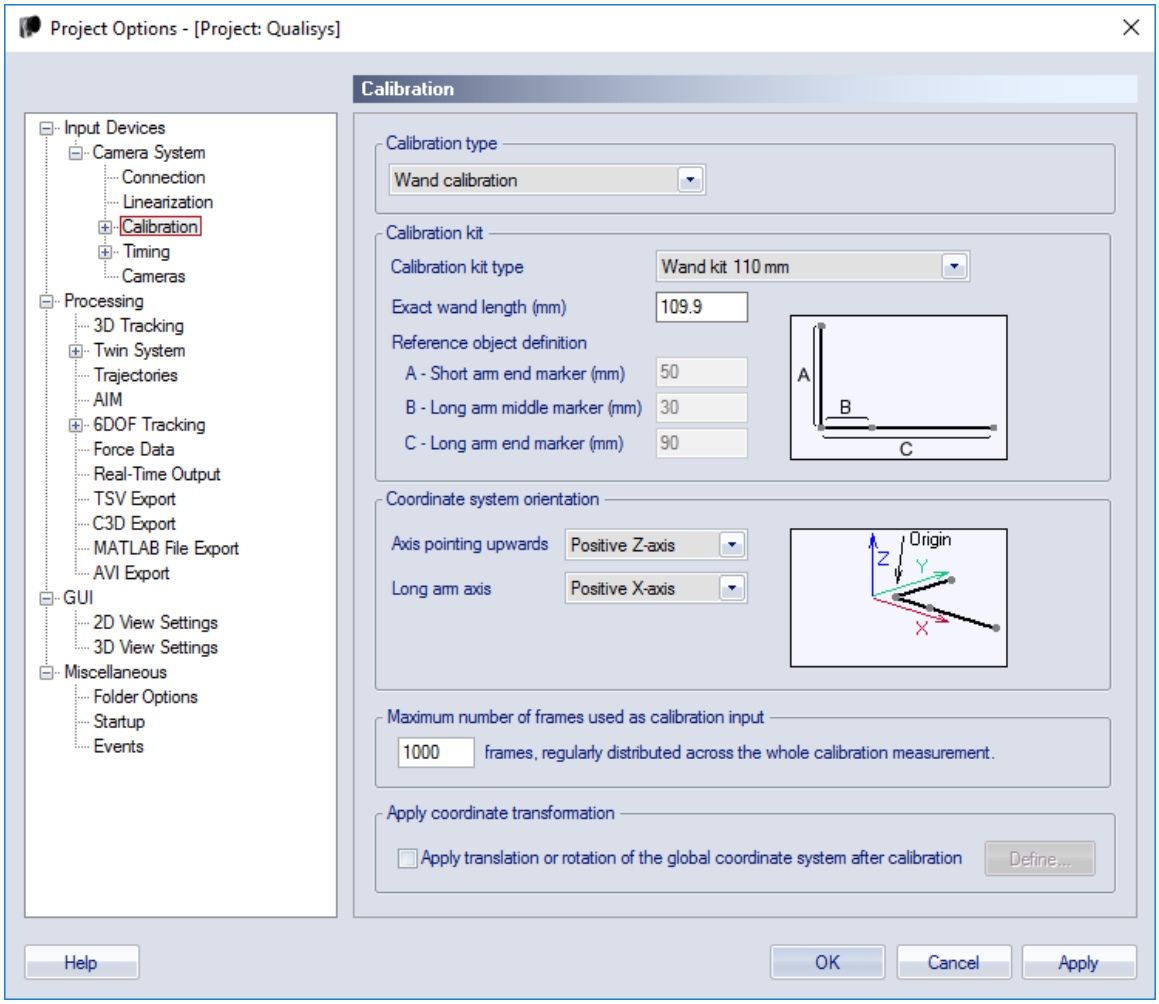

Figure D.4. The QTM 'Calibration' menu displaying the settings used to calibrate the Oqus cameras

The final aspects of the Qualisys system setup involved establishing the data sampling rate, choosing the data export settings, and attaching the markers to the targeted MoCap subject. The first step was accomplished by opening the 'Camera System' menu under the 'Input Devices' branch of the 'Project Options' window. Shown in the screenshot of Figure D.5, the marker capture frequency can be selected from a set of standard values within this menu; as mentioned in Subsection 6.2.1, a sampling frequency of 100Hz was used for the experiments. Next, the 'TSV Export' menu was opened via the 'Processing' branch of the same 'Project Options' window. The most important settings to note are that 3D data was exported (i.e., cartesian coordinates of each detected marker), time data was exported for every frame to help verify the sampling frequency, and unidentified trajectories (discussed in more detail in Appendix E) were excluded from export because they were unnecessary during data processing.

Figure D.6 shows a screenshot of the complete export setting used for the Qualisys system. Finally, the markers, which are made of polystyrene covered with retro-reflective tape, were attached the MoCap subject using marker-specific double-adhesive tape. A description of marker attachments for the main experiment is included in Subsection 6.2.1. Overall, for a user having little experience with Qualisys motion capture, the total system setup time was between one and two hours for each day of experiments.

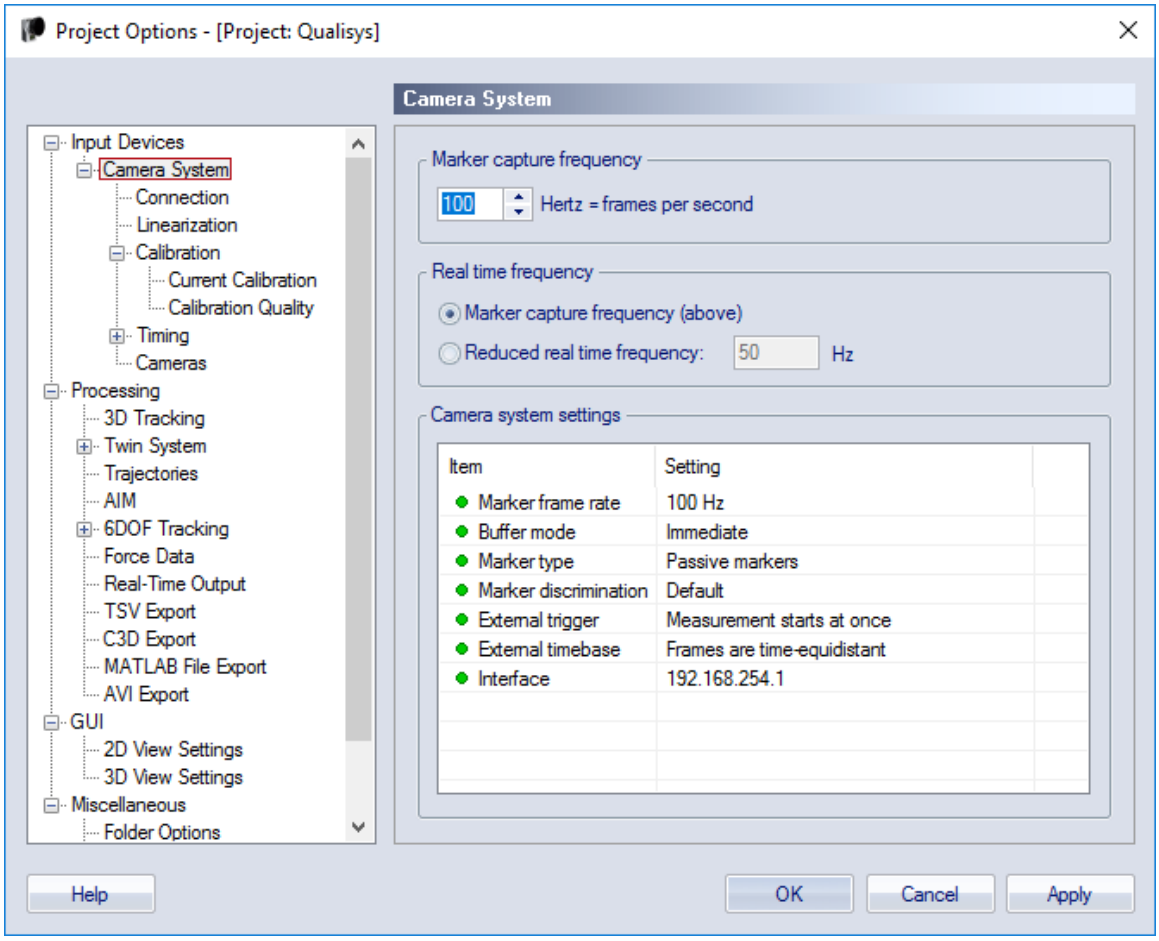

Figure D.5. The QTM 'Camera System' menu with the desired sampling frequency and other settings established

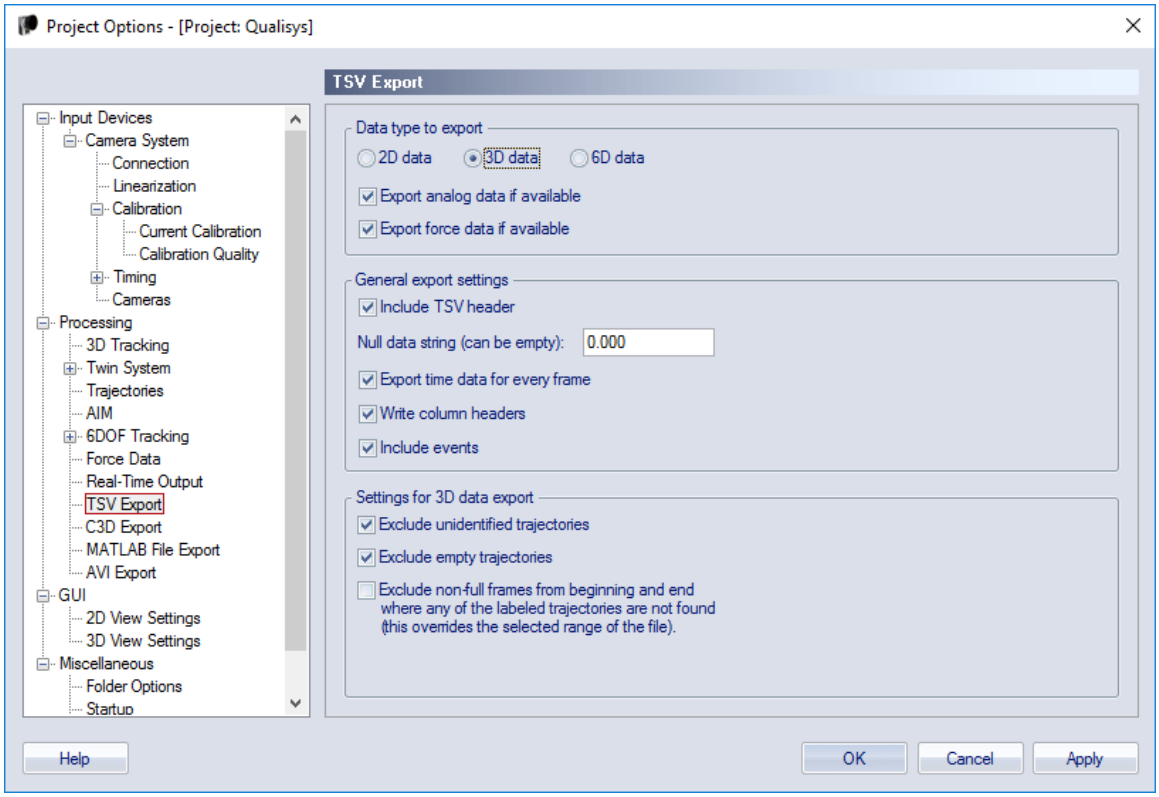

Figure D.6. The QTM 'TSV Export' menu with appropriate data export selections

Xsens System Setup

After launching the Xsens MT Manage program on the experimentation PC, the Awinda station (i.e., the wireless receiver) was connected to the PC via USB cable. Next, the MTw sensors were turned on by pressing the only button on their plastic housing; synchronized LED flashes on each sensor indicated that the sensors were properly synchronized with each other. The 'Scan for Devices' button in the MT Manager software was then selected; if successful, the Awinda receiver station would be listed in the 'Device List' section of MT Manager after the scan. After that, the 'Wireless Configuration' button was pressed, which opened a new window. In that window, the desired sampling rate (i.e., 100Hz) was selected from a dropdown menu adjacent to the detected Awinda station. Next, the 'Enable Wireless Master' button was pressed, which caused each MTw sensor to connect with the wireless receiver and be displayed in the 'MTw's' area of the window. The 'Start Measurement on Wireless Master' button was then pressed and 'Wireless Configuration' window was closed. Figure D.7 shows a screenshot of the MT Manager main window with 'Scan for Devices' and 'Wireless

Configuration' buttons highlighted, and Figure D.8 shows a screenshot of the 'Wireless Configuration' window after four MTw's were connected.

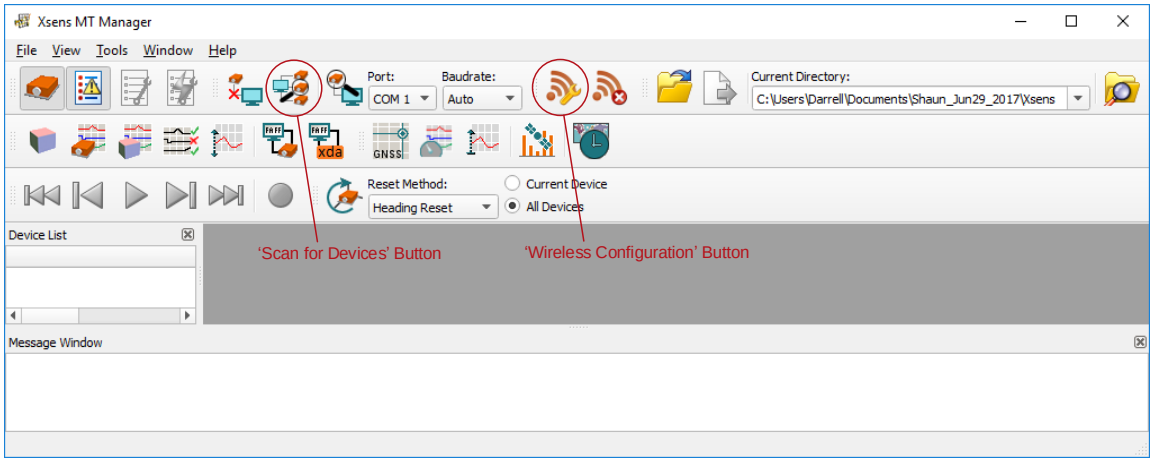

Figure D.7. The Xsens MT Manager main window with 'Scan for Devices' and 'Wireless Configuration' buttons highlighted

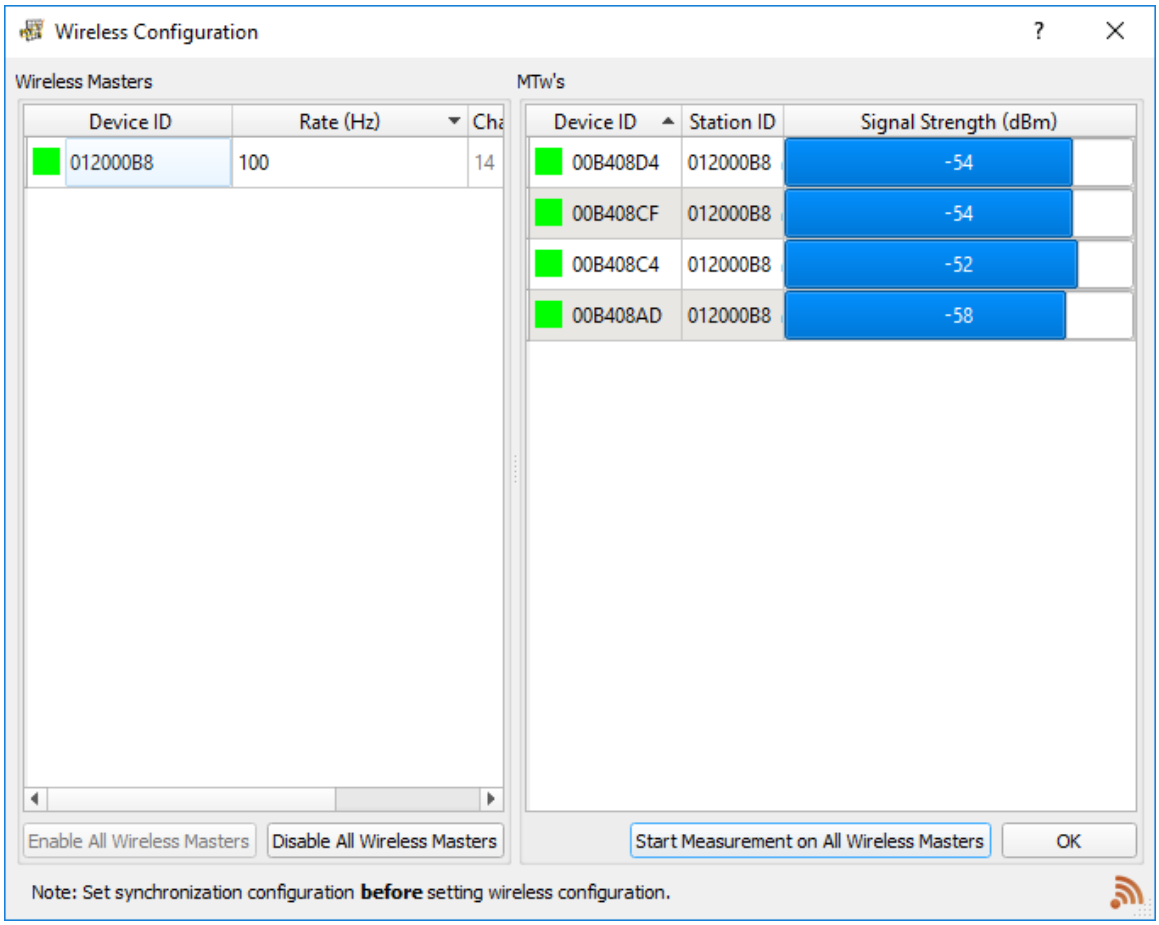

Figure D.8. The 'Wireless Configuration' window used to connect MTw IMU sensors to the receiver station and establish the sampling frequency

Desired data export settings were selected by accessing the 'ASCII Exporter' menu under the 'Exporters' branch of the 'Preferences' window, which was opened via the main window's 'Tools' dropdown list. The only essential data for the present study were the IMUs' orientations, which were exported as rotation matrix elements. Figure D.9 shows the complete export preferences used during the experiments. Comma-separated values file format was chosen for its ease of import into the Matlab workspace and consistency with the exoskeleton prototype's data storage. Finally, the Xsens setup was completed by attaching the hook-fastener face of each MTw to the exoskeleton's loop-fastener straps per the scheme illustrated in Figure 6.9 of Subsection 6.2.1. Overall, the Xsens system's setup time took about 5–10 minutes for an inexperienced user.

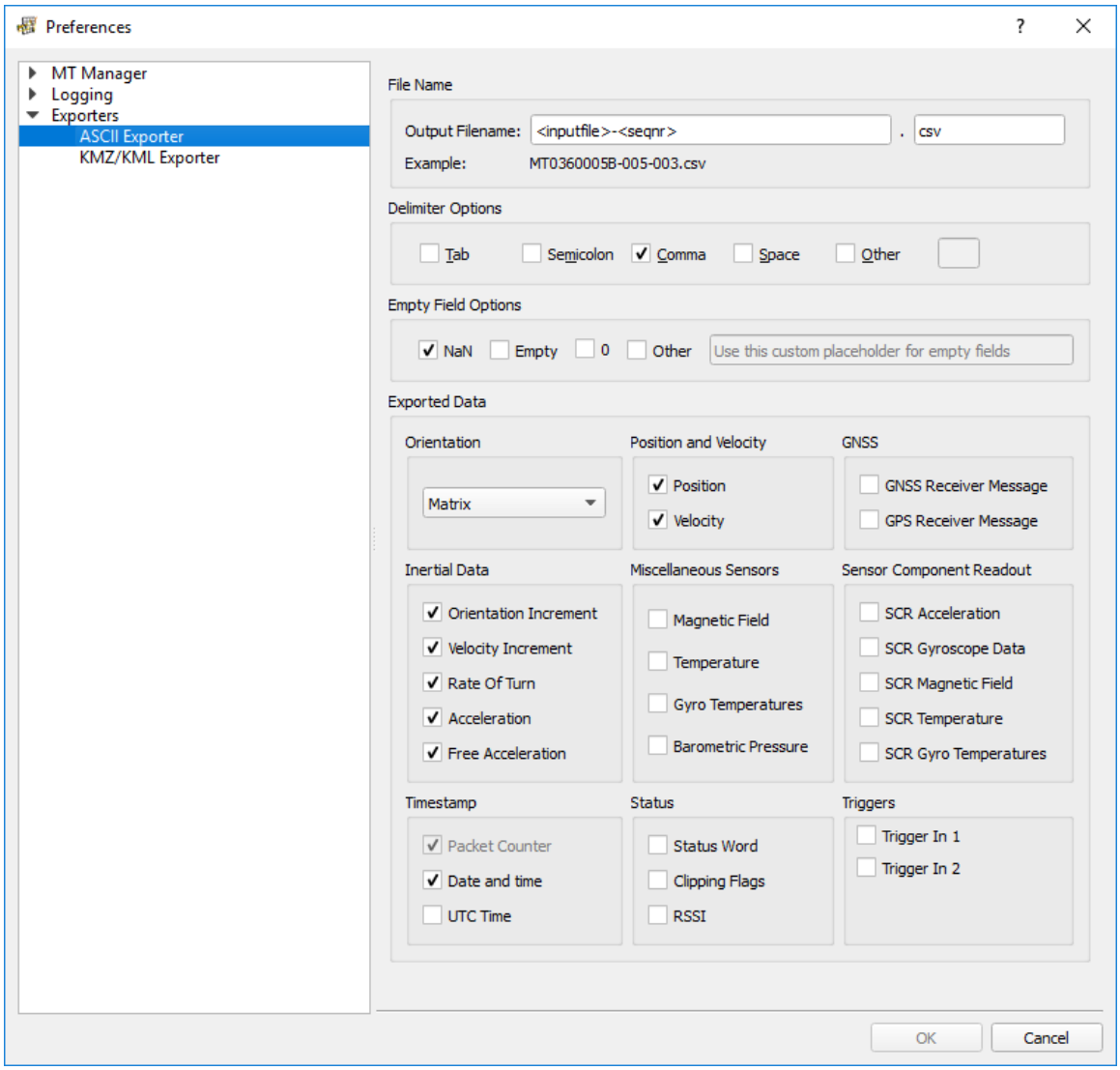

Figure D.9. The 'Preferences' window with export settings for the Xsens system

Appendix E.

Qualisys Data Processing Details and Evidence of Xsens Data Distortion

Qualisys Data Processing

After completing each motion capture trial within the Qualisys Track Manager (QTM) program, the resulting record files were consecutively opened for preliminary data processing. Because the system uses passive markers, each marker trajectory was initially unidentified within the program. Thus, each marker trajectory was manually identified and labelled for each movement trial; Figure E.1 shows an example screenshot of this process, with the identified and labelled marker trajectories in the top-right area, unidentified trajectories in the area below that, and a visualization of the captured data in the central window area. If any marker data was occluded (i.e., positional data missing for one or more time period), it was also necessary to combine data fragments into the same identified trajectory group; ideally, each marker trajectory would be filled to 100%, meaning that the marker's 3D position was successfully measured or interpolated for the entire motion capture session. Finally, any erroneously detected marker trajectories (e.g., originating from the infrared strobes of a camera within the field-of-view of another camera) were moved to the 'Discarded Trajectories' bin in the lower-right area of the QTM window.

Note that several Qualisys MoCap files had to be discarded because data associated with critical movement periods were missing. For the hip-flexion/extension trials, one stand-to-sit/sit-to-stand trial, one walking-gait trial, two left-turn-walking trials, one stair-descent trial, one jumping trial, and all lunge and kneeling trials, trajectory data for at least one of the redundant markers was lost for some period during the record session, but the data was ultimately usable. However, for one walking trial, all running trials, and one jumping trial, more than two marker positions within at least one segment group were lost during action intended for study, so the Qualisys data for these trials were unusable. The most plausible reason for this loss of data was occlusion caused by the subject being unable to hold their arms above the pelvis markers during the movements, especially for the extended mobility tests.

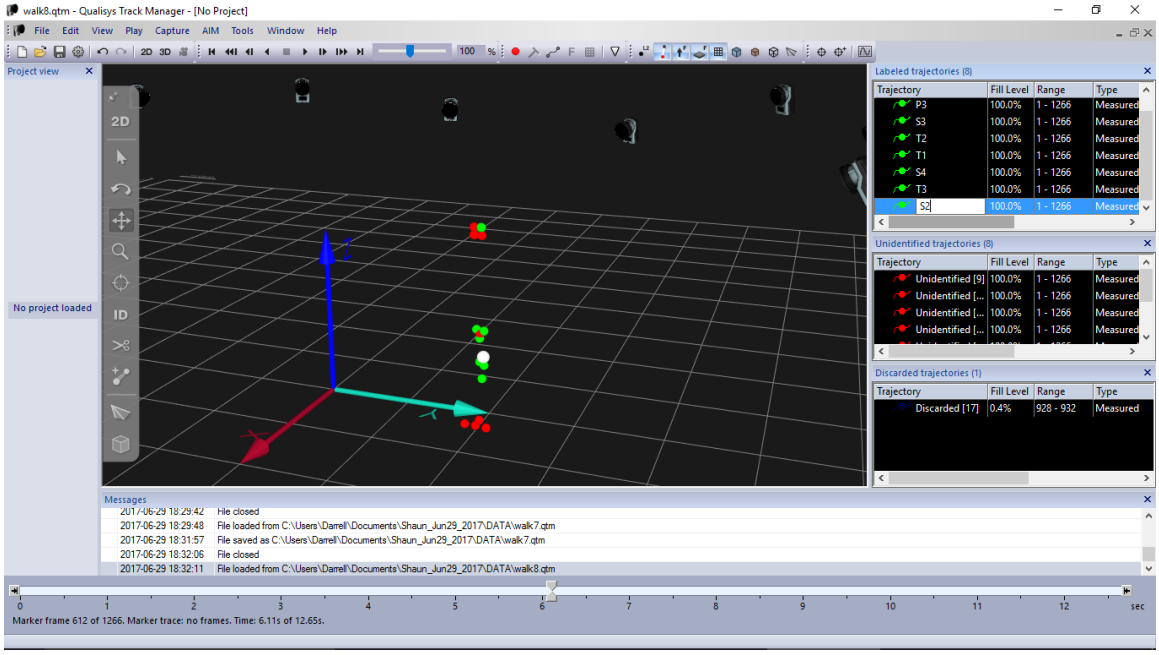

Figure E.1. Qualisys MoCap file illustrating the marker trajectory identification process

After identifying each marker trajectory and confirming that the trajectories were all sufficiently filled to justify further processing, each QTM MoCap file was exported into tab-separated values file format. TSV was chosen for data export format because it included a header row with identified marker trajectory labels. However, the trajectory timelines could not be sorted alphabetically by marker label in the export settings, so ordering was done afterwards using the custom sort feature in Microsoft Excel to facilitate batch processing within Matlab. Once sorted in Excel, the Qualisys data for each trial was saved as comma-separated values (CSV) for consistency with the data obtained from Xsens and the exoskeleton; it was then imported into the Matlab workspace using a Matlab script.

The first processing action performed on the Qualisys data following Matlab import was low-pass filtering the 3D position data of each marker using a two-way, fourth-order Butterworth filter with 40Hz cut-off frequency; these filter parameters were chosen to match those used on marker position data obtained in a similar study of lower-limb walking- and running-gait motions using Qualisys motion capture in [216]. Subsequently, the 3D positional data of the marker clusters on each limb segment were converted into segment orientation data (i.e., in the form of a rotation matrix) using the strategy outlined in [211]. That is, for each limb segment's marker cluster, one marker's

position was chosen as the origin for that segment's orientation frame. Next, the normalized vector from that origin marker position to another marker's position was taken as one of the three axes in the segment's frame. After that, the frame axis normal to the plane of the marker cluster was determined by the normalized cross-product of the first established axis and the vector from the origin position to a third marker's position. Finally, the limb segment's final frame axis was determined by the cross-product of the first two axes. Overall, this orientation-frame development process required three marker positions for each limb segment and guaranteed the mutual orthogonality of the frame axes. Figure E.2 illustrates the marker attachment scheme used for the experiment with labels for each marker; the figure also visualizes the limb segment orientation frames and the specific equations used to develop them from the Qualisys data. As implied by the axis-development equations, the position data associated with redundant markers P3, T4, S1, and F4 were ultimately left unused.

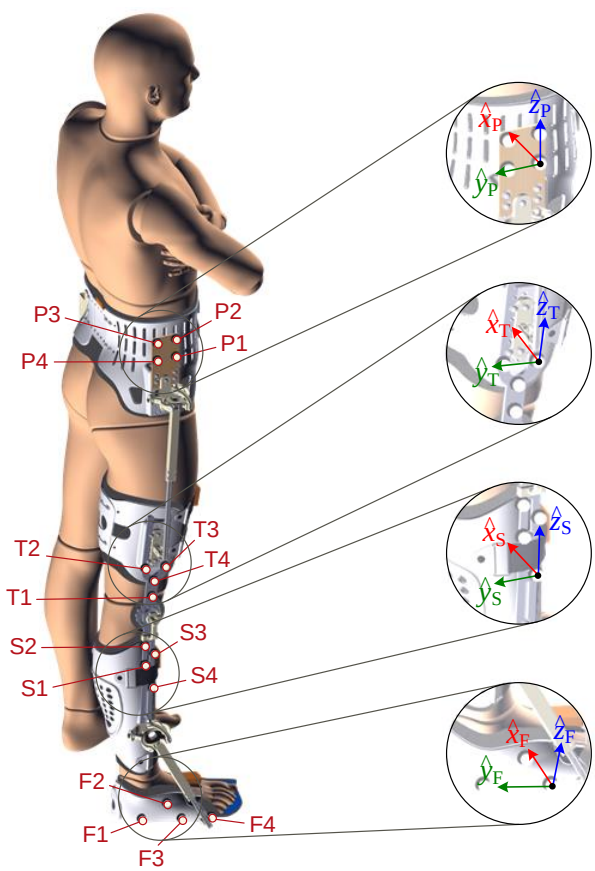

Pelvis Frame Equations:

$$\hat{z}_P = \frac{\overrightarrow{P2}-\overrightarrow{P1}}{\left\|\overrightarrow{P2}-\overrightarrow{P1}\right\|},\ \hat{x}_P = \frac{\left(\overrightarrow{P2}-\overrightarrow{P1}\right)\times\hat{z}_P}{\left\|\left(\overrightarrow{P2}-\overrightarrow{P1}\right)\times\hat{z}_P\right\|},\ \hat{y}_P = \hat{z}_P \times \hat{x}_P$$

Thigh Frame Equations:

$$\hat{y}_T = \frac{\overrightarrow{T2}-\overrightarrow{T3}}{\left\|\overrightarrow{T2}-\overrightarrow{T3}\right\|},\ \hat{x}_T = \frac{\left(\overrightarrow{T1}-\overrightarrow{T3}\right)\times\hat{y}_T}{\left\|\left(\overrightarrow{T1}-\overrightarrow{T3}\right)\times\hat{y}_T\right\|},\ \hat{z}_T = \hat{x}_T \times \hat{y}_T$$

Shank Frame Equations:

$$\hat{z}_S = \frac{\overrightarrow{S3}-\overrightarrow{S4}}{\left\|\overrightarrow{S3}-\overrightarrow{S4}\right\|},\ \hat{x}_S = \frac{\left(\overrightarrow{S2}-\overrightarrow{S3}\right)\times\hat{z}_S}{\left\|\left(\overrightarrow{S2}-\overrightarrow{S3}\right)\times\hat{z}_S\right\|},\ \hat{y}_S = \hat{z}_S \times \hat{x}_S$$

Foot Frame Equations:

$$\hat{y}_F = \frac{\overrightarrow{F1}-\overrightarrow{F3}}{\left\|\overrightarrow{F1}-\overrightarrow{F3}\right\|},\ \hat{x}_F = \frac{\hat{y}_F\times\left(\overrightarrow{F2}-\overrightarrow{F3}\right)}{\left\|\hat{y}_F\times\left(\overrightarrow{F2}-\overrightarrow{F3}\right)\right\|},\ \hat{z}_F = \hat{x}_F \times \hat{y}_F$$

Figure E.2. Marker attachment scheme and processing equations used to develop lower-limb segment frames from the Qualisys marker 3D position data

With a time-trajectory of lower-limb segment orientations derived for the pelvis, thigh, shank, and foot, joint angle trajectories were obtained by representing the inferior segment's orientation with respect to that of the superior segment and then performing inverse kinematics on the resulting rotation matrix. First, however, it was necessary to define a limb posture that would correspond to zero-angle values for each joint DOF. As there is no biomechanical standard for what is considered a zero-value joint angle, a common practice is to measure joint angles relative to a neutral-standing posture. Thus, for each movement trial, a sample set corresponding to neutral-standing posture was identified, and the orientation frames for each limb segment in this posture were saved. Note that the same time-synchronized sample was used to formulate the neutral-standing orientations for the exoskeleton-based measurements. The relative orientations between superior and inferior limb segments surrounding each joint were then determined with respect to the zeroed-angle orientation as follows:

$$ {}^{P}_{T}\mathbf{R}(t) = {}^{P}_{Ref}\mathbf{R}(t)\,{}^{Ref}_{T}\mathbf{R}(t)\left({}^{P}_{Ref}\mathbf{R}(t=t_{\mathrm{SP}})\,{}^{Ref}_{T}\mathbf{R}(t=t_{\mathrm{SP}})\right)^{\mathrm{T}} \tag{E.1} $$

$$ {}^{T}_{S}\mathbf{R}(t) = {}^{T}_{Ref}\mathbf{R}(t)\,{}^{Ref}_{S}\mathbf{R}(t)\left({}^{T}_{Ref}\mathbf{R}(t=t_{\mathrm{SP}})\,{}^{Ref}_{S}\mathbf{R}(t=t_{\mathrm{SP}})\right)^{\mathrm{T}} \tag{E.2} $$

$$ {}^{S}_{F}\mathbf{R}(t) = {}^{S}_{Ref}\mathbf{R}(t)\,{}^{Ref}_{F}\mathbf{R}(t)\left({}^{S}_{Ref}\mathbf{R}(t=t_{\mathrm{SP}})\,{}^{Ref}_{F}\mathbf{R}(t=t_{\mathrm{SP}})\right)^{\mathrm{T}} \tag{E.3} $$

where 'P', 'T', 'S', and 'F' respectively denote the pelvis, thigh, shank, and foot, and t_{SP} designates the sample time associated with standing posture. Variable t denotes time and 'Ref' indicates the Qualisys lab-room reference frame established during camera calibration, as described in Appendix D. Hereafter, the time-dependence of each orientation is implied. Also, the rotation matrices on the right side of each Equation (E.1)–(E.3) are obtained from the frame axes derived in Figure E.2 as:

$$ \begin{gathered} {}^{Ref}_{P}\mathbf{R} = \begin{bmatrix}\hat{x}_{\mathrm{P}} & \hat{y}_{\mathrm{P}} & \hat{z}_{\mathrm{P}}\end{bmatrix},\ {}^{Ref}_{T}\mathbf{R} = \begin{bmatrix}\hat{x}_{\mathrm{T}} & \hat{y}_{\mathrm{T}} & \hat{z}_{\mathrm{T}}\end{bmatrix},\ {}^{Ref}_{S}\mathbf{R} = \begin{bmatrix}\hat{x}_{\mathrm{S}} & \hat{y}_{\mathrm{S}} & \hat{z}_{\mathrm{S}}\end{bmatrix}, \\ {}^{Ref}_{F}\mathbf{R} = \begin{bmatrix}\hat{x}_{F} & \hat{y}_{F} & \hat{z}_{F}\end{bmatrix},\ \text{and}\ {}^{B}_{A}\mathbf{R} = \left({}^{A}_{B}\mathbf{R}\right)^{\mathrm{T}} \end{gathered} \tag{E.4} $$

Note that a right-side superscript 'T' denotes the matrix transpose operation, not to be confused with a left-side superscript or subscript 'T' that denotes 'thigh'. Finally, the joint angles are obtained using inverse kinematics:

$$ \begin{gathered} \theta_{y,Hip} = \operatorname{atan2}\left(-{}^{P}_{T}r_{31}, \sqrt{{}^{P}_{T}r_{11}{}^{2} + {}^{P}_{T}r_{21}{}^{2}}\right),\ \theta_{z,Hip} = \operatorname{atan2}\left(\frac{{}^{P}_{T}r_{21}}{\cos\left(\theta_{y,Hip}\right)}, \frac{{}^{P}_{T}r_{11}}{\cos\left(\theta_{y,Hip}\right)}\right),\ \text{and} \\ \theta_{x,Hip} = \operatorname{atan2}\left(\frac{{}^{P}_{T}r_{32}}{\cos\left(\theta_{y,Hip}\right)}, \frac{{}^{P}_{T}r_{33}}{\cos\left(\theta_{y,Hip}\right)}\right) \end{gathered} \tag{E.5} $$

$$\theta_{x,Knee} = \text{atan2}\left(\frac{{}^{T}_{S}r_{32}}{\cos\left(\theta_{y,Knee}\right)}, \frac{{}^{T}_{S}r_{33}}{\cos\left(\theta_{y,Knee}\right)} \right) \tag{E.6}$$

$$\theta_{y,Ankle} = \text{atan2}\left(-{}^{S}_{F}r_{31}, \sqrt{{}^{S}_{F}r_{11}{}^{2} + {}^{S}_{F}r_{21}{}^{2}} \right),\ \theta_{z,Ankle} = \text{atan2}\left(\frac{{}^{S}_{F}r_{21}}{\cos\left(\theta_{y,Ankle}\right)}, \frac{{}^{S}_{F}r_{11}}{\cos\left(\theta_{y,Ankle}\right)} \right),$$
$$\text{and } \theta_{x,Ankle} = \text{atan2}\left(\frac{{}^{S}_{F}r_{32}}{\cos\left(\theta_{y,Ankle}\right)}, \frac{{}^{S}_{F}r_{33}}{\cos\left(\theta_{y,Ankle}\right)} \right) \tag{E.7}$$

where ${}^{A}_{B}r_{ij}$ denotes the ith-row, j^{th}-column element of the ${}^{A}_{B}\mathbf{R}$ rotation matrix. Note that the angles provided by Equations (E.5)–(E.7) assume the conventional Tait-Bryan roll-pitch-yaw order of rotations. Note that the axis directions used here are consistent with those in Chapter 5 in relation to the human body; Table E.1 outlines the correspondence between Equation (E.5)–(E.7) angles and the anatomical motions of the human leg.

Table E.1. Correlation between Qualysis marker-derived joint rotations and anatomical motions for the human right-side lower limb

	Hip			*Knee*	*Ankle*		
Model Joint Rotation:	$+\theta_{z,Hip}$	$+\theta_{y,Hip}$	$+\theta_{x,Hip}$	$+\theta_{x,Knee}$	$+\theta_{z,Ankle}$	$+\theta_{y,Ankle}$	$+\theta_{x,Ankle}$
Anatomical Motion:	Int. Rot.	Abd.	Ext.	Flex.	Add.	Pro.	Pla.
Model Joint Rotation:	$-\theta_{z,Hip}$	$-\theta_{y,Hip}$	$-\theta_{x,Hip}$	$-\theta_{x,Knee}$	$-\theta_{z,Ankle}$	$-\theta_{y,Ankle}$	$-\theta_{x,Ankle}$
Anatomical Motion:	Ext. Rot.	Add.	Flex.	Ext.	Abd.	Sup.	Dor.

Note: The anatomical motion abbreviations are clarified in the List of Acronyms.

After the biological joint angles were computed from the Qualisys data, a fourth-order two-way low-pass Butterworth filter with 10Hz cut-off frequency was applied to the Qualisys-derived angle trajectories to remove any noise from the developed signals. The properties of the filter were selected based on those recommended in [217] for running gait motion studies with Qualisys optical MoCap system; they are also consistent with the filter used on the exoskeleton-captured data. Finally, it was necessary to identify the synchronization time (i.e., corresponding to an initial peak in knee flexion). In Matlab, this was accomplished by applying the 'findpeaks' function to the knee flexion angle for each processed motion trial, with a minimum peak-height of interest set to 80 degrees. The first local maximum in the knee flexion trajectory that met this requirement was taken as the synchronization identifier, and the sample time corresponding to this point was saved for each MoCap data set. Later, the same identifier would be located in the data sets obtained from the other MoCap systems to synchronize the sample times (i.e., sample time $t = 0$ is set at the synchronization point).

Xsens Data Processing Attempts and Evidence of Distortion

Dissimilar to the exoskeleton MoCap results, the Xsens data did not demonstrate a close convergence of detected lower-limb joint motions with the processed Qualisys results. The subsections below outline preliminary processing steps for the Xsens data, three approaches taken in attempts to extract sensical results from the collected Xsens data, and then an explanation of the discovered root problem. First, however, it is important to discuss a critical aspect of the data processing procedure for this experimental study. In theory, for the three motion capture systems to measure the same motions at each joint of the lower limb, the frame attached to the joint's superior segment (i.e., the reference frame for that joint's orientation) must have the same physical alignment with the user's body for each MoCap system.

For the Qualisys and exoskeleton systems, this alignment was achieved by placing the Qualisys marker clusters on the same (or parallel) orthotic surfaces as the base linkages of the exoskeleton modules. Therefore, within the limits of measurement uncertainties, the segment frames for these systems would share a common axis normal to that orthotic surface and any rotation within that surface could be eliminated by placing the markers along lines parallel to exoskeleton-attachment edges. As a result, frame alignment was rather straightforward between the Qualisys and exoskeleton systems. However, per the Xsens MTw attachment method (i.e., hook-and-loop fastener) and the effort to distance the sensors from possible sources of magnetic interference, the MTw's were attached to orthotic straps that did not share a common or parallel plane with the Qualisys marker attachments. Thus, the main task associated with the Xsens data processing was to achieve frame alignment with the other MoCap systems at each limb segment superior to a joint. In turn, the inferior segment frame alignment would be handled by the zeroing constant-offset rotation associated with standing posture.

As mentioned in Subsection 6.2.1, the Xsens system was prone to missing data packets. To complicate matters, the data from the four MTw sensors were exported independently of each other and experienced missing data at different sampling instances. Ultimately, the missing data was dealt with in three stages: beginning of data, within a sample set, and end of data. To start, differences in first-sample start time between the sensors were computed for each record session, if applicable, to determine

a common start time for the set of sensors. Once a common start time was identified for each trial, any sensor data exported before this time was removed from the data set (i.e., if one or more sensor experienced dropped data packets at the beginning of a record session).

Next, each sensor's data set was scanned for times between samples exceeding the sampling rate, which would indicate missing data packets within the sample set. Whenever these missing sections of data were detected, they were filled with not a number (NaN) values. Ideally, a more sophisticated interpolation procedure would have been used to fill the missing data with best approximations for their actual values; however, this process would have ultimately been ineffectual given the unforeseen problems with the Xsens data.

Lastly, if any sensor dropped packets at the end of a record session, effectively finishing sooner than the other sensors, the data from other sensors exceeding the earliest finish time were truncated to ensure each sensor had a common end time for a given record session. In the end, this preprocessing procedure ensured that the four sensors had equal-length and time-synchronized data sets for each record session, which greatly simplified further processing procedures. The inter-system synchronization identifier was also located within the Xsens data at this point using the same method as described for the Qualisys results. Although the Xsens frames did not initially align with biological frames, the synchronizing knee action could still be identified as a spike in the knee angles derived from the raw Xsens data for the thigh and shank.

Xsens Frame Alignment Processing: Approach #1

The first approach for processing the Xsens data involved applying constant frame rotations to each measured MTw sensor frame. As mentioned in Appendix D, the data exported from the MTw sensors had the form of rotation matrix elements. These rotation matrices corresponded to the coordinate frames attached to the sensor, which are given in the Xsens user manual [218] and illustrated on the left side of Figure E.3. By approximating an appropriate set of constant rotations to apply to the MTw sensor frames, the resulting frames would approximately match the orientations of Qualisys frames developed at each limb segment. Figure E.3 illustrates the raw frame orientations upon data export, the proposed correction rotations by which to post-multiply the raw

frames for each limb segment, and the resulting reoriented MTw frames that approximately match the Qualisys limb segment frames.

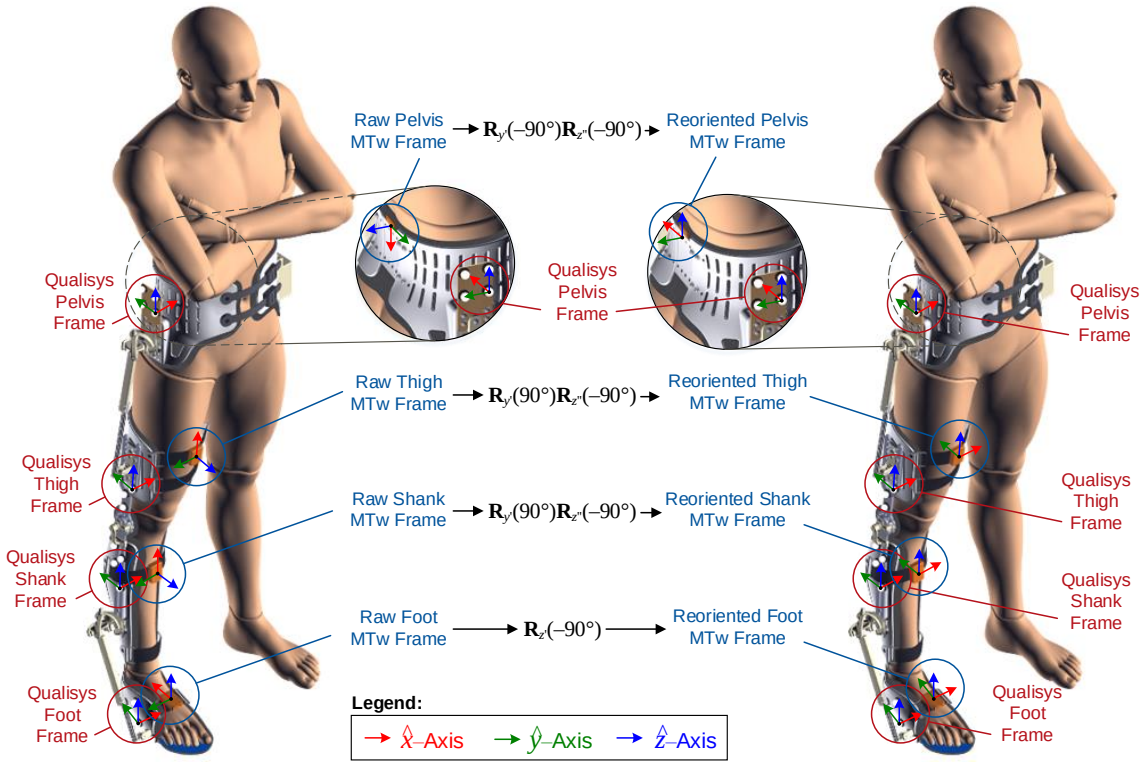

Figure E.3. Illustration of raw MTw frame conventions and first method for attempted alignment between Xsens and Qualisys frames

After completing the reorientation procedure for the MTw frames, the results were checked against those of the Qualisys and exoskeleton systems for preliminary verification. As shown in the example results of Figure E.4, which correspond to one walking gait cycle, all three systems tend to track the same trajectory trend at each joint for the sagittal plane motions (i.e., flexion/extension angles on the right side of the figure). However, the Xsens-detected motions in the other two planes do not tend to follow the same trend as the those measured with the other two systems. At this point in the data processing progression, the discrepancy of Xsens results was assumed to be caused by insufficient alignment of the MTw frames with the Qualisys frames. Thus, a more involved approach to achieve frame alignment was attempted, as outlined in the next subsection. Note that the Qualisys and Xsens results in Figure E.4 include 3-DOF rotations at the knee, which arise in general due to inexact frame alignments between thigh and shank sensors; the exoskeleton system is incapable of detecting these misalignment motions due to its single-DOF sensing at that joint. Moreover, note that the

line breaks visible in the Xsens data of the figure is the result of the dropped data-packets issue.

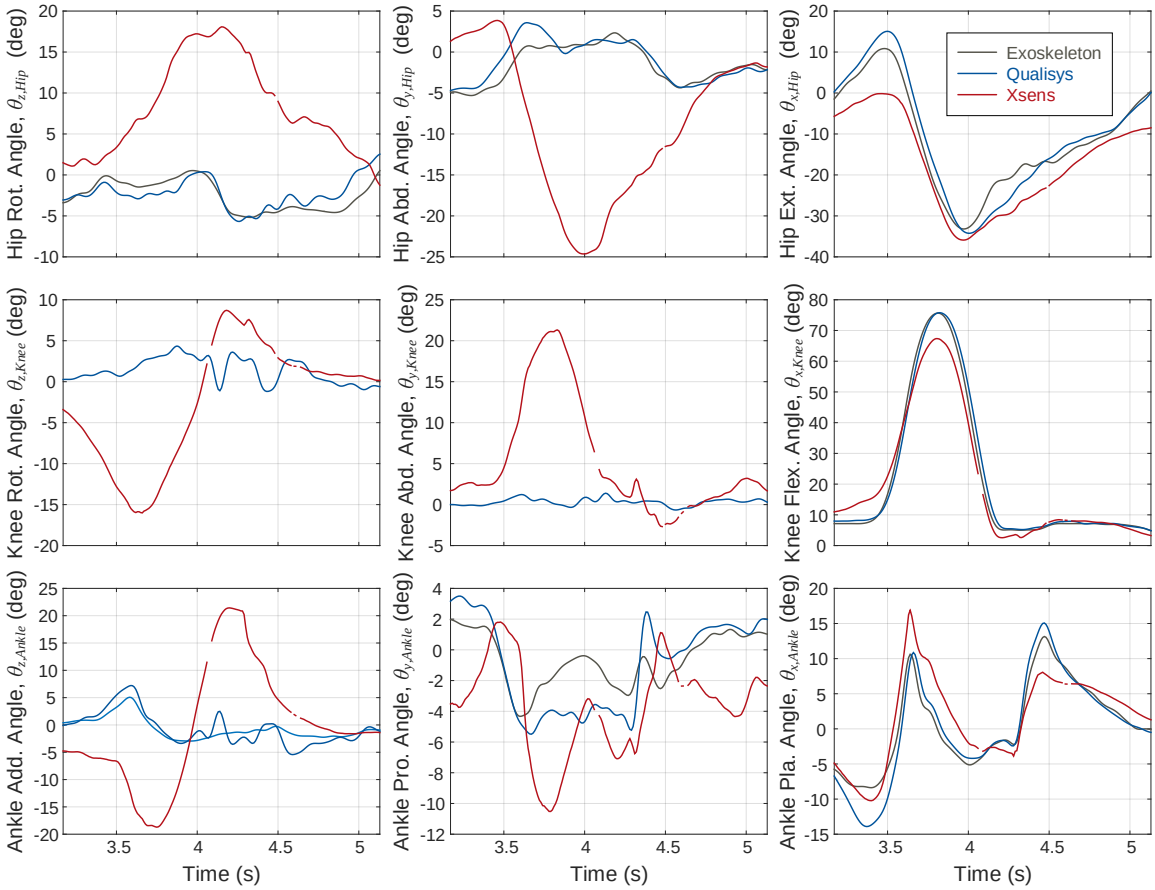

Figure E.4. Preliminary comparision of exoskeleton, Qualisys, and Xsens MoCap results from one cycle of normal walking gait

Xsens Frame Alignment Processing: Approach #2

The second approach to align the Xsens MTw frames with the Qualisys system frames was intended to fine-tune the alignment achieved by the first approach. As shown in Figure E.5, there were two types of constant but unknown rotations that related the Xsens frames with the Qualisys frames in theory: one constant rotation between the two systems' reference frames and another between each MTw frame and corresponding Qualisys limb segment frame (i.e., one constant rotation for each of the pelvis, thigh, shank, and foot). This holds true if the MTw sensors and Qualisys markers remain rigid in their attachment to the MoCap subject, and if magnetic disturbances do

not interfere with the MTw sensors. In such a case, for any given synchronized sample instant, the following relationship should exist:

$$\underbrace{{}^{Q_{Ref}}_{Q_{Seg}}\mathbf{R}}_{\substack{\text{measured}\\ \text{(Qualisys)}}} = \underbrace{{}^{Q_{Ref}}_{X_{Ref}}\mathbf{R}}_{\substack{\text{unknown}\\ \text{constant}}} \underbrace{{}^{X_{Ref}}_{X_{Seg}}\mathbf{R}}_{\substack{\text{measured}\\ \text{(Xsens)}}} \underbrace{{}^{X_{Seg}}_{Q_{Seg}}\mathbf{R}}_{\substack{\text{unknown}\\ \text{constant}}} \tag{E.8}$$

where a 'Ref' subscript denotes the system reference frame and 'Seg' subscript denotes the frame attached to a generalized lower-limb segment. Now, according to the Xsens user manual [218], the reference frame for each MTw is vertically upwards and magnetic north for the *z*- and *x*-axes, respectively; recall that the Qualisys reference frame was developed using the L-shaped reference piece, which produced a vertically upwards oriented *z*-axis as well, assuming the experimentation room floor is well leveled. Thus, the ${}^{Q_{Ref}}_{X_{Ref}}\mathbf{R}$ rotation matrix from Equation (E.8) should only consist of a rotation about the *z*-axis and possibly a small tilt rotation from the vertical. Consequentially, an exhaustive search based on these constraints is exponentially less computationally expensive than a truly exhaustive search involving 360 degrees for three independent rotations between the two reference frames.

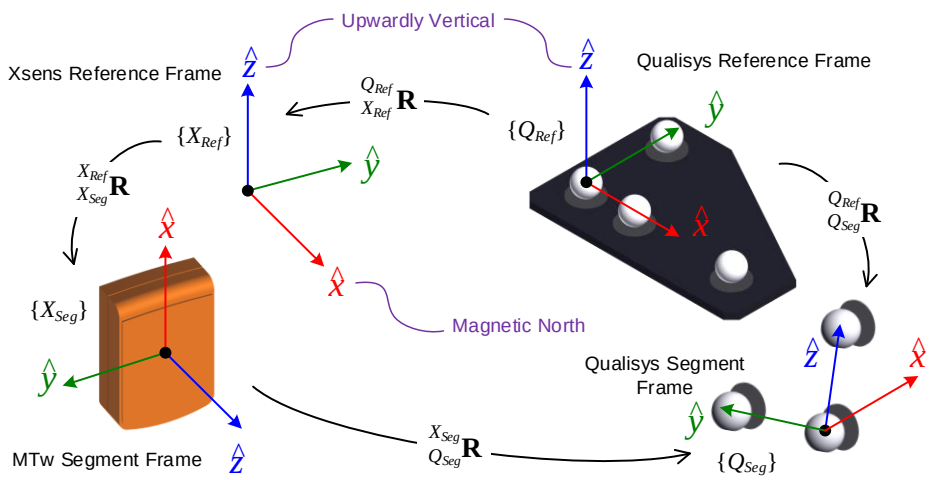

Figure E.5. Illustration of the Qualisys and Xsens system frames and the unknown, but constant, rotations between them

Per this realization, the ${}^{X_{Ref}}_{Q_{Ref}}\mathbf{R}$ rotation of Equation (E.8) was isolated:

$$\underbrace{{}^{X_{Seg}}_{Q_{Seg}}\mathbf{R}^{\mathrm{T}}}_{\substack{\text{unknown}\\ \text{constant}}} = \underbrace{{}^{Q_{Ref}}_{Q_{Seg}}\mathbf{R}^{\mathrm{T}}}_{\substack{\text{measured}\\ \text{(Qualisys)}}} \underbrace{{}^{Q_{Ref}}_{X_{Ref}}\mathbf{R}}_{\substack{\text{unknown}\\ \text{constant}}} \underbrace{{}^{X_{Ref}}_{X_{Seg}}\mathbf{R}}_{\substack{\text{measured}\\ \text{(Xsens)}}} \tag{E.9}$$

Next, two different samples within the Xsens data set were selected that corresponded to two different bodily postures of the MoCap subject and two different rotation matrices for each of ${}^{Q_{Ref}}_{Q_{Seg}}\mathbf{R}$ and ${}^{X_{Ref}}_{X_{Seg}}\mathbf{R}$, taken from the Qualisys and Xsens data, respectively. With

these matrices established, a search for the correct constant ${}^{Q_{Ref}}_{X_{Ref}}\mathbf{R}$ matrix was conducted in MATLAB; the criterion for success in this search was the production of two identical ${}^{X_{Seg}}_{Q_{Seg}}\mathbf{R}$ matrices from Equation (E.9) for a given ${}^{Q_{Ref}}_{X_{Ref}}\mathbf{R}$ guess and either pairing of ${}^{Q_{Ref}}_{Q_{Seg}}\mathbf{R}$ and ${}^{X_{Ref}}_{X_{Seg}}\mathbf{R}$ (i.e., for the two different postures considered). Knowing that the *z*-axes of the two systems' reference frames were parallel or nearly parallel, the search for ${}^{Q_{Ref}}_{X_{Ref}}\mathbf{R}$ was based on a 0–360 degree sweep in *z*-axes rotation with 0.1 degree incrementations, along with –1 degree to +1 degree search in both *x*- and *y*-axis rotations using a 0.5 degree incrementation. Figure E.6 shows the differences in roll-pitch-yaw rotation angles extracted from the two ${}^{X_{Seg}}_{Q_{Seg}}\mathbf{R}$ matrices for each considered ${}^{Q_{Ref}}_{X_{Ref}}\mathbf{R}$ matrix associated with one session of the hip flexion/extension movement study. As seen in the plot, there was no ${}^{Q_{Ref}}_{X_{Ref}}\mathbf{R}$ identified that would cause the two postures' ${}^{X_{Seg}}_{Q_{Seg}}\mathbf{R}$ matrices to be equal, because there is no point at which the roll-pitch-yaw angle differences are all zero. Results from other MoCap sessions produced the same lack of a correct solution. This provides evidence that one or both conditions for Equation (E.9) to be true were not achieved. These conditions are sensor-subject attachment rigidity and absence of magnetic interference. Note that the lines of Figure E.6 seem to have variable thicknesses, but this impression is the result of angle difference fluctuations due to the various levels of angle sweeps performed in the search code.

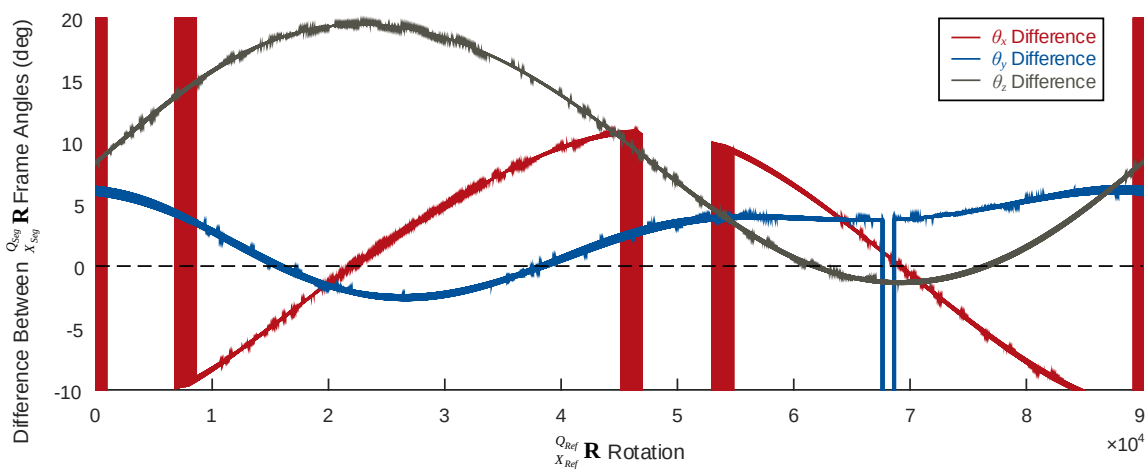

Figure E.6. ${}^{X_{Seg}}_{Q_{Seg}}\mathbf{R}$ angle differences between two subject postures versus ${}^{Q_{Ref}}_{X_{Ref}}\mathbf{R}$ search condition for the Qualisys and Xsens systems

Note: A point at which all lines intersect with the horizontal zero line would indicate an appropriate solution.

Xsens Frame Alignment Processing: Approach #3

The final approach for processing the Xsens MoCap data focused on the known motion restrictions that occurred at the knee joint. When the experiment's subject wore the exoskeleton system, the hinging knee brace component mechanically constrained the knee joint motions to a single plane. Therefore, the shank MTw sensor frame should experience the same motion restriction with respect to the thigh MTw sensor frame and only rotate in some oblique plane within the thigh-frame space. Upon identifying this plane, alignment of all limb segment frames would only involve searching for the appropriate rotation in that plane; at the pelvis, this holds true because the standing posture calibration procedure could be carried out on the pelvis frame with respect to the thigh frame instead of vice versa.

However, this plan for Xsens frame alignment was never completed because, upon visualizing the shank MTw's motion with respect to that of the thigh, the root problem associated with the Xsens data was uncovered. Figure E.7 shows the trajectory of a [1 1 1] vector in shank sensor's coordinate frame with respect to the thigh sensor's frame (i.e., when the origins of the two frames are coincident). The corresponding subject movements are the knee-flexion synchronizing action of several motion capture trials, which are clarified in the figure. If the Xsens data was accurate, the entire shank frame would rotate within a single plane of the thigh frame, so any point within the shank frame would also move parallel to that plane; the corresponding results obtained from the Qualisys data, as shown in the lower row of Figure E.7, illustrates this expected planar movement behavior. However, the Xsens results from the figure depict non-planar motions that tend to distort with varying intensity at different angles within the knee flexion/extension movement. Note that the trajectory color turns from blue to red as the knee flexion and re-extension action progresses (i.e., blue indicates the beginning of the action and red indicates the end).

The distortion from planar movements observed from the Xsens data in Figure E.7 is characteristic of magnetic interference on the MTw sensors, likely originating from the various ferromagnetic components of the exoskeleton or experimentation room. The increase and decrease in distortion at different angles of the knee can be explained by the corresponding fluctuation in distance between the shank and thigh sensors with magnetic components attached to the opposing limb segment or beneath the lab-room

floor. In fact, the presence of magnetic interference explains the failures of the previous two Xsens data-processing approaches as well. For Approach #2, a correct solution could only be found if the MTw sensors all had a consistent reference frame. However, in the presence of magnetic interference, the sensors cannot accurately detect magnetic north, causing inconsistent and time-fluctuating reference frames that would require a variable ${}^{Q_{Ref}}_{X_{Ref}}\mathbf{R}$ rotation matrix and, thereby, disqualify that strategy. In the results of Approach #1, the motions captured by the Xsens data followed a trend consistent with the Qualisys results for sagittal plane motions, but not for the motions in coronal or transverse planes. This is because the original *z*-axis of each MTw sensor was placed within the sagittal plane (see the left side of Figure E.3), and this axis does not depend on magnetometer data (i.e., it is developed with reference to the gravitational field [218]). However, the *x*-axis and, consequentially, the *y*-axis of each MTw is based on the accurate detection of magnetic north, which is prevented by magnetic interference. Therefore, the unaffected *z*-axis allowed accurate tracking of sagittal plane motions, but the corrupted *x*- and *y*-axes caused nonsensical results for coronal and transverse plane motions.

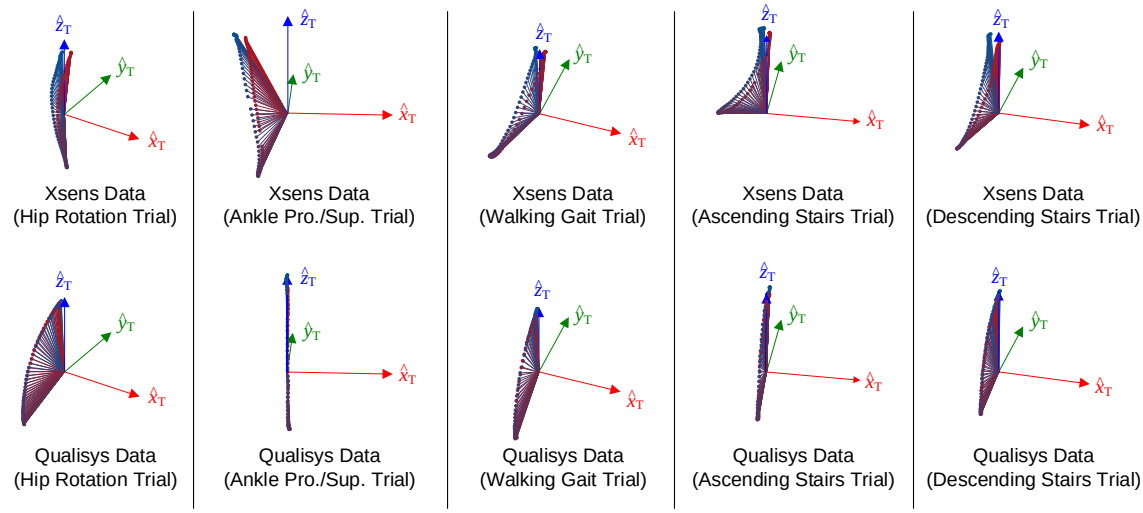

Figure E.7. Trajectory of a point in the shank frame with respect to the thigh frame from Xsens data (top) and Qualisys data (bottom) during knee flexing and extending action for various MoCap trials

Ultimately, despite the efforts to eliminate magnetic interference to the MTw sensors (i.e., placing them as far as possible from metallic components within the limits of their hook-and-loop-based attachment method), the above evidence strongly indicates the presence of magnetic interference in data obtained from the Xsens system. As a result, the motions detected by this system do not track those measured by the Qualisys

reference system to the same high-level of accuracy that is possible when magnetic interferences are not present in the experimental setting or apparatus. Therefore, the Xsens data is excluded from the presentation of final results in Chapter 6 and Appendix F. If it was imperative to the experiment that uncorrupted Xsens data be obtained, the exoskeleton system should have been rebuilt with minimal ferromagnetic materials and magnetic shielding for unavoidable instances, and then the experiment would be redone in a ferromagnetic-free environment. However, the Qualisys system was intended as the main reference system for the MoCap results due to its status as the gold standard in MoCap technology. Thus, the absence of Xsens data in the final results does not affect the overarching goal of the experiment. Moreover, comparative studies between the Xsens and Qualisys systems have been performed in prior research studies [212], [213], which show that the Xsens system can produce joint-angle measurements within 2–5 degrees root mean square error of the Qualisys system, depending on the limb segment analyzed and movement performed and in controlled experimental settings.

Appendix F.

Experimental Result Plots for Protocolary Movements Excluded from the Thesis Body

Figures F.1–F.9 provide the joint angle trajectory plots, angular error box plots, and, where available, photograph sequences for the movements from the experimental protocol that were not included in Chapter 6. Some noteworthy characteristics in the plots include the observable increases in error when the hip is flexed to a great extent in the hip flexion/extension, standing-to-sitting/sitting-to-standing, squatting, walking lunge, and left-leg-kneeling trials (see Figures F.1, F.7–F.9). The hip exoskeleton's approach towards a singular configuration is the primary cause (see Subsection 6.2.4). The bending-at-the-waist trial does not display such a localized error spike, likely because it involves a lesser magnitude of peak hip flexion.

Next, the left turning, descending stairs, standing-to-sitting, and left-leg kneeling results all display various ankle measurement errors that are notably larger than average. Considering the former two trials, a possible cause for these errors is the foot orthotic moving with respect to the subject's foot, especially at the heel. This would have a greater impact on the Qualisys measurement accuracy than that of the exoskeleton, because the exoskeleton's attachment to the foot orthotic involves a passive joint in the sagittal plane of the foot and its rotations do not affect the exoskeleton's measurements. Although the orthotic was meant to be attached rigidly to the body segment without interfering with the ankle joint's movements, the limited surface area of the foot made this task difficult in practice. Evidence supporting this possibility is that the error tends to be greatest during periods of large dorsiflexion, for which the articular and ground reaction forces would act to move the heel away from the foot orthotic. The Qualisys foot measurements for the descending-stairs trial may have also been degraded by occlusions caused by the frame of the portable stairs and subsequent data interpolation by the Qualisys Track Manager (QTM) software. As for the left-leg-kneeling trial, the erroneous spike in the Qualisys' ankle adduction/abduction measurement just prior to the 28-second mark is likely caused by missing data and inappropriate interpolation by the QTM software.

Finally, in the right-leg-kneeling trial of Figure F.9, the Qualisys system detects an extended hip angle (i.e., positive value) for most of the movement's duration whereas the exoskeleton measures a flexed hip angle (i.e., negative value). However, considering the joint trajectories within the 10–12 second span of that trial, which includes the third and fourth images in the figure's photo sequence, it appears that the correct state of the hip joint is flexed. That is, the knee seems to be in front of the hip joint in those photos, thus suggesting that the Qualisys measurements in that period may be erroneous. Although this reasoning is qualitative in nature, it draws into question the accuracy of the Qualisys measurements for the hip extension/flexion DOF during that movement trial as well.

Given the discussion above and in Subsection 6.2.4, the reported exoskeleton system errors may be inflated for trials in which Qualisys inaccuracy is probable. Aside from some examples of erroneous measurements, the experimental proceedings revealed other shortcomings in the optical MoCap technology. First, the limitations in measurement workspace were apparent and even affected several of the studied motions (e.g., this is the reason for only single cycles of gait and stair movements were analyzed). Next, the optical system's susceptibility to occlusion also influenced the subject's movement behaviours. To help prevent occlusion of the pelvis markers, the subject had to maintain a crossed-arm posture during MoCap sessions; this affected subject balance, especially during extended mobility tests. As mentioned in Appendix E, subject inability to maintain this posture during running and subsequent occlusion is the probable cause for the incomplete pelvis marker trajectories for all running trials. Stair traversal movements were also performed in a somewhat unnatural fashion in efforts to prevent occlusion caused by portable stair frame (i.e., the subject placed his right heel much closer to the edge of the top stair than he would in a typical nonexperimental setting). Finally, the Qualisys system involved by far the longest and most complex setup. These practical ramifications elucidate the well-documented disadvantages of optical MoCap systems, as discussed in Subsection 2.1.1.

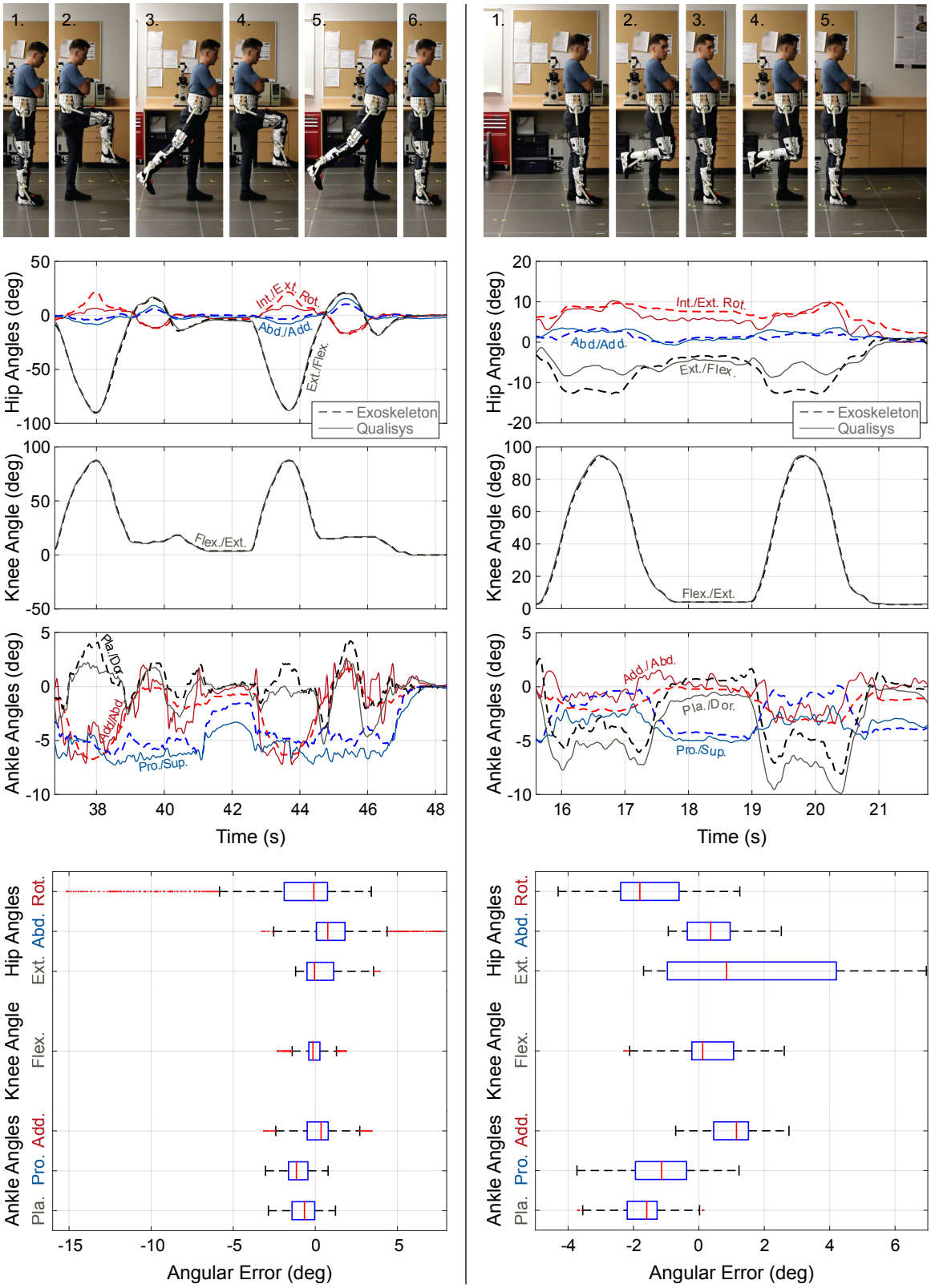

Figure F.1. **Photo sequence, joint trajectories, and box plots of angular errors in the exoskeleton's measurements for two cycles of hip extension/flexion (left) and knee flexion/extension (right)**

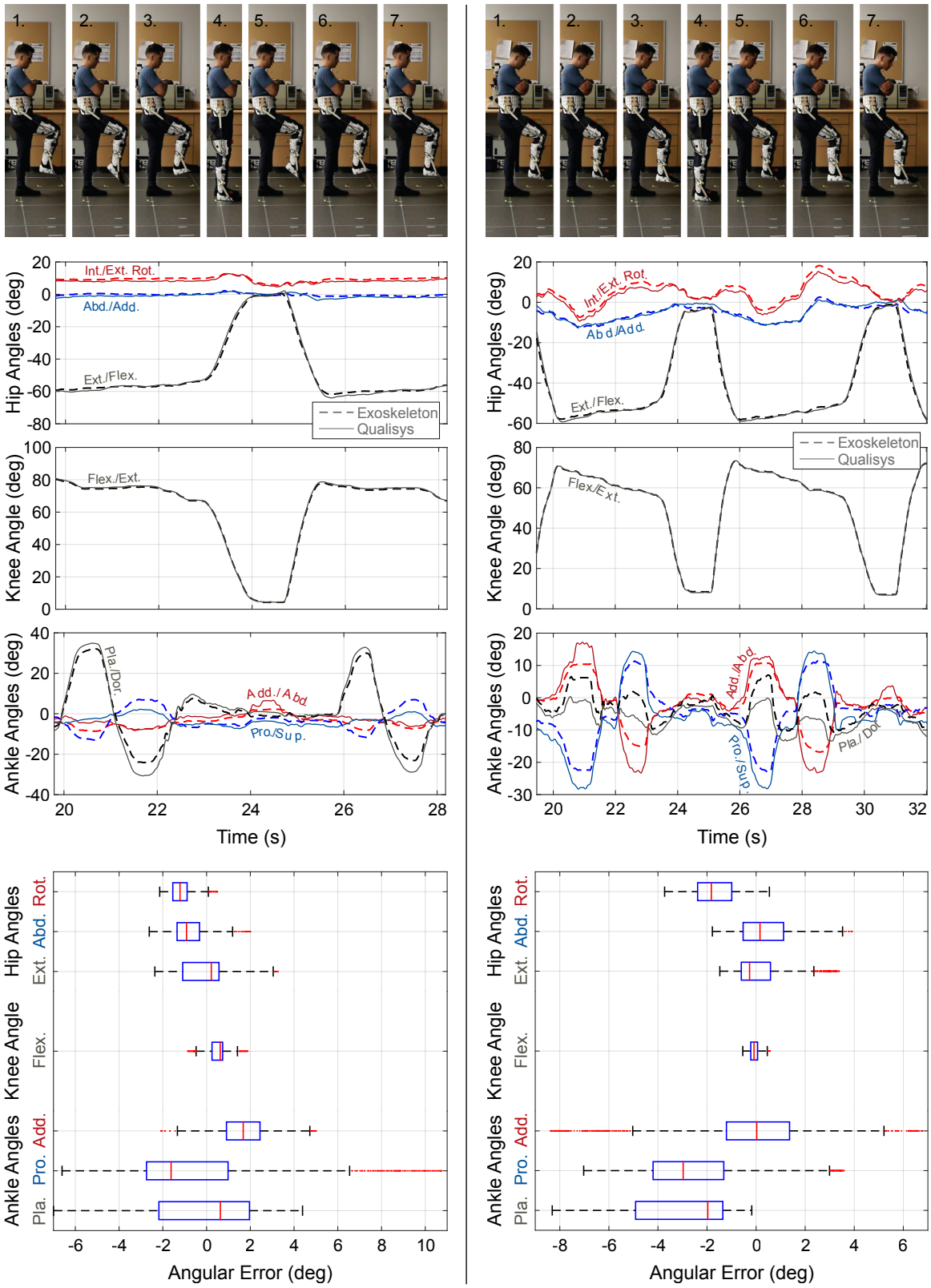

Figure F.2. **Photo sequence, joint trajectories, and box plots of angular errors in the exoskeleton's measurements for two cycles of ankle plantarflexion/dorsiflexion (left) and pronation/supination (right)**

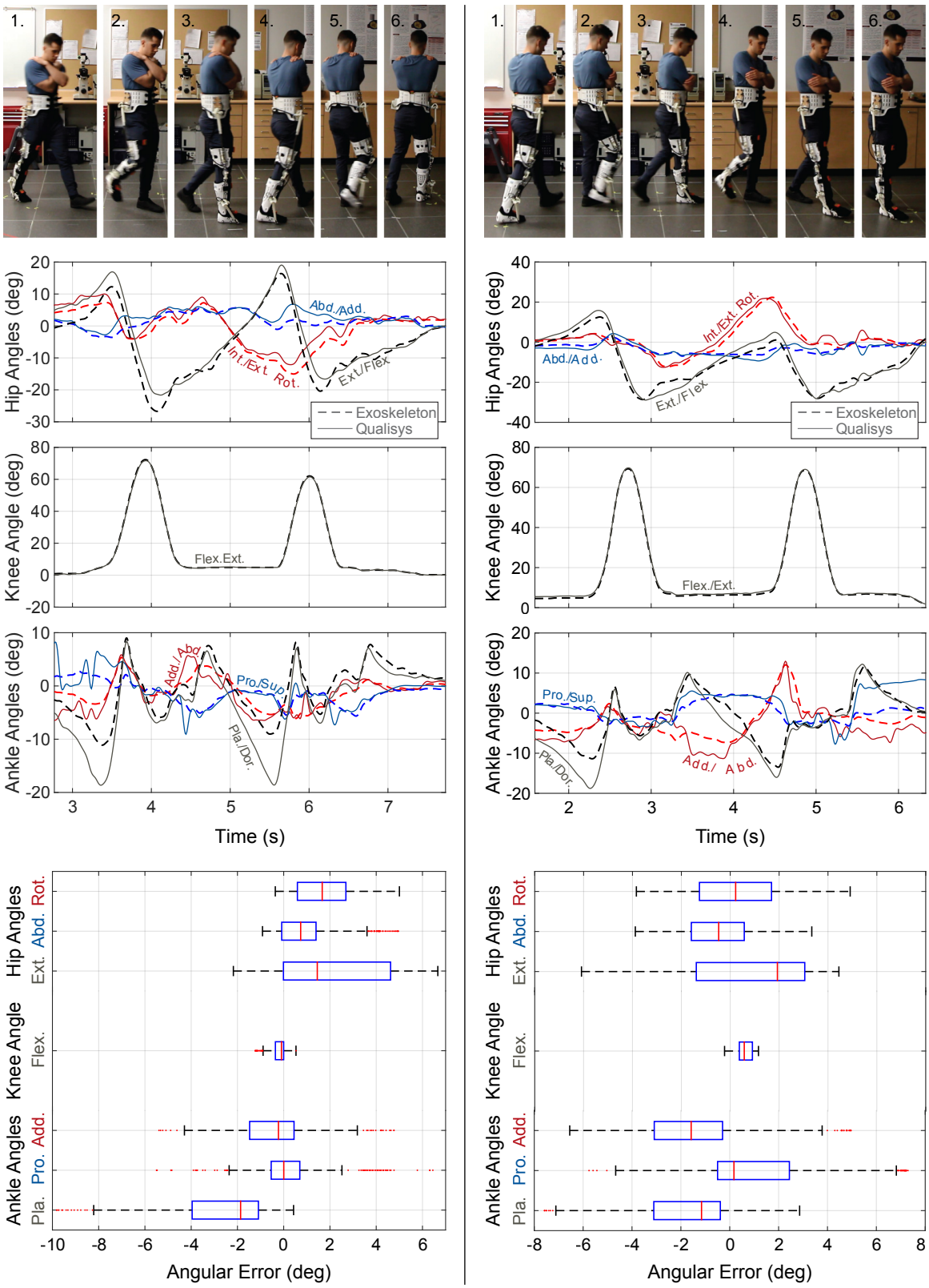

Figure F.3. **Photo sequence, joint trajectories, and box plots of angular errors in the exoskeleton's measurements for one cycle of walking with a left turn (left) and walking with a right turn (right)**

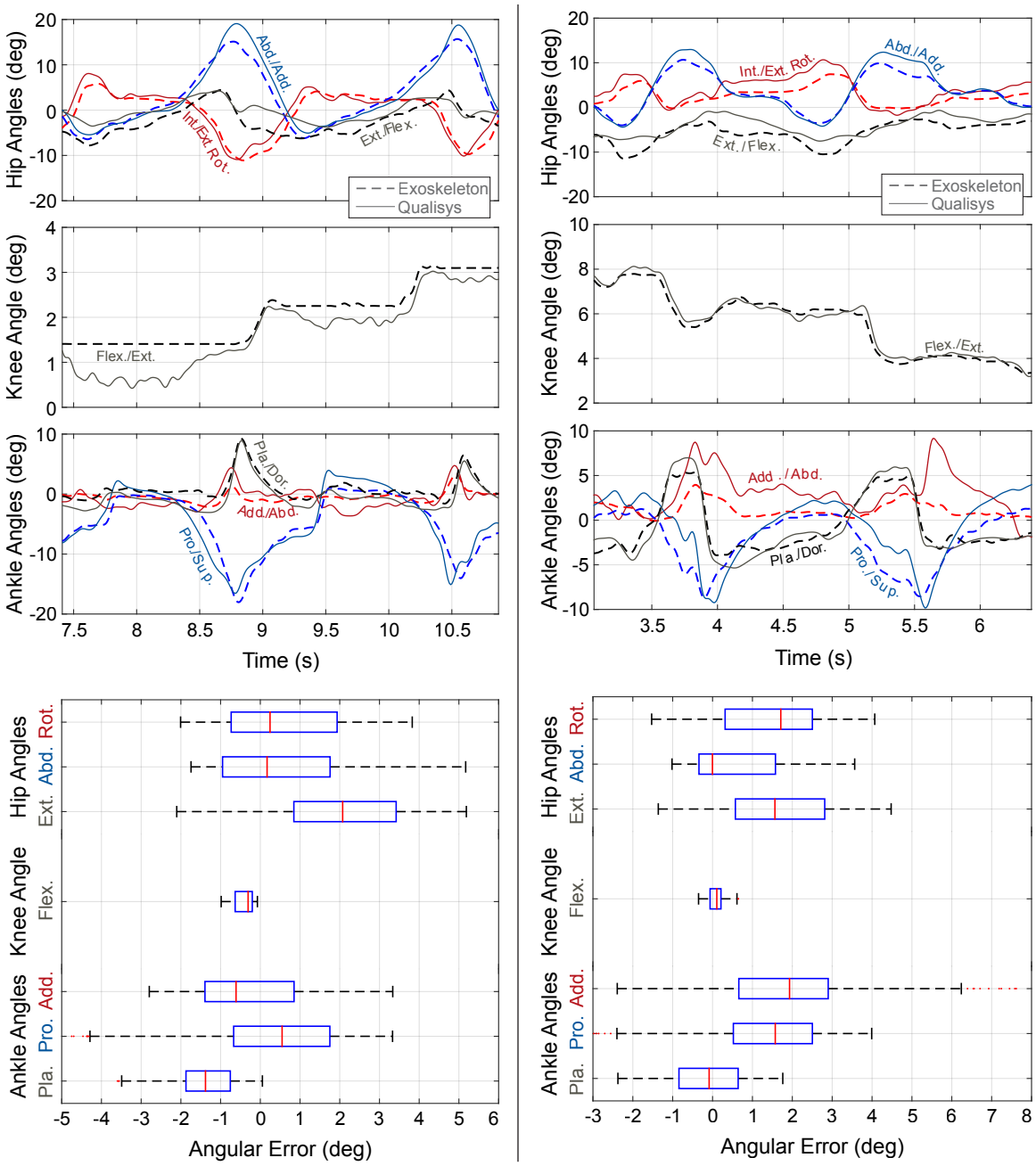

Figure F.4. Joint trajectories and box plots of angular errors in the exoskeleton's measurements for two cycles of leftward lateral walking (left) and rightward lateral walking (right)

Note: No photo sequence is available for these movements because the experimentation-room video camera temporarily shut off. The lateral walking movement involved maintaining a relatively straight-legged posture while alternatingly adducting and abducting at the hip (i.e., bringing the ankles together and then moving them apart, respectively) to achieve sideways movement; feet did not cross each other during the movement.

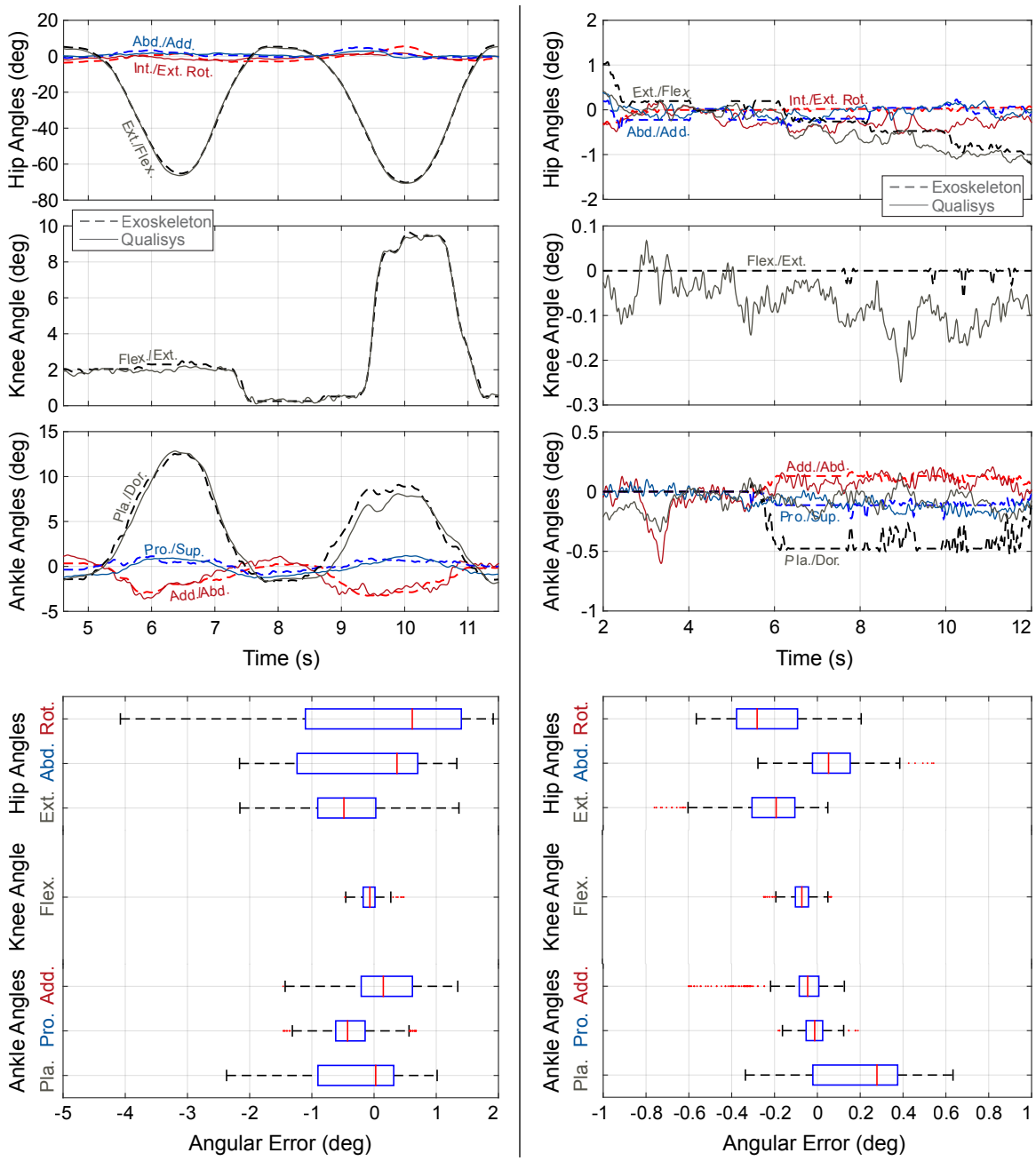

Figure F.5. Joint trajectories and box plots of angular errors in the exoskeleton's measurements for two cycles of bending at the waist (left) and ten seconds of standing still (right)

Note: No photo sequence is available for these movements because the experimentation-room video camera temporarily shut off. The bending-at-the-waist movement involved maintaining a relatively straight-legged posture while alternatingly flexing and extending at the hip (i.e., hinging so to bring the torso towards the floor and then back to a neutral-standing posture, respectively). Also, notice the greatly reduced angular range in the standing-still trial's plots relative to other trials' result plots.

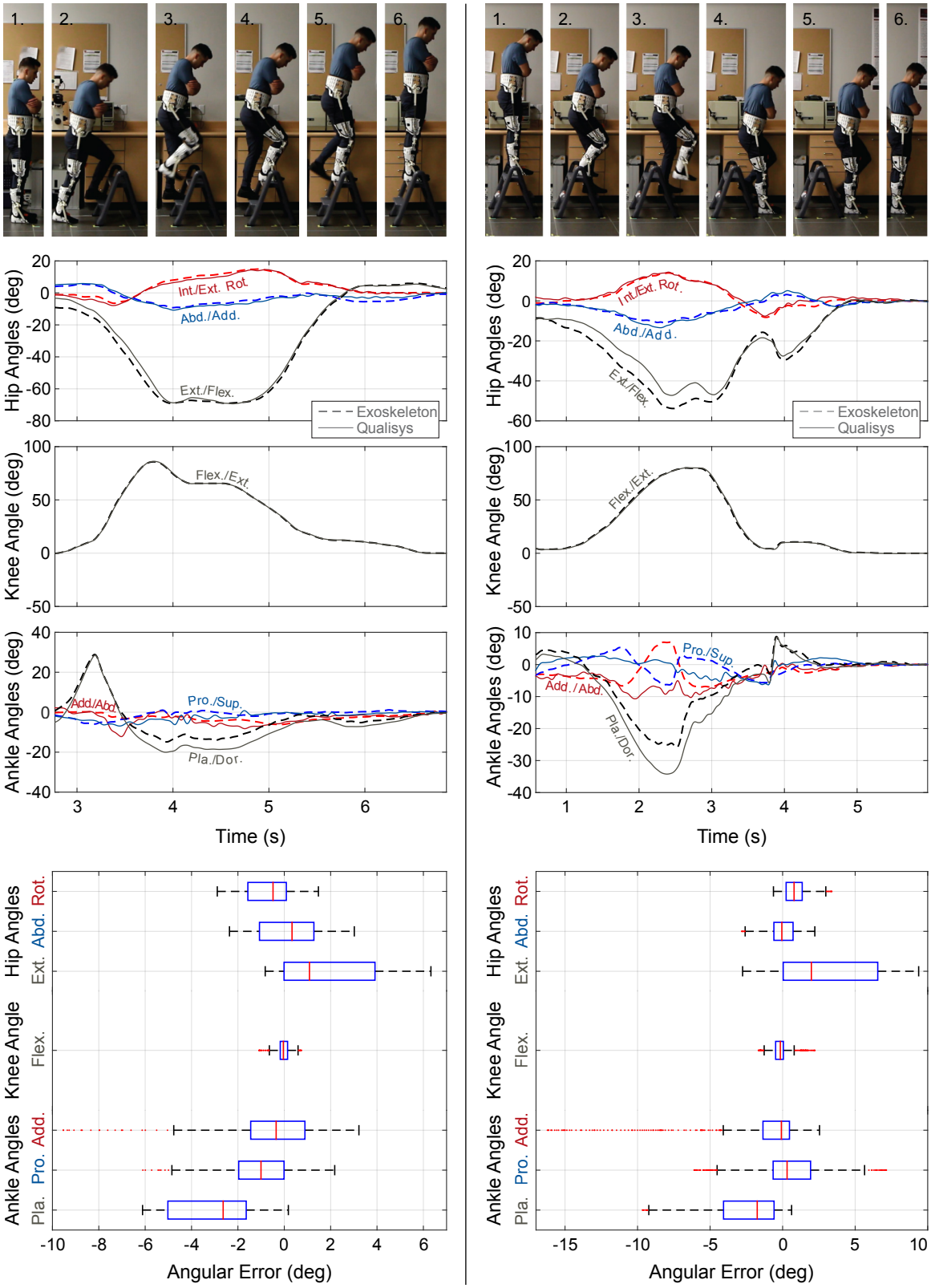

Figure F.6. **Photo sequence, joint trajectories, and box plots of angular errors in the exoskeleton's measurements for one cycle of ascending two stairs (left) and descending two stairs (right)**

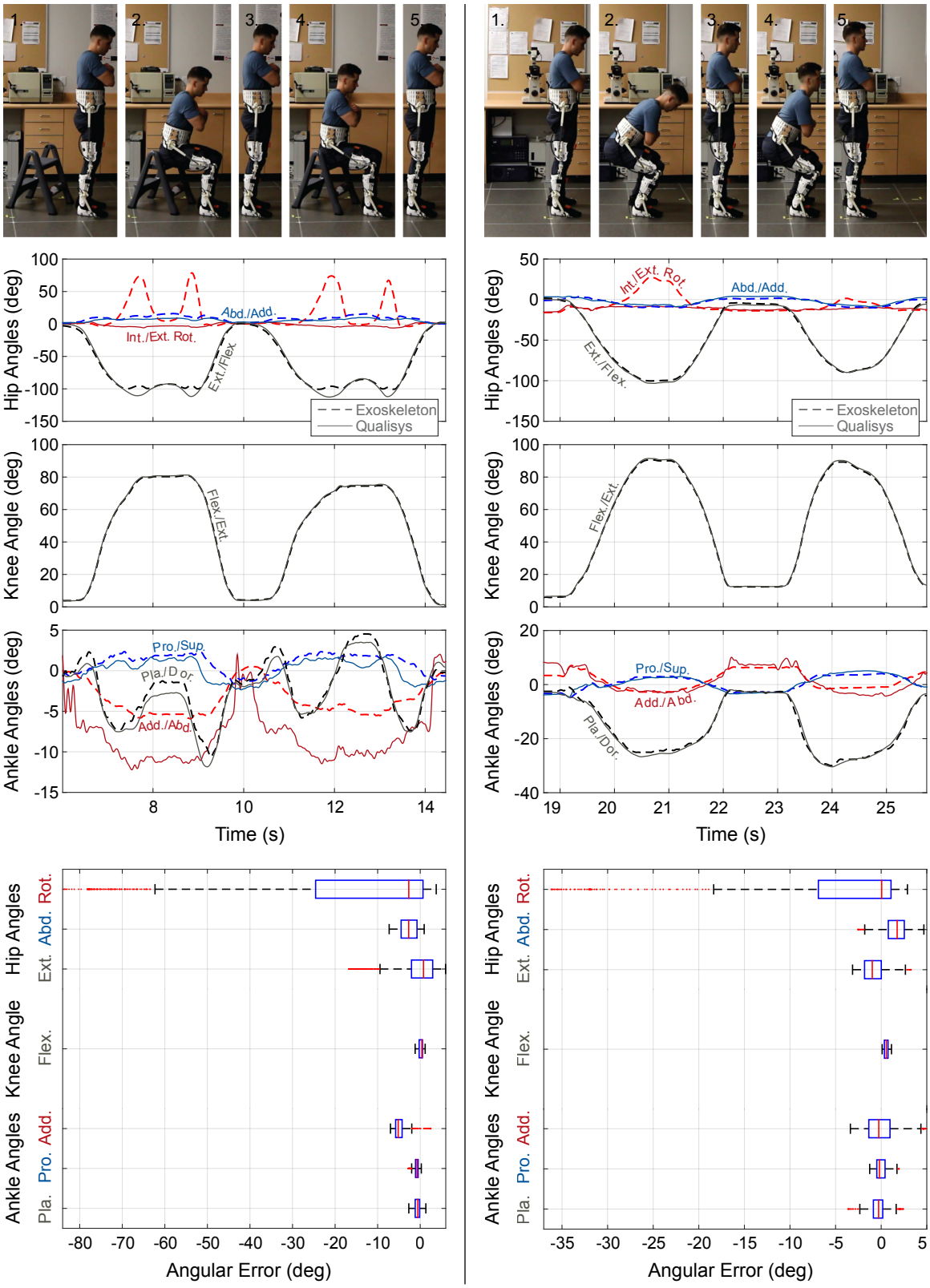

Figure F.7. **Photo sequence, joint trajectories, and box plots of angular errors in the exoskeleton's measurements for two cycles of sitting down and standing up (left) and squatting (right)**

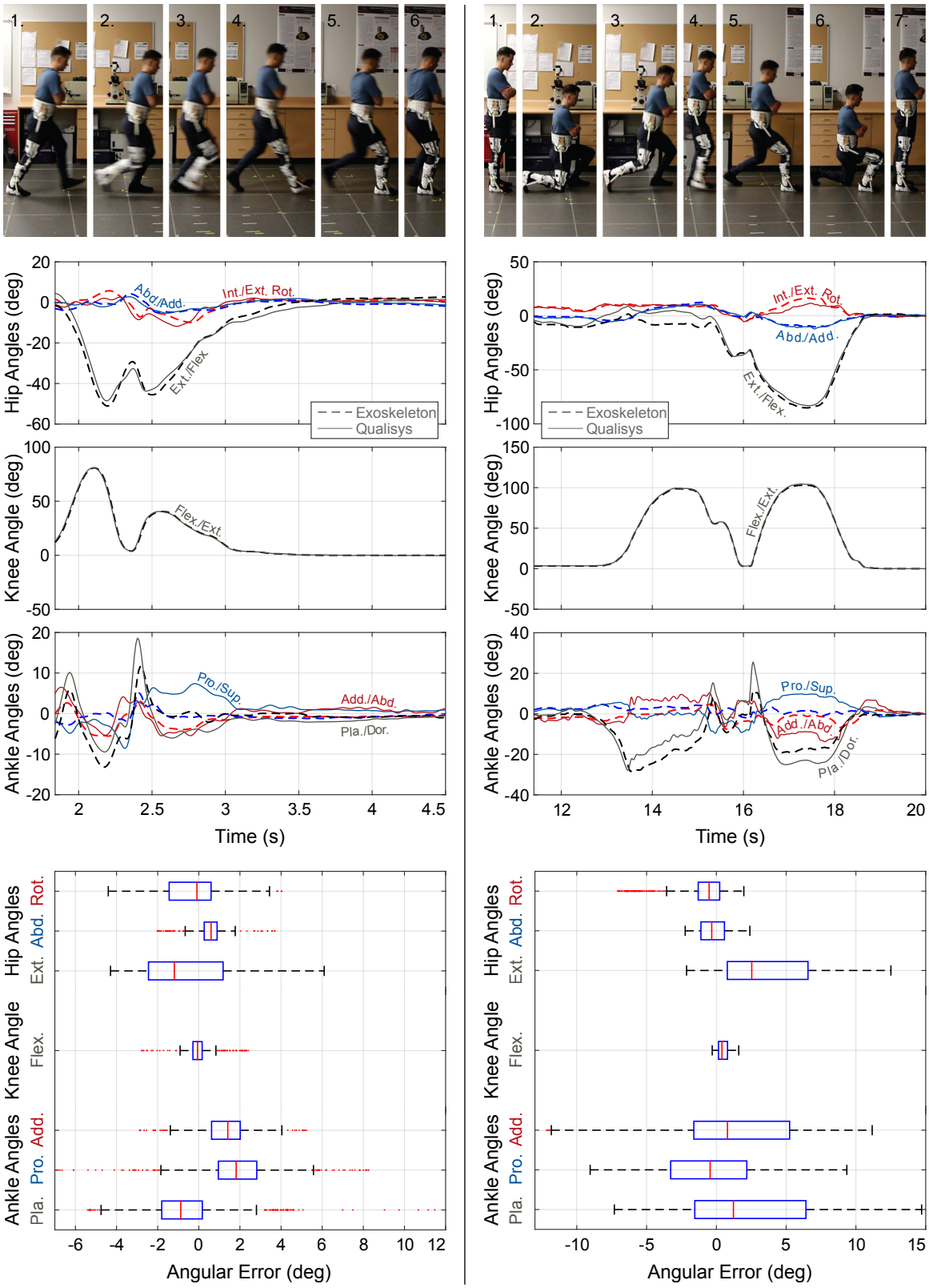

Figure F.8. **Photo sequence, joint trajectories, and box plots of angular errors in the exoskeleton's measurements for one cycle of fast walking (left) and lunge walking (right)**

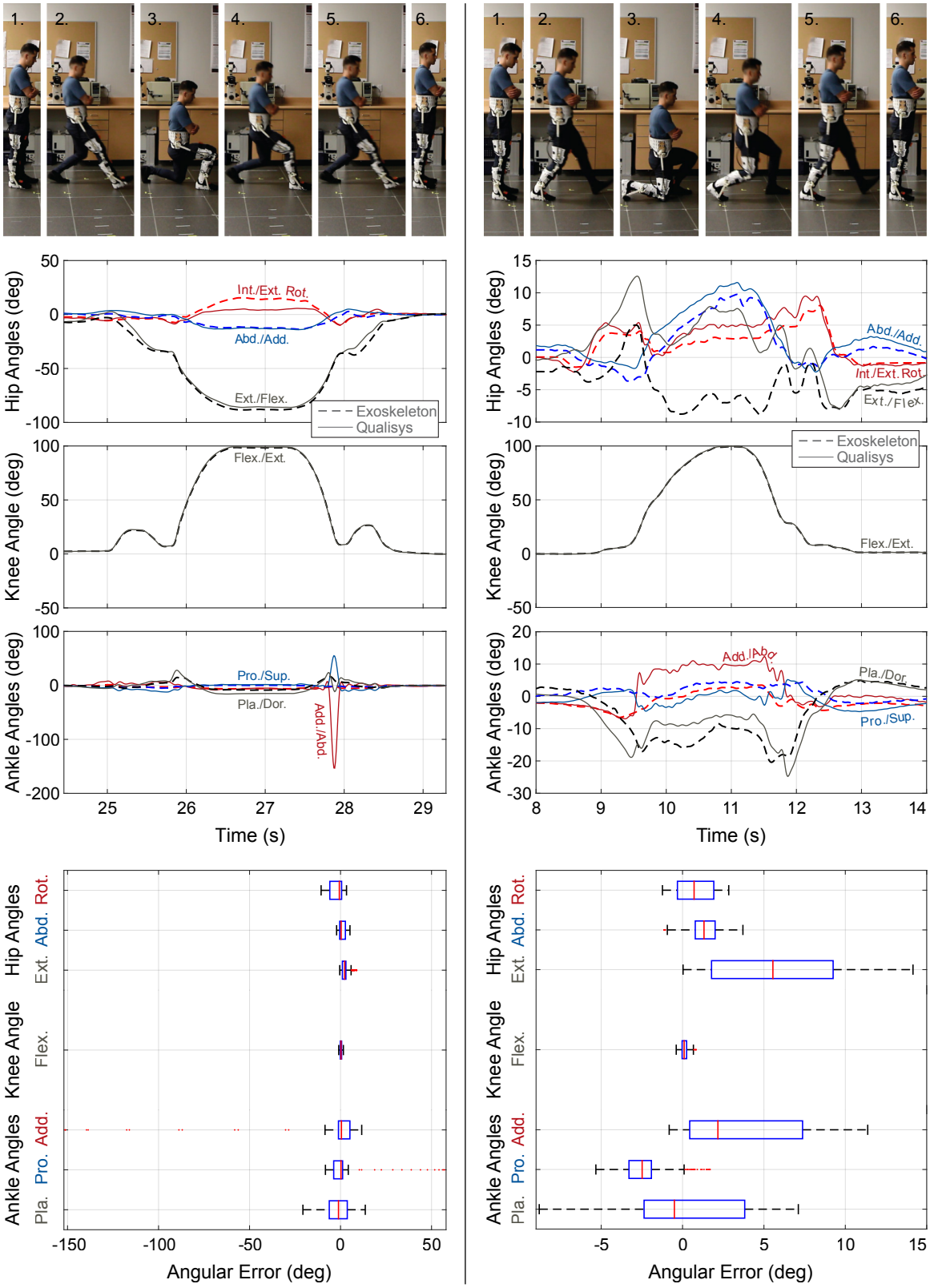

Figure F.9. **Photo sequence, joint trajectories, and box plots of angular errors in the exoskeleton's measurements for one cycle of left-leg kneeling (left) and right-leg kneeling (right)**